UNIVERSITÀ
DEGLI STUDI
DI BRESCIA

DOTTORATO DI RICERCA IN TECHNOLOGY FOR HEALTH

Settore Scientifico Disciplinare ING-INF/06

Ciclo XXXVI

A multidisciplinary experimental framework addressing the relationship between the mechanical behaviour and the structure of the knee articular cartilage

Candidato: Matteo Berni

Supervisore: Prof. Nicola Francesco Lopomo

Co-Supervisore: Ing. Massimiliano Baleani
IRCCS Istituto Ortopedico Rizzoli

Abstract

Articular cartilage is an extremely specialized connective tissue composing the synovial joints. The response of articular cartilage – along with the damping system provided by the other tissues composing the fundamental unit of synovial joints, i.e., the osteochondral unit – is essential in deploying multiaxial forces generated during locomotion. The dynamic interaction between homeostasis and remodelling of the osteochondral tissues is essential in maintaining joints functional capabilities. Several traumatic and degenerative pathologies may deregulate the dynamic remodelling of the osteochondral tissues, especially considering highly stressed articulation as the knee joint. The knowledge on osteochondral tissues is essential in understanding the onset and progression of several pathologies affecting synovial joints, moreover, allowing to elucidate the main aspects on which relative treatments should focus on. In this perspective, the approaches investigating the peculiarities – i.e., mechanical response, structure, and composition – of such a unit are away far from providing reliable and complete information, particularly concerning articular cartilage. Ex-vivo studies focusing on the knee articular cartilage mostly evaluate such a tissue through single-layer tests, yielding insights through multidisciplinary approaches only occasionally.

Within this thesis, a multidisciplinary experimental framework was developed to explore the relationship between functionality and structure of one of the three tissues composing the knee osteochondral unit, the articular cartilage, with a particular focus on tissue biomechanics. Although the approaches here proposed were tailored to articular cartilage, the peculiarities at the base of these techniques are defined aiming to extend their application to study the features of the osteochondral unit in a comprehensive way. First, an indentation protocol was optimized to investigate the articular cartilage viscoelastic response; the implementation of a reliable mechanical testing protocol is crucial to achieve reliable insight on the mechanical response of articular cartilage. Second, the relationship between articular cartilage functionality – i.e., mechanical response – and structure/composition has been investigated, evaluating articular cartilage through the previously optimized indentation protocol and, moreover, an experimental, spectroscopic-based approach. Third, considering the previously mentioned purpose and, further, moving towards a comprehensive evaluation of the osteochondral unit, the use of a specific contrast-agent X-ray imaging was explored to investigate the articular cartilage composition. Fourth, the suitability of a full-field, X-ray-based approach in studying the comprehensive response of the osteochondral unit was also assessed.

The implemented multidisciplinary framework represents a key step forward investigating the main features of the knee articular cartilage, providing the potential of assessing properly the efficacy of clinical and tissue-engineering treatments addressing the pathologies of the knee.

Abstract

La cartilagine è un tessuto connettivo specializzato, facente parte delle articolazioni sinoviali. Il comportamento meccanico della cartilagine – che contribuisce alla funzione di smorzamento delle forze svolta dai tessuti che compongono l'unità fondamentale delle articolazioni sinoviali, nota come unità osteocondrale – risulta essenziale per ridistribuire le forze multi-assiali che si sviluppano all'interno delle articolazioni stesse il movimento. L'interazione dinamica tra omeostasi e rimodellamento dei tessuti che costituiscono l'unità osteocondrale è cruciale per garantire la funzionalità articolare. Molteplici patologie di natura traumatica e degenerativa possono deteriorare il rimodellamento dinamico dei tessuti osteocondrali, specialmente considerando articolazioni altamente sollecitate come quella del ginocchio. Una conoscenza esaustiva dei tessuti osteocondrali è essenziale per comprendere l'insorgenza e la progressione di patologie che compromettono la funzionalità delle articolazioni sinoviali, in particolare con l'obiettivo di evidenziare i principali aspetti e fenomeni su cui i relativi trattamenti dovrebbero concentrarsi. In questa prospettiva, gli approcci attualmente impiegati nello studio dei tessuti osteocondrali – in particolare, volti all'indagine del loro comportamento meccanico, e della loro struttura e composizione – sono ben lontani dal fornire informazioni attendibili, riproducibili e complete, soprattutto in merito alla cartilagine articolare. Nello specifico, gli studi sperimentali ex-vivo che valutano le peculiarità della cartilagine articolare si focalizzano su tale tessuto dopo la sua separazione dalla struttura dell'unità osteocondrale, fornendo informazioni integrate a partire da approcci multidisciplinari solo in alcuni casi.

Nell'ambito di questa tesi di dottorato, un approccio sperimentale e multidisciplinare è stato sviluppato con l'obiettivo di esaminare la relazione tra funzionalità e struttura di uno dei tessuti che compongono l'unità osteocondrale del ginocchio, nello specifico la cartilagine articolare, con particolare attenzione alla sua biomeccanica. Nonostante le metodiche proposte siano state sviluppate tenendo conto delle particolarità del tessuto cartilagineo, le peculiarità alla base delle stesse sono state definite con lo scopo di estendere la loro applicazione allo studio dell'intera unità osteocondrale. In primo luogo, è stato ottimizzato un protocollo di test basato sulla metodica di indentazione per investigare il comportamento viscoelastico del tessuto cartilagineo; l'implementazione di un protocollo di test standardizzato risulta essenziale per ottenere informazioni affidabili e riproducibili sulla biomeccanica della cartilagine articolare. In secondo luogo, la relazione tra funzionalità e struttura/composizione di tale tessuto è stata studiata applicando il protocollo di test precedentemente ottimizzato, e un approccio sperimentale basato su spettroscopia. Inoltre, considerando sia l'obiettivo principale della tesi, ma nella prospettiva di investigare l'unità osteocondrale nella sua interezza, è stato utilizzato uno specifico agente di contrasto per imaging basato su X-ray con l'obiettivo di ottenere informazioni in merito alla composizione della cartilagine articolare. Infine, è stata valutata l'idoneità di un approccio comprensivo basato su raggi X per lo studio del comportamento meccanico dell'unità osteocondrale.

L'approccio multidisciplinare proposto rappresenta un importante passo in avanti nello studio delle caratteristiche principali del tessuto cartilagineo di ginocchio, offrendo la potenzialità di valutare appropriatamente l'efficacia di terapie e di approcci di ingegneria tessutale volte alla cura delle patologie articolari.

Acknowledgments

The activities developed within this thesis project were carried out at the Department of Information Engineering, the University of Brescia, at the Laboratorio di Tecnologia Medica, IRCCS Istituto Ortopedico Rizzoli, and at the Insigneo Institute and School of Medicine and Population Health, the University of Sheffield, from 2020 to 2024.

I wish to thank everyone who has contributed to this thesis and helped me throughout this path. Especially, I would like to mention the following person and founding sources.

I would like to express my gratitude to my supervisors, Professor Nicola Francesco Lopomo and Engineer Massimiliano Baleani. Without their assistance and dedicated involvement throughout the process, this thesis would have never been accomplished. My gratitude goes to Nicola, for his valuable and professional guidance during the thesis. I am grateful to Massimiliano for being my supervisor, for teaching me how to think critically, and transmitting his knowledge, moreover, providing a friendly working environment at the Laboratorio di Tecnologia Medica.

I want to thank my supervisor during my abroad period at the Insigneo Institute, Professor Enrico Dall'Ara. I learned a lot from you and enjoyed working and collaborating with you.

I would like to express my gratitude to the Reviewers, Professor Damien Lacroix and Professor Gianluca Tozzi for their professional and constructive feedbacks on my thesis.

I want to thank all the colleagues I have been working with. In particular, I would like to thank Eng. Paolo Erani, Eng. Roberta Fognani and Dr. Simone Fantoni for providing me with support experimental and imaging techniques, and for fruitful discussions. I send many thanks to Dr. Barbara Bordini and Dr. Monica Cosentino for the advices and the support in statistical analysis. I would like to express my gratitude to Dr. Carlo Golini, Prof. Leonardo Brizi, and Prof. Claudia Testa of the Department of Physics and Astronomy "Augusto Righi" – University of Bologna for the evaluations of the articular cartilage structure through single-sided Nuclear Magnetic Resonance. I wish to thank Dr. Carola Cavallo for providing advices, and for her expertise in biology and histology. I want to thank the group of the Istituto Nazionale di Fisica Nucleare, Department of Physics and Earth Sciences, and the Department of Chemical, Pharmaceutical and Agricultural Sciences – University of Ferrara for providing the contrast agent.

I want to express my deepest gratitude to the people who have always been there, and who will always be there, no matter what.

The studies developed within this dissertation were supported by the following funder: Italian Ministry of Health, grant number RF-2018-12368274, project title: HTO—Impact of high tibial osteotomy in preventing disease progression in medial knee osteoarthritis: Quantifying the effects on cartilage and subchondral bone by using a combined biomechanical and medical imaging approach.

Author’s Contribution

The studies reported in this dissertation are based on original research activities on the establishment of function-structure relationships of the knee articular cartilage, and towards the comprehensive assessment of the osteochondral unit of such a joint. The author was the main contributor to all studies. In the Studies I-IV, the author was involved in conceptualization, design, mechanical testing, data analysis and interpretation, data curation, and visualization. In the Studies I-III, the statistical analysis was performed by the author in collaboration with the Laboratorio di Tecnologia Medica of the IRCCS Istituto Ortopedico Rizzoli. In the Studies II-IV, support in the mechanical testing was provided by the Laboratorio di Tecnologia Medica of the IRCCS Istituto Ortopedico Rizzoli. In Study II, the analysis of the articular cartilage structure through single-sided Nuclear Magnetic Resonance was performed by the Department of Physics and Astronomy "Augusto Righi" of the University of Bologna. In Study III, the contrast agent was provided by the Istituto Nazionale di Fisica Nucleare, Department of Physics and Earth Sciences, and the Department of Chemical, Pharmaceutical and Agricultural Sciences of the University of Ferrara, while acquisitions and analysis of High Resolution Peripheral Quantitative Computed Tomography images were performed by the Laboratorio di Tecnologia Medica of the IRCCS Istituto Ortopedico Rizzoli and by Department of Industrial Engineering of the University of Bologna.

Table of Contents

List of Abbreviations

AC	Articular Cartilage
AFM	Atomic Force Microscopy
BV/TV	Bone Volume to Total Volume
CA	Contrast Agent
CC	Calcified Cartilage
CC	Confined Compression
CECT	Contrast Enhanced Computed Tomography
CE-HRpQCT	Contrast Enhanced-High Resolution peripheral Quantitative Computed Tomography
CNC	Computerized Numerical Control
CT	Computed Tomography
DVC	Digital Volume Correlation
ECM	Extra-Cellular Matrix
FCD	Fixed Charge Density
FRPE	Fibril-Reinforced, non-homogeneous, Poroelastic
GAGs	Glycosaminoglycans
HRpQCT	High Resolution peripheral Quantitative Computed Tomography
HU	Hounsfield Unit
LBPE	Linear Biphasic Poroelastic
MRI	Magnetic Resonance Imaging
NMR	Nuclear Magnetic Resonance
OA	Osteoarthritis
OC	Osteochondral
PBS	Phosphate-Buffered Saline
PE	Polyethylene
PGs	Proteoglycans
PMMA	Polymethyl methacrylate

PTFE	Polytetrafluoroethylene
qMRI	quantitative Magnetic Resonance Imaging
SB	Subchondral Bone
ShIRT	Sheffield Image Registration Toolkit
SNR	Signal-to-Noise Ratio
TB	Trabecular Bone
Tb.N	Trabecular Number
Tb.Sp	Trabecular Separation
Tb.Th	Trabecular Thickness
UC	Unconfined Compression
µCT	Micro Computed Tomography
3D	Three-Dimensional

Symbols and Notations

A	Cross-sectional area of permeation
avgε_z	Average Axial strain
C	Stiffness Matrix
CoV%	Percentage Coefficient of Variation
D	Diffusion coefficient
E	Elastic or Young's Modulus
E_{eq}	Equilibrium Elastic Modulus
E_f	Fibril Network Modulus
E_m	Non-fibrillar Matrix Modulus
E_0	Instantaneous Elastic Modulus
h	Thickness
H_A	Aggregate Modulus
I	Identity Tensor
k	Hydraulic Permeability
Q	Volume flow rate
sdX-disp	Standard deviation of the Displacement along X-axis
sdY-disp	Standard deviation of the Displacement along Y-axis
sdZ-disp	Standard deviation of the Axial displacement
sdε_z	Standard deviation of Axial strain
S_0	Maximum Load
$\mathbf{V}^f$	Velocity vector of the fluid phase
$\mathbf{V}^s$	Velocity vector of the solid phase
x	Fibrils volume fraction
X-disp	Displacement along X-axis
Y-disp	Displacement along Y-axis
Z-disp	Axial displacement

α	Solid-Liquid ratio
β	Stretched coefficient
Δp	Drop of pressure through AC thickness
δ^s	Axial stress of the solid matrix
$\boldsymbol{\delta}^s$	Solid stress tensor
$\boldsymbol{\delta}^f$	Fluid stress tensor
$\boldsymbol{\delta}^t$	Total stress tensor
$\boldsymbol{\delta}_1^{matrix}$	Stress in the drained porous matrix along the X-direction
$\boldsymbol{\delta}_2^{matrix}$	Stress in the drained porous matrix along the Y-direction
$\boldsymbol{\delta}_1^{fibrils}$	Stress in the collagen fibrils along the X-direction
$\boldsymbol{\delta}_2^{fibrils}$	Stress in the collagen fibrils along the Y-direction
$\boldsymbol{\varepsilon}$	Total elastic strain tensor
ε^s	Axial strain of the solid matrix
ε^l	Lateral strain
ε_z	Axial strain
μ_s	Shear modulus
v	Poisson's ratio
τ	Relaxation time
τ_1	Short-time constant
τ_2	Long-time constant
Φ^s	Solid phase volume fraction
Φ^f	Fluid phase volume fraction

1 Introduction

Human body is a complex system consisting of many subsystems and regulatory pathways. Musculoskeletal apparatus provides the body structure and support the ability to move. Joints represent the functional units of the musculoskeletal apparatus, which connect the skeletal structure and enable muscles to actuate physical activity. Among the synovial joints involved in the locomotion system, the knee plays a crucial role in many daily activities, e.g., standing, walking, and running. Although two fundamental units – i.e., tibiofemoral and patellofemoral joints – compose knee articulation, just the first one is mainly responsible for deploying the multiaxial forces developed during locomotion, which may exceed many times the body weight [1]. The damping system provided by tibiofemoral joint during daily activities is allowed by the complex structure of its functional unit, namely the osteochondral (OC) unit, which acts together with meniscal structures. Multi-level organization is the main peculiarity of the OC unit, which is composed by four different tissues, i.e., articular cartilage (AC), calcified cartilage (CC), subchondral bone (SB), and trabecular bone (TB) [2]. Among OC tissues, AC leads the shock-absorption response of the knee, thanks to its multiphasic and inhomogeneous architecture and composition, i.e., proteoglycans (PGs), collagen fiber network, and interstitial fluid [3]. CC and SB form a transition junction, promoting the integration between AC and TB and, furthermore, playing a crucial role in transferring the mechanical loads across different tissues [4].

The dynamic interaction between homeostasis and remodelling of the OC tissues is essential in maintaining the knee functional capabilities, as evidenced by the mechano-regulatory theories [5–7]. Cells composing cartilaginous and mineralized tissues sense mechanical signals and alter their responses accordingly, thus modifying the remodelling processes [8]. Several traumatic and degenerative pathologies may deregulate the dynamic remodelling of OC tissues, especially considering highly stressed articulation as the knee [1]. Osteoarthritis (OA) is a degenerative pathology that plagues several millions of people, impairing the homeostasis of the OC tissues right from the early stages [9]. The ever-growing incidence of OA makes this pathology a major healthcare issue [10], impacting on the individual patient and on the society [11]. This whole-joint pathology is accompanied by varying degrees of functional limitations due to the restricted joint movement, with symptoms worsen dramatically as OA progresses [12]. Due to the onset and progression of OA, the multifactorial crosstalk between cartilaginous and mineralized tissues deregulates, altering simultaneously structure, composition, and mechanical response of such a unit [13].

Although degenerative pathologies as OA strongly impair the overall quality of life, no effective treatments are currently available. Accordingly, prevention remains the most important strategy to mitigate the burden of such diseases. In this perspective, deepen the knowledge on the OC tissues is essential to properly understand the onset and progression of pathologies and, moreover, to elucidate the main aspects on which treatments should focus on. Nowadays, the approaches investigating the OC unit peculiarities are away far from a reliable and complete elucidation on how they relate to each other, especially considering the knee AC. In the last decades, many in vitro studies focused on the knee AC, mostly evaluating this tissue – and, eventually, the others composing the OC unit – through single-layer tests, specifically addressing its biomechanics. In addition, few studies applied and retrieved information through multidisciplinary approaches, i.e., by imaging or by Nuclear Magnetic Resonance (NMR) signals – thus to provide insights on tissue structure and composition – and mechanical testing to evaluated the tissue

response. A multidisciplinary approach tailored to the OC tissues should evaluate comprehensively their main features – i.e., structure, composition, and mechanical response –, moreover replicating, as close as possible, the in vivo boundary conditions. In this regard, it is particularly important to consider the AC biomechanics by maintaining its connection to the underlying bone structures, especially considering the strictly dependence of AC properties on such a bond [14,15].

In this thesis, a multidisciplinary experimental framework was developed addressing the relationship between the functionality and the structure of the main tissue composing the knee OC unit, i.e., AC, focusing on its biomechanics. Although the approaches here proposed are specifically tailored to the AC, the peculiarities of the techniques were defined aiming to extend their application to study comprehensively the features of the entire OC unit.

In **Study I**, a standardized testing protocol investigating the AC viscoelastic response was implemented. The purpose of Study I lies in the development of a reliable mechanical testing approach providing sound insights on the AC mechanical response, thus to offer knowledge able to improve tissue engineering approaches dealing with AC pathologies.

Study II and **Study III** focused on the relationship between functionality – i.e., mechanical response – and structure/composition of AC. Information achieved by applying the optimized testing protocol was combined to the insights retrieved through experimental techniques, i.e., single-sided NMR and contrast-enhanced X-ray micro-Computed Tomography (μCT), respectively. As a future development, an additional part is proposed aiming investigate the impact of degeneration on the features of the AC; more in detail, an in vitro approach is currently under consideration to simulate early degeneration via enzymatic digestion.

With the view of investigating the response of the OC unit to loading, **Study IV** investigated the suitability of a full-field, imaging-based approach – i.e., Digital Volume Correlation (DVC) – to study the comprehensive functional behaviour of such a unit. An experimental method was developed to validate the axial displacement and strain computed by X-ray-based DVC, applying a loading scenario peculiar of the knee OC unit, – i.e., contact pressure.

The multidisciplinary framework implemented in this dissertation could represent a first step forward in providing an exhaustive investigation of the main features of the knee AC. In addition, the developed pipelines could be potentially applied to the whole OC unit, thus to study its peculiarities by maintaining – as close as possible – the native boundary conditions. Moreover, the proposed approach could be employed to assess properly the efficacy of clinical and tissue-engineering treatments addressing traumatic and degenerative pathologies that impair the homeostasis and the functionality of load-bearing joints.

2 Knee joint

Diarthrodial joints are highly advanced and sophisticated anatomical structures, composed by several specialized tissues. Among diarthrodial joints, the knee is the most demanding and important articulation, playing a crucial role in locomotion [16]. The knee can be considered as a modified hinge-type synovial joint, allowing a wide range of motion [17]. Knee joint integrates femur, tibia and patella bones into one functional unit (**Fig. 2.1**), providing smooth locomotion in certain directions but limiting in others; due to the connection of such bones, the knee is composed by two articulations, i.e., tibio-femoral and patello-femoral. The tibio-femoral articulation connects the distal femur to the proximal tibia, enabling flexion-extension and intra-extra rotation [16], while the patello-femoral articulation occurs between the posterior surface of the patella and the trochlear surface of the distal anterior femur, and its main role is to transfer muscle forces [18,19].

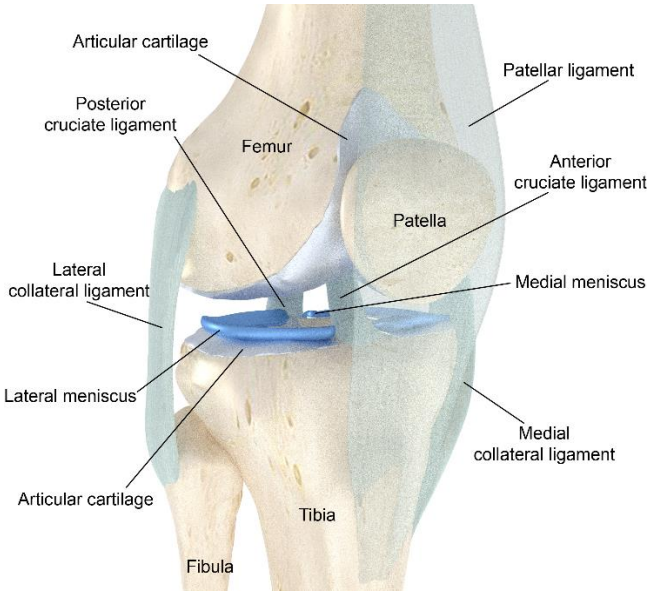

Fig. 2.1. Anatomy of the knee joint, in a front-lateral view.

Besides bones, knee is composed by different soft tissues (**Fig. 2.1**), each one contributing significantly to the joint functionality. A fibrous capsule surrounds the knee, which inner surface, named synovium, provides crucial functions, i.e., supplying nutrients to the joint soft tissues and secreting the synovial fluid [20]. Ligaments and tendons are passive viscoelastic, dense, fibrous connective structures mainly acting in tension, located outside the knee capsule and connecting bone to bone, or muscle to bone, respectively. The main functions of these structures differ from each other; in fact, ligaments provide joint stability, preventing dislocation [16], while tendons transmit mechanical forces though muscles, stabilizing the

skeleton during body movement [21]. Four primary ligaments stabilize the knee. The cruciate ligaments – anterior and posterior – connect femur and tibial antero-posteriorly, preventing tibial translation. The medial and lateral collateral ligaments originate from the femur, connecting its distal part to the lateral surface of the fibular head, and to the medial side of the tibia, respectively; the primary role of collateral ligaments is to restrain abnormal motion, mainly preventing varus-valgus angles [22]. Menisci are fibrocartilaginous structures located between the articulating surfaces of femur and tibia. These structures cover ~ 60% of the tibio-femoral contact area [23], increase the congruence of articulating surfaces [24] and, most importantly, represent a first, passive shock absorber mechanism protecting the knee joint from excessive loads [25].

Beyond menisci, the main mechanism of knee joint to deploy the multiaxial forces developed during daily activities is allowed by the outstanding structure complexity of its fundamental load-bearing unit, overall known as OC unit. Four levels of organization – i.e., AC, CC, SB and, finally, TB – are included in such a unit [26] (**Fig. 2.2**).

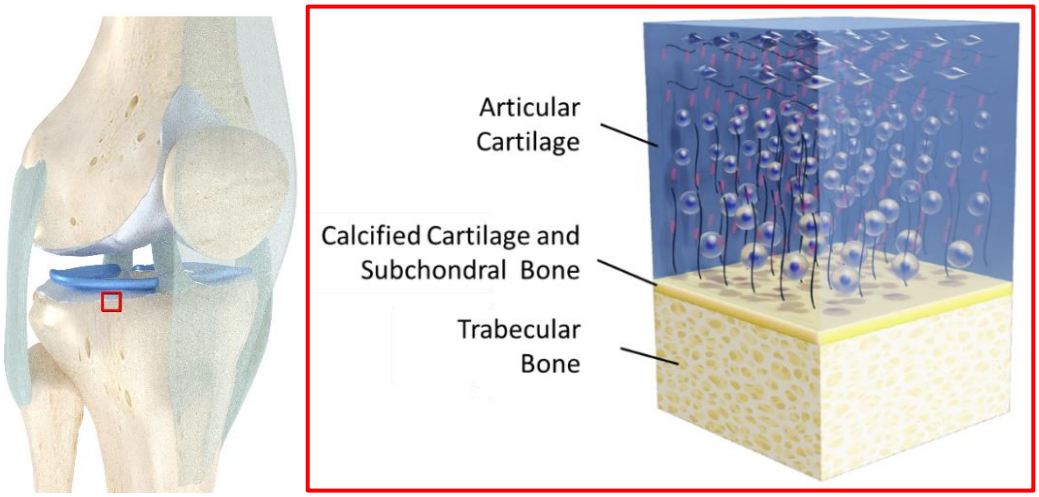

Fig. 2.2. Schematic representation of the knee joint OC unit.

AC represents a fibril-reinforced, composite material consisting of a solid matrix, mainly formed by structural macromolecules and interstitial fluid phase [3].

CC and SB layers form a transition area between the articular surface and the TB, characterized by a depth-dependent composition and structure. The junction of these layers is of great importance for ensuring and maintaining the integration between cartilage and bone, playing a crucial role also in transferring mechanical loads across different tissues [4]. CC is composed by a mineral matrix – made by collagen, sodium hyaluronate, and nanohydroxyapatite in varying proportions [27] – within which dispersed, hypertrophic chondrocytes are organized inside lacunae [28]. As a transition layer between AC and SB, CC functions as a membrane, maintaining joints homeostasis and providing channels for small molecules [29]. Moreover, CC can minimize shear stresses [30], transmitting and dissipating forces thanks to a network of collagen fibrils and to a high amount of mineral content – explaining why the elastic modulus of CC is equivalent to that of SB [31].

SB is a biphasic tissue, consisting of an inorganic – i.e., hydroxyapatite crystals – and organic – i.e., type I collagen, proteoglycan, glycosaminoglycans, and water – components, accountable for rigidity and

elasticity, respectively [32]. The structure of SB is uniquely designed to disperse axial loads across the joint, sparing the overlying AC [32]. The architecture and physiology of SB is depth-dependent, starting from the more compact bone layer adjacent to CC – named SB plate, and ranging from 10 μm to 3 mm in thickness – to the one closer to the medullary cavity [32]. Regarding this complexity, SB is able to adapt its structure and morphology in response to stresses acting on the joint. Adaptive function of SB is facilitated by the activities of osteoblasts and osteoclasts, and by the rich tissue vascularization, which plays a crucial role also in its remodelling by the exchange of oxygen, nutrients, and metabolic waste.

At the bottom of the OC unit, the trabecular (or cancellous) bone is a hierarchical spongy, and porous structure which, at the macrostructural scale, consists of an irregular network of trabecular struts and plates – providing a stiff framework for cellular spaces –, filled with bone marrow and cells [33].

At the microstructural scale, the structure of TB is arranged to optimize the load transfer. Mineral and collagen content and architecture determine the mechanical properties of TB tissue [34].

Since this thesis focused on a multidisciplinary assessment of the main features of the knee AC, only this tissue will be examined more specifically in the following.

3 Articular Cartilage

AC is an extremely specialized connective tissue, covering the ends of articulating bones. Focusing on knee joint, AC covers the distal and proximal part of femur and tibia, absorbing and distributing the mechanical loads [4], as well as providing almost frictionless surfaces – thanks also to the synovial fluid of synovium – for the articulation of bones. These functions require structure and composition able to dynamically respond and adapt to the mechanobiological stressors of the AC [35].

3.1 Structure and Composition of the Articular Cartilage

Although AC seems to be homogeneous at the macroscopic scale, its structure and composition are highly heterogeneous (**Fig. 3.1**). Accordingly, AC is defined as a multiphasic heterogeneous tissue, with limited healing capability due to its avascular nature [36]. More in detail, AC structure is defined by a sparse distribution of highly specialized cells – named chondrocytes – within a dense Extra-Cellular Matrix (ECM) [37]. Thanks to the ECM dense structure, a fluid content – named interstitial fluid – is entrapped within AC, which allows to maintain the unique mechanical properties of the tissue [38].

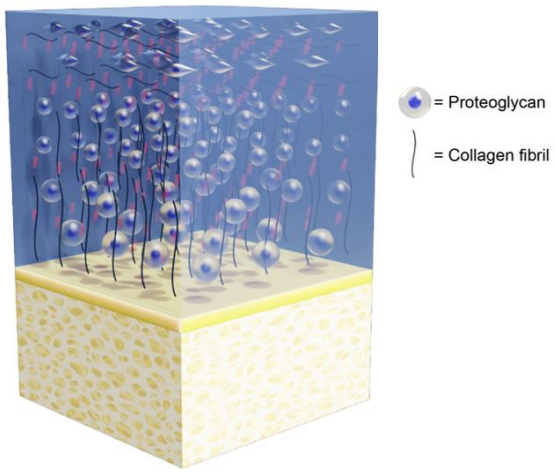

Fig. 3.1. Schematic representation of the inner structure and composition of AC.

3.1.1 Chondrocytes

Chondrocytes are the only active cells encapsulated within the ECM of AC. Chondrocytes present an ellipsoidal shape, and are made by a viscoelastic skeleton, a cell membrane, and fluid [39]. Chondrocytes derive from mesenchymal stem cells and occupy 1%–5% of the total AC [37]. The primary function of these cells is to synthesize and maintain a large volume of ECM components, e.g., collagen and PGs, providing the mechanical ability to withstand compressional, tensile and shear forces across diarthrodial

joints [40]. Chondrocytes organization and phenotype vary with depth [41]. In the superficial zone of AC, chondrocytes are abundant, secreting molecules helping lubrication despite the low metabolic rates [42]. Moving to the bottom of the tissue, a decrease of cells density is highlighted, while chondrocytes biosynthesis rates increases, i.e., producing molecules as type II collagen and aggrecan [43].

3.1.2 Extracellular Matrix

ECM represents ~ 90% of the AC total volume, and is composed by a fiber-based collagen network and by a locally entrapped negatively charged PGs within [44,45].

Collagen is the most abundant structural protein in the human body, ensuring tissues integrity [46]. Accordingly, it represents most of the structural macromolecule in ECM, accounting up to 60%-70% of the AC dry weight [4]. The ECM of AC is composed by different types of collagen, among which type II collagen forms ~90% of the tissue collagen network [47]. Other types of collagen – e.g., type III, IV, V, VI, IX, X and XI [48]– support type II in the crosslinking processes, stabilizing its network and providing additional cohesion or strength when type II is damaged [49]. The main function of the collagen network is to maintain the structural integrity of AC, providing tensile and shear stiffness [50,51]; in addition, collagen network is responsible in maintaining the osmotic swelling pressure caused by the negatively charged PGs entrapped within its structure [52], thus contributing to the compressive (fast) dynamic tissue response [53]. The collagen network presents a depth-wise division. Despite collagen content remains almost constant with depth – even if slightly higher in the superficial AC –, collagen fiber orientation changes from parallel to the surface in the superficial zone, to perpendicular in the deep zone [54].

Besides collagen, PGs are the most significant proteins in ECM, accounting for ~ 20% of the AC dry weight [55]. The structure of PGs is made usually by a protein core at which one or more linear glycosaminoglycan chains are covalently attached; in turn, each chain may be composed by more than a hundred monosaccharides, extending out from the main protein core, and remaining separated from one another due to charge repulsion [44]. Despite a large variety of PGs can be found in the ECM of AC – e.g., decorin, perlecan, biglycan, and fibromodulin –, aggrecan is the largest and the most abundant [4]. Aggrecan PGs are composed by a core protein – e.g., hyaluronic acid – at which glycosaminoglycans (GAGs) are attached through link proteins. GAGs contain sulfate substituents – e.g., chondroitin and keratin sulfates – at various positions, which are responsible of GAGs negative charge. Together with tissue osmolarity – i.e., ion concentration within the interstitial fluid – aggrecan PGs define the fixed charge density (FCD) inside the cartilage matrix. The main functions of PGs is strictly related to the peculiarities of the GAGs by which they are composed, providing to AC hydration, osmotic properties and swelling pressure, crucial to withstand compressive load [4]. PGs concentration is depth-dependent, with the majority reached in the AC deep-layer [56,57].

3.1.3 Interstitial Fluid

The interstitial fluid entrapped within the ECM is mostly composed by water, but it also contains gases, small proteins – needed for the tissue cells –, and electrolytes, i.e., sodium (Na^+), chloride (Cl^-), and calcium (Ca^{2+}) [38]. Interstitial fluid represents up to ~ 70-80% of the AC total weight [20]. The concentration of electrolytes inside the tissue is higher than that in the knee cavity fluid, causing an imbalance that produces a pressure gradient inside the tissue – the Donnan (ionic) osmotic pressure –; such a gradient plays a key role in mediating the mechanical response of AC, e.g., contributing strongly to the tissue stiffness under instant loads [58]. Interstitial fluid is free to flow through the porous ECM when AC is subjected to load

[59], providing nutrition to the tissue [60] and, moreover, contributing to its time-dependent response [61]. Interstitial fluid content is controlled by PGs concentration, the resulting swelling pressure, and by the collagen network orientation and stiffness [62]. Accordingly, interstitial fluid content decreases as function of depth and, most importantly, its amount can change due to age and joint pathological condition [63].

3.1.4 Articular Cartilage Layers and Regions

Considering the spatial distribution of the AC components, four layers can be identified within such a tissue, namely superficial, middle, deep layer, and CC [4].

The superficial layer represents ~ 10-20% of the AC thickness and it is characterized by a relative high number of flattened ellipsoid chondrocytes and thin collagen fibrils – primarily, type II and IX collagen – packed and aligned parallel to the articular surface [64]. The integrity of this layer is of paramount importance, as it is in direct contact with the synovial fluid and, even more important, provides tensile, and shear strength [65]. The middle – or intermediate – layer represents ~ 40-50% of the AC thickness and it is mainly composed by low-density spheroid-shaped chondrocytes, PGs, and thicker and randomly arranged collagen fibres [64]. The middle layer fulfils the key role of functionally bridging the superficial and deep zones and, moreover, represents the first line providing compressive strength [65]. The deep layer represents ~ 20-30% of AC thickness, and is composed by spheroid-shaped chondrocytes oriented perpendicular to the joint line, the highest PGs content, collagen fibrils with the largest diameter and with the same orientation of chondrocytes – i.e., perpendicular to the articular surface –, and the lowest water content [66]. The main function of the deep layer is to provide the highest compressive strength to AC [4]. Finally, CC is composed by hypertrophic chondrocytes, dispersed in a calcified matrix consisting of type I collagen, sodium hyaluronate, and nanohydroxyapatite in varying proportions [27]. CC represents the anchor of the collagen fibrils to the SB, securing AC to bone [67].

Besides the organization in layers, three regions can be identified within each layer – namely pericellular, territorial and inter-territorial region – mainly according to the proximity to the chondrocytes [4]. The pericellular matrix is a thin layer containing PGs and other proteins, enveloping the chondrocytes and representing the first path of the load-bearing signal transduction within AC [68]. The territorial matrix – thicker than the previous – is mainly composed by thin collagen fibrils, and represents the second cover of the chondrocytes [69]; the main function of this matrix is to protect chondrocytes against mechanical stress, contributing to the resiliency of AC [70]. The inter-territorial region consists of PGs in high concentration, and large collagen fibrils with a depth-dependent orientation – i.e., parallel to the articular surface in the superficial layer, obliquely in the middle layer, and perpendicular to the SB in the deep layer –; among the three matrix regions, inter-territorial one contributes the most to the AC biomechanics [71].

3.2 Articular Cartilage Pathological Condition

AC plays a key role in the functioning of diarthrodial joints, providing a wear-resistant, and nearly frictionless surface withstanding high cyclic loads, and transmitting them to the underlying tissues of the OC unit [72]. Nevertheless, due to its avascular nature and consequently limited healing capacity [36], AC may face structure alteration due to aging [73], traumatic events [74], sub-optimal treatments [75], or degenerative pathologies [72].

Focusing on the knee, OA is one of the most important chronic and trauma-induced disease [76], which can be classified as primary (idiopathic) and secondary OA [77]. Primary OA occurs due to natural phenomena and combination of risk factors, e.g., increasing age, obesity, knee malalignment, genetics and,

as recently suggested, low-grade systemic inflammation [78]. The Onset of secondary OA is attributable to causative factors, as trauma, surgery on the joint structures – i.e., meniscectomy and sub-optimal reconstruction of the anterior cruciate ligament –, congenital and other diseases, disorders of metabolism or of the bone [77].

Regardless the etiology, the ever-growing prevalence and incidence of OA makes this condition a major healthcare problem affecting a wide part of the population, i.e., more than 500 million people worldwide [9,79]. Despite OA prevalence increased with age, Global Burden of Disease data highlighted that the disease had an annual global increase of ~9% starting by the 28-years age, [80,81] suggesting the contribute of occupational and traumatic factors in spreading such a pathology in young and adult population. At the joint level, OA induces disabling features, especially pain and loss of functionality. As OA progresses, the symptoms worsen dramatically: pain becomes continuous and the performance of the joint is severely impaired, resulting in a significant, negative impact on social life, work productivity and psychological wellness of the subject. These systemic alterations are in a cause-and-effect relationship to the modifications occurring within the joint.

The pathogenesis of OA starts when the dynamic remodelling of OC tissues is altered by a not-yet-well-understood combination of harmful influences [6], affecting the whole articular compartment since the early stages [26]. In case of secondary (post-traumatic) OA, a preliminary phase is highlighted, consisting in a wide inflammatory response, which suggests that inflammatory cytokines contribute to the onset of such a pathology [82]. In regard of structural changes, the first visible sign of OA – detectable through histology – is represented by a fibrillation of the AC surface (**Fig. 3.2**, top-right corner); in addition, a loss of superficial PGs, destruction of collagen network, as well as an increase in the interstitial fluid content occur since the early OA [83,84]. As a results of collagen network degradation and FCD alteration, AC is no more able to withstand tensile stresses induced by swelling, resulting in an even more softening and swelling; due to such abnormal swelling, more PGs can escape from the ECM, reducing even more the FCD, and increasing tissue permeability [85].

As OA progresses, the fibrillation extents to the middle and deeper layers of the AC (**Fig. 3.2**, bottom-left corner), finally reaching the SB; as a results of growing fissures, fragment of the superficial layer are released into the joint space, inducing thinning of the AC [83]. In the meanwhile, chondrocytes acquire a hypertrophic phenotype, inducing the expression of inflammation- and catabolic-related genes [85]. Due to the abnormal production and release of matrix metalloproteinases – upregulating the proinflammatory cascade – and matrix-degrading enzymes, structure and, thus, functionality of the AC result to be irreversible altered [86]. Finally, due to the failure of reparative mechanism in restoring the AC homeostasis, direct bone-to-bone contact occurs, resulting in calcification of the residual AC, bone marrow lesions, cyst formation, with observations of changes to density, separation and quantity of the TB (**Fig. 3.2**, bottom-right corner) [87].

According to the above-mentioned alterations, the multi-factorial crosstalk between AC and bone tissue became a well-established paradigm in the OA progression [26], logically impairing the mechanical response of the whole OC unit [13].

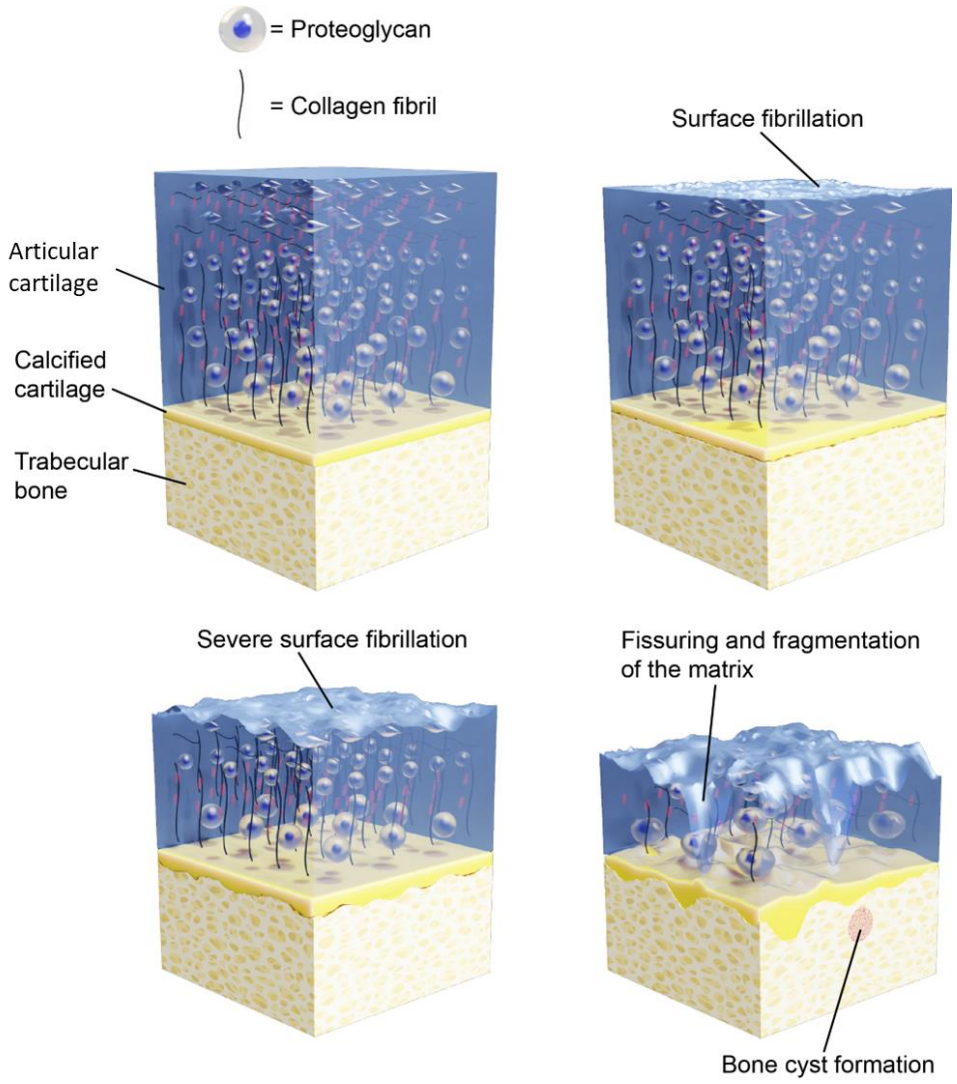

Fig. 3.2. Schematic representation of the alterations induced within AC and, more generally, OC unit by onset and progression of OA. (Top-Left corner) Structure and composition of the OC unit and, in particular, of AC in healthy condition. (Top-Right corner) As a first sign of OA, fibrillation of AC surface occurs. (Bottom-Left corner) As OA progresses, the fibrillation extents to the entire AC layer, finally leading to (Bottom-Right corner) calcification of the residual AC, bone marrow lesions, and cyst formation.

3.3 Biomechanics of the Articular Cartilage

As the main function of AC is to withstand to the complex stressors peculiar of load-bearing joints, the biomechanics represents a useful indicator of the onset of diseases impairing tissue functionality [14].

As reported in paragraph 3.1, AC mainly consists of a fluid – interstitial fluid – and a solid – ECM, primarily made by PGs and collagen network – phase; thus, it is reasonable to consider the response of the tissue as the one provided by a biphasic medium [4]. When AC withstands to an external load, an initial and rapid deformation – i.e., change in volume – is produced, primarily inducing i) an increase in the pressure of the interstitial fluid, and ii) a change in PGs molecular domains [4,88]. If the interstitial fluid

pressure exceeds the osmotic swelling one, the interstitial fluid flows through the porous ECM, generating a large frictional drag within it; moreover, exudation of the fluid from the tissue occurs but, thanks to the low permeability of AC, its quick squeezed out of the matrix is prevented [88]. By decreasing the interstitial fluid content, PGs concentration within the ECM increases, together with the osmotic swelling pressure, the repulsive force produced by charges interaction, and the bulk – i.e., collagen network – compressive stress [89]. Thanks to the characteristics of PGs entrapped within the collagen network – playing a key role in resisting to tensile stresses, but easily folding under compression – AC can withstand external loads once the interstitial fluid flow reaches the equilibrium [88]. These phenomena carry on until they are balance by the load acting on AC [88]. Once the external load is removed – and thanks to PGs, acting hydrophilically like a sponge soaking up water – the interstitial fluid flows back into the tissue [90].

According to the above reported phenomena, two main mechanisms are responsible for the viscoelastic response of AC, i.e., flow dependent and flow independent [91]. The flow dependent viscoelasticity is identified as the frictional drag produced by the movement of the interstitial flow through the porous ECM [59]; such a phenomenon is known as biphasic viscoelastic behaviour [50]. The flow independent viscoelasticity is attributable to the intrinsic mechanical response of the molecules composing the ECM, i.e., motion and re-arrangement of PGs and collagen fibres [92]. Both the reported viscoelastic phenomena contribute to the response of AC under compression, shear, and tension. Moreover, the extent of their response depends on the rate at which the load is applied to the tissue. In case of loads applied at physiological rates, both the interstitial fluid and the solid matrix can be considered as almost-incompressible, allowing a proper response of the AC; in case of concentrated forces – i.e., high load applied at high rate – such a mechanism fails, exposing the tissue to injury [88]. The normal structure of the AC – and, thus, its functionality – can be impaired by the deviations induced by trauma, or degenerative pathologies. As reported in paragraph 3.2, such deviations mainly regard i) the increase in the interstitial fluid amount, ii) the decrease of PGs content, and iii) the degradation of the collagen network. These alterations definitely modify the relationship between such components, deregulating the structure and the mechanical response of AC.

3.3.1 Constitutive Models of the Articular Cartilage

Considering the extremely complex response of AC once subjected to stressors, many efforts are made to describe properly its mechanical behaviour [93]. Although the multiphasic, nonlinear and anisotropic nature of AC, the simplest model describes its response as monophasic, homogeneous, isotropic, linear elastic material. Therefore, its response can be summarized mainly by single parameter, named Young's (or Elastic) modulus, E [94], achieved through the following relation

$$E = \frac{\delta^s}{\varepsilon^s} \tag{3.1}$$

where δ^s and ε^s are the axial stress and strain, respectively, and s refers to the solid matrix. Moreover, two additional parameters can describe the isotropic and elastic behaviour of AC, i.e., The Poisson's ratio, υ, and the Shear modulus, μ_s. The Poisson's ratio of the tissue can be computed as

$$\upsilon = \frac{\varepsilon^l}{\varepsilon^s} \tag{3.2}$$

where ε^l is the lateral strain of AC. Shear modulus can be calculated starting from the values of E and υ

$$\mu_s = \frac{E_s}{(1 + \upsilon_s)} \tag{3.3}$$

Besides the isotropic, linear elastic model, the Hayes model [95] allows to determine the Instantaneous Elastic modulus, E_0, of the tissue, in particular by considering the features and the geometries related to the testing protocol – i.e., indentation – and to AC, i.e., thickness. More in detail, E_0 can be computed as follows

$$E_0 = \left({}^{S_0}/_{\omega_0}\right) \frac{(1-\upsilon^2)}{2ak\left({}^{a}/_{h}, \upsilon\right)} \tag{3.4}$$

where S_0 is the maximum load value reached prior to load relaxation, ω_0 is the indentation depth, ν is the Poisson's ratio, a is the radius of the contact area between AC and the indenter, h is the AC thickness, and k is a correction factor dependent on the ratio a/h, and on ν. Despite the slightly improvement introduced, the Hayes model can provide only the instantaneous or equilibrium response of AC, without describing its time dependence behaviour [96]. The simplest models describing the time dependent response of the AC derived from arrangements of mechanical elements, i.e., series or parallel of springs and dashes [97]. An improvement to such models is achieved by assuming the continuum-based formulations – e.g., Fung's quasi-linear viscoelasticity [98] –, by incorporating a relaxation function that describes elastic moduli as functions of time, as defined by the following equation

$$\delta\left(\varepsilon, t\right) = E \int_{0^-}^{t} G(t-s) \exp\left(B\varepsilon(s)\right) \frac{d\varepsilon}{ds}(s)\, ds \tag{3.5}$$

where G (t) is the reduced relaxation function, defined by the formula

$$G(t) = G_\infty \left(1 + C(E_1(t/\tau_2) - E_1(t/\tau_1)\right) \tag{3.6}$$

where C represents the intensity, and τ_1 and τ_2 are the short-time and the long-time constant, respectively. With the normalization condition G(0) = 1, where $G(\infty) = 1/(1+C \ln(\tau_2/\tau_1))$.

The main limitation of these models lies in not considering phenomena related to the contribute of fluid phase in withstanding loads. Overcoming – partially – this drawback, stretched exponential model – based on the polymer dynamics theory, which considers the interactions between the structures of PGs – is capable of describe flow dependent and independent phenomena by a multiple-constants, negative exponential, as reported by the following equation

$$\delta(t) = \delta_0 e^{-(t/\tau)^{\beta}} \tag{3.7}$$

where δ_0 is the maximum stress of the relaxation function, τ is the time constant, and β ($0 < \beta < 1$) is the stretching parameter. Nevertheless, the efficacy of the stretched exponential model is limited to the analysis of the AC response during stress-relaxation [99].

Aiming to consider comprehensively the viscoelasticity of the tissue – i.e., explaining at the same time flow dependent and independent phenomena –, the linear biphasic poroelastic (LBPE) theory describes the AC as a binary mixture of immiscible solid and fluid phases, both intrinsically incompressible and non-dissipative [50]. The only dissipative factor is the fluid flow within AC. The constitutive equations describing the stress-strain relations for the solid matrix, fluid and total stress are the following

$$\boldsymbol{\delta}^s = -\boldsymbol{\Phi}^s p\, \boldsymbol{I} + \boldsymbol{\delta}^E \tag{3.8}$$

$$\boldsymbol{\delta}^f = -\boldsymbol{\Phi}^f p\, \boldsymbol{I} \tag{3.9}$$

$$\boldsymbol{\delta}^t = \boldsymbol{\delta}^s + \boldsymbol{\delta}^f = -p\boldsymbol{I} + \boldsymbol{\delta}^E \tag{3.10}$$

where $\boldsymbol{\delta}^s$, $\boldsymbol{\delta}^f$, and $\boldsymbol{\delta}^t$ are the solid, fluid, and total stress tensor, respectively, $\boldsymbol{\Phi}^s$ and $\boldsymbol{\Phi}^f$ are the volume fraction for the solid and fluid phase, p is the fluid pressure, $\boldsymbol{I}$ is the identity tensor and $\boldsymbol{\delta}^E$ is the effective solid stress in excess of the local fluid pressure. In this context, the internal forces acting inside AC exposed to loads are attributable to a mixture of i) the stress withstanding by the solid phase, ii) the pressure developed within the fluid phase, and iii) the frictional drag between phases during the fluid flow [91]. Dissipative effects due to frictional drag are assumed to be responsible for the time dependence of the AC mechanical properties. The solid phase – i.e., ECM – is described as an isotropic, linearly elastic, and permeable material, for which the effective solid stress can be described as follows

$$\boldsymbol{\delta}^E = C\mathcal{E} \tag{3.11}$$

where C is the stiffness matrix, and $\boldsymbol{\varepsilon}$ is the total elastic strain tensor. During the application of instantaneous loads AC acts as an incompressible elastic material. The solid phase alone resists the deformation once the phenomena related to the fluid flow reached the equilibrium.

The fluid flow within AC can be expressed by the Darcy's law for porous media

$$Q = Ak\frac{\Delta p}{h} \tag{3.12}$$

where Q is the volume flow rate, A is the cross-sectional area of permeation, k is the permeability, Δp is the drop of pressure through the thickness h of AC. By assuming the solid and fluid phases incompressible and homogeneous, the continuity equation results to be expressed as follows

$$\nabla \cdot \left(\boldsymbol{\Phi}^s \boldsymbol{V}^s + \boldsymbol{\Phi}^f \boldsymbol{V}^f\right) = 0 \tag{3.13}$$

where $\boldsymbol{V}^s$ and $\boldsymbol{V}^f$ are the vectors of velocity of the solid and fluid phase, respectively. According to LBPE theory, three material properties describe the tissue behaviour, namely Aggregate modulus, H_A, calculated at the equilibrium, Poisson's ratio, v, and Hydraulic Permeability, k, which resulted to be strain, strain-rate, and thickness dependent [100]. Since LBPE theory considers the fluid dependent phenomena as the only responsible of the tissue viscoelasticity, a further refinement of such a theory includes a flow-independent component based on the solid phase behaviour – i.e., by adding parameters related to magnitude, short- and long-term relaxation time [101]. Despite additional and improved multi-phases models have been proposed – i.e., i) triphasic model, including a ionic phase that describes the electro-kinetic behaviour [102]; ii) quadriphasic model, describing swelling phenomena more accurately by assuming cations and anions separately [103] – LBPE model is, to date, one of the two models mostly used in describing the AC mechanical behaviour [14]. The second model is the fibril-reinforced, non-homogeneous, poroelastic (FRPE) model, which describes the microstructural conformation of AC [104]. More in detail, FRPE model describes the contribute of the collagen network and of the non-fibrillar matrix – i.e., PGs saturated with fluid – separately, therefore considering their different effort in withstanding the external load [14]. FRPE model extends the previous LBPE model by reinforcing the matrix with a network of nonlinear fibrils distributed in the radial, circular and vertical directions; in this regard, the response to compressive loads is provided only by non-fibrillar matrix, while the response to tensile and shear loads lies in the contributes of fibrillar – with an increasing stiffness as a function of the strain – and non-fibrillar components. Consequently, the contribute evidenced as H_A in the LBPE model is split here into the Fibril Network modulus, E_f, and Non-fibrillar Matrix modulus, E_m. The solid material stress can be described as combination of matrix and fibril stresses, in particular as follows

$$\boldsymbol{\delta}_1^E = \boldsymbol{\delta}_1^{matrix} + \frac{x}{3}\boldsymbol{\delta}_1^{fibrils} \tag{3.14}$$

$$\boldsymbol{\delta}_2^E = \boldsymbol{\delta}_2^{matrix} + \frac{x}{3}\boldsymbol{\delta}_2^{fibrils} \tag{3.15}$$

$$\boldsymbol{\delta}_3^E = \boldsymbol{\delta}_3^{matrix} \tag{3.16}$$

where $\boldsymbol{\delta}_i^{matrix}$ and $\boldsymbol{\delta}_i^{fibrils}$ are the normal stresses in the drained porous matrix and collagen fibrils, and x is the fibril volume fraction. Finally, models that consider the contributes of chondrocytes are also developed, i) describing the AC as a heterogeneous material, which response depends on the properties and on the configuration of the constituent components [14], and ii) explaining the local response of chondrocytes through models of different complexity [105,106].

3.4 Evaluation of the Articular Cartilage

Aiming to determine the main features of AC and, therefore, to understand its complex response, a wide spread of methods have been developed and applied through the years. Evaluating the AC by sound methods is essential to i) gain a comprehensive knowledge on how pathologies alter its structure and, thus, mechanical response, and ii) to properly develop and evaluate the efficacy of tissue engineering approaches and treatments to address diseases that impair tissue homeostasis. In this perspective, two of the main approaches used to evaluate the AC features are mechanical testing and diagnostic (pre-clinical and clinical) imaging; such approaches not only faced a progressive and continuous update through the last decades but – most importantly – allow to integrate the achieved insights, thus providing a multidisciplinary framework essential for understanding the AC.

3.4.1 Mechanical testing

As highlighted in previous paragraphs, AC is a highly heterogeneous tissue, which constituents respond differently to the loading scenario at which the tissue is exposed to. Aiming to investigate properly its mechanical response, particular attention must be paid in defining the boundary condition at which the AC is exposed. By starting from the physiological condition peculiar of the tissue, and regardless the adopted technique, a pre-requirement entails the use of a fluid during testing, thus to prevent dehydration of AC; saline solution or phosphate-buffered saline (PBS) are the solutions used practically in most of cases [14].

Considering the AC composition, and regardless the testing technique involved, different protocols can be applied to investigate its elastic and viscous response. The simplest protocol involves a monotonic test, in which a nominal constant compressive strain – or stress – is applied until a specific level is reached (**Fig. 3.3**). In this case, the achievable information entails the instantaneous response of the tissue – i.e., Instantaneous modulus, E_0 –, which extent depends on the strain – or stress – reached, and on the rate at which the tissue is deformed – or loaded [107–110].

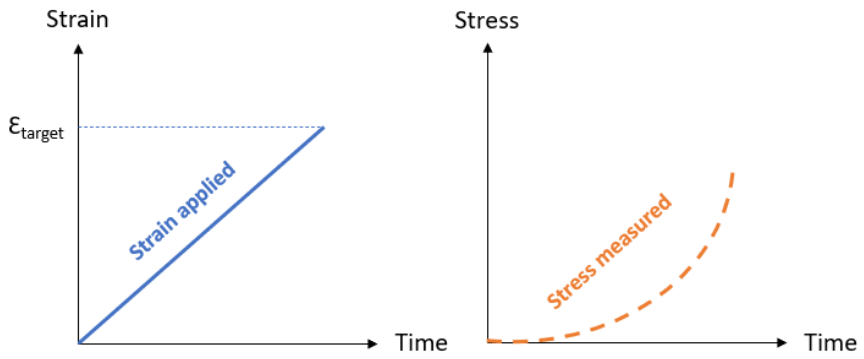

Fig. 3.3. Example of monotonic testing protocol, in which (Left) a nominal compressive strain is applied up to a specific level (ε_{target}), and (Right) the consequent stress is measured.

With the purpose of investigating the AC viscoelastic response, the main protocols used are creep and stress-relaxation [90]. Regarding the creep (**Fig. 3.4**), a constant load – generally choose basing on the resultant stress which, in case of knee AC, ranging between 0.5 and 20.0 MPa in terms of peak normal stress and contact pressure [111] – is applied to the sample up to a certain level and then maintained, monitoring the displacement – so, the strain – over time. Creep protocol tries to replicate the functioning of load-bearing joints, in which the articular tissues respond based on the external load.

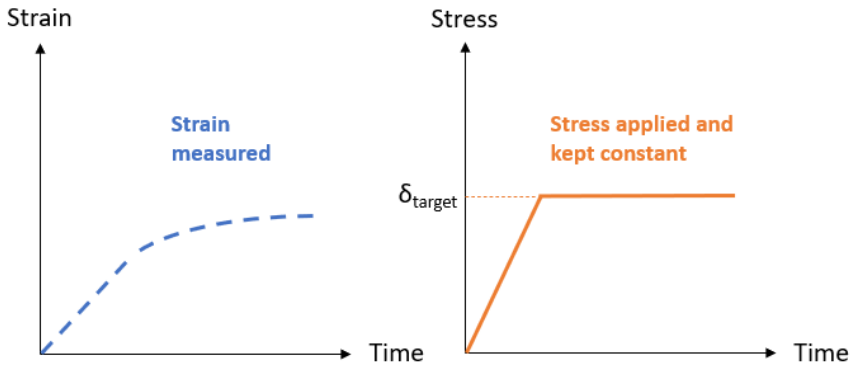

Fig. 3.4. Example of creep testing protocol, in which (Right) a nominal compressive stress is applied up to a specific level (δ_{target}) and maintained, while (Left) the consequent strain is monitored.

Stress-relaxation (**Fig. 3.5**) entails the application of a displacement – resulting in a certain level of strain which, in case of knee AC, ranging between 7% and 23% [112–114] –, monitoring the resultant force over time. As reported in paragraph 3.3, both fluid dependent and independent phenomena occur when a load – or a displacement – is applied to AC. In particular, the initial, transient response is attributable to the collagen network re-arrangement, the time-dependent creep or stress-relaxation is primarily related to the interstitial fluid flow and, finally, the equilibrium response is dependent on the properties of ECM.

Accordingly, creep and stress-relaxation allowed – together with suitable constitutive parameters, e.g., provided by LBPE and FRPE models – the evaluation of parameters related to both solid and fluid constituents of AC, moreover providing the possibility to investigate instantaneous, equilibrium, and rate-dependent phenomena through multi-steps solicitations.

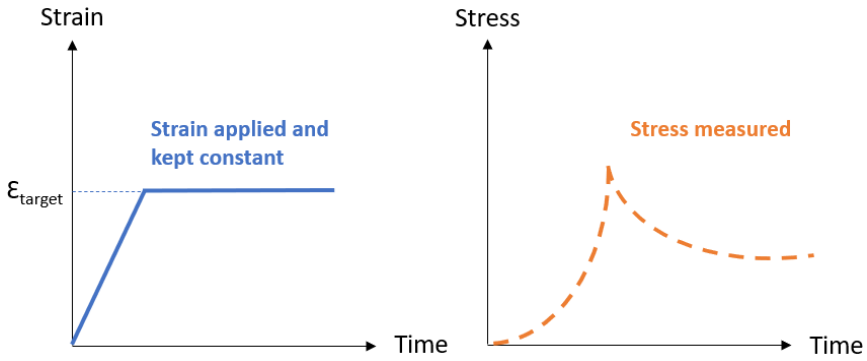

Fig. 3.5. Example of stress-relaxation testing protocol, in which (Left) a nominal compressive strain is applied up to a specific level (ε_{target}) and maintained, while (Right) the consequent stress is monitored.

Dynamic testing protocols allow to evaluate the frequency-dependent response of the tissue, by applying cyclic strain – or stress – and monitoring the resultant stress – or strain (**Fig. 3.6**). The frequencies generally applied fall within the physiological range, i.e., between 0.01 Hz and 2.0 Hz [115]. Besides Dynamic modulus, dynamic protocols allowed to compute energy dissipation, hysteresis, and phase lag.

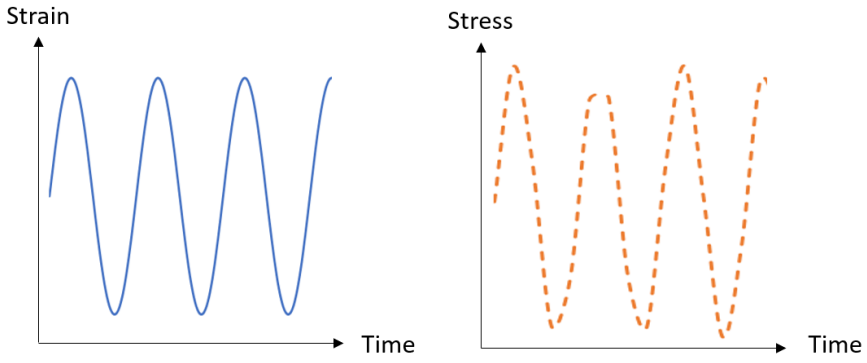

Fig. 3.6. Example of dynamic test, in which (Right) a sinusoidal strain is applied, while (Left) the consequent stress is monitored.

Moving on the techniques mainly used to evaluate the AC response, it must be noted that – besides tensile and shear forces interest such a tissue [116] – its main response is in withstanding external compressive loads. Accordingly, the main testing techniques investigating the AC mechanics entail

compression. Considering the wide spread of geometries and testing configurations used to measure the compressive response of the tissue, three major categories can be defined, namely confined compression, unconfined compression, and indentation. In Confined Compression (CC, **Fig. 3.7 left**), the response of a cylinder of pure cartilaginous tissue – i.e., obtained by coring a section of AC, after excising the latter from the underlying SB – is compressed between a metal and a porous plate, within an impermeable confining – i.e., with a diameter close to the one peculiar of the sample – chamber. Aiming to prevent the achievement of inaccurate data and, consequently, the computing of inaccurate properties, it is crucial to avoid contact between the metal impermeable plate and the inner side of the confining chamber [107].

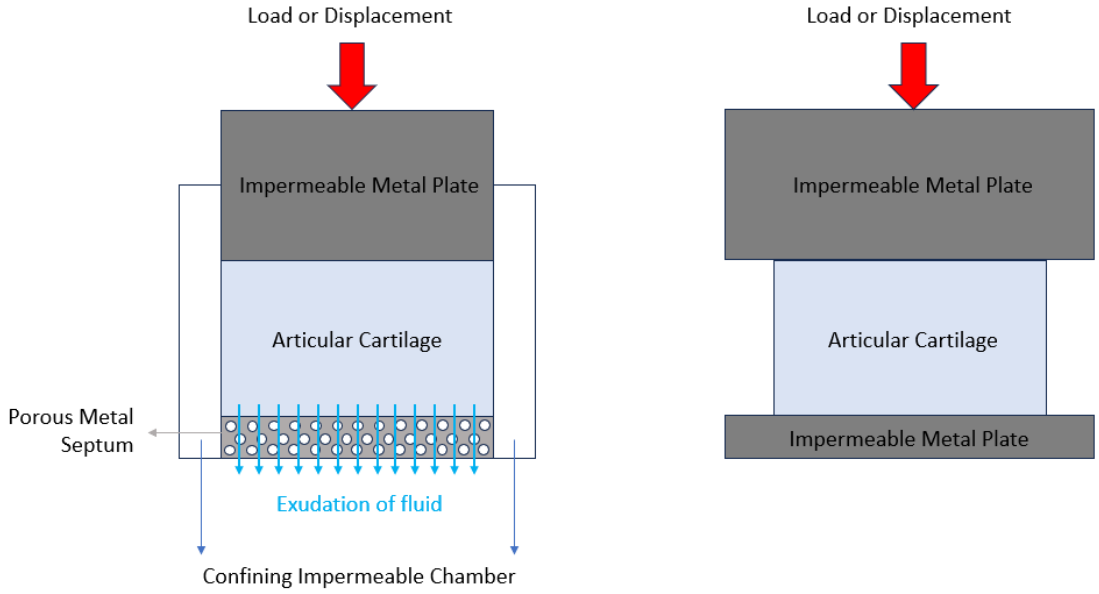

Fig. 3.7. Schematic representation of (Left) confined and (Right) unconfined compression test.

Once the compressive load – or displacement – is applied perpendicular to the plates, ECM and frictional drag developed within the tissue due to the fluid flow provide the first response; then, the exudated fluid flows through the porous platen, until an equilibrium is reached [90]. Confined compression technique involves generally the application of a stress-relaxation protocol, although a creep can be also used [50]. In this context, the AC mechanical properties AC are computed by fitting the monitored signals, i.e., stress or strain vs time, to the LBPE model [50], achieving the Aggregate modulus, H_A, Poisson's ratio, v, the Hydraulic Permeability, k, and the relaxation time, τ [58]; strain and strain-rate dependency of these parameters can be also investigated by applying a multi-ramps protocol [117].

Unconfined compression (UC, **Fig. 3.7 right**) technique involves the use of two impermeable platens, between which a cylinder of AC is solicitated by a stress-relaxation or a creep protocol; in this case, it is crucial that the platens diameter is higher than the cylinder one, thus to compress uniformly the entire sample surface. UC can be used to assess the instantaneous and the equilibrium response of the tissue, i.e., by providing the Instantaneous modulus, E_0, and the Equilibrium modulus, E_{eq}, respectively [14]. In addition, and through the application of a multi-ramps stress-relaxation protocol, it is also possible to

compute parameters related to the solid and fluid phases of AC, i.e., by fitting the experimental data to the FRPE model, thus to estimate the Fibril Network modulus, E_f, the Non-fibrillar Matrix modulus, E_m, and the Hydraulic Permeability, k [104]. A variation of CC and UC allows also to investigate the AC response without excising it from the underlying SB, thus to maintain the continuity between OC tissues; in this case, it is essential the parallelism between SB and plates surfaces [118].

With the perspective of evaluating the mechanical response of AC by maintaining its continuity with the other OC tissues, indentation technique is applied to OC cores, sub-regions or to the entire surface of articulations [119,120]. In this case, a load – or a displacement – is applied perpendicular to the surface – after evaluating its local slope – through spherical (**Fig. 3.8 left**) or plane-ended indenter (**Fig. 3.8 right**) with a diameter lower than the sample dimension, i.e., generally spanning in the range of tens of microns to a few millimetres [119,121,122]; accordingly, this approach is suitable to investigate the distribution of the mechanical properties onto the entire surface of the sample of interest [119,123]. As reported for the other approaches, i.e., CC and UC, indentation allows to apply stress-relaxation and creep protocol to investigate the AC response; despite E_0 and E_{eq} are the main parameters achievable through such a technique, also H_A, v, and k can be computed by fitting experimental data to the LBPE model [124].

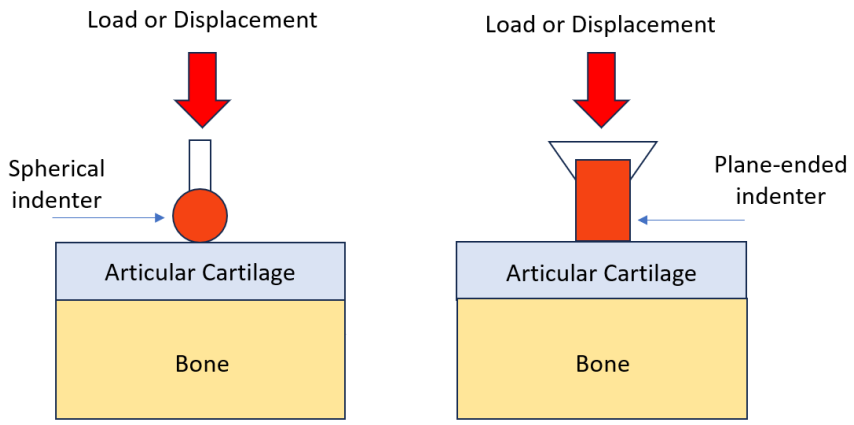

Fig. 3.8. Schematic representation of (Left) spherical and (Right) plane-ended indentation.

As above reported, besides compression, AC is exposed also to tensile and shear force. Accordingly, other techniques are used to investigate how the tissue responds to such scenarios. In this perspective – and despite compression and indentation are, by far, the most applied –, the main techniques to date applied are tensile, shear, and nanoindentation tests. In tensile test, rectangular or dogbone-shaped samples are evaluated to estimate the AC viscoelastic, equilibrium, dynamic and failure response [125,126]; such a test allows to detect the relative movement of the collagen network – i.e., by considering the orientation of collagen fibres in the superficial layer of the tissue – and PGs [127]. Regarding shear test, cylindrical and cuboids samples are investigated to assess the AC response in terms of the intrinsic viscoelasticity of the collagen network (mainly) and PGs. Last, nanoindentation approaches, i.e., through atomic force microscopy (AFM), allow to understand the AC mechanics at a lower length scale compared to the previous techniques. More in detail, AFM evaluates the surface of a sample thanks to its interaction – in terms of Van Der Waals forces – with a cantilever probe – made by polymeric or glassy material [14]. AFM permits

to investigate properly the hetereogenous response of the AC components at micron and submicron level, e.g., individual matrix fiber properties [107], stiffness gradients between the ECM and pericellular matrix [128], and dynamic of cytoskeleton and sub-membranous structures [129].

The techniques above mentioned are generally non-destructive approaches – i.e., do not require embedding or processes that modify structure and composition of the tissue –, and can/or cannot entail resection of AC form the other OC tissues. Regardless of this evidence, all the reported experimental techniques are currently used to investigate the mechanical response of AC in healthy and pathological conditions [14]. By focusing on the protocols that avoid resection of AC from the OC unit – thus to maintain the native boundary condition of such a tissue –, the insights retrieved by mechanical testing can be integrated to the outcomes derived from methods investigating other features of the tissue, i.e., structure and composition. In this perspective, experimental and clinical imaging – which proved to be extremely sensitive tools for diagnosis of articular pathologies, and for the evaluation of tissues structural features [130] – can be used to develop multidisciplinary frameworks predicting the tissue mechanical properties – and their changes due to the onset and progression of diseases – [131], thanks to the correlations between structure and functionality of AC [132].

3.4.2 Imaging

Imaging techniques represent non-invasive and powerful tools in the assessment of articular tissues. Experimental and clinical imaging permits to monitor in real-time the progression of pathologies, especially OA, enabling good spatial resolution for the quantitative evaluation of AC [130]. The two main approaches involved in imaging AC are based on ionizing and nonionizing radiation, i.e., Computed Tomography (CT) and Magnetic Resonance Imaging (MRI).

CT imaging is based on the physical principle of attenuation, by which the density of a material – or of a tissue – exposed to X-ray can be measured through its attenuation, expressed as Hounsfield unit (HU). Accordingly, the contrast between mineralized and soft tissues – which is the case of the OC unit – is high, due to the relative electron-dense inorganic component (calcium hydroxyapatite) of the bone matrix [133]. Three-dimensional (3D) representation of the sample/anatomical district structure is obtained by reconstructing data acquired at multiple viewing angle, thus to obtain a spatial distribution of the material/tissue HU [134]. CT resolution may vary depending on the application, i.e., from a few up to tens of micrometres, considering sample and small animals in preclinical assessments, or in vivo assessments, respectively [133]. Therefore, CT techniques allow to investigate macrostructural – e.g., 3D-based joint space narrowing, subchondral sclerosis and bone cysts, osteophyte formations [135] – and microstructural features – e.g., in the case of TB, the ratio of mineralized bone volume to total volume, BV/TV, trabecular thickness, Tb.Th, trabecular separation, Tb.Sp, trabecular number, Tb.N [133] – of a sample/anatomical district. Despite CT imaging provides reliable information about bone tissue – moreover allowing to identify the thickness of soft tissues through recent improvements [136] –, it is unable to give quantitative insights about the AC structure, requested to properly identify the onset of pathologies [130]. To fulfil partially this gap, contrast agents (CA) may be used to enhance the contrast of AC, in particular exploiting the negative charge of PGs that compose the tissue [90]. In this context, the primary choice lies on ionic and anionic CAs – mainly iodine- but also metal-based [137] –, which are used due their electrostatic interaction with PGs, i.e., with a distribution inverse or direct proportionality to PGs, respectively [137]. Therefore, contrast-enhanced CT (CECT) based on ionic CAs is capable of providing information only about PGs distribution pattern, without evaluating collagen structure and orientation.

Considering the limitations of CT imaging to study AC – in particular, i) the reduced use of CAs – especially ionic ones [137] – in clinical practice due to possible adverse side effects, ii) possible alteration of tissue composition and, thus, of the mechanical response due to its exposure to CA [138], avoiding its evaluation through multidisciplinary approaches, and iii) that no information about collagen network is achievable neither through CECT –, a step forward in the quantitative assessment of such a tissue is provided by quantitative MRI (qMRI). The physical principle at the base of MRI is the use of nonionizing radiation to excite protons of suitable nuclei, among which hydrogen represents the most important due to its concentration within soft tissues [130]. More in detail, protons are subjected firstly to a strong magnetic field – against which they can arrange parallel or perpendicular – generating a net magnetic vector in the direction of such a field. Then, pulsed radiofrequencies – specific to the application – are applied and removed progressively, inducing a rotation of the net magnetic vector into the transverse plane; the time-dependent re-arrangement of this vector – i.e., the intensity of the collected signal – is responsible of the proton relaxation [130]. By applying such a principle, qMRI provides specific pulse sequences – i.e., T_2 mapping, delayed gadolinium-enhanced MRI of cartilage (dGEMRIC), $T_{1\rho}$ – able to detect the biochemical changes leading up to morphological degeneration of the AC matrix, therefore improving the diagnostic of degenerative pathologies as OA [139]. T_2 is influenced mainly by free water molecules [140], and, moreover, by collagen content [141], i.e., structure of the collagen network [142]. dGEMRIC entails the use of a contrast agent – gadolinium diethylenetriaminepentacetate (Gd-DTPA^{2-}), injected intravenously [143] – which, due to its negative charge, diffuses within AC inversely with its FCD, allowing to evaluate GAGs and PGs content [144]. $T_{1\rho}$ is strictly related to the FCD [145] which, considering the AC composition, is reflection of PGs content; accordingly, through such a sequence water and PGs content – and, moreover, their depletion – are detectable, representing an alternative to dGEMRIC [143].

Despite MRI represents a key diagnostic tool in evaluating the main features of AC – allowing an early identification of their degradation –, its application entails some limitations, as the difficult optimization in balancing in-plane spatial resolution, slice thickness, and signal-to-noise ratio (SNR) [143]. More in detail, qMRI provides maps of signals distribution but with an in-plane resolution – ranging between 0.3 mm and 0.6 mm considering the fields generally used during ex vivo and in vivo assessments [140] – not suitable to investigate properly the depth-dependent phenomena peculiar of the AC, and with a slice thickness – i.e., 2 mm to 5 mm – making difficult the evaluation of changes on articular and samples surfaces. NMR approach, i.e., the new generation of low-field solutions, combines cost reduction and high adaptability; a particular advantage of low-field NMR approaches relates to the enhancement of relaxation contrast of the investigated signals, especially T_1, in correspondence of such fields [146]. In this perspective, single-sided NMR devices proved to be key tools in evaluating different kinds of biological tissues, allowing to reach a high resolution – up to a few micrometres – in the signals retrieved form the detection of a sensitive volume directly in contact with the surface of a permanent magnet [146]. Regarding the OC tissues, single-sided NMR device is capable of achieving depth-dependent insights about the structure and the composition of both AC [147] and bone tissue [148], moreover highlighting changes induced by degradation and pathologies [149,150].

4 Aims and Hypotheses

In this thesis, a multidisciplinary experimental framework was developed addressing the need to analyse the relationship between the functionality and the structure of AC, specifically focusing on its biomechanics.

The specific aims of this thesis can be summarized as follow:

- To optimize a mechanical testing approach providing reliable information about the mechanical response, i.e., viscoelasticity, of the AC (**Study I**)

- To investigate – by non-destructive techniques – the relationships between the functionality and the structure/composition of AC (**Study II and III**)

- To investigate the suitability of a full-field, imaging-based approach in evaluating the functional response of the OC unit, moving towards its comprehensive assessment (**Study IV**)

The multidisciplinary framework implemented in this thesis could represent a first step forward an exhaustive investigation of the main features of the AC. Moreover, the entire OC unit could be potentially investigated through the developed pipelines, providing potential tools to assess properly the efficacy of treatments responding to pathologies of the articular tissues composing load-bearing joints.

5 Study I – A Methodological Approach Investigating the Mechanical Properties of the Articular Cartilage through Indentation

In the following, the published scientific paper about the optimization of an indentation procedure for assessing the mechanical response of the AC is reported. In this regard, the approval required to enclose such paper to this PhD dissertation thesis was obtained by Materials Editorial Office on 8th August 2023.

Berni M, Erani P, Lopomo NF, Baleani M. Optimization of In Situ Indentation Protocol to Map the Mechanical Properties of Articular Cartilage. Materials (Basel). 2022 Sep 16;15(18):6425. doi: 10.3390/ma15186425. PMID: 36143736

materials

MDPI

Article

Optimization of In Situ Indentation Protocol to Map the Mechanical Properties of Articular Cartilage

Matteo Berni [1,*], Paolo Erani [1], Nicola Francesco Lopomo [2] and Massimiliano Baleani [1]

[1] Laboratorio di Tecnologia Medica, IRCCS Istituto Ortopedico Rizzoli, 40136 Bologna, Italy
[2] Dipartimento dell'Ingegneria dell'Informazione, University of Brescia, 25121 Brescia, Italy
* Correspondence: matteo.berni@ior.it

Abstract: Tissue engineering aims at developing complex composite scaffolds for articular cartilage repair. These scaffolds must exhibit a mechanical behavior similar to the whole osteochondral unit. In situ spherical indentation allows us to map the mechanical behavior of articular cartilage, avoiding removal of the underlying bone tissue. Little is known about the impact of grid spacing, indenter diameter, and induced deformation on the cartilage response to indentation. We investigated the impact of grid spacing (range: *a* to 3*a*, where *a* is the radius of the contact area between cartilage and indenter), indenter diameter (range: 1 to 8 mm), and deformation induced by indentation (constant indentation depth versus constant nominal deformation) on cartilage response. The bias induced by indentations performed in adjacent grid points was minimized with a 3*a* grid spacing. The cartilage response was indenter-dependent for diameters ranging between 1 and 6 mm with a nominal deformation of 15%. No significant differences were found using 6 mm and 8 mm indenters. Six mm and 8 mm indenters were used to map human articular cartilage with a grid spacing equal to 3*a*. Instantaneous elastic modulus E_0 was calculated for constant indentation depth and constant nominal deformation. E_0 value distribution did not change significantly by switching the two indenters, while dispersion decreased by 5–6% when a constant nominal deformation was applied. Such an approach was able to discriminate changes in tissue response due to doubling the indentation rate. The proposed procedure seems to reduce data dispersion and properly determine cartilage mechanical properties to be compared with those of complex composite scaffolds.

Keywords: knee; bovine; human; cartilage; osteochondral unit; mechanical properties; mapping; indentation; in vitro; experimental procedure

Citation: Berni, M.; Erani, P.; Lopomo, N.F.; Baleani, M. Optimization of In Situ Indentation Protocol to Map the Mechanical Properties of Articular Cartilage. *Materials* **2022**, *15*, 6425. https://doi.org/10.3390/ma15186425

Academic Editor: Iulian Vasile Antoniac

Received: 27 July 2022
Accepted: 13 September 2022
Published: 16 September 2022

1. Introduction

Articular cartilage is a highly specialized connective tissue representing an integral part of the musculoskeletal system [1]. It is composed of a dense extracellular matrix–consisting of a three-dimensional collagen network, negatively charged proteoglycans and chondrocyte cells, and interstitial fluid [1]. The interaction between these constituents defines the articular cartilage mechanical response [2], accounting for its site-dependent, depth-dependent, and time-dependent behavior [3]. Addressing the joint biomechanics, the main functions of such a tissue are to ensure low friction articulation, more homogeneous contact pressure distribution, and shock absorption [4,5].

Articular cartilage behavior has been extensively investigated both by in vivo and ex vivo techniques. In vivo investigations either involve the use of arthroscopic instruments, with associated surgical risks and procedural costs, or non-invasive imaging, which offers a limited accuracy in predicting tissue mechanical features. Therefore, although in vivo investigations are more relevant from a clinical point of view, as they allow a monitoring of disease progression and treatment response, ex vivo assessments are still the most reliable and commonly used technique to determine the mechanical peculiarities of articular cartilage.

Ex vivo investigations involve testing of either the whole osteochondral unit or articular cartilage excised samples. Although tensile, shear, sliding, and torsional loading conditions have been applied, most of the experimental approaches involve compression testing [6]. The functional assessment of articular cartilage by confined or unconfined compression requires specimens with strict geometrical features, mainly related to specimen planarity and homogeneity. Therefore, tissue excision from the underlying subchondral bone is needed. Although compressive approaches provide valuable information on articular cartilage response, specific bias in the investigated behavior might be introduced by interrupting articular cartilage continuity and removing subchondral bone tissue, i.e., altering the boundary conditions peculiar to the osteochondral unit.

Ex vivo indentation is an alternative method that allows us to map the mechanical response of the articular cartilage without altering its boundary conditions [7,8]. Although both cylindrical and spherical indenters have been used, they are not equivalent. Indeed, the indenter geometry impacts strain distribution within the articular cartilage: a cylindrical indenter determines non-physiological strain concentration near the edge of the plane-ended probe, while a spherical indenter induces strain distribution closely resembling the one predicted in vivo [9,10]. Interestingly, neglecting micro- and nano-scale studies, a great variance in the indenter diameter, falling within the range 1.0 ÷ 6.35 mm, has been found in the literature [7,10–15]. Although there are at least four studies suggesting that indenter diameter with millimeter-scale size affects the response of articular cartilage [16–19], a sound assessment of the indenter diameter effect is still missing. This gap raises the question of the comparability of cartilage response to indentation across studies.

The choice of the indenter diameter also affects the minimum grid spacing allowed to map the articular cartilage response. Decreasing grid spacing is desirable as it determines an in increase in the number of map nodes, i.e., indentation points become closer to each other. Therefore, reduced grid spacing can capture abrupt and subtle changes in articular cartilage mechanics. On the other hand, too small grid spacing could introduce artefact effects due to interactions between adjacent indentations. In two studies investigating the cartilage response to indentation at a micrometer scale, the authors recommend a minimum grid spacing of 2.5a (82 µm) [20] and 3a [21], where a is the radius of the contact area between the articular cartilage and the spherical indenter. Such analyses have not been found for the millimeter scale. Given the hierarchical structure of the cartilage tissue, the best compromise between surface refinement and artefact reduction must be identified at the millimeter scale to properly map cartilage mechanical properties.

In addition to indenter diameter, the indentation depth determines the extension of the contact area between the indenter and the articular cartilage surface and, finally, the volume of tissue undergoing large deformation. Generally, indentation protocols reported in the literature set a constant indentation depth regardless of the thickness of the tissue, determining nominal deformation magnitude depending on articular cartilage thickness [7,11–13,20,22,23]. However, it has been demonstrated that cartilage response to indentation depends on deformation induced by the indenter [24]. Applying a displacement equal to a fixed percentage of the articular cartilage thickness should allow us to induce a constant nominal deformation level and determine the corresponding cartilage response. Such an approach should reduce the data dispersion. However, this approach requires the a priori measurement of articular cartilage thickness to be performed without damaging the tissue at the indentation point.

Addressing the above-mentioned open issues should allow us to acquire more consistent and comparable parameters describing the response of the articular cartilage to indentation when supported by the underlying subchondral bone tissue. The data thus achieved are essential to both describe the biomechanical behavior of the whole osteochondral unit and provide accurate information for tissue engineering aimed at developing a complex composite scaffold for articular cartilage repair. Accordingly, the primary goal of this study was to optimize the indentation procedure for assessing the mechanical response of the whole osteochondral unit, evaluating the impact of grid spacing (range: a to 3a,

where *a* is the radius of the contact area between cartilage and indenter), indenter diameter (range: 1 to 8 mm), and deformation induced by indentation (constant indentation depth versus constant nominal deformation) on cartilage response.

2. Materials and Methods

2.1. Sample Collection and Management

Portions of skeletally mature bovine knees were used to develop and optimize our indentation experimental procedure. Bovine knees were collected from on-farm livestock within 24 h from culling. Parallelepiped-shaped samples—with a minimum thickness of 20 mm and a nominal area functional to the specific test—were extracted from the articular surface of ten knees (Supplementary Figure S1) by using a diamond-coated blade (MDP200, Remet, Bologna, Italy). Cutting was performed in a circular saw (TR60, Remet, Bologna, Italy) under continuous water cooling to minimize tissue heating. Samples were then wrapped in gauze soaked in phosphate-buffered saline (PBS) solution 1X (7.4 pH, Life Technologies Europe B.V., Bleiswijk, The Netherlands) and frozen at −20 °C [25].

The day before testing, the frozen sample was thawed overnight at 4 °C [26,27]. The day of the test, the sample was removed from refrigerator and embedded in a 5 mm thick polymethylmethacrylate baseplate (Restray NF, S.P.D.: Mulazzano, Italy) needed to constrain it to the X-Y motorized table of the testing machine (Mach-1 V500css, Biomomentum Inc., Laval, QC, Canada). During the polymerization process, the articular cartilage surface was kept moist with a gauze soaked in PBS. The entire phase was carried out at room temperature and completed within 1 h of sample removal from the refrigerator [27]. All tests were performed maintaining tissue samples fully submerged in PBS and completed by the end of the day.

2.2. A Priori Estimate of the Articular Cartilage Thickness at the Indentation Point

The most straightforward method to measure articular cartilage thickness when a tissue sample is constrained to a material testing machine entails needle probing [28]. In order to obtain reliable information, we had to keep into account that needle insertion creates a discontinuity (i.e., a small hole of the order of magnitude of half a millimeter in the articular cartilage undergoing the indentation test), which may alter the articular cartilage response to indentation, especially when small-diameter indenters are used. Therefore, needle insertion on the indentation point prior to an indentation test should be avoided. Since the articular cartilage is a continuous layer, it was assumed that tissue thickness below the indentation point could be estimated by measuring the thickness in nearby positions. Articular cartilage thickness was measured in the four corners of a 6 mm × 6 mm square whose geometric center coincided with the indentation point. Therefore, the distance between the needle insertion points and the indentation point was 4.2 mm (see Section 2.3).

Articular cartilage thickness was measured by using a 27G × $\frac{1}{2}$″ intradermal needle attached to the actuator of the testing machine [11]. Needle insertion speed was set to 0.5 mm/s [11]. The needle was directed vertically towards the specimen until the cartilage surface was penetrated. Needle insertion was stopped when the load reached 7 N [13]. Apparent articular cartilage thickness was calculated as the difference between the vertical position corresponding to a first variation in the measured compressive load—occurring when the needle tip touched the cartilage surface—and the position consistent with an increase in the slope of force–displacement curve, occurring when the needle tip touched the cartilage/subchondral bone interface [13]. The articular cartilage thickness was calculated by multiplying the apparent articular cartilage thickness by the cosine of the surface angle (see Appendix A) between the vertical direction and the direction normal to the surface [13]. Cartilage thickness in the geometric center was estimated as the mean of the thickness values measured in the four corners (estimated thickness). Then, the articular cartilage thickness was measured directly in the geometric center following the above-described procedure (effective thickness). The percentage prediction error committed by the proposed a priori approach was calculated as the difference between the estimated and effective

thickness divided by the effective thickness, expressed as a percentage. One hundred thickness evaluations were performed.

2.3. Optimization of Grid Spacing

When performing automated mapping of articular cartilage for its mechanical characterization, it is crucial to define the proper minimum distance on a square grid, or grid spacing, avoiding mutual influence between nearby indentations. As a rule, the grid spacing is set equal to a multiple of the radius (a) of the contact area between the articular cartilage and the spherical indenter. Thus, an experimental assessment was employed to investigate whether an indentation (perturbing indentation) performed at three different distances (a, $2a$, $3a$) away from the indentation point might affect the response of the cartilage in the measuring indentation point (measuring indentation).

The indenter diameter and indentation depth determine the value of a. A spherical indenter of 8 mm in diameter was selected for this series. This value is greater than those used in the published reports; in fact, it represents the worst-case scenario as it determines the maximum extension of articular cartilage compression. In order to maximize the effect of the perturbing indentation, the indentation depth was set to 0.25 mm, 25% greater than what is commonly used in the literature (0.20 mm) [7,13,14,29]. Considering a sphere-plane Hertzian contact [30], the value of the contact radius a was equal to 1.4 mm. Perturbing indentations were performed at 1.4 mm (a), 2.8 mm ($2a$), or 4.2 mm ($3a$) away from the indentation point. The distance between two adjacent rows or columns was 6 mm—i.e., $4a$ rounded to the upper integer—to avoid any interference among indentation points. The resulting indentation scheme is shown in Figure 1.

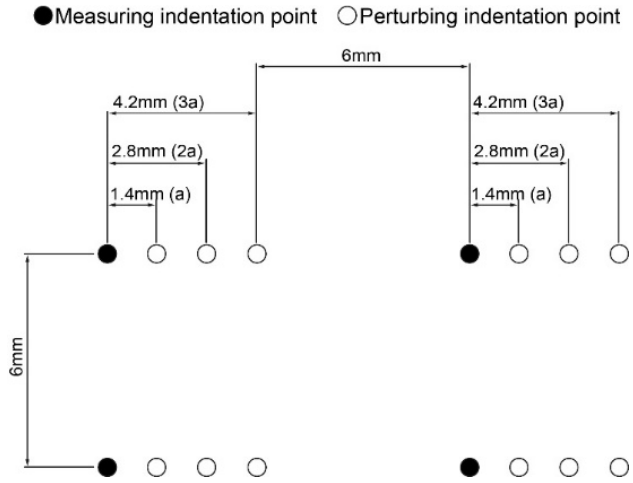

Figure 1. Scheme of the orthogonal grid used to evaluate the effect of perturbing indentations on the response of articular cartilage in the measuring indentation points.

The described approach entails four indentations on each measuring indentation point, one without (noPI) and three with a preliminary perturbing indentation performed at a distance a (PIa), $2a$ (PI2a), or $3a$ (PI3a). Indentation series on measuring indentation points were repeated after a resting period of 40 min [23]. In order to minimize the bias due to change in cartilage response over repeated indentations, a preliminary indentation was performed to precondition the tissue in each measuring indentation point. Additionally, a full counterbalanced order was adopted in selecting the distance from the indentation point where to perform the perturbing indentation. Accordingly, the total number of permutations was 24 (4!, i.e., the factorial of four). A total of 72 points (measuring indentations) were evaluated to achieve three times the number of total permutations and guarantee the full counterbalanced order. All indentations were performed in displacement control in the direction normal to the surface (see Appendix A). The indentation rate was set to 0.25 mm/s. Then, the indenter was held in position for 120 s before releasing from the

articular cartilage. When the perturbing indentation was planned, measuring indentation was performed 60 s after the perturbing one.

The first part of the load–displacement curve, up to the load peak, was evaluated by applying the Hayes model to calculate the instantaneous elastic modulus (E_0) [31]. Poisson's ratio was set to 0.45 [32]. The load–time curve (load relaxation) was fitted by a stretched exponential function [33–35], and the three characterizing parameters—S_0, τ, and β, where S_0 is the maximum load value reached prior to load relaxation, τ is the time constant, and β is the stretching parameter—were calculated. E_0, S_0, τ, and β values, achieved with a preliminary perturbing indentation, were normalized with the corresponding values achieved in the same measuring indentation point without performing a perturbing indentation (noPI).

2.4. Effect of Indenter Diameter on Articular Cartilage Response

In order to cover the whole range used in previous studies evaluating articular cartilage mechanics, seven spherical indenters, with diameter spanning from 1 to 6 mm, with 1 mm increments, and an additional indenter of 8 mm were selected in this study (Supplementary Figure S2) [7,10–15]. Grid spacing was set to 6 mm (see Section 2.3). An a priori estimate of the articular cartilage thickness at the indentation point was performed (see Section 2.2). Aiming to produce the same extent of deformation regardless of the articular cartilage thickness, a nominal deformation corresponding to 15% of the tissue thickness was imposed [36,37]. The deformation rate was set to 0.15 s^{-1} [38–40].

Seven indentations, with indenters differing in size, were performed on each indentation point. As in the previous test, a preliminary indentation was performed to precondition the tissue. Then, the seven indentations were performed at 40 min time intervals. Since the number of possible permutations was 5040 (7!, i.e., the factorial of seven), it was not possible to adopt a full counterbalanced order. Therefore, the fully counterbalanced order adopted here was limited to the first two indentations of each series of seven indentations, achieving a number of permutations limited to 42. For the remaining five indentations of each series, the indentation order was defined to ensure that each indenter was placed the same number of times, i.e., six, in each of the remaining last five positions. A total of 126 points were evaluated to investigate three times 42 respecting the above-described scheme, and thus to minimize the bias due to change in cartilage response over repeated indentations.

The load–displacement curve up to the load peak was evaluated by applying the Hayes model, where Poisson's ratio was set to 0.45, to calculate the instantaneous elastic modulus (E_0).

2.5. Pilot Study on a Human Tibial Plateau

A pilot trial was performed on a human tibial plateau (donor gender: male; donor age: 50 years old) to assess the comparability and repeatability of the indentation experimental procedure. The tibial plateau was processed by following the same procedure reported for bovine knee samples management, and constrained to the X-Y motorized table of the testing machine (Mach-1 V500css, Biomomentum Inc., Laval, QC, Canada, see Section 2.1 and Supplementary Figure S3).

Indentation parameters were defined based on the results of the tests performed on bovine articular cartilage. Therefore, 6 mm and 8 mm indenters were used to map the articular cartilage with a grid spacing equal to 3*a*, calculated for the 8 mm indenter. The orthogonal grid was overlaid to the tibial plateaus, identifying a total of 15 points on the articular cartilage surface. An a priori estimate of the articular cartilage thickness at the indentation points was performed. All indentations were performed in displacement control to a depth of 0.20 mm or 15% of the estimated articular cartilage thickness, whichever was greater, in the direction normal to the surface (see Appendix A). Two deformation rates were used: 0.15 s^{-1} and 0. 30 s^{-1}.

The described approach entails four indentations on each indentation point. As previously reported, a preliminary indentation was performed to precondition the tissue.

Then, the indentation series were repeated after a resting period of 40 min. The indenter diameter and the deformation rate were selected randomly for each indentation point.

The load–displacement curve, limited to the indentation depth of 0.20 mm, was evaluated by applying the Hayes model, with Poisson's ratio set to 0.45, to calculate the instantaneous elastic modulus ($E_{0\ 0.20mm}$). The same evaluation to calculate the instantaneous elastic modulus ($E_{0\ 15\%def}$) was performed on the load–displacement curve limited to a nominal deformation of 15%, determined by using the a priori estimate of the articular cartilage thickness.

2.6. Data Analysis

Fitting of experimental data was performed choosing a specific mathematical model to describe the data trend—i.e., the Hayes' model or the stretched exponential function (see Appendix B)—and determining function parameters by minimizing the root mean square error by using a numerical computing environment (MATLAB R2021a, MathWorks, Natick, MA, USA).

Paired cartilage thickness data, i.e., the estimated and effective thickness value for each investigated point, were analyzed by using the paired-sample Wilcoxon test performed using a commercial software (SPSS version 14.0.1, SPSS Inc., Chicago, IL, USA).

E_0, S_0, τ, and β normalized values achieved after perturbing indentations were analyzed by using the Friedman test, followed by the Nemenyi post hoc test, both performed using a free software environment (R version 4.1.2, R Core Team, R: A Language and Environment for Statistical Computing, Vienna, Austria, https://www.R-project.org/). This statistical analysis was also used to identify differences among E_0 values determined by indenting the articular cartilage with indenters of different size.

The paired-sample Wilcoxon test was also used to identify differences between E_0 values determined by indenting the articular cartilage with indenters of different size, two indentation rates, and two applied deformations on the human tibial plateau in the pilot study.

3. Results

3.1. A Priori Estimate of the Articular Cartilage Thickness at the Indentation Point

We investigated 100 different points on the articular cartilage surface for a total of 500 needle indentations (400 indentations performed in the corners and 100 in the geometric centers of 100 squares). The achieved cartilage thickness values measured in the geometric centers fell in the range of 0.5–2.4 mm. The distributions of the estimated and effective thickness values are shown in Figure 2.

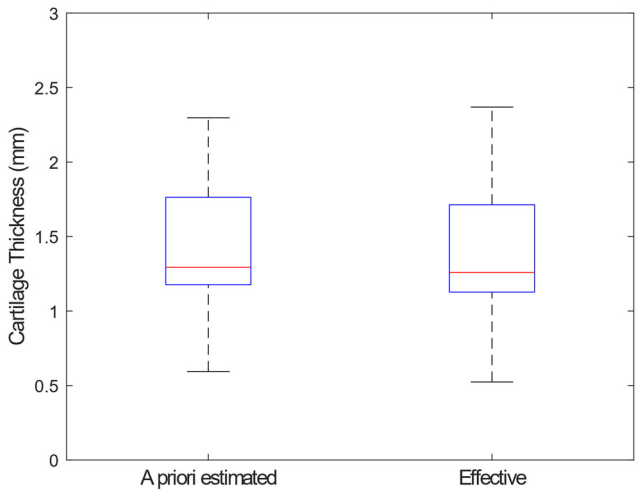

Figure 2. Box plot of the estimated and effective thickness values.

No statistical difference was found between two distributions (paired-sample Wilcoxon test, $p = 0.56$). The 5th, 25th, 50th, 75th, and 95th percentile of the percentage prediction error distribution was −10.6%, −4.7%, 0.5%, 6.5%, and 16.4%, respectively. The complete dataset is provided as supplementary material (Supplementary Table S1).

3.2. Optimization of Grid Spacing

Four indentations were performed on each of the 72 points for a total of 288 indentations. The execution of a preliminary indentation (perturbing indentation), close to the indentation point where tissue properties were going to be investigated, changed the response of the articular cartilage. Indeed, the Friedman test showed a significant difference among the four groups (noPI, PI*a*, PI2*a*, PI3*a*) regardless of the analyzed parameter ($p < 0.001$ for all four parameters E_0, S_0, τ, and β). The variation in tissue response depended on the distance from the preliminary perturbing indentation. The Nemenyi post hoc test showed a significant difference between noPI and PI*a* regardless of the analyzed parameter ($p < 0.001$ for all four parameters E_0, S_0, τ, and β). Conversely, the post hoc test showed a significant difference between noPI and PI2*a* only for S_0 ($p < 0.001$). A significant difference was also found between noPI and PI3*a* for τ ($p < 0.001$) and β ($p = 0.01$). The distributions of normalized values of E_0, S_0, τ, and β for Pi*a*, PI2*a*, and PI3*a* groups are shown in Figure 3. The effect of the perturbing indentation was also marked by the increase in data dispersion associated with the decreasing distance from the preliminary perturbing indentation. The complete dataset is provided as supplementary material (Supplementary Table S2).

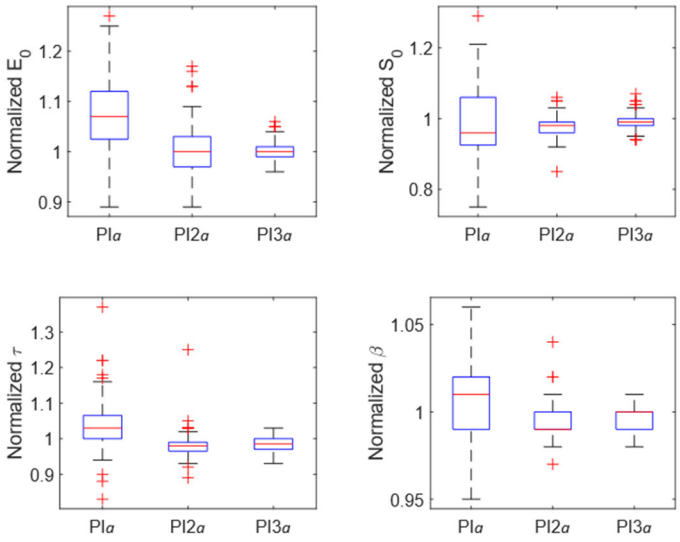

Figure 3. Box plots of the normalized values of E_0 (**top left**), S_0 (**top right**), τ (**bottom left**), and β (**bottom right**) for PI*a*, PI2*a*, and PI3*a* groups.

3.3. Effect of Indenter Diameter on Articular Cartilage Response

Seven indentations were performed on each of the 126 points for a total of 882 indentations. The distributions of E_0 values determined with indenters having different diameter are shown in Figure 4. The indenter diameter affected the instantaneous response of the articular cartilage: the Friedman test showed a significant difference among the seven groups ($p < 0.001$). Collected data showed an increase in E_0 by increasing the indenter diameter up to 6 mm (Nemenyi post hoc test: $p < 0.001$ for all comparison between E_0 values determined with 6 mm indenter and E_0 values determined with indenter smaller than 6 mm). The same results were achieved comparing E_0 values determined with a 8 mm indenter and E_0 values determined with an indenter smaller than 6 mm. Conversely, no significant difference was found comparing E_0 values determined with 6 mm and 8 mm indenters. The complete dataset is provided as supplementary material (Supplementary Table S3).

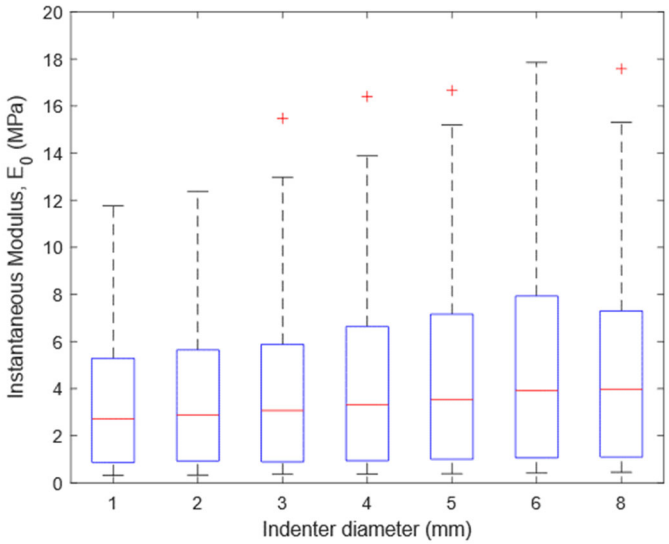

Figure 4. Box plot of E_0 values determined with indenters having different diameters, achieved by evaluating 126 points over the articular surface of ten bovine knees.

3.4. Pilot Study on a Human Tibial Plateau

The estimated cartilage thickness of the 15 points identified by overlaying the orthogonal grid to the tibial plateau fell in the range 0.9–2.9 mm with a median of 1.5 mm. The 5th, 25th, 50th, 75th, and 95th percentile of the distribution of the indentation depth imposed to achieve a 15% nominal deformation was 0.15 mm, 0.020 mm, 0.23 mm, 0.29 mm, and 0.44 mm, respectively.

The distributions of E_0 values determined with different testing conditions are shown in Figure 5.

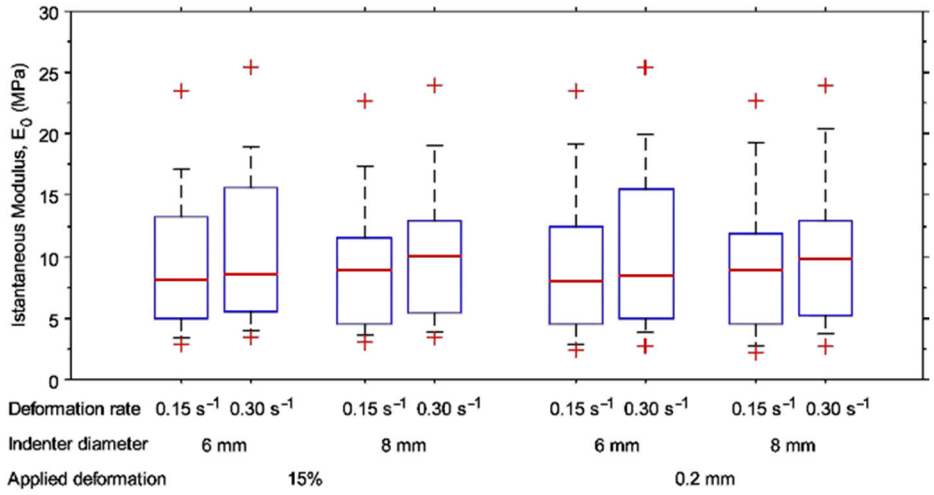

Figure 5. Box plots of $E_{0\ 15\%def}$ and $E_{0\ 0.20mm}$ values determined using 6 mm and 8 mm indenters and of E_0 to indent the articular cartilage of the tibial plateau at two different deformation rates (0.15 s^{-1} and 0.30 s^{-1}).

No significant differences were found between E_0 values determined with 6 mm and 8 mm indenters. Conversely, the paired-sample Wilcoxon test showed a significant increase in E_0 values by doubling the indentation rate regardless of the testing conditions ($p < 0.001$). Moreover, a significant difference was found between the distribution of $E_{0\ 0.20mm}$ and $E_{0\ 15\%def}$ values, achieved with the same testing conditions ($p = 0.03$, Supplementary Figure S4). Additionally, the dispersion of $E_{0\ 0.20mm}$ values was in general 5–6% greater than E_0 15%def values. The complete dataset is provided

(Supplementary Table S4), and changes in E_0 in relation to the investigated testing parameters are highlighted (Supplementary Figures S5–S16).

4. Discussion

We aimed to optimize the indentation procedure for mapping the mechanical properties of articular cartilage when supported by underlying bone tissue, i.e., the response of the whole osteochondral unit to indentation with a spherical indenter. The main novelty of the proposed approach was to perform the indentation tests by controlling the nominal deformation and, consequently, the deformation rate imposed to the articular cartilage while optimizing two indentation parameters such as grid spacing and indenter size.

The proposed approach requires the a priori knowledge of the cartilage thickness. Different methods have been proposed to measure it, the most accurate one entailing needle probing [13,28,41–46]. This method has been carried out after the indentation test since the indentation protocol commonly relies on the application of a constant displacement, or indentation depth, regardless of the thickness of the articular cartilage [7,11–13,22,23]. Additionally, the direct measurement cannot be performed before the indentation test because it creates a discontinuity in the cartilage tissue at the indentation point. However, the articular cartilage thickness can be estimated by measuring the thickness in nearby positions, as shown in this study. The achievable accuracy (see Section 3.1) is comparable to, or even better than, that reported for non-contact methods (stereomicroscopy, range 7.9–10.5% [42]; ultrasonography, range 0–31% [45,47]). Therefore, the estimation of articular cartilage thickness, on the basis of thickness measurements carried out in the surrounding area of the indentation point, could be an alternative to non-contact methods.

Mapping the mechanical properties of articular cartilage surfaces requires the definition of a grid to be superimposed to the joint surface. The definition of the optimal grid spacing would allow us to achieve the maximum resolution of the gridded cartilage surface properties, minimizing any mutual influence between nearby indentations. In the literature, some indentation-based studies mapping articular cartilage properties reported the number of the positions per unit surface area—or the density—of the superimposed grid, without any consideration of the possible mutual influence between nearby indentations [13,46]. However, few studies investigating cartilage mechanics at the nano- or micro-scale reported that the minimum distance between subsequent points should be at least three times ($3a$) the contact radius resulting between the probe and the cartilage surface [19,21]. Consistently, our findings show that decreasing the grid spacing to $2a$ increases the data dispersion and statistically alters the cartilage instantaneous response. A reduction in the grid spacing to a further (a) increases data dispersion and, more importantly, significantly alters the whole mechanical response of the articular cartilage. The observed effect could be explained considering that indentation determines interstitial fluid flow through the tissue in the surrounding area. Therefore, any further indentation performed too close to the previously indented point, and before tissue equilibrium has been recovered, might be affected by locally increased fluid content, as suggested by the trend of τ and β found decreasing the distance of the preliminary perturbing indentation from the indentation point. Looking at the collected values, it could be argued that the $2a$ grid spacing represents an acceptable compromise between accuracy and grid resolution. However, the root mean square percentage error (RMSPE) values—calculated comparing the 72 stretched exponential functions describing the response of the cartilage without perturbation (noPI) with each of the stretched exponential functions describing the response of the perturbed cartilage (PIa, PI2a, PI3a) in the same 72 measuring points—progressively decrease by increasing the distance between the two points where the perturbing and measuring indentation were performed; accordingly, a minimum extent of RMSPE is reached considering a $3a$ grid spacing for all the investigated points (Supplementary Figure S17). Therefore, it seems recommendable to set the grid spacing to $3a$ to minimize the bias induced by mutual influence between nearby indentations in the articular cartilage response.

As for the choice of the indenter diameter, at a first glance, the wide range of E_0 values is noteworthy. Such a wide range was somehow expected since tissue samples were collected from both femoral condyles and tibial plateaus of ten bovine knees. Despite the wide range of E_0 values, the present results highlighted an increasing trend in E_0 values as a function of indenter diameter up to 6 mm. Neglecting the studies carried out at nano- and micro-scale [14,48], since indentation length scale affects the response of the articular cartilage [49], such an effect was partially investigated in two studies [18,19]. Although in the cited studies, the measured parameters were different or calculated using a different approach, a partial comparison is still possible. Chandwadkar found an apparent increasing trend in peak load values increasing the indenter diameter from 1 mm to 5 mm by 2 mm at a time [19]. Moore et al. found that doubling the indenter diameter (from 3.175 mm to 6.350 mm) led to a rise in the cartilage contact modulus, which includes contributions from fluid and solid stresses [18]. Therefore, both studies do not contradict our findings. Moore and colleagues suggested that increasing the indenter radius, while maintaining the indentation depth fixed (indentation depth: 0.15 mm), increases the interaction depth in the assumed Hertzian contact. The articular cartilage is not homogeneous, showing higher water and lower glycosaminoglycan content in the surface layer. Therefore, decreasing the indenter diameter would make the tissue response more surface-sensitive. A further contribution might be ascribed to the interstitial fluid: the greater the indenter diameter, the greater the tissue volume, with its fluid content, perturbed by indentation. This might change the extent of the contribution of the extracellular matrix and interstitial fluid in supporting the external load. These considerations do not necessarily imply that small indenters must be avoided. However, the reported bias in the instantaneous response of articular cartilage must be considered when comparisons with other studies are made, taking the indenter diameter into account.

Evaluating the human articular cartilage response through indentation test and, above all, aiming at defining a standard indentation protocol, which would allow the comparison between different studies, requires us to properly identify the main peculiarities of the indentation procedure. A nominal deformation corresponding to 15% of the tissue thickness instead of a fixed indentation depth was applied to induce the same nominal deformation regardless of the cartilage thickness and considering the contact features between highly congruent surfaces and the average condition peculiar to the human knee joint [36,37]. E_0 values determined by indenting human articular cartilage fell within the range reported in the literature [7,13,35,50]. The pilot study carried out on a human tibial plateau showed no differences between E_0 values achieved by indenting articular cartilage with 6 mm and 8 mm diameter indenters, regardless of the rate or applied indentation, in agreement with the data collected by testing bovine cartilage. The experimental procedure was sensitive to the deformation rate. It is well known how such a parameter—also known as indentation rate, loading rate or displacement rate—impacts the tissue response [8,51,52]. Moreover, the dependence of the cartilage behavior on the deformation rate was detected at the millimeter [18], micro- [14,53], and nano-scale [53,54]. From this perspective, and independent from the investigated scale, the rate at which the tissue is indented directly impacts the cartilage response. Accordingly, our results highlighted a statistical increase in the cartilage elastic response, i.e., E_0, by raising the deformation rate from 0.15 s^{-1} to 0.30 s^{-1}, regardless of the applied indentation (15% of the thickness or 0.2 mm). However, the amount of deformation applied to the articular cartilage impacts the articular cartilage response. A significant difference was found between $E_{0\,0.20mm}$ and $E_{0\,15\%def}$ values, the values of the latter being slightly higher. It is worth noting that the median value of the distribution of the indentation depth imposed to achieve a 15% nominal deformation was 0.23 mm, i.e., slightly higher than the fixed value for the indentation depth of the $E_{0\,0.20mm}$ group [12,55–57]. Additionally, maintaining the nominal deformation of the cartilage thickness fixed at 15% seems to reduce dispersion. Reduction in data dispersion would allow us to improve the statistical power in detecting a correlation among different parameters

and, more in general, to provide more accurate information for tissue engineering aimed at developing a complex composite scaffold for articular cartilage repair.

Some limitations must be highlighted. First, the pilot study was carried out on one human tibial plateau. A larger sample size would allow us to evaluate more accurately the proposed procedure in terms of data dispersion of parameters describing the cartilage response. Second, the deformation-based protocol here proposed relies on the a priori assessment of cartilage thickness. From this perspective, a procedure based on the evaluation of such a parameter in nearby positions was implemented, specifically by applying the needle technique [41]. This technique creates four discontinuities, i.e., four small holes, around the indentation point of the order of magnitude of half a millimeter. The need for measuring cartilage thickness could be overcome by operating in pressure control mode. This alternative approach might also determine a reduction in data dispersion. Nevertheless, indenting articular surfaces by a pressure-based protocol is not yet feasible due to technological limitations; such an approach would require an accurate sensor capable of measuring the contact pressure at the indenter/cartilage interface on a small area of the indenter surface located on the indenter axis.

5. Conclusions

Aiming to fulfill tissue engineering approaches treating pathologies affecting articular cartilage, a sound assessment of the cartilage behavior must be provided. The present study represents a step forward in properly evaluating how grid spacing, indenter diameter, and induced deformation by indentation all impact the articular cartilage response. Grid spacing should be set to $3a$ to minimize bias induced by indentations performed in adjacent grid points. Indenter diameter should be set to least at 6 mm to avert a bias in E_0 values and to allow data comparison among different studies. When grid spacing and indenter diameter are selected to minimize bias in articular cartilage response, the deformation-based approach—15% of the cartilage thickness—represents a reliable method to investigate articular cartilage behavior by indentation test aiming at reducing data dispersion. The proposed procedure would allow a sound assessment of the articular cartilage mechanical properties to be compared with those of complex composite scaffolds.

Supplementary Materials: The following supporting information can be downloaded at https://www.mdpi.com/article/10.3390/ma15186425/s1, Figure S1: Example of a bovine knee tibial plateau (left), from which samples suitable for indentation test were extracted (right). Figure S2: Spherical indenters used to test knee articular cartilage, starting from 1 mm (left) to 8 mm (right) diameter indenter. Figure S3: The human tibial plateau constrained to the X-Y motorized table of the testing machine. The 6 mm diameter indenter is also visible. Figure S4: Distributions of E_0 values determined with different imposed deformation, i.e., a nominal deformation of 15%, and a 0.20 mm displacement. Figure S5: E_0 values determined for the investigated points onto the human tibial plateau by using 6 mm and 8 mm indenters (nominal deformation of 15% of the cartilage thickness, 0.15 s^{-1} indentation rate). Figure S6: E_0 values determined for the investigated points onto the human tibial plateau by using 6 mm and 8 mm indenters (nominal deformation of 15% of the cartilage thickness, 0.30 s^{-1} indentation rate). Figure S7: E_0 values determined for the investigated points onto the human tibial plateau by using 6 mm and 8 mm indenters (indentation depth of 0.20 mm, 0.15 s^{-1} indentation rate). Figure S8: E_0 values determined for the investigated points onto the human tibial plateau by using 6 mm and 8 mm indenters (indentation depth of 0.20 mm, 0.30 s^{-1} indentation rate). Figure S9: E_0 values determined for the investigated points onto the human tibial plateau by using 0.15 s^{-1} and 0.30 s^{-1} indentation rates (nominal deformation of 15% of the cartilage thickness, 6 mm indenter diameter). Figure S10: E_0 values determined for the investigated points onto the human tibial plateau by using 0.15 s^{-1} and 0.30 s^{-1} indentation rates (nominal deformation of 15% of the cartilage thickness, 8 mm indenter diameter). Figure S11: E_0 values determined for the investigated points onto the human tibial plateau by using 0.15 s^{-1} and 0.30 s^{-1} indentation rates (indentation depth of 0.20 mm, 6 mm indenter diameter). Figure S12: E_0 values determined for the investigated points onto the human tibial plateau by using 0.15 s^{-1} and 0.30 s^{-1} indentation rates (indentation depth of 0.20 mm, 8 mm indenter diameter). Figure S13: E_0 values determined for the

investigated points onto the human tibial plateau by applying a nominal deformation of 15% of the cartilage thickness, or an indentation depth of 0.20 mm (indentation rate of 0.15 s^{-1}, 6 mm indenter diameter). Figure S14: E_0 values determined for the investigated points onto the human tibial plateau by applying a nominal deformation of 15% of the cartilage thickness, or an indentation depth of 0.20 mm (indentation rate of 0.15 s^{-1}, 8 mm indenter diameter). Figure S15: E_0 values determined for the investigated points onto the human tibial plateau by applying a nominal deformation of 15% of the cartilage thickness, or an indentation depth of 0.20 mm (indentation rate of 0.30 s^{-1}, 6 mm indenter diameter). Figure S16: E_0 values determined for the investigated points onto the human tibial plateau by applying a nominal deformation of 15% of the cartilage thickness, or an indentation depth of 0.20 mm (indentation rate of 0.30 s^{-1}, 8 mm indenter diameter). Figure S17: Root mean square percentage error (RMSPE) calculated comparing the 72 stretched exponential functions describing the response of the cartilage without perturbation (noPI) with each of the stretched exponential function describing the response of the perturbed cartilage (PI*a*, PI2*a*, PI3*a*) in the same 72 measuring points. Table S1: Dataset on a priori estimate and effective measurement of the articular cartilage thickness. Table S2: Dataset on the effect of nearby indentation on the estimate of articular cartilage mechanical parameters. Table S3: Dataset on the impact of the indenter diameter on the estimate of articular cartilage instantaneous modulus. Table S4: Dataset on the impact of testing parameters on the estimate of the articular cartilage instantaneous modulus.

Author Contributions: Conceptualization, M.B. (Matteo Berni), N.F.L. and M.B. (Massimiliano Baleani); methodology, M.B. (Matteo Berni), P.E. and M.B. (Massimiliano Baleani); validation, M.B. (Matteo Berni) and M.B. (Massimiliano Baleani); formal analysis, M.B. (Matteo Berni) and M.B. (Massimiliano Baleani); investigation, M.B. (Matteo Berni) and P.E.; data curation, M.B. (Matteo Berni); writing—original draft preparation, M.B. (Matteo Berni), with major contributions by M.B. (Massimiliano Baleani); writing—review and editing, P.E., N.F.L. and M.B. (Massimiliano Baleani); supervision, N.F.L. and M.B. (Massimiliano Baleani); project administration, M.B. (Massimiliano Baleani); funding acquisition, M.B. (Massimiliano Baleani). All authors have read and agreed to the published version of the manuscript.

Funding: This research was supported by the Italian Ministry of Health, grant number RF-2018-12368274, project title: HTO—Impact of high tibial osteotomy in preventing disease progression in medial knee osteoarthritis: Quantifying the effects on cartilage and subchondral bone by using a combined biomechanical and medical imaging approach.

Institutional Review Board Statement: Ethical approval CE-AVEC 585/2021/Sper/IOR, no. 0010371.

Informed Consent Statement: Informed consent was obtained from patient for the research use of retrieved tissues.

Data Availability Statement: Data supporting reported results are available in the Supplementary Materials.

Acknowledgments: The authors would like to thank the butcher's store Il Cerbero (Cesena, Italy) for the donation of bovine knees; Roberta Fognani, Margherita De Luca, and Alice Polenzani for their help in carrying out the tests; Barbara Bordini and Monica Cosentino for the statistical analysis; Luigi Lena for the illustrations; and Lucia Mancini for her help in revising the manuscript.

Conflicts of Interest: The authors declare no conflict of interest.

Appendix A

The spatial orientation of the cartilage surface, i.e., the angle between the normal to the cartilage surface and the axis of the actuator (vertical direction), was calculated at each indentation point through an automated procedure. The spatial coordinates were measured in the four corners of a 0.2 mm × 0.2 mm square, whose geometric center coincided with the indentation point. The orientation of the cartilage surface was assumed to be the plane that would best fit the set of four points calculated by minimizing a function error. On the basis of this assumption, the normal to the best-fit plane is the normal to the cartilage surface.

Appendix B

The Hayes model [31] is described by the function:

$$E_0 = (S_0/\omega_0)\,(1 - \nu^2)/2ak(a/h,\nu)$$

where
S_0 is the maximum load value reached prior to load relaxation;
ω_0 is the indentation depth;
ν is the Poisson's ratio;
a is the radius of the contact area between the articular cartilage and the spherical indenter;
h is the thickness of the articular cartilage; and
k is a correction factor dependent on a/h and ν.

The stretched exponential model [35] is described by the function:

$$S(t) = (S_0 - S_{eq})\, e^{-(t/\tau)\beta} + S_{eq}$$

where
S_0 is the maximum load value reached prior to load relaxation;
τ is the time constant;
β is the stretching parameter; and
S_{eq} is the equilibrium load value reached at the end of the relaxation.

Since the main focus was on the load relaxation behavior of articular cartilage, changes in S_{eq} values were not investigated.

References

1. Sophia Fox, A.J.; Bedi, A.; Rodeo, S.A. The Basic Science of Articular Cartilage: Structure, Composition, and Function. *Sports Health* **2009**, *1*, 461–468. [CrossRef] [PubMed]
2. Ebrahimi, M.; Turunen, M.J.; Finnilä, M.A.; Joukainen, A.; Kröger, H.; Saarakkala, S.; Korhonen, R.K.; Tanska, P. Structure-Function Relationships of Healthy and Osteoarthritic Human Tibial Cartilage: Experimental and Numerical Investigation. *Ann. Biomed. Eng.* **2020**, *48*, 2887–2900. [CrossRef] [PubMed]
3. Laasanen, M.S.; Töyräs, J.; Korhonen, R.K.; Rieppo, J.; Saarakkala, S.; Nieminen, M.T.; Hirvonen, J.; Jurvelin, J.S. Biomechanical properties of knee articular cartilage. *Biorheology* **2003**, *40*, 133–140. [PubMed]
4. McMahon, L.A.; O'Brien, F.J.; Prendergast, P.J. Biomechanics and mechanobiology in osteochondral tissues. *Regen. Med.* **2008**, *3*, 743–759. [CrossRef] [PubMed]
5. Espinosa, M.G.; Otarola, G.A.; Hu, J.C.; Athanasiou, K.A. Cartilage Assessment Requires a Surface Characterization Protocol: Roughness, Friction, and Function. *Tissue Eng. Part C Methods* **2021**, *27*, 276–286. [CrossRef]
6. Marchiori, G.; Berni, M.; Boi, M.; Filardo, G. Cartilage mechanical tests: Evolution of current standards for cartilage repair and tissue engineering. A literature review. *Clin. Biomech.* **2019**, *68*, 58–72. [CrossRef]
7. Seitz, A.M.; Osthaus, F.; Schwer, J.; Warnecke, D.; Faschingbauer, M.; Sgroi, M.; Ignatius, A.; Dürselen, L. Osteoarthritis-Related Degeneration Alters the Biomechanical Properties of Human Menisci Before the Articular Cartilage. *Front. Bioeng. Biotechnol.* **2021**, *9*, 659989. [CrossRef]
8. Kabir, W.; Di Bella, C.; Choong, P.F.M.; O'Connell, C.D. Assessment of Native Human Articular Cartilage: A Biomechanical Protocol. *Cartilage* **2021**, *13* (Suppl. 2), 427S–437S. [CrossRef]
9. Warner, M.D.; Taylor, W.R.; Clift, S.E. Finite element biphasic indentation of cartilage: A comparison of experimental indenter and physiological contact geometries. *Proc. Inst. Mech. Eng. Part H J. Eng. Med.* **2001**, *215*, 487–496. [CrossRef]
10. Swann, A.C.; Seedhom, B.B. Improved techniques for measuring the indentation and thickness of articular cartilage. *Proc. Inst. Mech. Eng. Part H* **1989**, *203*, 143–150. [CrossRef]
11. Seidenstuecker, M.; Watrinet, J.; Bernstein, A. Viscoelasticity and histology of the human cartilage in healthy and degenerated conditions of the knee. *J. Orthop. Surg. Res.* **2019**, *14*, 256. [CrossRef] [PubMed]
12. Antons, J.; Marascio, M.G.M.; Nohava, J.; Martin, R.; Applegate, L.A.; Bourban, P.E.; Pioletti, D.P. Zone-dependent mechanical properties of human articular cartilage obtained by indentation measurements. *J. Mater. Sci. Mater. Med.* **2018**, *29*, 57. [CrossRef] [PubMed]
13. Sim, S.; Chevrier, A.; Garon, M.; Quenneville, E.; Lavigne, P.; Yaroshinsky, A.; Hoemann, C.D.; Buschmann, M.D. Electromechanical probe and automated indentation maps are sensitive techniques in assessing early degenerated human articular cartilage. *J. Orthop. Res.* **2017**, *35*, 858–867. [CrossRef] [PubMed]
14. Bae, W.C.; Schumacher, B.L.; Sah, R.L. Indentation probing of human articular cartilage: Effect on chondrocyte viability. *Osteoarthr. Cartil.* **2007**, *15*, 9–18. [CrossRef]

15. Kiviranta, P.; Lammentausta, E.; Töyräs, J.; Kiviranta, I.; Jurvelin, J.S. Indentation diagnostics of cartilage degeneration. *Osteoarthr. Cartil.* **2008**, *16*, 796–804. [CrossRef]
16. Korhonen, R.K.; Laasanen, M.S.; Töyräs, J.; Rieppo, J.; Hirvonen, J.; Helminen, H.J.; Jurvelin, J.S. Comparison of the equilibrium response of articular cartilage in unconfined compression, confined compression and indentation. *J. Biomech.* **2002**, *35*, 903–909. [CrossRef]
17. Simha, N.K.; Jin, H.; Hall, M.L.; Chiravarambath, S.; Lewis, J.L. Effect of indenter size on elastic modulus of cartilage measured by indentation. *J. Biomech. Eng.* **2007**, *129*, 767–775. [CrossRef]
18. Moore, A.C.; Zimmerman, B.K.; Chen, X.; Lu, X.L.; Burris, D.L. Experimental characterization of biphasic materials using rate-controlled Hertzian indentation. *Tribol. Int.* **2015**, *89*, 2–8. [CrossRef]
19. Chandwadkar, S.A. Indentation Protocol to Determine Viscoelastic Properties of Cartilage before and after Crosslinking. Ph.D. Thesis, Purdue University, West Lafayette, IN, USA, 2017. Available online: https://scholarworks.iupui.edu/bitstream/handle/1805/15092/Indentation%20Protocol%20to%20Determine%20Viscoelastic%20Properties%20of%20Cartilage%20Before%20and%20After%20Crosslinking.pdf;jsessionid=0455762F255B53B8074AC2952AD83A12?sequence=1 (accessed on 15 July 2022).
20. Moshtagh, P.R.; Pouran, B.; Korthagen, N.M.; Zadpoor, A.A.; Weinans, H. Guidelines for an optimized indentation protocol for measurement of cartilage stiffness: The effects of spatial variation and indentation parameters. *J. Biomech.* **2016**, *49*, 3602–3607. [CrossRef]
21. Campbell, S.E.; Ferguson, V.L.; Hurley, D.C. Nanomechanical mapping of the osteochondral interface with contact resonance force microscopy and nanoindentation. *Acta Biomater.* **2012**, *8*, 4389–4396. [CrossRef]
22. Pordzik, J.; Bernstein, A.; Watrinet, J.; Mayr, H.O.; Latorre, S.H.; Schmal, H.; Seidenstuecker, M. Correlation of Biomechanical Alterations under Gonarthritis between Overlying Menisci and Articular Cartilage. *Appl. Sci.* **2020**, *10*, 8673. [CrossRef]
23. Jin, H.; Lewis, J.L. Determination of Poisson's ratio of articular cartilage by indentation using different-sized indenters. *J. Biomech. Eng.* **2004**, *126*, 138–145. [CrossRef] [PubMed]
24. Mäkelä, J.T.A.; Korhonen, R.K. Highly nonlinear stress-relaxation response of articular cartilage in indentation: Importance of collagen nonlinearity. *J. Biomech.* **2016**, *49*, 1734–1741. [CrossRef] [PubMed]
25. Ebrahimi, M.; Ojanen, S.; Mohammadi, A.; Finnilä, M.A.; Joukainen, A.; Kröger, H.; Saarakkala, S.; Korhonen, R.K.; Tanska, P. Elastic, Viscoelastic and Fibril-Reinforced Poroelastic Material Properties of Healthy and Osteoarthritic Human Tibial Cartilage. *Ann. Biomed. Eng.* **2019**, *47*, 953–966. [CrossRef]
26. Wan, C.; Ge, L.; Souza, R.B.; Tang, S.Y.; Alliston, T.; Hao, Z.; Li, X. T1ρ-based fibril-reinforced poroviscoelastic constitutive relation of human articular cartilage using inverse finite element technology. *Quant. Imaging Med. Surg.* **2019**, *9*, 359–370. [CrossRef] [PubMed]
27. Nickmanesh, R.; Stewart, R.C.; Snyder, B.D.; Grinstaff, M.W.; Masri, B.A.; Wilson, D.R. Contrast-enhanced computed tomography (CECT) attenuation is associated with stiffness of intact knee cartilage. *J. Orthop. Res.* **2018**, *36*, 2641–2647. [CrossRef]
28. Shepherd, D.E.; Seedhom, B.B. Thickness of human articular cartilage in joints of the lower limb. *Ann. Rheum. Dis.* **1999**, *58*, 27–34. [CrossRef]
29. Steineman, B.D.; LaPrade, R.F.; Santangelo, K.S.; Warner, B.T.; Goodrich, L.R.; Haut Donahue, T.L. Early Osteoarthritis After Untreated Anterior Meniscal Root Tears: An In Vivo Animal Study. *Orthop. J. Sports Med.* **2017**, *5*, 2325967117702452. [CrossRef]
30. Bushby, A.; Jennett, N. Determining the Area Function of Spherical Indenters for Nanoindentation. *MRS Proc.* **2000**, *649*, Q7.17. [CrossRef]
31. Hayes, W.C.; Keer, L.M.; Herrmann, G.; Mockros, L.F. A mathematical analysis for indentation tests of articular cartilage. *J. Biomech.* **1972**, *5*, 541–551. [CrossRef]
32. Li, G.; Lopez, O.; Rubash, H. Variability of a three-dimensional finite element model constructed using magnetic resonance images of a knee for joint contact stress analysis. *J. Biomech. Eng.* **2001**, *123*, 341–346. [CrossRef] [PubMed]
33. June, R.K.; Fyhrie, D.P. A comparison of cartilage stress-relaxation models in unconfined compression: QLV and stretched exponential in combination with fluid flow. *Comput. Methods Biomech. Biomed. Eng.* **2013**, *16*, 565–576. [CrossRef]
34. Brown, C.P.; Nguyen, T.C.; Moody, H.R.; Crawford, R.W.; Oloyede, A. Assessment of common hyperelastic constitutive equations for describing normal and osteoarthritic articular cartilage. *Proc. Inst. Mech. Eng. Part H J. Eng. Med.* **2009**, *223*, 643–652. [CrossRef] [PubMed]
35. Kumar, R.; Pierce, D.M.; Isaksen, V.; Davies, C.L.; Drogset, J.O.; Lilledahl, M.B. Comparison of Compressive Stress-Relaxation Behavior in Osteoarthritic (ICRS Graded) Human Articular Cartilage. *Int. J. Mol. Sci.* **2018**, *19*, 413. [CrossRef]
36. Liu, F.; Kozanek, M.; Hosseini, A.; Van de Velde, S.K.; Gill, T.J.; Rubash, H.E.; Li, G. In vivo tibiofemoral cartilage deformation during the stance phase of gait. *J. Biomech.* **2010**, *43*, 658–665. [CrossRef]
37. Liu, C.; Liu, C.; Ren, X. Quantitative evaluation of subchondral bone microarchitecture in knee osteoarthritis using 3T MRI. *BMC Musculoskelet. Disord.* **2017**, *18*, 496. [CrossRef]
38. Alsaaod, M.; Luternauer, M.; Hausegger, T.; Kredel, R.; Steiner, A. The cow pedogram-Analysis of gait cycle variables allows the detection of lameness and foot pathologies. *J. Dairy Sci.* **2017**, *100*, 1417–1426. [CrossRef]
39. Nilsson, J.; Thorstensson, A. Adaptability in frequency and amplitude of leg movements during human locomotion at different speeds. *Acta Physiol. Scand.* **1987**, *129*, 107–114. [CrossRef]
40. Danion, F.; Varraine, E.; Bonnard, M.; Pailhous, J. Stride variability in human gait: The effect of stride frequency and stride length. *Gait Posture* **2003**, *18*, 69–77. [CrossRef]

41. Jurvelin, J.S.; Räsänen, T.; Kolmonen, P.; Lyyra, T. Comparison of optical, needle probe and ultrasonic techniques for the measurement of articular cartilage thickness. *J. Biomech.* **1995**, *28*, 231–235. [CrossRef]
42. Horbert, V.; Lange, M.; Reuter, T.; Hoffmann, M.; Bischoff, S.; Borowski, J.; Schubert, H.; Driesch, D.; Mika, J.; Hurschler, C.; et al. Comparison of Near-Infrared Spectroscopy with Needle Indentation and Histology for the Determination of Cartilage Thickness in the Large Animal Model Sheep. *Cartilage* **2019**, *10*, 173–185. [CrossRef] [PubMed]
43. Xie, L.; Lin, A.S.; Levenston, M.E.; Guldberg, R.E. Quantitative assessment of articular cartilage morphology via EPIC-microCT. *Osteoarthr. Cartil.* **2009**, *17*, 313–320. [CrossRef] [PubMed]
44. Hadjab, I.; Sim, S.; Karhula, S.S.; Kauppinen, S.; Garon, M.; Quenneville, E.; Lavigne, P.; Lehenkari, P.P.; Saarakkala, S.; Buschmann, M.D. Electromechanical properties of human osteoarthritic and asymptomatic articular cartilage are sensitive and early detectors of degeneration. *Osteoarthr. Cartil.* **2018**, *26*, 405–413. [CrossRef] [PubMed]
45. Steppacher, S.D.; Hanke, M.S.; Zurmühle, C.A. Ultrasonic cartilage thickness measurement is accurate, reproducible, and reliable—validation study using contrast-enhanced micro-CT. *J. Orthop. Surg. Res.* **2019**, *14*, 67. [CrossRef]
46. Veronesi, F.; Berni, M.; Marchiori., G.; Cassiolas, G.; Muttini, A.; Barboni, B.; Martini, L.; Fini, M.; Lopomo, N.F.; Marcacci, M.; et al. Evaluation of cartilage biomechanics and knee joint microenvironment after different cell-based treatments in a sheep model of early osteoarthritis. *Int. Orthop.* **2021**, *45*, 427–435. [CrossRef]
47. Suh, J.K.; Youn, I.; Fu, F.H. An in situ calibration of an ultrasound transducer: A potential application for an ultrasonic indentation test of articular cartilage. *J. Biomech.* **2001**, *34*, 1347–1353. [CrossRef]
48. Miller, G.J.; Morgan, E.F. Use of microindentation to characterize the mechanical properties of articular cartilage: Comparison of biphasic material properties across length scales. *Osteoarthr. Cartil.* **2010**, *18*, 1051–1057. [CrossRef] [PubMed]
49. Oyen, M.; Shean, T.; Strange, D.; Galli, M. Size effects in indentation of hydrated biological tissues. *J. Mater. Res.* **2012**, *27*, 245–255. [CrossRef]
50. Shepherd, D.E.; Seedhom, B.B. The 'instantaneous' compressive modulus of human articular cartilage in joints of the lower limb. *Rheumatology* **1999**, *38*, 124–132. [CrossRef]
51. Han, G.; Chowdhury, U.; Eriten, M.; Henak, C.R. Relaxation capacity of cartilage is a critical factor in rate- and integrity-dependent fracture. *Sci. Rep.* **2021**, *11*, 9527. [CrossRef]
52. Li, H.; Li, J.; Yu, S.; Wu, C.; Zhang, W. The mechanical properties of tibiofemoral and patellofemoral articular cartilage in compression depend on anatomical regions. *Sci. Rep.* **2021**, *11*, 6128. [CrossRef] [PubMed]
53. Wahlquist, J.A.; DelRio, F.W.; Randolph, M.A.; Aziz, A.H.; Heveran, C.M.; Bryant, S.J.; Neu, C.P.; Ferguson, V.L. Indentation mapping revealed poroelastic, but not viscoelastic, properties spanning native zonal articular cartilage. *Acta Biomater.* **2017**, *64*, 41–49. [CrossRef] [PubMed]
54. Nia, H.T.; Han, L.; Li, Y.; Ortiz, C.; Grodzinsky, A. Poroelasticity of cartilage at the nanoscale. *Biophys. J.* **2011**, *101*, 2304–2313. [CrossRef] [PubMed]
55. Chen, S.S.; Falcovitz, Y.H.; Schneiderman, R.; Maroudas, A.; Sah, R.L. Depth-dependent compressive properties of normal aged human femoral head articular cartilage: Relationship to fixed charge density. *Osteoarthr. Cartil.* **2001**, *9*, 561–569. [CrossRef]
56. Thambyah, A.; Broom, N.D. Further insight into the depth-dependent microstructural response of cartilage to compression using a channel indentation technique. *Comput. Math. Methods* **2013**, *2013*, 358192. [CrossRef]
57. Wilson, W.; Huyghe, J.M.; van Donkelaar, C.C. Depth-dependent Compressive Equilibrium Properties of Articular Cartilage Explained by its Composition. *Biomech. Modeling Mechanobiol.* **2007**, *6*, 43–53. [CrossRef]

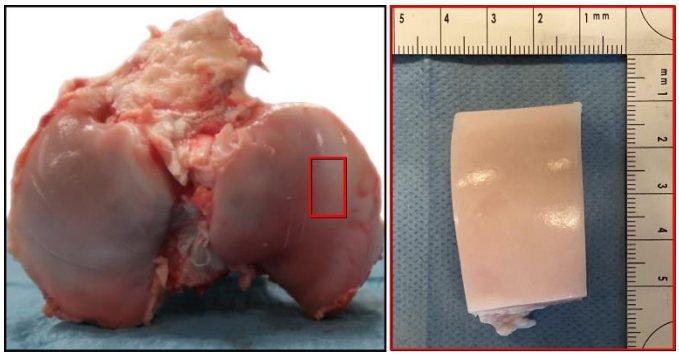

Supplementary Figure S1. Example of a bovine knee tibial plateau (Left), from which samples suitable for indentation test were extracted (Right).

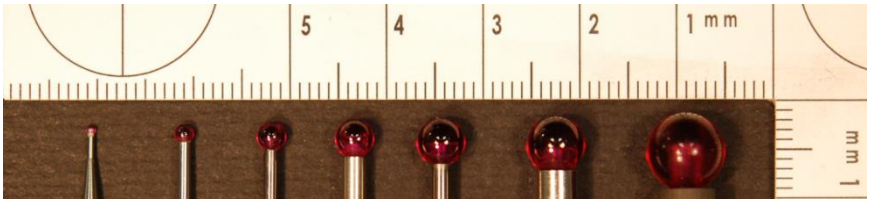

Supplementary Figure S2. Spherical indenters used to test knee articular cartilage, starting from 1-mm (Left) to 8-mm (Right) diameter indenter.

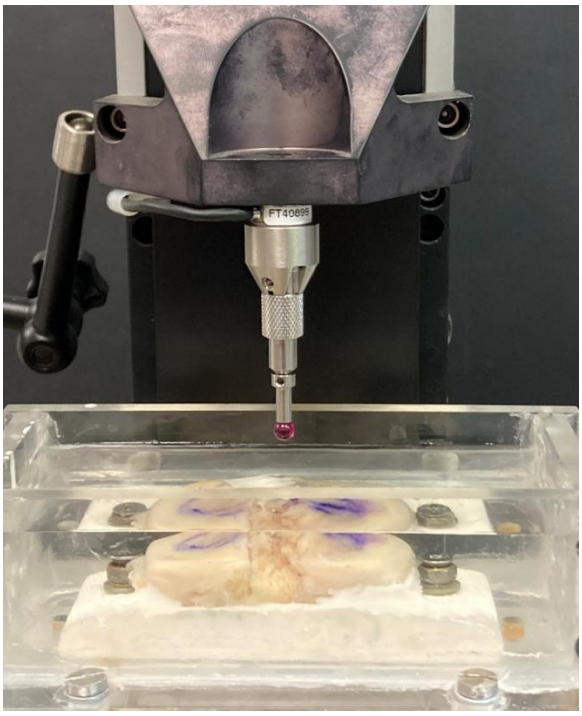

Supplementary Figure S3. The human tibial plateau constrained to the X-Y motorized table of the testing machine. The 6-mm diameter indenter is also visible.

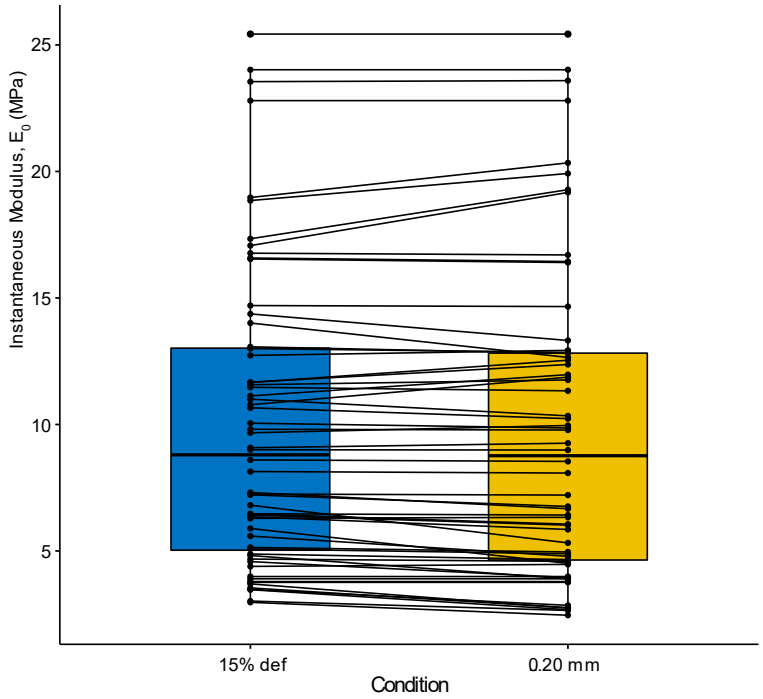

Supplementary Figure S4. Distributions of E_0 values determined with different imposed deformation, i.e., a nominal deformation of 15%, and a 0.20 mm displacement.

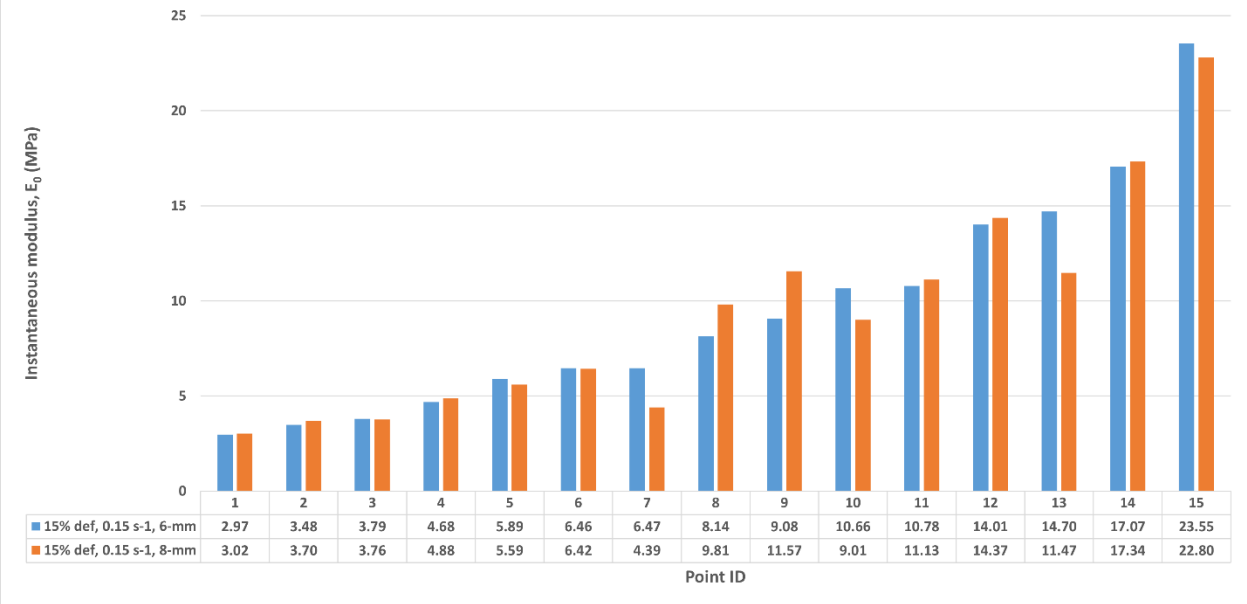

	1	2	3	4	5	6	7	8	9	10	11	12	13	14	15
15% def, 0.15 s-1, 6-mm	2.97	3.48	3.79	4.68	5.89	6.46	6.47	8.14	9.08	10.66	10.78	14.01	14.70	17.07	23.55
15% def, 0.15 s-1, 8-mm	3.02	3.70	3.76	4.88	5.59	6.42	4.39	9.81	11.57	9.01	11.13	14.37	11.47	17.34	22.80

Supplementary Figure S5. E_0 values determined for the investigated points onto the human tibial plateau by using 6-mm and 8-mm indenters (nominal deformation of 15% of the cartilage thickness, 0.15 s^{-1} indentation rate).

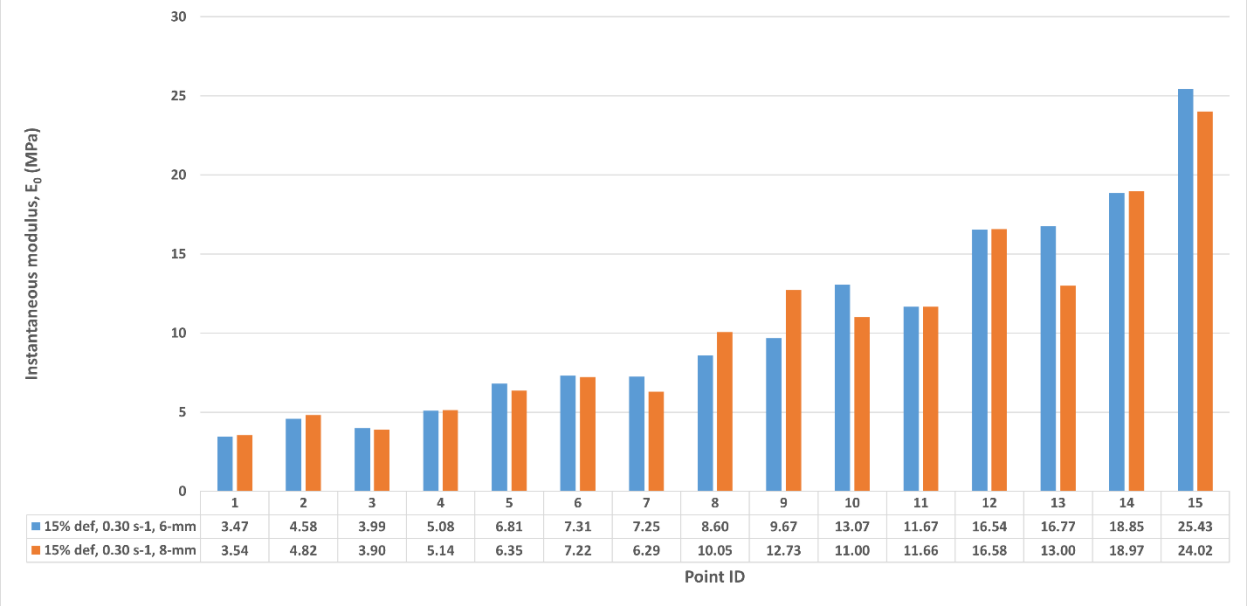

	1	2	3	4	5	6	7	8	9	10	11	12	13	14	15
15% def, 0.30 s-1, 6-mm	3.47	4.58	3.99	5.08	6.81	7.31	7.25	8.60	9.67	13.07	11.67	16.54	16.77	18.85	25.43
15% def, 0.30 s-1, 8-mm	3.54	4.82	3.90	5.14	6.35	7.22	6.29	10.05	12.73	11.00	11.66	16.58	13.00	18.97	24.02

Supplementary Figure S6. E_0 values determined for the investigated points onto the human tibial plateau by using 6-mm and 8-mm indenters (nominal deformation of 15% of the cartilage thickness, 0.30 s^{-1} indentation rate).

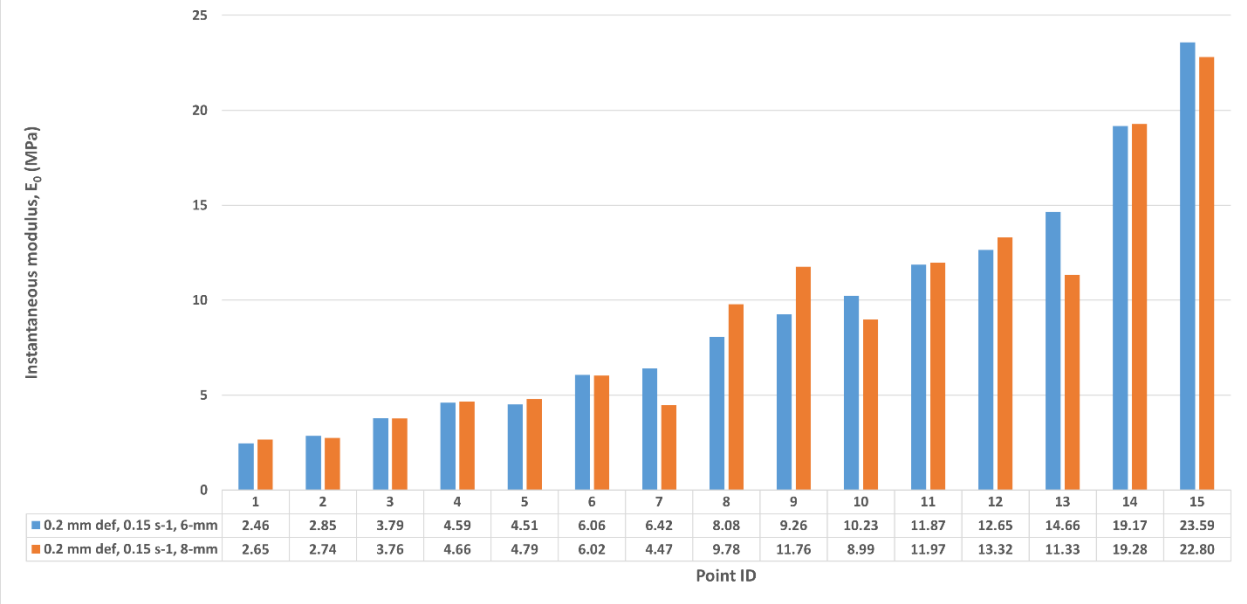

	1	2	3	4	5	6	7	8	9	10	11	12	13	14	15
0.2 mm def, 0.15 s-1, 6-mm	2.46	2.85	3.79	4.59	4.51	6.06	6.42	8.08	9.26	10.23	11.87	12.65	14.66	19.17	23.59
0.2 mm def, 0.15 s-1, 8-mm	2.65	2.74	3.76	4.66	4.79	6.02	4.47	9.78	11.76	8.99	11.97	13.32	11.33	19.28	22.80

Supplementary Figure S7. E_0 values determined for the investigated points onto the human tibial plateau by using 6-mm and 8-mm indenters (indentation depth of 0.20 mm, 0.15 s^{-1} indentation rate).

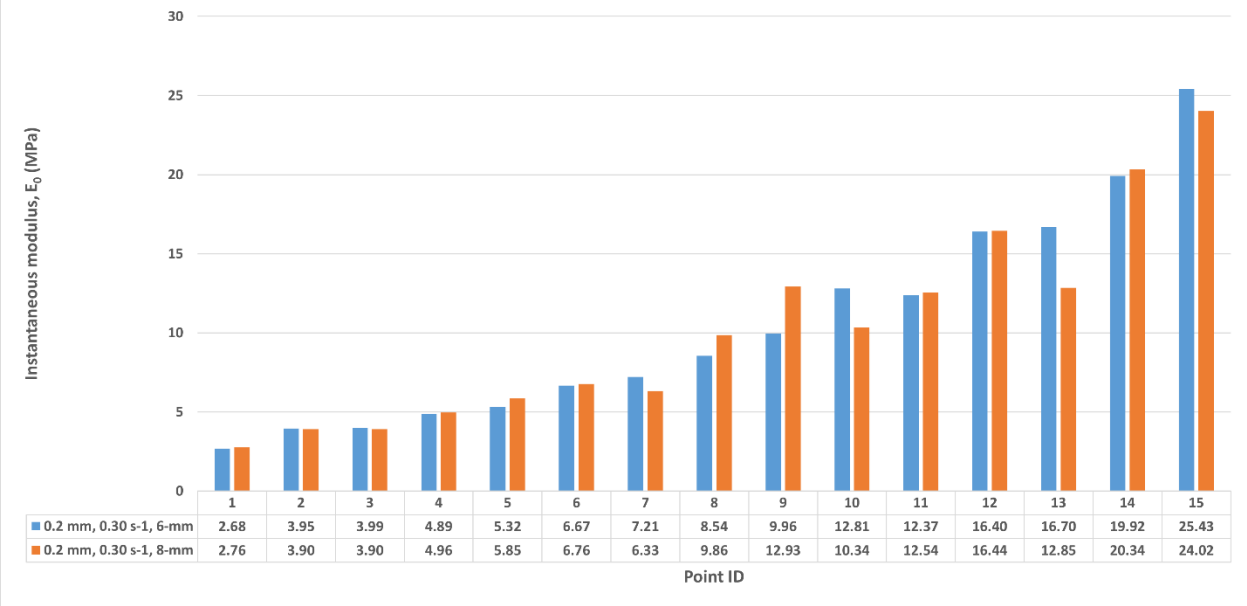

	1	2	3	4	5	6	7	8	9	10	11	12	13	14	15
0.2 mm, 0.30 s-1, 6-mm	2.68	3.95	3.99	4.89	5.32	6.67	7.21	8.54	9.96	12.81	12.37	16.40	16.70	19.92	25.43
0.2 mm, 0.30 s-1, 8-mm	2.76	3.90	3.90	4.96	5.85	6.76	6.33	9.86	12.93	10.34	12.54	16.44	12.85	20.34	24.02

Supplementary Figure S8. E_0 values determined for the investigated points onto the human tibial plateau by using 6-mm and 8-mm indenters (indentation depth of 0.20 mm, 0.30 s^{-1} indentation rate).

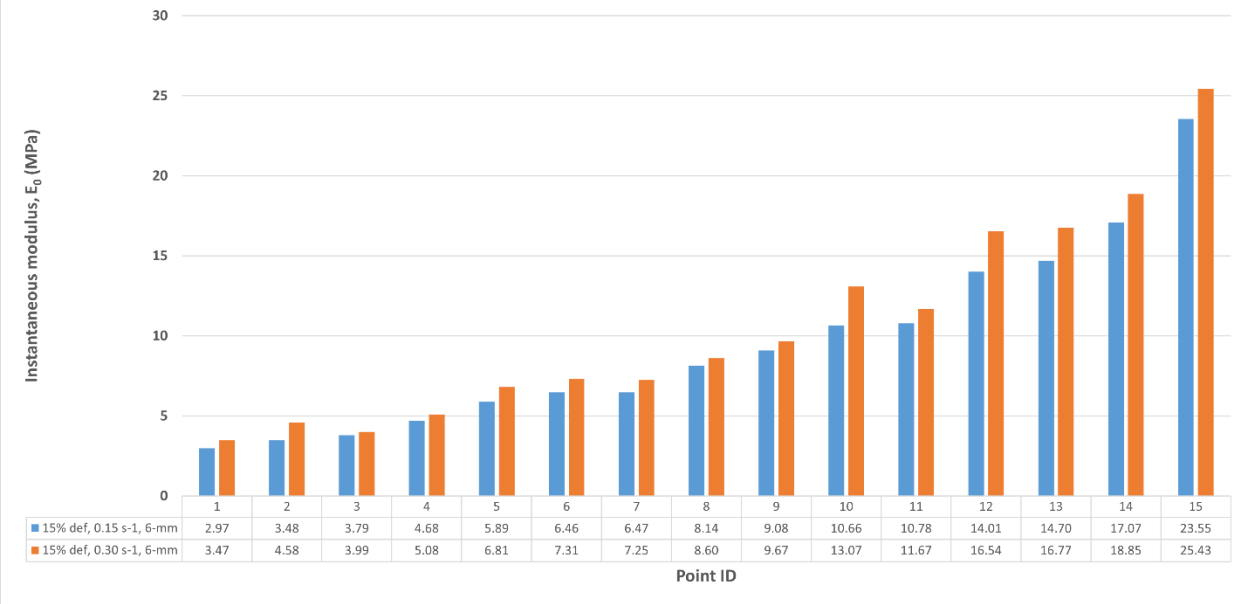

	1	2	3	4	5	6	7	8	9	10	11	12	13	14	15
15% def, 0.15 s-1, 6-mm	2.97	3.48	3.79	4.68	5.89	6.46	6.47	8.14	9.08	10.66	10.78	14.01	14.70	17.07	23.55
15% def, 0.30 s-1, 6-mm	3.47	4.58	3.99	5.08	6.81	7.31	7.25	8.60	9.67	13.07	11.67	16.54	16.77	18.85	25.43

Supplementary Figure S9. E_0 values determined for the investigated points onto the human tibial plateau by using 0.15 s^{-1} and 0.30 s^{-1} indentation rate (nominal deformation of 15% of the cartilage thickness, 6-mm indenter diameter).

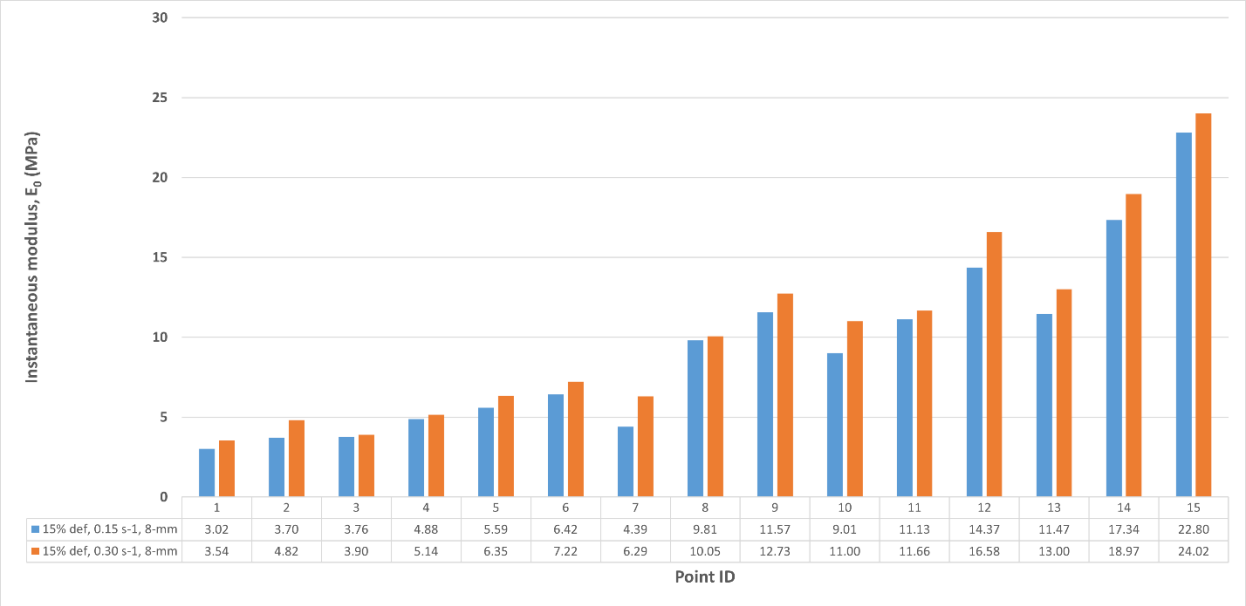

	1	2	3	4	5	6	7	8	9	10	11	12	13	14	15
15% def, 0.15 s-1, 8-mm	3.02	3.70	3.76	4.88	5.59	6.42	4.39	9.81	11.57	9.01	11.13	14.37	11.47	17.34	22.80
15% def, 0.30 s-1, 8-mm	3.54	4.82	3.90	5.14	6.35	7.22	6.29	10.05	12.73	11.00	11.66	16.58	13.00	18.97	24.02

Supplementary Figure S10. E_0 values determined for the investigated points onto the human tibial plateau by using 0.15 s^{-1} and 0.30 s^{-1} indentation rate (nominal deformation of 15% of the cartilage thickness, 8-mm indenter diameter).

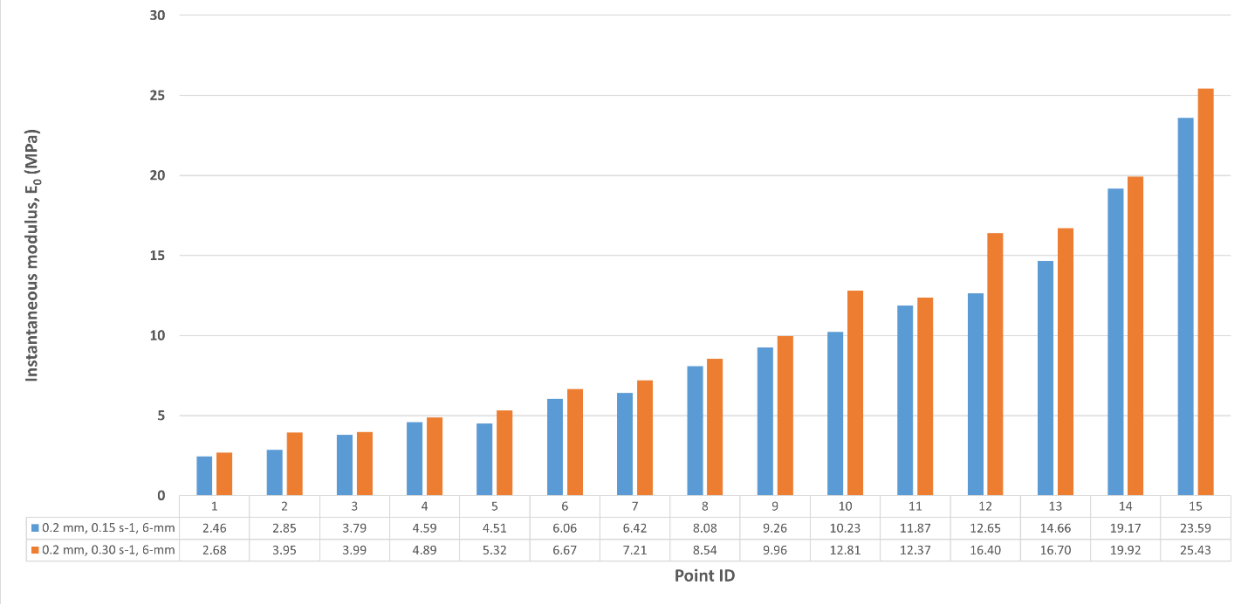

	1	2	3	4	5	6	7	8	9	10	11	12	13	14	15
0.2 mm, 0.15 s-1, 6-mm	2.46	2.85	3.79	4.59	4.51	6.06	6.42	8.08	9.26	10.23	11.87	12.65	14.66	19.17	23.59
0.2 mm, 0.30 s-1, 6-mm	2.68	3.95	3.99	4.89	5.32	6.67	7.21	8.54	9.96	12.81	12.37	16.40	16.70	19.92	25.43

Supplementary Figure S11. E_0 values determined for the investigated points onto the human tibial plateau by using 0.15 s^{-1} and 0.30 s^{-1} indentation rate (indentation depth of 0.20 mm, 6-mm indenter diameter).

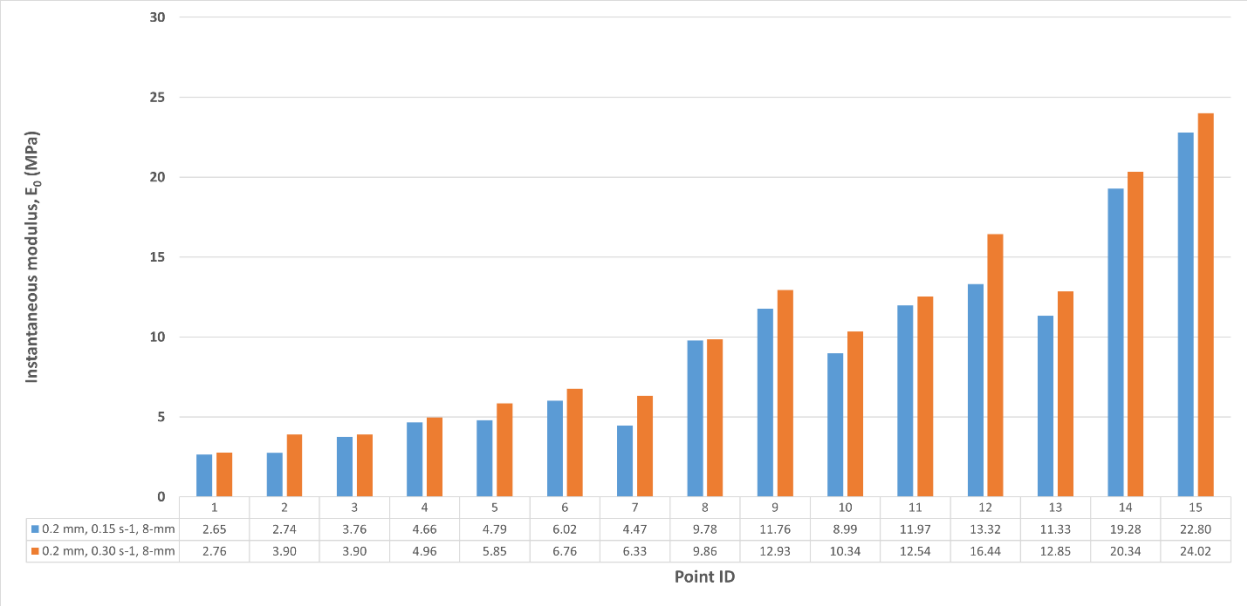

	1	2	3	4	5	6	7	8	9	10	11	12	13	14	15
0.2 mm, 0.15 s-1, 8-mm	2.65	2.74	3.76	4.66	4.79	6.02	4.47	9.78	11.76	8.99	11.97	13.32	11.33	19.28	22.80
0.2 mm, 0.30 s-1, 8-mm	2.76	3.90	3.90	4.96	5.85	6.76	6.33	9.86	12.93	10.34	12.54	16.44	12.85	20.34	24.02

Supplementary Figure S12. E_0 values determined for the investigated points onto the human tibial plateau by using 0.15 s^{-1} and 0.30 s^{-1} indentation rate (indentation depth of 0.20 mm, 8-mm indenter diameter).

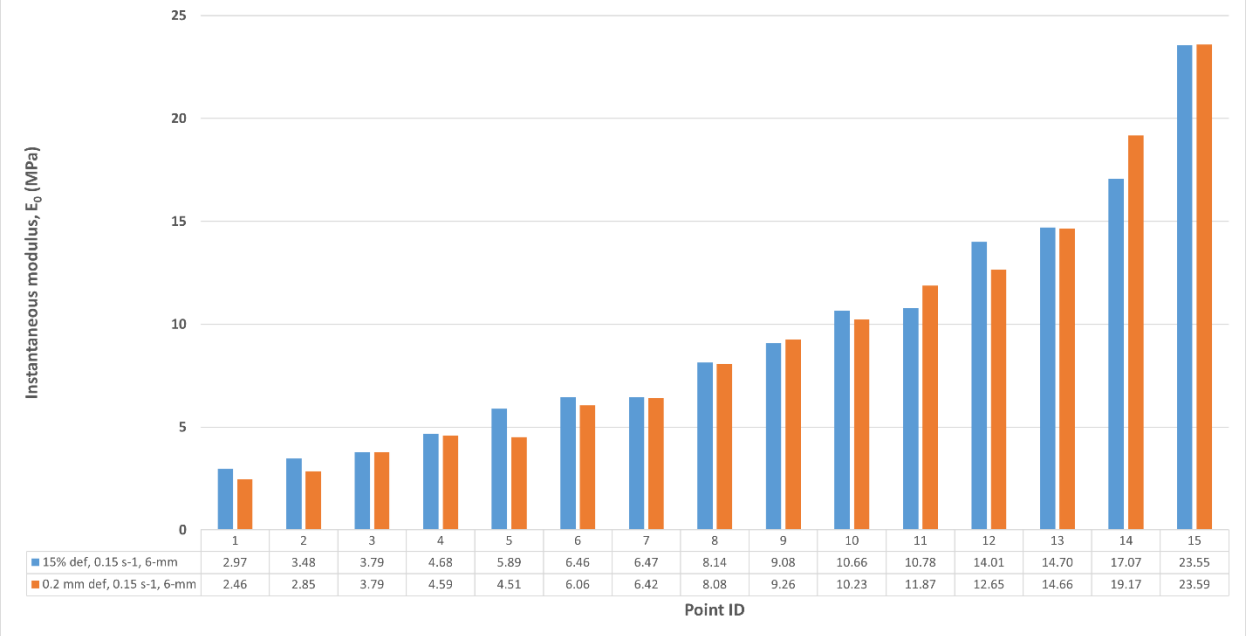

	1	2	3	4	5	6	7	8	9	10	11	12	13	14	15
15% def, 0.15 s-1, 6-mm	2.97	3.48	3.79	4.68	5.89	6.46	6.47	8.14	9.08	10.66	10.78	14.01	14.70	17.07	23.55
0.2 mm def, 0.15 s-1, 6-mm	2.46	2.85	3.79	4.59	4.51	6.06	6.42	8.08	9.26	10.23	11.87	12.65	14.66	19.17	23.59

Supplementary Figure S13. E_0 values determined for the investigated points onto the human tibial plateau by applying a nominal deformation of 15% of the cartilage thickness, or an indentation depth of 0.20 mm (indentation rate of 0.15 s^{-1}, 6-mm indenter diameter).

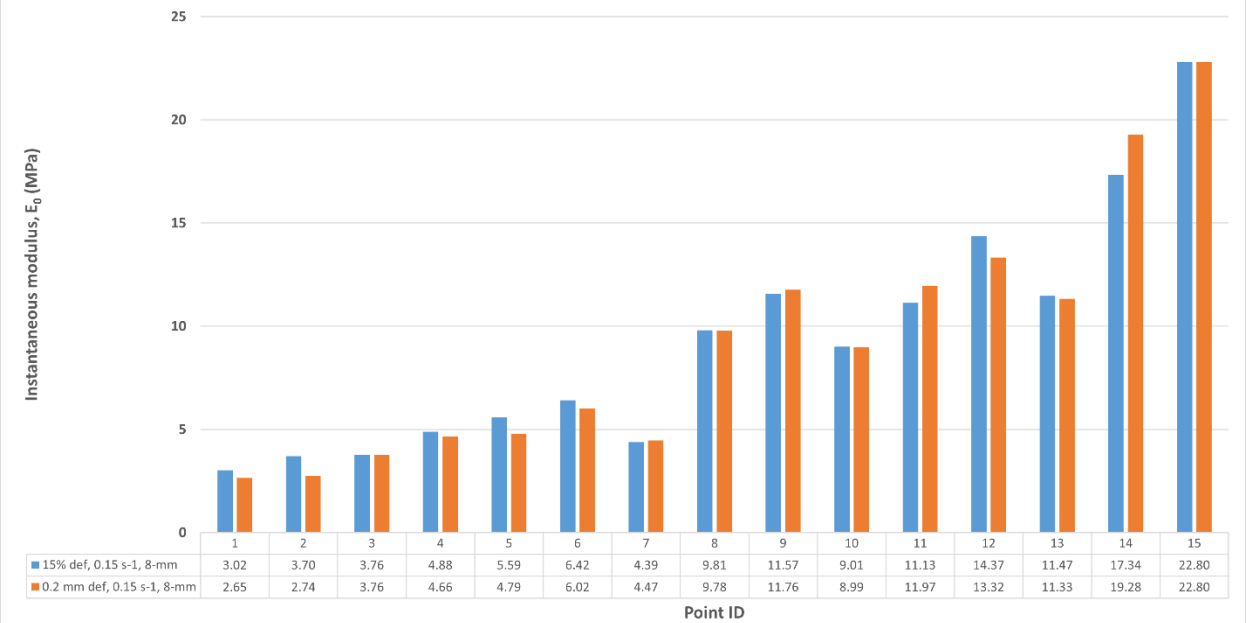

	1	2	3	4	5	6	7	8	9	10	11	12	13	14	15
15% def, 0.15 s-1, 8-mm	3.02	3.70	3.76	4.88	5.59	6.42	4.39	9.81	11.57	9.01	11.13	14.37	11.47	17.34	22.80
0.2 mm def, 0.15 s-1, 8-mm	2.65	2.74	3.76	4.66	4.79	6.02	4.47	9.78	11.76	8.99	11.97	13.32	11.33	19.28	22.80

Supplementary Figure S14. E_0 values determined for the investigated points onto the human tibial plateau by applying a nominal deformation of 15% of the cartilage thickness, or an indentation depth of 0.20 mm (indentation rate of 0.15 s^{-1}, 8-mm indenter diameter).

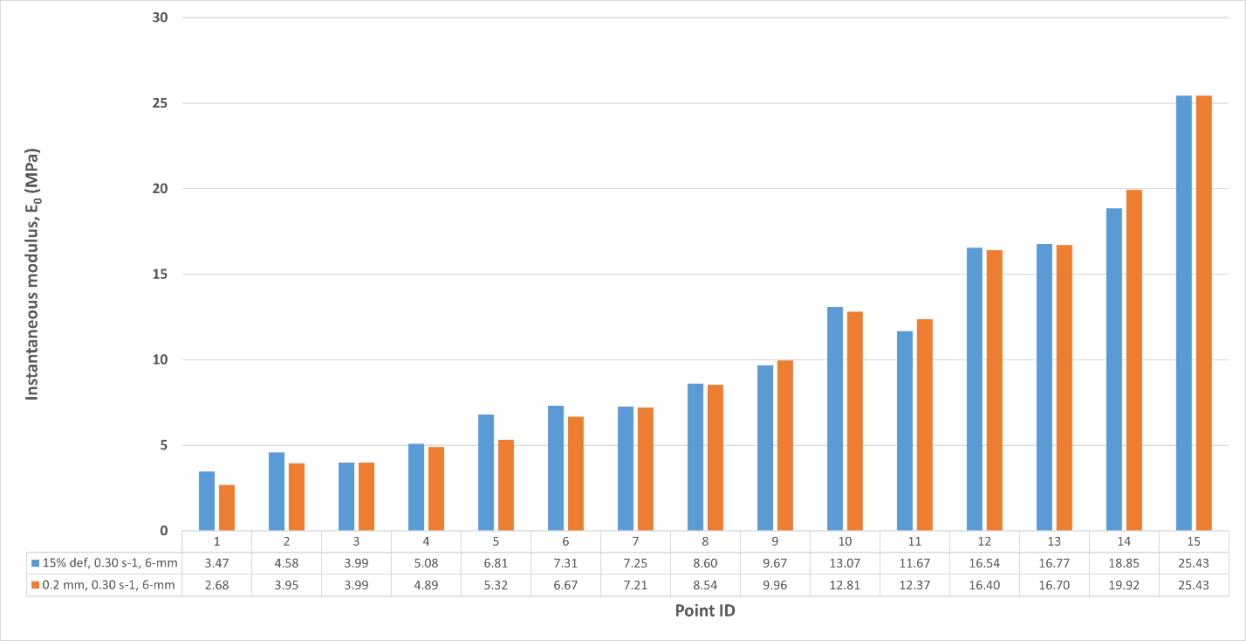

	1	2	3	4	5	6	7	8	9	10	11	12	13	14	15
15% def, 0.30 s-1, 6-mm	3.47	4.58	3.99	5.08	6.81	7.31	7.25	8.60	9.67	13.07	11.67	16.54	16.77	18.85	25.43
0.2 mm, 0.30 s-1, 6-mm	2.68	3.95	3.99	4.89	5.32	6.67	7.21	8.54	9.96	12.81	12.37	16.40	16.70	19.92	25.43

Supplementary Figure S15. E_0 values determined for the investigated points onto the human tibial plateau by applying a nominal deformation of 15% of the cartilage thickness, or an indentation depth of 0.20 mm (indentation rate of 0.30 s^{-1}, 6-mm indenter diameter).

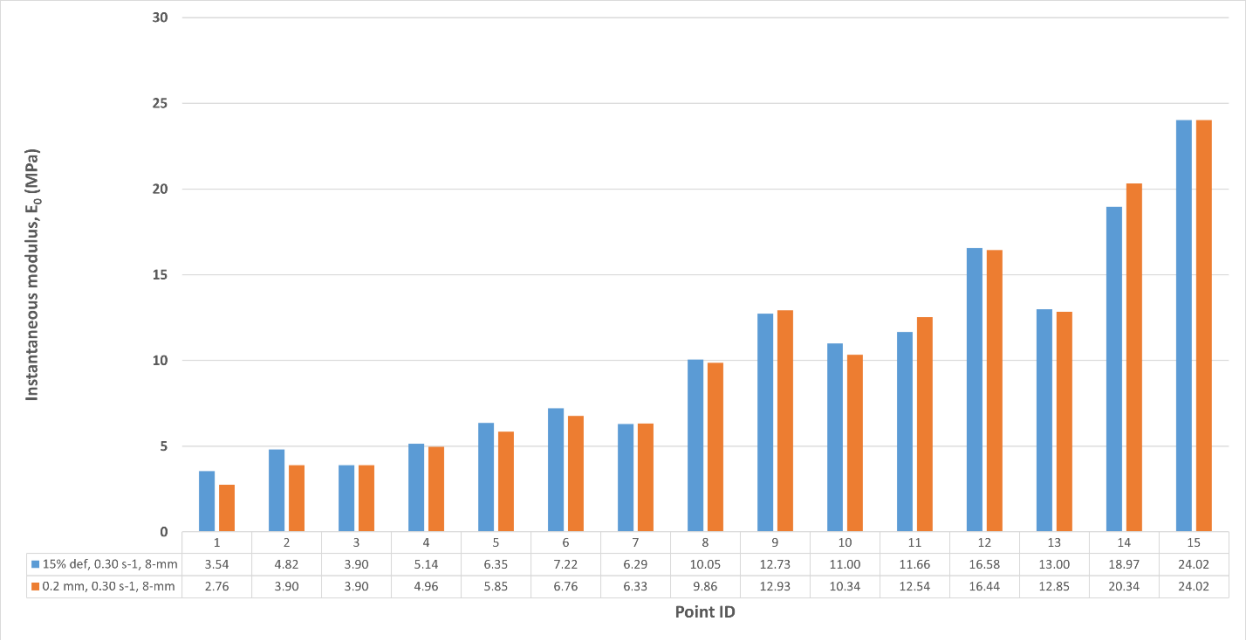

	1	2	3	4	5	6	7	8	9	10	11	12	13	14	15
15% def, 0.30 s-1, 8-mm	3.54	4.82	3.90	5.14	6.35	7.22	6.29	10.05	12.73	11.00	11.66	16.58	13.00	18.97	24.02
0.2 mm, 0.30 s-1, 8-mm	2.76	3.90	3.90	4.96	5.85	6.76	6.33	9.86	12.93	10.34	12.54	16.44	12.85	20.34	24.02

Supplementary Figure S16. E_0 values determined for the investigated points onto the human tibial plateau by applying a nominal deformation of 15% of the cartilage thickness, or an indentation depth of 0.20 mm (indentation rate of 0.30 s^{-1}, 8-mm indenter diameter).

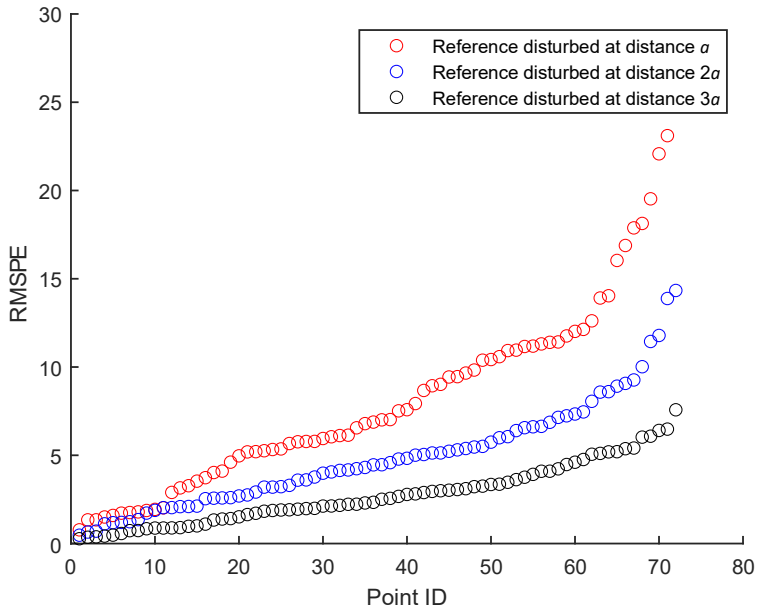

Supplementary Figure S17. Root mean square percentage error (RMSPE) calculated comparing the 72 stretched-exponential functions describing the response of the cartilage without perturbation (noPI) with each of the stretched-exponential function describing the response of the perturbed cartilage (PI*a*, PI2*a*, PI3*a*) in the same 72 measuring points.

6 Study II – Analysis of Structure-Function Relationships of Articular Cartilage through single-sided NMR Mouse and Mechanical Indentation Tests – A preliminary Study

6.1 Introduction

AC is a highly specialized tissue, which plays a crucial role in deploying the mechanical stress at which load-bearing joints are constantly subjected [151]. AC functions are allowed by its extremely heterogeneous structure, mainly composed by a fluid – i.e., water, small proteins, and electrolytes [38] – and a solid phase [3]. Regarding the latter, depth-dependent arrangement of its component – i.e., PGs, collagen fibres network, and cells – provides to AC resistance to compressive – together with the contribute of interstitial fluid – and shear stress [30], moreover allowing a smooth transition from AC to the underlying mineralized tissues composing joints. The narrow equilibrium between structure, composition, and functionality of AC can be obliterated by traumatic or degenerative pathologies. Among them, OA is the main degenerative disease impairing human joints, affecting several millions of people worldwide [9]. OA alters the remodelling processes at the base of the OC tissues homeostasis right from the early stages, decreasing the mechanical response of the OC unit, i.e., of AC [13]. Throughout OA, different changes are induced within the AC thickness [152]; thus, depth-dependent evaluations are required to investigate specifically OA changes and their impact on the AC mechanical response.

Accordingly, the development and the optimization of approaches investigating the main features of AC and, moreover, how these change within its thickness, are crucial to properly understand the complex relationship between heterogeneity and mechanical response of the tissue, with the final aim of gaining insights on how pathologies impair such relationship.

With the purpose of achieving more relevant information on the pathophysiological condition of AC, in vivo investigation should be performed through arthroscopic devices. Nevertheless, ex vivo evaluations still represent the most commonly used approach to assess the characteristics of AC.

In studying biological tissues, low-field NMR provides the possibility of enhancing the contrast of the investigated signals across tissue thickness [146,153], moreover combining cost reduction and high adaptability. In this regards, single-sided NMR scanners mainly consist of small, permanent magnets – which enable their portability – and enable the investigation of samples with a surface extent up to a few hundred of mm^2 [154]. The signal is obtained by the evaluation of a sensitive volume, which extent is given by the combination of the resonance properties of the coil, and the static field gradient aligned to the coil normal axis [146]. Considering that single-sided NMR is more suitable for materials with a homogeneous structure, its application to heterogeneous and imperfected – e.g., with a curvature – surfaces leads to a partial averaging of the signal within the structures composed by different layers. However, this approach was found to be acceptable for the main human joints [154]. By using single-sided NMR , information about AC are retrieved in terms of variation of T_2, T_1 and diffusion coefficient, D, across the depth of the layer in contact with the device [155]. T_2 and T_1 relaxation times correlates to phenomenon related to the water content and to the interaction of the fluid phase with the main macromolecules that compose ECM of AC, i.e., collagen and PGs, respectively [156]. D coefficient is related to the structure of collagen fibrils

and to PGs arrangement; consequently, the restriction of the water within such a structure defines the measure of D. Relaxometry studies proved that variation of such signals within AC is related to water content, presence of metabolites, as well as tissue structure [147]. In this regard, phenomena related to water relaxation are not only content-dependent but, moreover, lie also on the kind of interaction with existing interfaces [154]. Accordingly – and considering that analyses through single-sided NMR already succeeded in evaluating healthy and pathological AC [149,150,157,158] –, such a technique could differentiate the main layers composing such a tissue, which may represent a key insight to evaluate the AC features through non-destructively approaches.

Besides evaluating AC structure and composition, mechanical properties can be an equal sensitive indicator of AC status [84]. In this perspective, indentation is one of the main ex vivo approaches involved in the evaluation of AC mechanical response [107]. In addition to the insights retrieved by the other techniques – e.g., confined and unconfined compression –, indentation allows to map tissues properties onto articular surface and, most importantly, do not require detachment of AC from the underlying OC tissues to investigate its features [159]. Due to the possibility of maintaining – as close as possible – the boundary conditions peculiar of the OC unit, information about the viscoelastic behaviour of AC – which already proved to be sensitive to OA progression [84,159,160] – obtained by indentation should be more accurate and reliable in terms of the effective response of the tissue.

The implementation of techniques retrieving insights about AC in a non-destructive way not only allows to integrate multidisciplinary information but, most importantly, provides the possibility of leading longitudinal assessments of such a tissue. This opportunity is of paramount importance, since it allows to investigate i) the effects of enzymatic degradation simulating different grades of severity of pathologies, thus to better understand their etiology and the dynamic beneath their progression, and ii) the efficacy of treatments responding to diseases impairing the features of AC.

According to the above reported evidence, the primary aim of this study was to provide a multidisciplinary framework evaluating the main peculiarities of AC in a non-destructive way. In this perspective, an indentation protocol based on nominal deformation was applied to the AC of OC cores excised from the articular surfaces – i.e., femoral condyles, and tibial plateau – of bovine knees with the purpose of investigate the tissue viscoelastic properties. Structural information about AC was evaluated through tissue thickness by single-sided NMR exploring four parameters, namely T_2, T_1, diffusion coefficient D, and solid-liquid ratio, α. Lastly, with the view of applying the proposed framework to study the impact of degenerative processes on AC, a first exploratory assessment of preliminary relationships between AC mechanical and structural parameters was proposed.

6.2 Materials and Methods

By considering the multiple steps that defined the pipeline of the current study, in the following the relative workflow was reported.

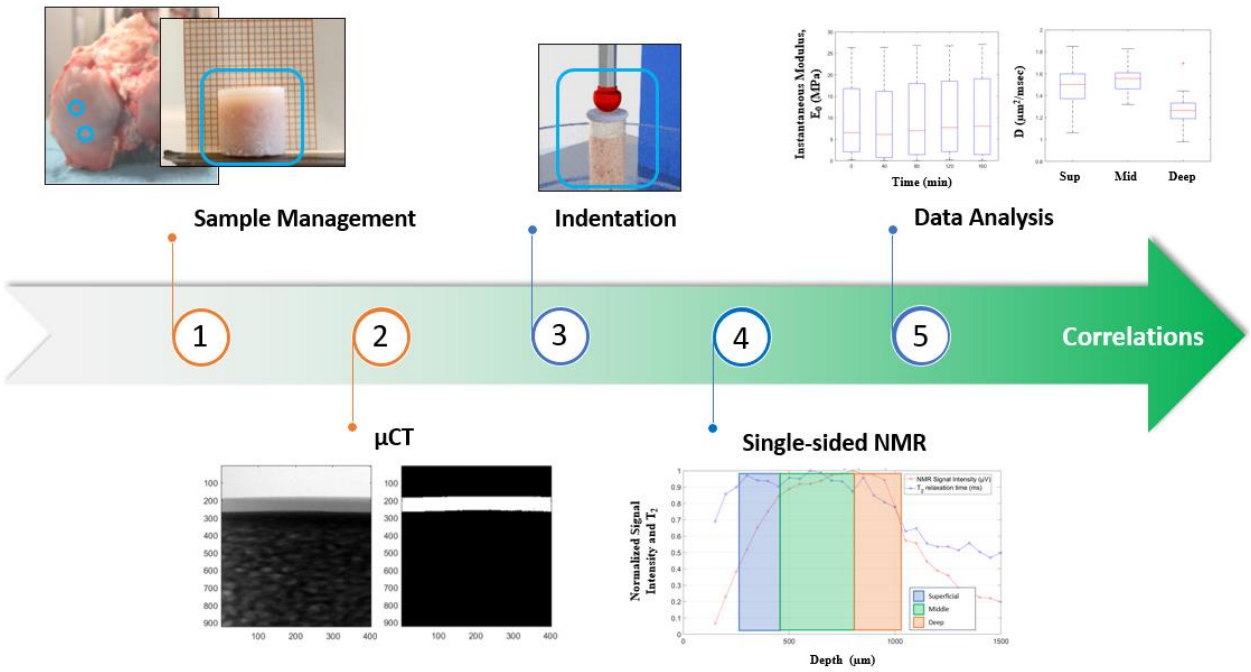

Fig. 6.1. The workflow of the study about the analysis of structure-function relationships of AC through single-sided NMR mouse and mechanical indentation tests.

6.2.1 Sample Collection and Management

Cuboid samples – N = 16, with a minimum thickness of ~ 20 mm, and a minimum nominal area of ~ 25 x 25 mm^2 – were extracted from the articular surfaces of N = 11 bovine knees through the use of a diamond-coated blade (MDP200, Remet, Bologna, Italy) assembled in a circular saw (TR60, Remet, Bologna, Italy) (**Fig. 6.2**). Cutting process was performed under continuous water cooling, avoiding dehydration and heating of the OC tissues. At least one cuboid was extracted from each knee. Cuboid samples were then wrapped in gauze soaked in PBS 1X (7.4 pH, Life Technologies Europe B.V., Bleiswijk, The Netherlands) and frozen at −20 °C in separate sealed containers [161,162]. By following, an additional step was performed, strictly required by one of the approaches applied to study the AC. In particular, cuboid samples were thawed at 4°C in PBS 1X for one hour, and then cored by the use of a 10-mm diameter diamond-tipped cylindric cutter attached to a CNC milling machine (ProLIGHT Machining Center, PLM 2000). Before each coring, cuboid samples were spatially tilted, exposing to the cylindric cutter a surface as flat as possible.

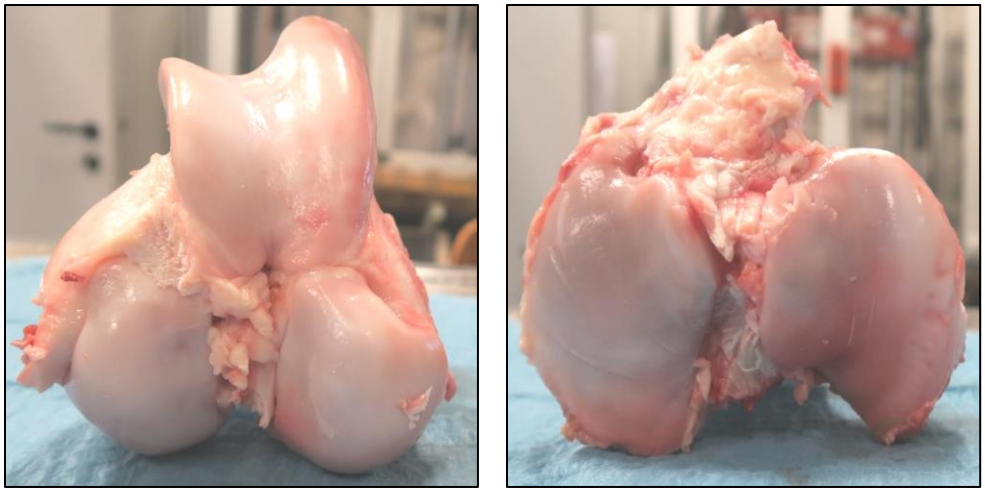

Fig. 6.2. Dissected bovine knee joints showing (Left) femoral and (Right) tibial articular surfaces, from which cuboids samples were excised.

Some precautions were implemented to avoid heating and damage of AC over coring, in particular i) samples were completely submerged in PBS 1X, and ii) multiple steps of holing – each one of 0.5 mm along the vertical axis – were performed for each core, moreover leaving a break of ~ 10 seconds between subsequent hole-steps. Such a procedure required ~ 10 minutes for each OC core, and allowed to collect at least two OC cores – 10-mm in diameter and height, including AC, SB and TB (**Fig. 6.3**) – from each cuboid sample. After harvesting, OC cores were enveloped in PBS 1X-soaked gauze, and frozen at −20 °C in separate sealed containers. A total of N = 36 OC cores – at least two for each cuboid – were obtained as output of the entire Sample Management process.

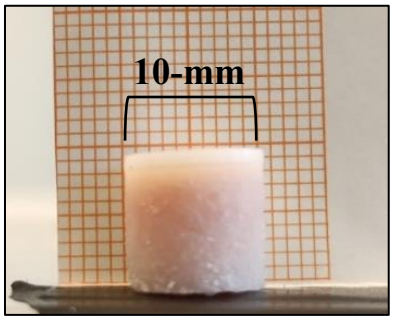

Fig. 6.3. OC core retrieved from the processing of a cuboid sample, extracted from the bovine knee articular surface.

The procedure of i) excising cuboid samples from bovine knees, ii) coring such samples, and iii) subsequent assessments – see the following paragraphs – were spaced in time and by freezing cycles aiming to standardize the management procedure for all the samples.

6.2.2 Estimation of AC Thickness by µCT

The day before testing, subgroups of N = 6 frozen OC cores were thawed overnight at 4 °C in PBS 1X [163]. The day of the test, and prior to indentation, each OC core was investigated to estimate AC thickness. This preliminary step is required in order to apply an indentation testing protocol based on nominal deformation. After blotting each core from excess of PBS, it was hosted in a custom-made polymethyl methacrylate (PMMA, plexiglas) sample holder, and then placed inside a µCT system (SkyScan 1072, SkyScan, Aartselaar, Belgium) (**Fig. 6.4**).

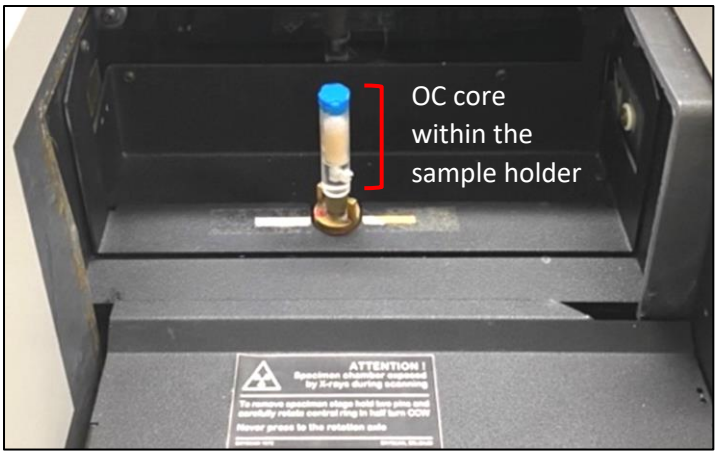

Fig. 6.4. Custom-made polymethyl methacrylate sample holder hosting OC cores during µCT acquisitions, performed to compute the AC thickness.

Before scanning, the position of the sample holder inside the µCT was adjusted to include the whole AC layer, and few millimetres of both air and TB within the Field of View (FoV). Subsequently, four planar images of such a FoV were acquired (X-ray tube voltage = 50 kV, current = 197 µA, 1-cm Al filter, pixel size = 11.52 µm, exposure time = 5.9 s), each after a rotation of 45° around the sample vertical axis. The entire procedure required ~ 5 minutes/OC core. Afterwards, AC thickness of the core was computed by a custom-made Matlab script (MATLAB 2022b, MathWorks, Natick, MA, USA). In particular, AC was segmented through a semi-automatic procedure consisting of the following steps: i) a preliminary crop of the planar images to exclude residual portion of the sample holder material, i.e., plexiglas; ii) an optimal grey-level threshold was imposed aiming to differentiate AC, mineralized tissues, and air, thus to obtain binarized images; iii) exclusion of possible undesired contributes, i.e., pixels with an original grey-level within the distribution characteristic of the AC, through a continuity approach. Examples of the outcomes achieved by the above-mentioned procedure were reported in **Fig. 6.5**. For each OC core, the outcome of such analysis was therefore considered as input parameter for the following indentation tests.

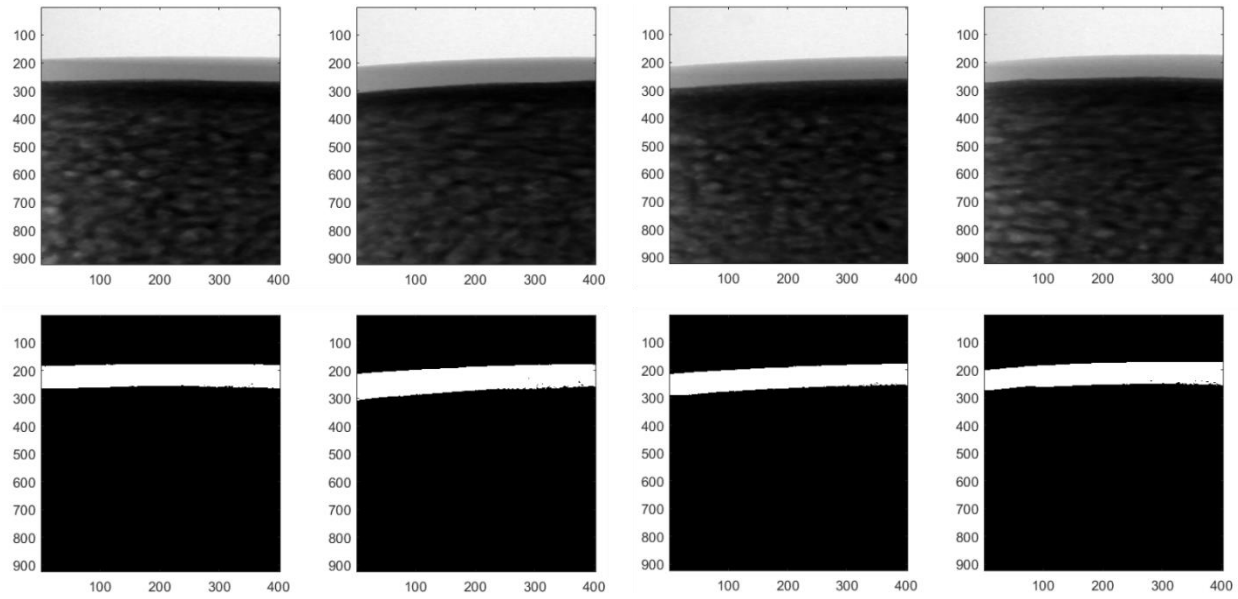

Fig. 6.5. (Top) Planar images acquired by μCT, each one obtain after a rotation of 45° around the sample vertical axis. (Bottom) Binarization of the planar images, obtained after applying the developed procedure, from which AC thickness was computed.

6.2.3 Indentation Test

After the estimation of the AC thickness, the subgroup of N = 6 OC cores was subjected to indentation to investigate the viscoelastic response of AC. Firstly, OC cores were hosted within the cavities – inner diameter of 10 mm, depth of 5 mm – of an ad-hoc designed, polymeric samples holder. In addition to the interlock – i.e., OC cores and cavities had the same diameter –, the cores were constrained at the bottom by PMMA (Restray NF, S.P.D.: Mulazzano, Italy). Beneath each cavity a steel screw was fitted, thus to facilitate the removal of the cores after test. The process of interlock and polymerization required ~ 30 minutes, during which AC surface was kept moist by a gauze soaked in PBS 1X at room temperature. Subsequently – and before testing – the whole setup was constrained within a plexiglas chamber, and then submerged in PBS 1X for 30 minutes; in the meanwhile, the plexiglas chamber was constrained to the X-Y motorized table of the testing machine (Mach-1 V500css, Biomomentum Inc., Laval, QC, Canada) (**Fig. 6.6**). Last, each OC core underwent a preliminary indentation to precondition the tissue. With the twofold objective of i) verifying eventual damages induced by coring to the viscoelastic properties of AC – which, for example, could lead to a high variability of AC mechanical properties of the same specimen –, and ii) increasing the reliability of the outcomes, N = 5 repetitions/core were performed, each one after a resting period of 40 min [164]. A nominal deformation corresponding to 15% of the AC thickness [165] was imposed – with a deformation rate of 0.15 s^{-1} [166] – in the center of each OC core by a 6-mm spherical indenter, thus to apply the same deformation to the AC regardless its width. With the purpose of investigating the viscous response of AC, the indenter was held in position for 300 s before releasing from AC surface [161]. The entire testing protocol required ~ 7 hours for each subgroup of N = 6 OC cores. At the end of the testing procedure, OC cores were enveloped again in a gauze soaked in PBS 1X, and frozen at −20 °C in separate sealed containers until the next assessment.

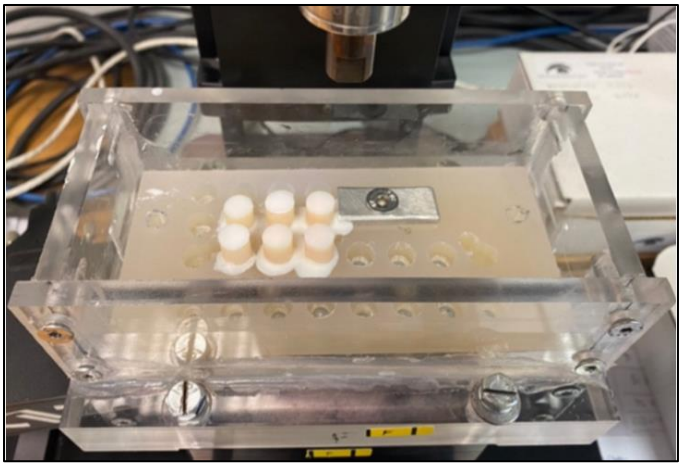

Fig. 6.6. Plexiglas chamber – constrained to the X-Y motorized table of the testing machine – in which the custom-made samples holder is constrained.

6.2.4 Single-sided NMR

The assessment of depth-dependent information about AC structure was performed by the Department of Physics and Astronomy of the University of Bologna, Italy.

The day of the evaluation, OC cores were individually defrosted in PBS 1X at room temperature for 20 minutes. To minimize dehydration of AC during the assessment, OC core was placed within a cylindrical glass tube, sealing the top by a cap and a wet sponge, and placing a slide of Polytetrafluoroethylene (PTFE) on the inner-bottom of the glass tube, directly in contact with the AC surface.

The setup containing the OC core was placed in contact with the top surface of a single-sided Profiler NMR-MOUSE PM10 (polarizing magnetic field strength $B_0 = 0.327$ T, Larmor frequency 13.8 MHz), with the purpose of investigating the laminar structure of AC. The device was equipped by a KeaII spectrometer, and by a high-precision lift. The polarizing field generated by the permanent magnet consisted in a constant gradient intensity of 14 T/m along the direction perpendicular to B_0, uniform within the sensitive volume. The high-precision lift allowed to adjust the vertical distance between the cylindrical glass tube and the permanent magnet (Magritek, NZ), thus to perform the NMR assessment through a multi-step approach along the depth of AC. In this regard and aiming to obtain a balance between the signal-to-noise (SNR) ratio and the penetration depth assessable within AC layer, four 2 mm-spacers were inserted between the permanent magnet and the surface coil. Regarding the evaluable depth, the maximum value achievable through the developed setup resulted to be 3 mm. Last, a specific scanning protocol was applied to measure NMR parameters – i.e., T_2, T_1, D, and α –, consisting in four sequences named Carr-Purcell-Meiboom-Gill (CPMG), Saturation Recovery (with CPMG), Stimulated Spin Echo (with CPMG), and build-up Double-Quantum-like (with CPMG) [154,167]. Meaning of T_2, T_1, and D parameters was reported in the Introduction (paragraph 6.1). α parameter (μV/msec) is related to the ratio between the solid phase and a phenomena related to the fluid phase – i.e., interactions between the components of the hydrogen molecules and the macromolecules composing ECM of AC.

The scanning protocol consisted of two steps, i) the profile analysis through AC thickness, and ii) the analysis within the three layers of AC, i.e., superficial, middle, and deep layer.

The profile analysis was achieved by applying a fast CPMG sequence – echo time of 91.5 μs, which correspond to a slice thickness of 75 μm – at different depth within AC thickness, starting from the maximum depth afforded by the device configuration, and proceeding with a 50 μm step size in-depth. Signal intensity and T_2 profiles were obtained by normalization on their maximum values. The analysis of NMR parameters profile through AC thickness by CPMG sequence lasted for ~ 30 minutes.

By evaluating local trends in the achieved signal intensity profile, the three layers composing the AC were identified, i.e., in correspondence of the initial increase, maximum and subsequent decrease regions, for superficial, middle, and deep layers, respectively. Then, NMR sequences were run by considering such boundary conditions, i.e., by positioning a 210 μm-thick scanning volume at the center of each layer. The three layers analysis required ~ 3.5 hours. Considering the timing of each step, the whole NMR assessment required ~ 4 hours/OC core. After NMR assessment, OC cores were wrapped in a gauze soaked in PBS 1X, and frozen at −20 °C in separate sealed containers.

6.2.5 Data Analysis

Distribution of AC thickness computed by μCT was assessed via Kolmogorov-Smirnov test. In case of non-normal distribution, data was presented as quartiles range, i.e., 5^{th}, 25^{th}, 50^{th}, 75^{th}, and 95^{th}.

Regarding mechanical testing, the loading part of the indentation curve, i.e., force vs displacement, of each test was fitted – up to the peak load – by the Hayes model, thus to compute the Instantaneous Elastic Modulus, E_0 (MPa), of AC [95]. Poisson's ratio was set to 0.45 [168]. The viscous response of AC was evaluated by fitting the load-time curve during relaxation by a stretched exponential function [160,169], implemented by minimizing the root mean square error through a custom-made Matlab script (MATLAB 2022b, MathWorks, Natick, MA, USA). The three characterizing parameters – S_0, τ, and β, where S_0 (N) is the maximum load value reached prior to load relaxation, τ (sec) is the time constant, and β (a.u.) is the stretching parameter – were computed for each individual test. Finally, Equilibrium Modulus, E_{eq} (MPa), was calculated from the measured equilibrium force – i.e., the value reached in the final stage of relaxation – corrected, by using the Hayes equation, to consider the involved geometries [161].

Distribution of the mechanical parameters was assessed via Kolmogorov-Smirnov test. In case of non-normal distribution, inter-variability of such parameters was evaluated – across subsequent indentations – through box plot. Variability of the mechanical parameters across subsequent indentations was evaluated as percentage Coefficient of Variation (CoV%), i.e., percentage ratio between standard deviation and average values. In case of non-normal distribution, CoV% was reported through box plot. The median values of the mechanical parameters across subsequent indentations were considered for each OC core, with the purpose of investigating preliminary correlation with NMR parameters.

Regarding NMR assessment, and considering the limitation related to the maximum depth evaluable, the estimate of deep layer thickness could be affected by a bias. Therefore, the thickness of the deep layer was computed by considering the percentage range of distribution of the thickness of the three layers composing AC, aiming to partially overcome this issue. More in detail, since the average thickness of the superficial and middle layer can be assumed as 15% and 50% of the AC total thickness, respectively [4], the thickness of the deep layer was assumed as the remaining 35%. Moving on the analysis of NMR parameters, and considering their monomodal, quasi-continuous distribution, a mono-exponential fit was used to estimate T_1 and T_2 of each AC layer, while a log-linear and a linear fit were used with the purpose of computing D and α, respectively. As for mechanical parameters, the fitting procedure was performed through MATLAB scripts. Consequently, four parameters, T_2, T_1, D, and α, were obtained for each AC layer. Distribution of NMR parameters for each layer was assessed via Kolmogorov-Smirnov test. Then,

Kruskal-Wallis test – followed by a post-hoc comparison between groups through Wilcoxon test – was applied to investigate statistical difference between AC layers ($p < 0.05$). To correct statistical difference for multiple testing, post hoc comparisons were performed by using a Bonferroni correction; accordingly, $p < 0.017$ was set as threshold for statistical significance.

To verify the assumption at the base of the estimate of AC thickness by NMR assessment and, thus, the accuracy of such a technique, Pearson correlation test was applied to such outcome and to the measures of thickness performed by µCT approach. µCT was considered as the reference method primarily due to i) the absence of theoretical assumptions from literature, ii) the reduced time required, and iii) the higher resolution, i.e., ~12 µm vs 50 µm, considering µCT and NMR, respectively.

The presence of preliminary relationships between mechanical and NMR parameters was assessed by Spearman correlation test. First, possible relationships between individual – as computed – parameters were investigated. Second, and in absence of moderate correlations – defined as $\rho^2 < 0.6$ – between individual parameters, the analysis was extended to possible compositions of them. In this regards, weighted NMR parameters – i.e., T_{2w}, T_{1w}, D_w, and α_w – were computed by weighting the values corresponding to the individual AC layers for the thickness – provided by NMR assessment – of such layers. Third, the weighted NMR parameters were multiplied – or divided – by the AC thickness estimated through µCT, thus to obtain information related to the whole thickness – or to the unit of thickness –, respectively.

Aiming to investigate preliminary correlations with AC elasticity – i.e., E_0, S_0 –, T_{1w} and T_{2w} parameters were multiplied by AC thickness. In this regard, it must be highlighted that the response to mechanical stimuli of AC depends on the amount of tissue [170] and, moreover, to its condition, i.e., healthy or pathological [119]. In addition, AC instantaneous response depends mainly on the tissue water content [58] which, in addition, represents one of the main factors influencing T_1 and T_2 [156]. By multiplying T_{1w} and T_{2w} by AC thickness, parameters related to the total amount of water content are achievable.

With the purpose of exploring preliminary correlations with AC viscous parameters – i.e., τ, β, and the drop of response between instantaneous and equilibrium response, defined as $(E_0 - E_{eq})$ –, D_w was divided by AC thickness, while α_w was multiplied by AC thickness. AC viscous response depends on flow dependent and independent phenomena [91]. The exponent of the stretched exponential function – i.e., $(1/\tau)^{\beta}$ – applied to describe the trend of the load during relaxation is related to the rate at which viscous phenomena are exhausted. The extent of the difference between E_0 and E_{eq} depends on the water content within AC. In case of a high water content, a higher amount of response is lost during relaxation due to water-related phenomena – i.e., flow, first, and exudation, then – thus reaching a lower E_{eq} and, consequently, a wide difference between E_0 and E_{eq} – i.e., $E_0 >> E_{eq} \Rightarrow (E_0 - E_{eq}) \approx E_0$. In contrast – so in case of low water content –, a reduced amount of response is lost during relaxation, yielding a value of E_{eq} closer to E_0 – i.e., $E_{eq} \approx E_0 \Rightarrow (E_0 - E_{eq}) \rightarrow 0$. D parameter is related to the structure of collagen fibrils and to PGs arrangement, which define the 3D geometry of the confining space; accordingly, the level of restriction of the water within such a geometry influences the extent of D. By dividing D_w by AC thickness, a diffusion coefficient per unit of thickness is achievable, with a rate as physical dimension. Regarding α, its value represent the ratio between solid and water content, so the lower is the latter, the higher the parameter resulted to be. By multiplying α_w by AC thickness, a parameter related to the total (solid/fluid) ratio within the tissue is achievable.

6.3 Results

With the purpose of evaluating the distribution of mechanical and NMR parameters and, moreover, to exploratory investigate preliminary relationships between them, data corresponding to N = 1 OC core was

excluded due to a technical problem occurred during testing. Accordingly, in the following results about N = 35 OC cores were reported.

6.3.1 Estimation of AC Thickness by µCT

The analysis highlighted a non-normal distribution of AC thickness. More in detail, AC thickness distribution is described as follows: the 5th, 25th, 50th – i.e., median value –, 75th, and 95th percentile were found to be equal to 0.83 mm, 0.95 mm, 1.21 mm, 1.79 mm, and 2.90 mm, respectively.

6.3.2 Indentation-based mechanical parameters

Kolmogorov-Smirnov highlighted a non-normal distribution for all the mechanical parameters. Therefore, inter-variability of such parameters across OC cores and indentations were reported as boxplot diagrams in **Fig. 6.7**, **Fig. 6.8**, and **Fig. 6.9**.

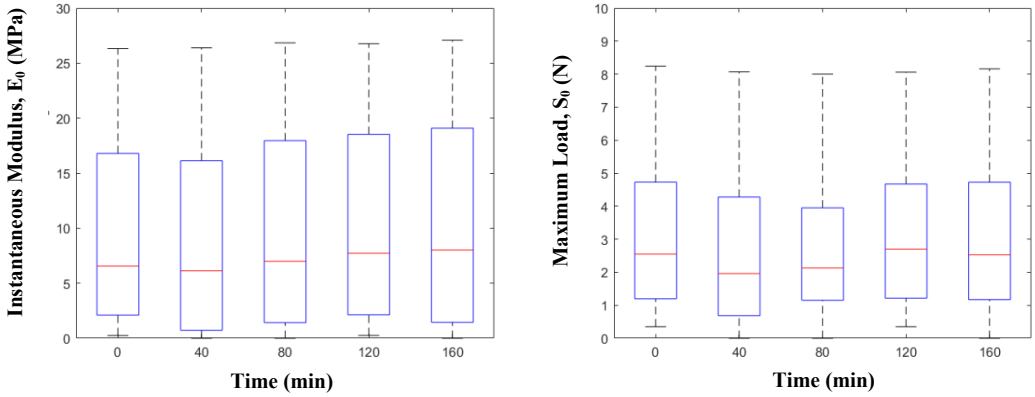

Fig. 6.7. Boxplot diagrams of the elastic parameters, i.e., (Left) Instantaneous Elastic Modulus, E_0, and (Right) Maximum Load, S_0, across OC cores and indentations. The boxes indicate the 25th and 75th percentiles and the line within the boxes marks the medians. Whisker length is equal to 1.5×interquartile range.

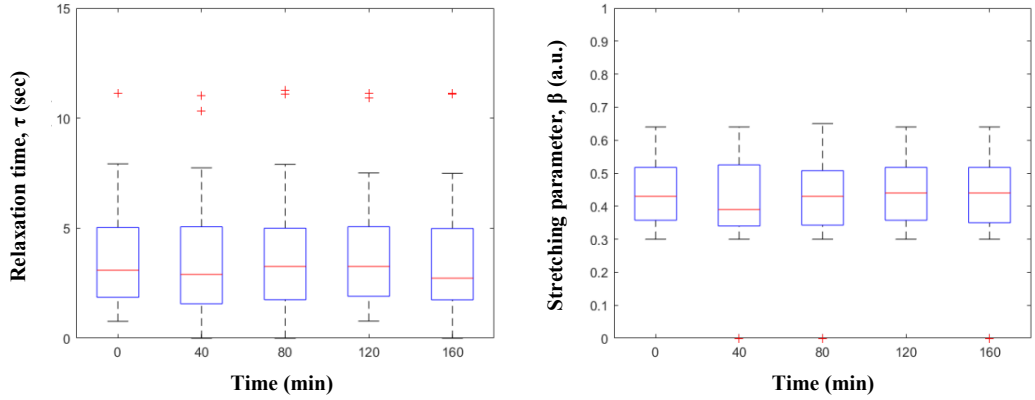

Fig. 6.8. Boxplot diagrams of the viscous parameters, i.e., (Left) Relaxation Time, τ, and (Right) Stretching parameter, β, across OC cores and indentations. The boxes indicate the 25th and 75th percentiles and the line within the boxes marks the medians. Whisker length is equal to 1.5×interquartile range. Plus signs represent outliers.

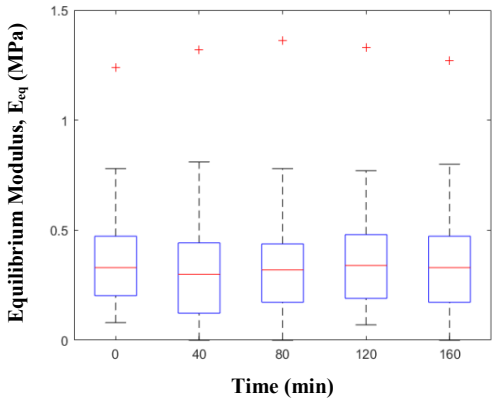

Fig. 6.9. Boxplot diagram of the equilibrium parameter, i.e., Equilibrium Modulus, E_{eq}, across OC cores and indentations. The boxes indicate the 25th and 75th percentiles and the line within the boxes marks the medians. Whisker length is equal to 1.5×interquartile range. Plus signs represent outliers.

Distributions of the mechanical parameters across subsequent indentations were quite similar. This evidence is supported by the limited spread of the mechanical parameters CoV% – i.e., 25th and 75th percentiles in the range (0.56 ÷ 7.42)%, with very few cases above 20% for S_0 and E_{eq} – of each OC core. Details about the non-normal distribution – verified by Kolmogorov-Smirnov test – of the mechanical parameters variability within each OC cores were reported in **Tab. 6.1**. Due to the narrow range of variation, the median value among subsequent indentions of each mechanical parameter was considered – for each OC core – in searching relationships with NMR results.

		CoV%				
		E_0	**S_0**	**τ**	**β**	**E_{eq}**
Percentiles	5th	1.24	1.02	0.80	0.20	0.97
	25th	3.22	1.63	1.77	0.56	2.16
	50th	5.87	2.78	2.34	0.80	3.55
	75th	7.40	5.15	3.54	1.34	7.42
	95th	11.36	23.06	9.78	2.85	23.59

Tab. 6.1. Non-normal distribution of the intra-variability of the mechanical parameters.

6.3.3 Single-sided NMR

Results about the fast CPMG sequence highlighted a replicable, and a high variable trend for signal intensity and T_2, respectively; despite this evidence, the analysis of signal intensity and T_2 profiles allowed to identify the three layers of AC (**Fig. 6.10**).

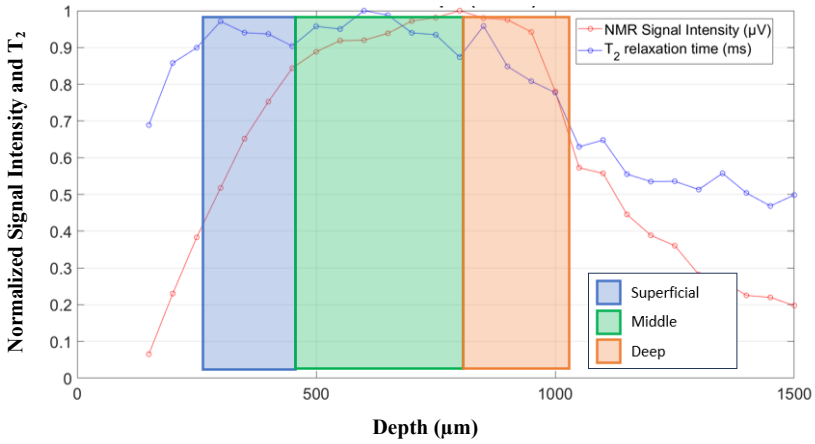

Fig. 6.10. Examples of the trend of signal intensity and T_2 trend across AC thickness, and of the analysis allowing to compute the thickness of AC layer.

AC thickness estimated through NMR approach – and the relative assumption about deep layer – showed a non-normal distribution, described as follows: the 5th, 25th, 50th – i.e., median value –, 75th, and 95th percentile resulted to be equal to 0.98 mm, 1.35 mm, 1.62 mm, 2.04 mm, and 2.92 mm, respectively.

Regarding NMR depth-dependent analysis, Kolmogorov-Smirnov test highlighted a non-normal distribution for all the parameters. Kruskal-Wallis test followed by a post-hoc Wilcoxon test – with a Bonferroni correction – highlighted statistical difference in NMR parameters among the three layers (**Fig. 6.11**, **Fig. 6.12**). More in detail, except for two comparisons – i.e., T_1 and D parameters, between superficial and middle layers –, a $p < 0.017$ was found as a result of the difference among the layers.

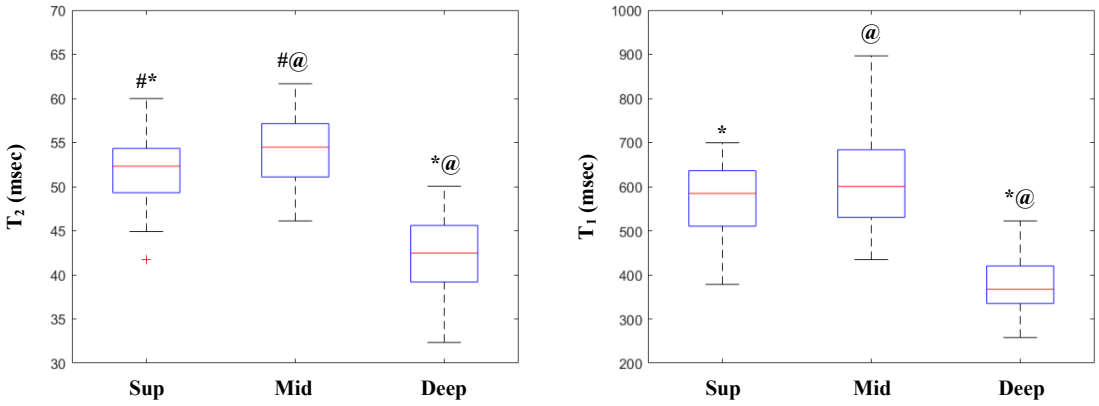

Fig. 6.11. Boxplots of (Left) T_2, and (Right) T_1 among cartilage layers. The boxes indicate the 25th and 75th percentiles and the line within the boxes marks the medians. Whisker length is equal to 1.5×interquartile range. Plus signs represent outliers. Statistically significant difference ($p < 0.017$) is highlighted by symbol $^{\#}$ between superficial and middle layer, by symbol * between superficial and deep layer, and by symbol $^{@}$ between middle and deep layer.

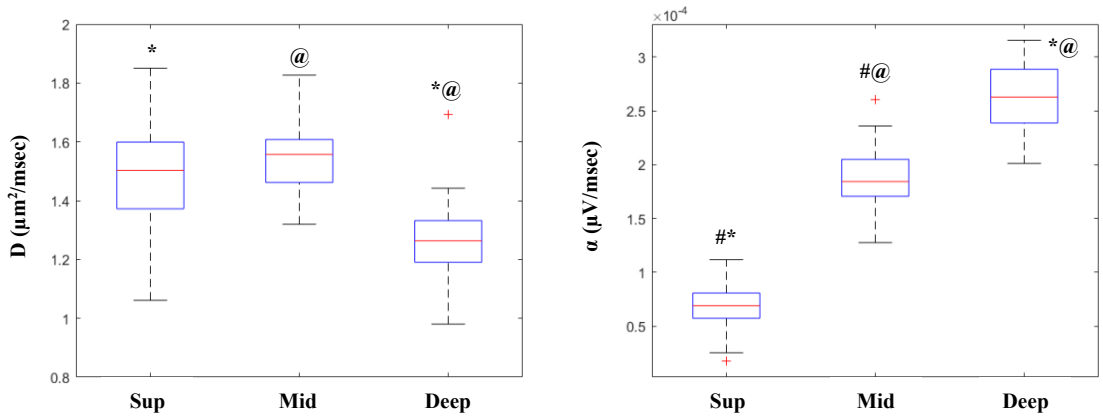

Fig. 6.12. Boxplots of (Left) D, and (Right) α among cartilage layers. The boxes indicate the 25th and 75th percentiles and the line within the boxes marks the medians. Whisker length is equal to 1.5×interquartile range. Plus signs represent outliers. Statistically significant difference ($p < 0.017$) is highlighted by symbol $^{\#}$ between superficial and middle layer, by symbol * between superficial and deep layer, and by symbol $^{@}$ between middle and deep layer.

Variation of T_2, T_1, and D parameters across AC layers showed a similar trend, i.e., increase from the superficial to the middle layer, followed by a decrease within the deep layer. Regarding α parameter, a monotonic, increasing trend moving from superficial to deep layer was highlighted.

6.3.4 Comparison between the different approaches in estimating AC thickness

The accuracy in estimating AC thickness by NMR technique – and the relative assumption on the deep layer thickness – over the measure provided by the μCT was investigated by Pearson correlation. The analysis highlighted a significant, but moderate ($\rho^2 = 0.54$) correlation between the two different datasets. Considering μCT as the reference method – see the relative consideration in paragraph 6.2.5 –, the percentage difference between the outputs of the different approaches highlighted a non-normal distribution, i.e., -37%, -20%, and -0.8% as 25th, median, and 75th percentiles, respectively.

6.3.5 Relationships between indentation and single-sided NMR parameters

Starting from the exploratory analysis of preliminary correlations between individual mechanical and NMR parameters, no moderate to strong relationship was highlighted. The same evidence was achieved by evaluating correlations between individual mechanical parameters and NMR composite parameters, the latter obtained by weighting the values peculiar of the individual AC layers for the layers thickness.

A further step regarded the evaluation of preliminary correlations between mechanical parameters – considered both their individual values, and the ones related to the exponent of the stretched exponential function – and composite NMR parameters. Regarding these last, the previously weighted NMR parameters were additionally multiplied – or divided – by the amount of the tissue, i.e., full AC thickness, computed by μCT approach. Preliminary – but significant – trends were evidenced (**Tab. 6.2**). An example of the achieved relationship was reported in **Fig. 6.13**.

	E_0	S_0	$(1/\tau)^{\beta}$	$(E_0 - E_{eq})$
T_{2w} x AC thickness	$\rho < 0$ $\rho^2 = 0.70$ $p < 0.001$	$\rho < 0$ $\rho^2 = 0.44$ $p < 0.001$	$\rho < 0$ $\rho^2 = 0.23$ $p < 0.01$	$\rho < 0$ $\rho^2 = 0.70$ $p < 0.001$
T_{1w} x AC thickness	$\rho < 0$ $\rho^2 = 0.75$ $p < 0.001$	$\rho < 0$ $\rho^2 = 0.51$ $p < 0.001$	$\rho < 0$ $\rho^2 = 0.18$ $p < 0.05$	$\rho < 0$ $\rho^2 = 0.75$ $p < 0.001$
D_w /AC thickness	$\rho > 0$ $\rho^2 = 0.58$ $p < 0.001$	$\rho > 0$ $\rho^2 = 0.36$ $p < 0.001$	$\rho > 0$ $\rho^2 = 0.23$ $p < 0.01$	$\rho > 0$ $\rho^2 = 0.58$ $p < 0.001$
α_w x AC thickness	$\rho < 0$ $\rho^2 = 0.52$ $p < 0.001$	$\rho < 0$ $\rho^2 = 0.31$ $p < 0.001$	$\rho < 0$ $\rho^2 = 0.18$ $p < 0.05$	$\rho < 0$ $\rho^2 = 0.53$ $p < 0.001$

Tab. 6.2. Spearman correlations between mechanical parameters and composite NMR parameters.

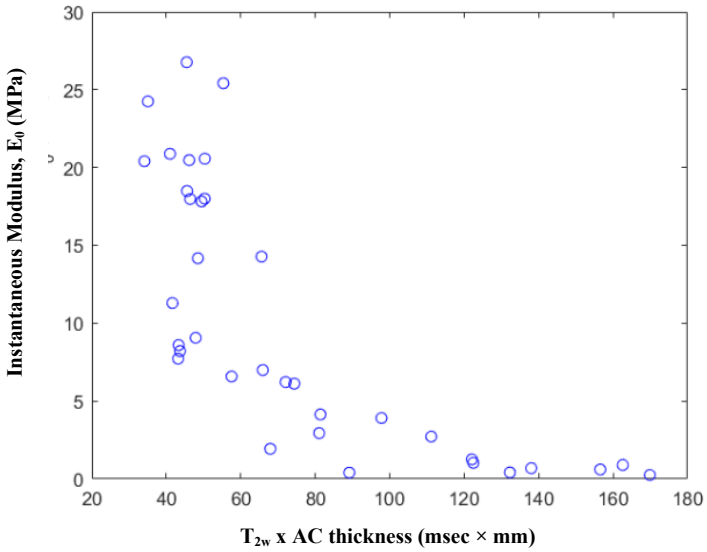

Fig. 6.13. Example of a promising trends retrieved from the exploratory analysis of preliminary correlations between mechanical and NMR parameters.

6.4 Discussion

The main purpose of this investigation was to provide a multidisciplinary experimental framework evaluating the mechanical and structural features of AC when supported by the underlying mineralized tissues. An indentation protocol – based on nominal deformation – was applied to evaluate the viscoelastic response of AC. Despite the wide spread of response, the proposed testing protocol yielded sound information on the elastic, viscous and equilibrium parameters peculiar of AC. Low-field single-sided NMR

device was applied to investigate parameters related to the structure of AC. Although the evaluation of NMR parameters in a heterogeneous tissue as AC is not trivial, the proposed approach highlighted variations of structure-related parameters within tissue thickness. Last, the exploratory evaluation of preliminary correlations between mechanical and structure-related parameters highlighted some promising trends. According to such evidence, the main novelty of this study lies in the possibility of evaluating depth-dependent features of AC and their relation with the mechanical properties of the tissue, with the view of evaluating such information on degenerative and treated tissues to better understand the impact of pathologies, and to assess the efficacy of treatments responding to such diseases, respectively.

Regarding the investigated mechanical parameters, the applied protocol allowed to detect changes between subsequent indentation. Although the efficacy of such a protocol has been already proved [171], this evaluation was considered mandatory due to the additional process at which AC specimens were subjected, i.e., coring. In this regard, and despite the extent of the indented area is about one order of magnitude smaller than the dimension of the specimens, AC response could have been experienced a variation due to the excise of its lateral boundary. The retrieved information allowed to confirm the absence of macroscopic AC damages due to the additional coring process, underlying once more the reliability of the protocol, i.e., narrow range of distribution of CoV%. Consequently, it is possible to state that the wide range of distribution of the mechanical properties highlighted by this study is strictly related to AC variability, and not to changes induced by the testing protocol. The primary reason behind this scattering lies in the different areas of the knee joint from which OC cores were excised, i.e., femoral condyles and tibial plateau. Several studies highlighted a wide spread of compressive response – and, thus, mechanical properties – across knee articular surfaces, both considering human [172–175] and animal AC [15,175–177]. Despite numerous studies investigated the mechanical properties of AC, a comparison with the values herein achieved is not possible due to differences in the type of test and, moreover, in testing protocol [75]. In addition, it must be highlighted that AC response strongly depends on the applied stimuli, in particular by their extent and rate [90], making it even more challenging arguing about the retrieved results. In this regard, the development and the application of a standardize protocol – at least in terms of the extent of stimuli and its rate of application – is of paramount importance to compare properly the outcomes of different studies.

In this study, structure-related parameters were retrieved by single-sided NMR approach. The depth-profiles obtained for the AC of all the OC cores investigated, as well as the extent of the NMR parameters retrieved by the analysis of their profiles, are consistent with the findings provided by previous studies applying single-sided NMR to bovine AC [147,155]. More in detail, a different trend of the NMR signals intensity between the AC layers is highlighted, i.e., an initial increase of the NMR signal intensities, followed by a stationary and a decrease phase. Accordingly, data analysis demonstrated a significant difference in the computed parameters between AC layers; two exceptions must be reported, i.e., T_1 and D did not show difference between superficial and middle layers. AC presents a heterogeneous structure, in which solid and fluid content – as well as their organization – are depth-dependent [4]. The AC superficial layer is characterized by a small concentration of PGs [57,178] and by a structure of thin collagen fibrils, aligned parallel to the articular surface [4,64,178]. In the middle layer, a progressive increase and a random alignment are detected for PGs content and collagen network, respectively [179]. The deep layer is characterized by the maximum concentration of PGs and by collagen fibrils with the largest diameter, oriented perpendicular to the joint line [66]. As concern water content, a decrease from the superficial to the deep layer is highlighted [90,180]. To argue properly about differences of NMR parameters across AC

thickness, their meaning, together with the structural features influencing the most their extent, is reported in the following. T_2 signal intensity is related to the water content [181] and to the structural integrity of the ECM [182], resulting sensitive to the integrity and arrangement – i.e., content and orientation – of the collagen network through the magic angle effects – caused by changes in the dipolar interactions between water hydrogen protons loosely bounded along collagen fibrils [183,184]. Therefore, a higher T_2 defines the superficial – where the water content has the highest concentration – and middle layers – where the water content is less restricted due to the random arrangement of the collagen network – compared to the deep layer. As for T_2, also T_1 signal depends on the reorientation phenomena of the water molecules but, moreover, also on the magnetization transfer between macromolecules and water protons [185]. Consequently, a high T_1 relaxation time occurred in the superficial and middle layers, where the high concentration of water molecules provides more possibility of interacting with glycosaminoglycans and PGs. In addition to T_2 and T_1, D and α highlighted significant differences through AC layers. Considering the nature of D, i.e., a diffusion coefficient, its decrease from the superficial/middle to deep layer can be explained as the increase of ECM concentration with depth, i.e., a higher amount of PGs and a progressive rearrangement of the collagen fibrils orientation. α is computed by the analysis of the signal acquired by applying a modified version of a sequence used in NMR spectroscopy, namely Double-Quantum sequence [167], developed to investigate cross-linking features. Moreover, and considering that α summarized the solid/fluid ratio –, its monotonic increase can be related to the depth-dependent changes of the AC structure and composition, for which the amount of water content decreases trough AC thickness due to the progressive increase of PGs content, collagen fibrils diameter [186] and collagen concentration [178].

Regarding the assessment of AC thickness, the analysis highlighted a discrepancy between μCT and NMR approach. A main theoretical assumption underlies NMR approach, for which the thickness of the deep layer was not directly measurable due to setup constraints. In addition, a limited contribution could be ascribed to the different working condition of these approaches, i.e., in air for few minutes, and in moist environment, for μCT and NMR, respectively. According to these evidence, and moreover considering the percentage difference between the outcomes of the two approaches (see paragraph 6.3.4), it is possible to state that NMR overestimates AC thickness compared to μCT approach. Consequently, and with the perspective of investigating preliminary relationships between mechanical properties and weighted NMR parameters – i.e., T_{2w}, T_{1w}, D_w, and α_w –, it must be highlighted that the computation of these latter is affected by bias. More in detail, despite the overestimate induced by NMR in evaluating AC thickness may reflect equally to the superficial and middle layer, its impact on deep layer strongly depend on the full-thickness of AC, producing a sample-dependent repercussions on its evaluation. Despite this limitation, weighting NMR parameters of the individual AC layers for the layer thickness currently represents the best option – over the use of a simple mean, or median value of thickness – to assess more in detail the existing relationships between AC structure and mechanical properties.

The exploratory analysis about preliminary relationships between individual mechanical and NMR parameters did not reveal moderate to strong correlations. Nevertheless, some promising trends were highlighted by combining NMR parameters with information related to the amount of tissue – i.e., i) by weighting layer-dependent NMR parameters for the layer thickness and, moreover, ii) by multiplying or by dividing the parameters computed through the previous step by the total amount of tissue. First, negative trends between AC elastic parameters and structure-related variables were highlighted. These trends were evidenced in the first place by elastic instantaneous parameters, i.e., E_0 and S_0, and AC thickness. A possible explanation to this finding might be that the higher is the amount of the tissue, the softer it appears to be –

so the higher is the AC thickness, the lower is the instantaneous response. By adding to such trends an information about the AC structure – i.e., by multiplying the AC thickness by T_{2w}, or by T_{1w} – more significant trends were highlighted, i.e., decreasing of the sum of squared differences. Second, the analysis suggested a positive trend between a viscous parameter – i.e., summarized in the exponent of the function describing the decrease of the load during relaxation – and D_w divided by AC thickness. The exponent of the stretched exponential function defines the drop rate of the load during relaxation, while the parameter (D_w /AC thickness) has a rate as physical dimension – i.e., μm/sec –, and can be considered as a diffusion coefficient for thickness unit. Accordingly, the relationship between $(1/\tau)^{\beta}$ and (D_w /AC thickness) might be explained as follows: the higher the diffusion coefficient for thickness unit – e.g., the wider are the mesh of the ECM –, the faster the relaxation phenomena will be exhausted. Third, an additional negative relationship is suggested between the structure and the viscous response of AC. More in detail, a correlation was found between the drop of response during relaxation, i.e., (E_0 - E_{eq}), and α_w multiplied by AC thickness. The drop of response during relaxation is due mainly to the water content of AC. In this regard, a strong reduction between the values of E_0 and E_{eq} can be due to a high water content – over the solid one – in composing AC. The phenomena related to the water content – i.e., flow followed by exudation – leaves only the reduced solid content to respond to stimuli at the end of the relaxation phenomena, i.e., at the equilibrium. Considering the meaning of α, its extent is related to the solid/fluid ratio of AC, e.g., the higher the fluid content, the lower α. Therefore, by multiplying α_w by AC thickness, a parameter dependent on the total water content within AC is obtained. According to such considerations, the suggested relationships can be explained as follows: the higher the AC water content – so the lower is α_w multiplied by AC thickness –, the higher is the drop of response during relaxation due to water-related phenomena – so the wider is the difference between E_0 and E_{eq}.

The main objective of this study was to investigate the presence of preliminary relationships between structure-related and mechanical parameters of AC, with the view of improving the significance of such relationships by a more resolute evaluation of the structural features through AC thickness. To achieve this goal, single-sided NMR technique was applied to achieve information about the structure-related parameters through AC thickness thank to its high-resolution. To the best knowledge of the authors, this is the first study proposing – preliminary – the assessment of relationships between the features of AC by taking into account their variation across AC thickness. This insight could play a key role in deepen the knowledge about the link between functionality and structure of AC. Numerous studies highlighted correlations between AC mechanical properties and structure-related parameters, the latter derived from MRI [187–195]. Despite MRI can provide quantitative information within AC thickness with an in-plane resolution up to hundreds of microns [140], currently it is not possible to achieve a resolution comparable to the one peculiar of techniques as single-sided NMR. Keeping in mind the discrepancy in resolution, in the following the preliminary findings highlighted herein are discussed considering the insights provided by previous studies evaluating AC through mechanical testing and MRI. Negative correlations between AC elastic (instantaneous) parameters and MRI-derived variables were highlighted by literature. Hananouchi et al. found negative correlation between AC stiffness and T_2 relaxation time in human knee [191]. Namiranian et al. reported negative trends between AC stiffness and both E_0 and MRI-derived T_1 relaxation time [188]. Other studies highlighted relationships – with negative to positive trends – between mechanical and MRI-derived parameters, but focusing on the response of AC at the equilibrium and under dynamic stimuli. More in detail, correlations between MRI parameters and i) equilibrium and dynamic moduli [187,189,190], ii) with parameters related to the linear biphasic poroelastic model [192–194] and iii) to the

fiber-reinforced poroelastic model [195] were reported. It must be noted that almost all the above reported studies explored the presence of relationships through the Pearson correlation method, therefore hypothesizing that AC structure/composition and mechanical response were linearly related. Despite the exploratory nature of the analysis herein proposed, the preliminary findings of this study suggest that relationships between parameters related to AC structure and mechanical response might not be linearly and, moreover, that both physicochemical peculiarities and the amount of the tissue should be considered in searching correlations. The latter evidence is supported by the moderate extent of relationships herein found – providing ρ^2 even above 0.7 –, quite higher than the correlation coefficients reported by the above-mentioned studies – which reported only the Pearson coefficient, ρ, assuming values generally below 0.7 which, in turn, correspond to ρ^2 below 0.5.

Last, some caveats must be highlighted. First, the investigated specimens were subjected to multiple freezing-thawing cycles in order to perform on them multidisciplinary assessments. Despite the impact of freezing on AC features is a well-known issue [196], freezing-thawing cycles seem to affect the most the dynamic response of the tissue compared to the instantaneous and equilibrium behaviour [197–200]. Consequently, subjecting the samples to multiple freezing-thawing cycles was considered as the best approach to standardize their evaluations in time, therefore avoiding bias due to different managements. Second, the single-sided NMR assessment herein proposed is constrained to 3 mm in depth. As mentioned above, this represent a major limitation of this approach, especially considering that AC thickness of bovine [201] and – most importantly, with the view of applying the developed framework to study the impact of degenerative pathologies on AC features – human knee [202,203] can be close – or even more – than 3-mm thick. Third, the relatively small sample size do not allow to assess eventual relationships between structure-related and mechanical parameters with enough statistical power. Despite this limitation, the preliminary results achieved suggest the presence of such relationships. In this regard, the starting point recommended by this study suggests to avoid assumptions about the distribution and the trend of the relationships between structure and mechanical properties of AC and, most importantly, to consider possible combination of the individual parameters retrieved by quantitative assessments.

6.5 Conclusion and Future Perspectives

With the purpose of providing a sound and comprehensive evaluation of the AC main features, this study provides a multidisciplinary experimental framework yielding reliable and depth-dependent insights about the structure and the mechanical response of such a tissue, respectively. AC viscoelastic parameters should be investigated through a multi-repetition, nominal deformation-based testing approach, thus to provide i) information about eventual setup issues or related to tissue condition and, most importantly, ii) to support the application of a standardize protocol in order to compare properly the outcomes of different studies. The assessment of parameters related to AC structure should be performed with a depth-dependent prospective, thus to highlight how the retrieved information change due to AC heterogeneity. Last, relationships between parameters related to the structure and the functionality of AC should be investigated without making assumptions on their distribution and linearity, moreover considering the possibility of combining the parameters to better describe the peculiarities of the tissue. The proposed experimental framework allows to integrate multidisciplinary information about AC, moreover providing the possibility to carry out longitudinal assessments on AC thanks to the non-destructive feature of the techniques. This opportunity is of paramount importance, since it allows to investigate i) the effects of enzymatic degradation simulating different grades of severity of pathologies, thus to better understand their etiology and the

dynamic beneath their progression, and ii) the efficacy of treatments responding to diseases that modify the features of AC.

Regarding the first point, it is currently under investigation the development of an experimental approach simulating the features of OA early stages – i.e., superficial fibrillation (abrasion), matrix discontinuity at the superficial zone, and matrix depletion up to 1/3 of AC thickness [83]. The foundations of the study have already been laid, by taking into account the approaches provided by the relative literature, in particular defining the type of enzymes digesting the two main component of AC ECM, i.e., PGs and collagen network [204], their concentration and the time of treatments.

7 Study III – Structure-Function Relationships of Articular Cartilage through Contrast-Enhanced CT and Indentation

7.1 Introduction

Articular cartilage (AC) is one of the tissues composing the osteochondral (OC) unit of load-bearing joints, and is mainly responsible of shock-absorption and deployment of the stresses developed within the articulations during locomotion [127]. The key role of AC is provided by the interplay between its phases, i.e., solid and fluid [90]. The solid phase is primarily composed by PGs and collagen fibers, whose 3D arrangement defines the ECM [90]. Therefore, ECM is characterized by a depth-dependent structure, in which the collagen fibers – with a depth-dependent orientation, from parallel to perpendicular to the articular surface starting from the superficial and moving to the deep layer of AC – entrapped negatively charged PGs aggrecans, the latter presenting a concentration gradient that increases with AC depth [90]. The fluid phase, also known as interstitial fluid, is mainly composed by water and electrolytes, e.g., cations as Na^+ [205]. As a consequence of the external stimuli at which load-bearing joints are exposed, the interaction between AC solid and liquid phases generates phenomena at the base of the mechanical behaviour of such a tissue, mainly known as instantaneous response, fluid-independent and -dependent mechanisms [206]. The initial and rapid deformation of AC produced by external loads is withstand by the instantaneous response of the tissue, which is primarily related to the change in PGs molecular domains, and to an increase in the pressure of the interstitial fluid [4,88]. The viscoelastic behaviour of AC is related instead to fluid dependent and independent phenomena [91]. The fluid independent mechanisms can be ascribed to the response of the molecules composing the ECM, so attributable to the 3D re-arrangement of both PGs and collagen fibres [207]. The fluid dependent mechanism is identified as the frictional drag induced by the transition of the interstitial flow within ECM [59]. In addition to these mechanisms, the AC mechanical response depends also on electrochemical phenomena. Commonly the net density charge within AC is mainly ruled by the negatively charged PGs, conferred by the functional groups of GAGs. Consequently, cationic solutes dissolved in the interstitial fluid – i.e., Na^+ – are attract electrostatically by the PGs local arrangement. Due to this mutual electrostatic attraction, the electrolytes concentration within AC are higher than in the knee cavity, causing an imbalance which leads to a gradient of pressure within the tissue, known as Donnan osmotic pressure [102]. Donnan pressure plays a crucial role in the AC mechanical behaviour, strongly contributing to its instantaneous response [58]. Moreover, and concurrently with repulsion between PGs [208], the subtle electrochemical equilibrium is also involved in the swelling, time-dependent phenomena related to the interstitial fluid flowing within and outward the ECM.

The interaction between the phases of AC can be deregulated by traumatic and degenerative pathologies, which can modify the articular tissues homeostasis, essential to provide an appropriate equilibrium in the remodelling and re-arrangement processes defining the AC mechanical response [209]. In this regard, a loss of PGs – together with an alteration of their arrangement –, a fibrillation of the collagen network, and an increase in the interstitial fluid content are among the first degenerative signs that occur

within AC [84]. Considering the economic burden of traumatic and degenerative diseases impairing human joints [210], providing diagnostic approaches that perform a sound assessment of the pathophysiological condition of AC is of paramount importance.

Clinical imaging based on X-ray is among the diagnostic techniques eligible to investigate the features of musculoskeletal tissues [130]. X-ray imaging represents a diagnostic approach trading-off between 3D information, spatial resolution, and radiation dose, especially considering High Peripheral Quantitative Computed Tomography (HRpQCT) [211]. Despite HRpQCT systems provide quantitative insights about patients joints [133,212,213], only qualitative morphological information can be directly retrieved by acquiring soft tissues, due to their low radiopacity [130]. To fulfil this gap, contrast agents (CAs) may be used to enhance the visualization of soft tissues through X-ray imaging, i.e., by exploiting the features of the main components of the tissue [137]. Therefore, Contrast Enhanced Computed Tomography (CECT) approaches can be employed to investigate AC, by targeting its components through CAs that exploit the phenomena at the base of their interactions, e.g., electrochemical [137]. By considering that the specific components of AC define the CA that could enhance their detection through X-ray imaging, the net molecular charge and the osmolarity are accountable for the interaction between the target component of the tissue and the CA. By focusing on CECT of AC, exploiting the potential of ionic CAs – both considering anionic and cationic ones – represents the primary choice [137]. The diffusion of ionic CAs within AC depends on the electrostatic interaction between their molecules and the negatively charged PGs [137]. A cationic CA – i.e., Ca4+ – was developed specifically to be electrostatically attracted by PGs [214]. Despite the use of Ca4+ can provide useful insights about the composition and structure of AC – i.e., the depth-dependent distribution of PGs – in a non-destructive way, its employment addressing biomechanical purposes is still to verify. In this regard, increasing intra-tissue contrast is essential to investigate the 3D distribution of displacements and strains within the OC unit by using full-field techniques as Digital Volume Correlation (DVC). The insights retrieved by combining a CECT approach – employing the cationic iodine-based CA above described – and DVC technique could be essential in the development of tissue engineering scaffolds treating pathologies that impair the OC unit response [215]. Nevertheless, before the use of Ca4+ to address biomechanical purposes it is mandatory to verify its effect on the AC mechanical behaviour, thus to highlight and to understand the presence of a possible bias induced on the retrieved results. The elucidation of the Ca4+ impact and, more widely, of CAs on the AC mechanical response is even more important by considering their potential clinical application. Despite the safety of CAs is generally verified by regulatory authorities – in case of Ca4+, preliminary findings suggest the absence of cytotoxicity due to its use [214] – potential alterations induced by their clinical application – e.g., due to a different osmolarity and/or molecular charge led within the tissue – may produce a significant impact not solely on AC mechanical behaviour but, most importantly, on the rate of cell death [138].

The main purpose of the study was to investigate possible effect induced on the AC mechanical behaviour by a cationic CA, Ca4+, toward its application addressing the biomechanical research. OC cores were retrieved from tibio-femoral surfaces of bovine knees. The viscoelastic and equilibrium response of AC was evaluated by indentation, by applying the same testing protocol before and after the exposure to Ca4+. Considering that the Ca4+ diffusion phenomena within AC requires several hours [216], a control group was exposed to the same experimental pipeline – by replacing Ca4+ with a control solution – in order to highlight an eventual effect related to a degradation of the tissue. OC cores exposed to Ca4+ were acquired by X-ray imaging – HRpQCT – to investigate the distribution of Ca4+ within AC and, consequently, the arrangement of PGs – to which Ca4+ molecules are electrostatically attracted. Last, with the view of applying the multidisciplinary approaches implemented to study the main features of AC,

preliminary correlations between the mechanical properties of the tissue and the outcomes retrieved by the analyses of HRpQCT images were investigated.

7.2 Materials and Methods

By considering the multiple steps that defined the pipeline of the current study, in the following the relative workflow was reported.

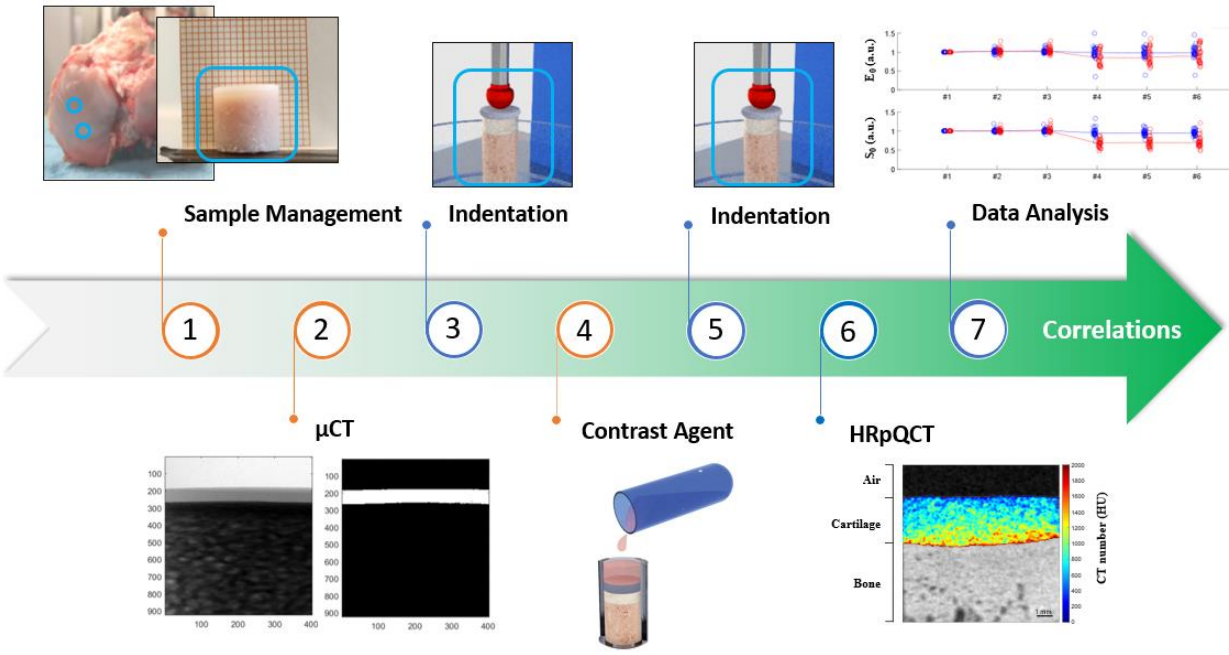

Fig. 7.1. The workflow of the study about the investigation of the structure-function relationships of AC through CECT and indentation.

7.2.1 Preparation of the Contrast Agent and of the Relative Solution

The synthesis of the CA was performed by the Department of Physics and Earth Sciences and by the Department of Chemical, Pharmaceutical and Agricultural Sciences of the University of Ferrara. The CA solution was made by the Department of Industrial Engineering of the University of Bologna.

The employed CA was Ca4+, with the following formulation (5,50-[Malonylbis(azanediyl)]bis[N1,N3-bis(2-aminoethyl)-2,4,6-triiodoisophthalamide] chloride). The molecules of Ca4+ were characterized by the following features, i.e., i) six iodine atoms, ii) a net positive charge of +4, iii) a molecular weight of 1354 g/mol, and iv) a iodine fraction per molecule of 0.5084. The synthesis of Ca4+ salts was performed according to evidences retrieved by literature [214,216]. CA solution was obtained by dissolving Ca4+ salts in PBS 1X (7.4 pH, Life Technologies Europe B.V., Bleiswijk, The Netherlands), achieving a concentration of 10 mg/ml. The pH of the CA solution was balanced to 7.4 value by adding NaOH 4M. The osmolarity of both PBS 1X and CA solution was measured by an osmometer (TypM 10/25µl, Löser Messtechnik, Germany).

7.2.2 Sample Collection and Management

OC cuboids samples (N = 20) were excised from the tibio-femoral surfaces of N = 7 bovine knees, retrieved from on-farm livestock within 24 h from culling. Cuboid samples – at least one from each knee – were excised by employing a diamond-coated blade mounted on a circular saw (MDP200 and TR60, respectively; Remet, Italy). Dehydration and heating of the tissues were avoided by performing the procedure under continuous water cooling. Cuboid samples were then wrapped in soaked gauzes (PBS 1X) and frozen at −20 °C [161,162]. On a different day, cuboids samples were thawed at 4°C in PBS 1X for one hour, and then exposed to a diamond-tipped cylindric cutter attached to a CNC milling machine (ProLIGHT Machining Center, PLM 2000) with the aim of excising cylindrical OC cores (10-mm in diameter and height, including AC, subchondral and TB). Before each coring, cuboid samples were spatially tilted, thus to retrieve cores with an AC surface as flat as possible. OC cores were then stored at -20°C in a PBS 1X-soaked gauze. A total of N = 72 OC cores – at least two for each cuboid – were obtained as output of the Sample Management process. Two subgroups were defined, i.e., control and treated, each composed by N = 36 OC cores. In this regard, OC cores were distributed properly in the two subgroups, by ensuring that each OC core of the treated group had a relative sample in the control group, retrieved from the same cuboid and, moreover, excised spatially close to the first one.

7.2.3 Estimation of AC Thickness by µCT

OC cores were thawed overnight at 4°C in PBS 1X [163]. The next day, OC cores were individually evaluated to estimate AC thickness before indentation. After dabbing from excess of PBS 1X, OC cores were inserted in a PMMA sample holder and, then, placed inside a µCT system (SkyScan 1072, SkyScan, Aartselaar, Belgium). The vertical quote of the sample holder was adjusted within the system, thus to include in the Field of View (FoV) not only the entire AC layer, but also a few millimetres of air and TB. Consequently, four planar images were acquired – each after a rotation of 45° around the sample vertical axis – by applying the following acquisition protocol: X-ray tube voltage = 50 kV, current = 197 µA, 1-cm Al filter, pixel size = 11.52 µm, exposure time = 5.9 s. The entire procedure required ~ 5 minutes/OC core. AC thickness was computed through a custom-made Matlab script (MATLAB 2022b, MathWorks, Natick, MA, USA), which entailed the following steps: i) a preliminary crop to exclude residual portion of the sample holder from the planar images; ii) a binarization process, achieved by applying an optimal grey-level threshold to differentiate AC from air and mineralized tissues; iii) the application of a continuity approach to exclude eventual pixels with an original grey-level similar to those peculiar of the AC. The achieved results (see paragraph 6.2.2 for more details) were considered as input for the following indentation tests.

7.2.4 Indentation Test and Exposure to Contrast Agent and Control solutions

OC cores, in subgroups of N = 5 or 6 samples, were tested by indentation technique. OC cores were hosted within the cavities – inner diameter of 10 mm, depth of 20 mm – of a custom made samples holder made by polyethylene (PE). Before placing OC cores within the cavities, a silicone-based grease was applied to the AC lateral surface. Subsequently, OC cores were constrained to the bottom of the cavities, by applying polymethylmethacrylate (PMMA, Restray NF, S.P.D.: Mulazzano, Italy) at their bone-ends and, moreover, thanks to the interlock constraint, i.e., cores and cavities had the same diameter. The process of interlock and polymerization required ~ 30 minutes, during which AC surfaces were kept moist by a gauze soaked in PBS 1X at room temperature. Subsequently – and before testing – PBS 1X (0.5 ml) was

placed on the AC surfaces, and OC cores rested for 30 minutes. The silicone-based grease on the AC lateral surface allowed to maintain the volume of PBS 1X over the top surface of the tissue, preventing any leakage of the solution toward the bottom of the cavities. In the meanwhile, the PE samples holder was constrained to the X-Y motorized table of the testing machine (Mach-1 V500css, Biomomentum Inc., Laval, QC, Canada). Subsequently, OC cores underwent a preliminary indentation to precondition the AC, followed by N = 3 repetitions/core, each performed after a resting period of 40 min [164]. The testing protocol consisted in a nominal deformation equal to 15% of the AC thickness [165], applied in the center of each OC core with a deformation rate of 0.15 s^{-1} [166], and by a 6-mm spherical indenter. The deformation was maintained for 300 s [161], thus to evaluate the AC viscous response. The entire testing protocol required ~ 3 hours for each subgroup of OC cores. After the test, and without removing OC cores from the cavities, the top surface of AC was exposed to a static bath consisting of 0.5 ml of Ca4+ (see paragraph 7.2.1) or of PBS 1X solution – the latter replacing the previous one present during indentation tests – for 22 hours at room temperature [216], depending on the subgroup to which the OC cores belonged. Thanks to the silicone-based grease, the diffusion of Ca4+ within AC is limited to the top surface of the tissue – avoiding lateral seepages –, thus to replicate as close as possible the diffusion phenomenon peculiar of the in vivo environment. Regardless the subgroup, the OC cores were tested again after 22 hours by the same indentation protocol previously applied, i.e., an initial pre-conditioning indentation, followed by N = 3 repetitions.

7.2.5 HRpQCT Imaging

The HRpQCT acquisitions, and the analysis of the relative images were performed by the Department of Industrial Engineering of the University of Bologna, and by the Laboratorio di Tecnologia Medica of the IRCC Rizzoli Orthopaedic Institute.

Following the second repetition of the indentation test, OC cores exposed to Ca4+ were acquired by a HRpQCT system (XtremeCT II, SCANCO Medical AG, Brüttisellen, Switzerland). Before scanning, the CA solution was removed from the top AC surface of each OC core. Afterward, the samples holder was placed within HRpQCT – taking care to align the axial direction of the OC cores to the scanning axis –, and acquired through a specific imaging protocol (X-ray tube voltage = 68 kV, current = 1460 µA, filtration = 1 mm Al + 0.2 mm Cu, pixel size = 60.7 µm, scan time = 10 min). Last, OC cores were removed from the samples holder, and stored at -20°C in a PBS 1X-soaked gauze.

7.2.6 Data Analysis

Distribution of AC thickness computed by µCT was assessed via Kolmogorov-Smirnov test. In case of non-normal distribution, data was presented as quartiles range, i.e., 5^{th}, 25^{th}, 50^{th} – median –, 75^{th}, and 95^{th}. Statistical difference between control and treated group was assessed by Wilcoxon test ($p < 0.01$).

Concerning indentation, by setting a Poisson's ratio value of 0.45 [168] the Hayes model was fitted to the loading part of the force vs displacement curve, thus to compute the Instantaneous Elastic Modulus, E_0 (MPa), of AC [217]. The relaxation portion of the load vs time curve was fitted to a stretched exponential function [160,169], implemented by a custom-made Matlab script (MATLAB 2022b). The outcomes of the latter fitting provided – for each indentation test – the following mechanical parameters: the maximum load value reached prior to load relaxation, S_0 (N), the time constant, τ (sec), and the stretching parameter, β (a.u.). In addition, the Equilibrium Modulus, E_{eq} (MPa), was calculated by using the Hayes equation [161] to correct the equilibrium force measured at the end of relaxation.

Distribution of mechanical parameters was assessed via Kolmogorov-Smirnov test. Variability of the mechanical parameters across the three subsequent indentations before the static bath was evaluated as percentage Coefficient of Variation (CoV%), i.e., percentage ratio between standard deviation and average values. In case of non-normal distribution, CoV% data was presented as quartiles range, i.e., 5^{th}, 25^{th}, 50^{th} – median –, 75^{th}, and 95^{th}. If a narrow variation was highlighted by CoV%, median values of the mechanical parameters across the three indentations before the static bath were considered to investigate eventual statistical differences between control and treated group (Wilcoxon test, $p < 0.01$).

Possible effect of the static bath – regardless the solution at which OC cores were exposed – on the AC mechanical parameters was evaluated by applying a tailored statistical model, i.e., Interrupted Time Series, ITS [218,219]. ITS can be applied to a time series of a specific outcome to evaluate the effect of an intervention at a known point in time [218]. In the view of applying ITS, for each OC core the trend over time of the mechanical parameters was normalized to the values retrieved from the first indentation; then, the normalized series of each parameter – i.e., for each OC core, one series for each of the five parameters – were pooled, and the statistical model was applied (significant difference, $p < 0.01$).

With the purpose of highlighting possible correlations with HRpQCT outcomes, the median values of the mechanical parameters – obtained from the three subsequent indentations performed before the exposure to Ca4+ – were considered for each OC core of the treated group.

Images obtained after the reconstruction of HRpQCT datasets were further analysed to achieve information on AC thickness, and on the Ca4+ volumetric distribution. In this regard, custom-made Matlab codes were implemented. First, a manual crop was used to reduce the volume to analyse. Second, a semi-automatic segmentation step was performed by means of "volumeSegmenter" Matlab package, under "Automate" options. This step allowed to separate the volumes of AC from residuals of Ca4+ solution (above), and from mineralized tissues (below). More in detail, a seed was selected for each volume to segment, and the "Adaptive Threshold" function was run in the slices interval of interest. Consequently, the binary masks obtained were applied to estimate AC thickness. The retrieved volumes were then exploited to compute – for each OC core – a depth-dependent attenuation profile – i.e., CT number (HU) – of Ca4+. By the analysis of such profiles, the subdivision of AC volumes in superficial, middle and deep layer was performed, together with the relative thickness and average attenuation of the layers.

Distribution of HRpQCT outcomes was assessed via Kolmogorov-Smirnov test. Pearson correlation test was applied to AC thickness provided by μCT and by HRpQCT in order to verify their reliability.

The presence of preliminary relationships between mechanical parameters and HRpQCT outcomes was assessed by Spearman correlation test. In this regard, weighted CT number, CT_w, was computed for each OC core, i.e., by weighting the values corresponding to the individual AC layers for the layers thickness, provided by HRpQCT assessment.

7.3 Results

7.3.1 Osmolarity of Solutions

The measurements of osmolality yielded (307 ± 1) mOsm/kg and (419 ± 1)mOsm/kg for PBS and Ca4+ solution, respectively.

7.3.2 Estimation of AC Thickness by µCT

The analysis highlighted a non-normal distribution of AC thickness for control and treated group. More in detail, AC thickness distribution of both groups is reported in **Tab. 7.1**. No statistical difference was highlighted between control and treated group.

		AC thickness (mm)	
		Control	**Treated**
Percentiles	5^{th}	0.89	0.80
	25^{th}	1.19	1.05
	50^{th}	1.50	1.63
	75^{th}	2.08	2.22
	95^{th}	2.65	3.03

Tab. 7.1. Non-normal distribution of AC thickness for control and treated group.

7.3.3 Indentation-based mechanical parameters

Kolmogorov-Smirnov highlighted a non-normal distribution for all the mechanical parameters, and regardless the group. Distribution of the mechanical parameters across subsequent indentations – before the static bath – resulted to be quite similar. In this regard, the distribution of CoV% – which was non-normally distributed for all the mechanical parameters – were reported in **Tab. 7.2** and **Tab. 7.3**, for control and treated group, respectively.

		CoV%				
		E_0	S_0	τ	β	E_{eq}
Percentiles	5^{th}	0.76	0.39	0.20	0.13	0.66
	25^{th}	1.40	0.85	1.03	0.27	1.82
	50^{th}	1.91	1.67	1.57	0.49	2.84
	75^{th}	3.19	1.99	3.31	0.77	4.21
	95^{th}	6.19	4.77	7.98	2.45	10.90

Tab. 7.2. Control group. Non-normal distribution of the mechanical parameters CoV% across the three subsequent indentation before the static bath, i.e., before the exposure to PBS 1X for 22 hours.

		CoV%				
		E_0	S_0	τ	β	E_{eq}
Percentiles	5^{th}	0.76	0.33	0.40	0.17	0.53
	25^{th}	1.29	1.01	0.74	0.27	1.37
	50^{th}	2.61	1.91	1.26	0.59	2.13
	75^{th}	4.95	3.17	3.47	0.89	4.31
	95^{th}	8.95	10.88	8.27	3.65	12.17

Tab. 7.3. Treated group. Non-normal distribution of the mechanical parameters CoV% across the three subsequent indentation before the static bath, i.e., before the exposure to Ca4+ for 22 hours.

Due to the narrow range of variation showed by the CoV% – i .e., 25^{th} - 75^{th} percentile range between 1% and 5% for all the parameters, and regardless the group –, the median values of the mechanical parameters across the three indentations before the static bath were considered – for each OC core – to verify statistical difference between control and treated group. No statistical difference was highlighted by the analysis, regardless of the mechanical parameter.

7.3.4 Effect of the Static Bath, and of the Contrast Agent on the AC mechanical parameters

As reported in paragraph 7.2.6, ITS statistical model was applied to the normalized trend over time of the mechanical parameters to investigate eventual effect of the static bath and, in particular, of the Ca4+. Trends and distribution of the normalized mechanical parameters were reported in **Fig. 7.2** and **Fig. 7.3**.

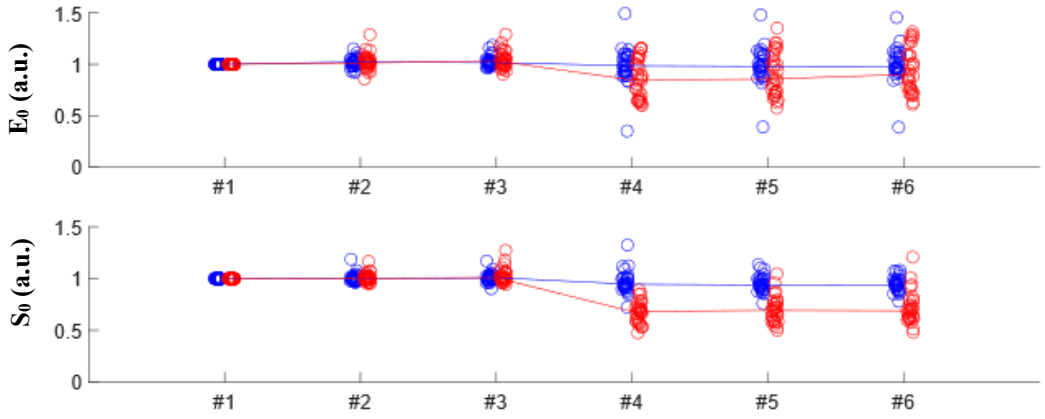

Fig. 7.2. Normalized distribution (dots) and trends (solid lines) of the mechanical parameters – i.e., by starting from the top, E_0, and S_0 – across subsequent indentations, for control (blue) and treated (red) group. The static bath occurred after the third repetition, and before the fourth repetition.

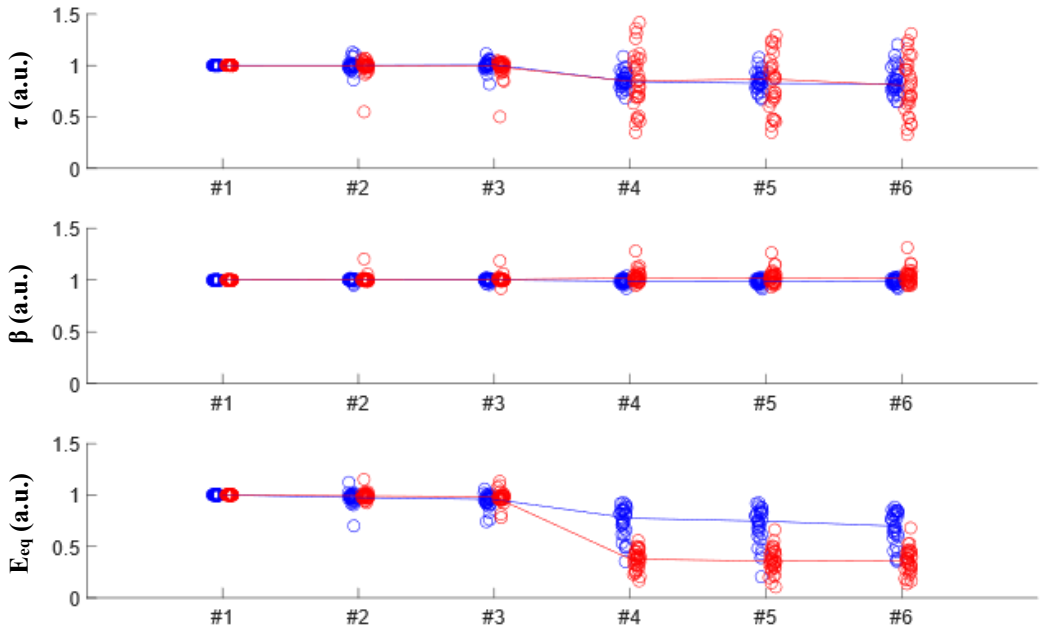

Fig. 7.3. Normalized distribution (dots) and trends (solid lines) of the mechanical parameters – i.e., by starting from the top, τ, β, and E_{eq} – across subsequent indentations, for control (blue) and treated (red) group. The static bath occurred after the third repetition, and before the fourth repetition.

First, the normalization process highlighted similar trend before the static bath for control and treated group, supporting the evidence reported at the end of the previous paragraph (7.3.3). Second, and focusing on the condition after the static bath, a clear difference between the trend of the groups was showed. In this regard, ITS model highlighted a significant decrease in E_0 and S_0 trend after exposing AC to Ca4+ for 22 hours; no significant modification of E_0 and S_0 trend was highlighted by the control group (see **Fig. 7.2**). No significant difference was highlighted in the normalized trend of τ and β of the two investigated groups (see **Fig. 7.3**). A significant decrease in the trend of E_{eq} was highlighted by the control and treated group (see **Fig. 7.3**).

7.3.5 HRpQCT outcomes

3D images of N = 5 OC cores were not investigated due to a technical problem occurred during the acquisition. Accordingly, results about N = 31 OC cores were reported in the following. Morphology of AC – i.e., thickness – resulted clearly recognizable in HRpQCT reconstructions (**Fig. 7.4**, in which the results about N = 3 different OC cores were reported). In this regard, AC thickness estimated through the HRpQCT-Matlab approach showed a non-normal distribution, described as follows: the 5^{th}, 25^{th}, 50^{th} – i.e., median value –, 75^{th}, and 95^{th} percentile resulted to be equal to 0.63 mm, 0.74 mm, 1.51 mm, 2.17 mm, and 2.72 mm, respectively. Besides morphology, the analysis highlighted also an enhancement of the internal features of AC, thanks to the contrast provided by the Ca4+. The band of penetration – i.e., maximum and minimum CT number – resulted to be similar among OC cores with different AC thickness (**Fig. 7.4**).

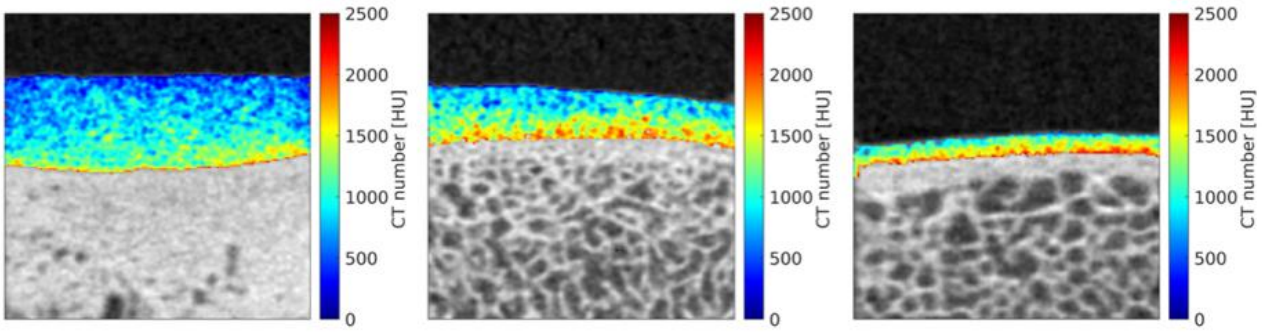

Fig. 7.4. Planar sections of N = 3 different OC cores from HRpQCT reconstructions, after 22 hours of treatment by Ca4+. Quantitative distribution of Ca4+ within the tissue is detectable.

In this regard, the gradient of attenuation across AC thickness highlighted a peak value (equal to 1, on the vertical axis) in correspondence of the SB (0 value on the horizontal axis) (**Fig. 7.5**, left). The decreasing trend of the attenuation allowed to differentiate between the three layers composing AC – i.e., superficial, middle, and deep –, each one characterized by a peculiar value of attenuation (**Fig. 7.5**, right), and by a relative thickness.

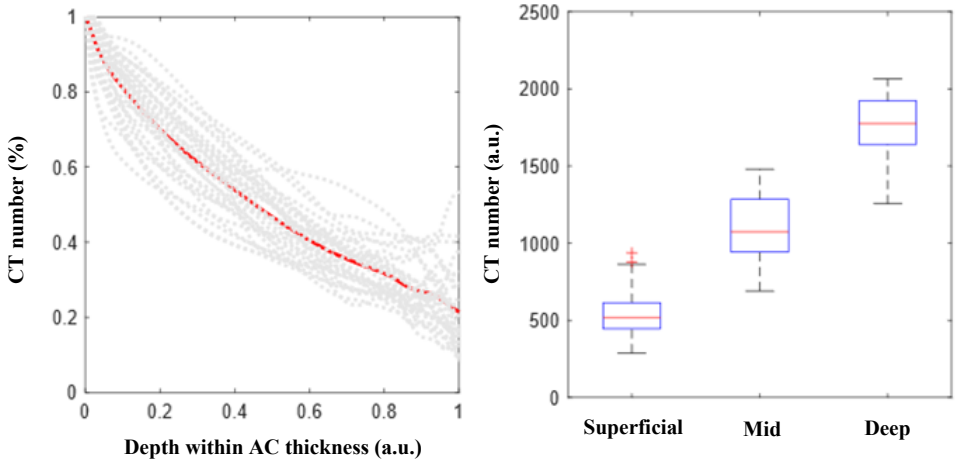

Fig. 7.5. (Left) Global normalized depth-wise profile of Ca4+ distribution within AC (solid red line) was evaluated as average among the profiles of single samples (dotted grey lines, one for each sample). (Right) Distribution of the median values of attenuation between the AC layers, considering the outcomes retrieved by the analysis of N = 31 OC cores.

Kolmogorov-Smirnov test highlighted a non-normal distribution of the computed attenuations, also considering their weighted values, i.e., by weighting the CT values of the individual AC layers for the thickness of such layers.

7.3.6 Comparison between the different approaches in estimating AC thickness

The following evaluation was limited to N = 31 OC cores (see the previous paragraph). The replicability of measuring AC thickness by two different imaging approaches was investigated by Pearson correlation. The analysis highlighted a significant and strong (ρ^2 = 0.85) correlation between μCT and HRpQCT estimates. The percentage difference between the values provided by the two approaches – i.e., by considering μCT as the reference method – highlighted a non-normal distribution, i.e., -5.6%, 12.8%, and 26.2% as 25th, median, and 75th percentiles, respectively.

7.3.7 Relationships between indentation parameters and HRpQCT outcomes

Preliminary analysis of correlations between AC mechanical parameters and HRpQCT outcomes were limited to N = 31 OC cores (see paragraph 7.3.5). By applying the Spearman test, preliminary relationships were suggested (**Tab. 7.4**). No significant correlation was highlighted between E_{eq} and CT_w.

	E_0	S_0	τ	β
CTw	$\rho > 0$, $\rho^2 = 0.64$ $p < 0.0001$	$\rho > 0$ $\rho^2 = 0.32$ $p < 0.01$	$\rho < 0$ $\rho^2 = 0.53$ $p < 0.0001$	$\rho > 0$ $\rho^2 = 0.30$ $p < 0.01$

Tab. 7.4. Spearman correlations between AC mechanical parameters and HRpQCT outcomes, achieved by considering the results of N = 31 OC cores.

7.4 Discussion

The primary aim of the study was to verify possible effects induced by a X-ray CA – i.e., cationic iodine-based, Ca4+ – on the mechanical behaviour of AC. This assessment is mandatory toward considering the eventual use of such a CA addressing biomechanical research. A testing protocol based on nominal deformation was applied before and after exposing AC to the CA solution, thus to elucidate alterations in the response of the tissue. A control group was exposed to the same experimental pipeline – by employing PBS 1X solution to mimic the physiological environment in terms of osmolarity and pH – to highlight eventual discrepancies in the results, e.g., possible degradation of the tissue due to the time. The retrieved results highlighted a significant effect of the Ca4+ on the AC elastic response, i.e., E_0 and S_0. In addition, a significant effect of the static bath was also observed in terms of AC equilibrium response, regardless the group. OC cores exposed to Ca4+ were acquired by HRpQCT system, thus to fully exploit the potential provided by the CA. In this regard, qualitative and quantitative outcomes were achieved from the analysis of HRpQCT images, in particular providing the thickness of AC and, more important, the Ca4+ distribution within AC. Concerning this last point, the attenuation within the tissue achieved resembled the peculiar depth-dependent arrangement of PGs, moreover allowing to differentiate the contribution of the AC layers. Last, with the view of applying the multidisciplinary approach implemented to study the main features of AC, the scoping assessment of possible relationships between the attenuation of contrast-enhanced AC and the mechanical parameters highlighted some promising trends. According to the above-reported evidence, the novelties of this study lied mainly in the following points. First, a sound experimental approach allowed

to provide reliable evidence about the effect of Ca4+ on the mechanical response. Second, the potential provided by Ca4+ allowed to retrieve – by employing a standard clinical imaging – paramount information about the composition of AC.

Regarding the AC mechanical response – and by focusing on the data computed from the indentations performed before the static bath –, the absence of statistical difference between the control and treated group in terms of AC thickness and, moreover, of all the mechanical parameters allows to state that similar groups of OC cores were considered by this study. This evidence represents a crucial point, considering that the wide scattering in the mechanical response of the tibio-femoral AC [15,172,175–177] makes it difficult to form similar groups with the purpose of performing a control-treated study. In this regard, retrieving OC cores from the same areas of the tibio-femoral joint and, more importantly, spatially close each other can be a viable solution.

ITS statistical model applied on the normalized series of mechanical parameters allowed to detect changes in the AC response due to the static bath. The normalized trends allowed to highlight an increase of the mechanical parameters dispersion after the exposure to the static bath, regardless of the solution (see the variation in the scattering of normalized data in **Fig. 7.2** and **Fig. 7.3**). Considering that this evidence is common to both the groups investigated, its occurrence could be ascribed to possible changes in the tissue due to the time occurring since the beginning of the assessment. In this regard, it must be pointed out that the approach proposed by this study was the best option aiming to i) investigate eventual effects of Ca4+ after the achievement of an equilibrium of its diffusion within AC [216], and ii) provide reliable insights about the AC mechanical behaviour, before and after the exposure to the control or to the Ca4+ solution.

ITS statistical model highlighted a significant effect of Ca4+ on the elastic behaviour of AC, i.e., decrease of E_0 and S_0, suggesting a softening of the tissue induced by the CA. This effect could be explained mainly by considering the interaction between the electrostatically charged molecules of Ca4+ and the relative targeted AC component, i.e., PGs. Typically, PGs tend to outstretch in space due to their mutual electrostatic repulsion [220], moreover inducing a Donnan osmotic pressurization of the interstitial fluid within the tissue [221]. Considering the 3D arrangement of the AC ECM, the mutual repulsion between PGs – together with the relative osmotic pressurization – might induce an effect on the collagen network – especially in the deep layer of AC, where PGs are more abundant [56,57] and the collagen fibers are perpendicular to the articular surfaces [54] – which, in turn, is responsible in maintaining the osmotic pressure [52], therefore contributing to the compressive (fast) dynamic response of the tissue [53]. By adding to AC positively-charged molecules – as the ones of Ca4+ – a variation of the FCD within the tissue might occur, mainly due to the partial charge shielding of PGs. In this regard, the repulsion between PGs diminishes as a result of the shielding of the negatively-charged glycosaminoglycans (GAGs), considering either the interaction of the ones belonging to the same PG aggrecan, and the interaction between GAGs of different PGs. Thereby, the spatial expansion of PGs might decrease, reducing the osmotic pressurization of the interstitial fluid and, consequently, the containment function requested to the collagen network might lose of intensity. By focusing on this complex dynamic of interaction and, moreover, by considering the biomechanics of AC – and, moreover, that the fixed charged density provided by PGs and by the relative Donnan osmotic pressurization plays a key role in the tissue instantaneous response [222,223], together with the effort provided by the collagen network containment function –, it seems reasonable a decrease in the elastic response of AC [224].

No significant effect of the CA was highlighted by ITS statistical model in terms of AC viscous parameters. Considering the cationic nature of the Ca4+ and its effect on tissue FCD, an alteration of the

AC viscous response would have been possible. As above reported, FCD of AC is mainly related to the negatively-charged PGs and to the osmotic pressurization of the interstitial fluid, which both contribute to the elastic and viscous response of the tissue [225,226]. It has already been proven that FCD plays a key role in the stress-relaxation extent and rate of AC, in particular considering the concentration of solution cations [227]. Furthermore, an altered osmolarity could also have produced changes in the AC viscoelastic relaxation [228]. Nevertheless, information about porosity, permeability, and spatial hindrance of Ca4+ molecules are required to properly argue about such phenomena [228].

Regarding the equilibrium response of AC, i.e., E_{eq}, ITS model highlighted a significant effect both in case of control and CA solution. The overall decrease herein highlighted could be ascribed to the intrinsic degradation of AC, that might occurred in absence of preservation factors [229]. The higher decrease on E_{eq} highlighted by the group exposed to Ca4+ (see **Fig. 7.3**) could be related to phenomena induced by a variation of the FCD of AC, in particular due to a decrease in the collagen fibers tension [228] as a consequence of the reduced electrostatic repulsion between PGs [224] and, moreover, to the increased osmolarity [58].

In this study, insights about the distribution of Ca4+ were retrieved by HRpQCT. In particular, by the analysis of the 3D images – i.e., attenuation trend – it was possible to detect the depth-dependent distribution of the CA within AC, which reflected the inhomogeneous arrangement of PGs peculiar of the tissue. The superficial layer of AC is characterized by a small concentration of PGs [57,178], the latter increasing moving to the middle and deep layer [179]. Accordingly, the attenuation trends computed by this study showed higher values in the middle and deep zones of AC, confirming the outcomes retrieved by previous works employing the same CA to visualize AC [132,214,230–233]. In addition, the approach herein proposed allowed to differentiate the contribution of the three layers of AC, providing useful insights about the composition of the tissue in a non-destructive way.

Regarding the assessment of AC thickness, the analysis highlighted similarity between μCT and HRpQCT approach, i.e., no statistical difference between the estimates and, moreover, a Pearson coefficient (ρ^2) of 0.85. This evidence suggests that both the approaches seem to be reliable in evaluating AC morphology. Nevertheless, it should be noted that HRpQCT underestimated AC thickness compared to μCT. This finding could be explained by considering the different extent of time required by the two approaches to acquire the images mandatory to compute the AC thickness, i.e., less than 5 minutes and ~ 15 minutes for μCT and HRpQCT, respectively. Therefore, the beginning of dehydration phenomena could be the reason behind the lower values provided by the latter approach. Despite this limitation, weighting the attenuation values of the individual AC layers for the layers thickness represents the best option – over the use of a simple mean, or median value – to assess more in detail the existing relationships between AC structure/composition and mechanical properties.

The exploratory investigation of preliminary relationships between the features of AC – i.e., among the mechanical properties and the depth-dependent attenuation related to the PGs arrangement – highlighted some promising trends. First, and assuming the deep relationship between the distribution of Ca4+ within AC and the one of PGs, significative and positive correlations were highlighted between the attenuation and the elastic response of AC, i.e., E_0 and S_0 (Spearman, ρ^2 = 0.64 and 0.32, respectively). The fixed negative charge of PGs and the relative osmotic pressurization of the interstitial fluid contribute significantly to the AC compressive response [234], even at the nanoscale [235]. Moreover, it was demonstrated that the combined electrostatic and non-electrostatic contributions of PGs may explain up to more than 98% of the AC modulus [221]. According to such evidence, the positive relationships highlighted

between the attenuation of AC and the elastic parameters of the tissue can be explained by considering that the higher the PGs content, the stiffer the AC instantaneous response results to be.

Second, significant correlations were highlighted between attenuation and the parameters describing AC viscous response, i.e., τ and β (Spearman, $\rho < 0$ and $\rho > 0$, respectively; $\rho^2 = 0.53$ and 0.30, respectively). τ is a relaxation time, and its extent is related to the physical characteristics – e.g., polymer length, and concentration – of the system [227]. The negative correlation between τ and attenuation could be explained as follows: the higher the attenuation – thus, the higher the PGs content –, the lower is the FCD of the tissue due to the high amount of $Ca4+$ molecules electrostatically attracted to PGs, the lower is the collagen network tension – which is not compensated by electrostatic repulsion [228] –, the faster the viscous phenomena related to the water content are exhausted due to regime reached by the fibrils of collagen, now more prone to dissipate more energy through viscoelastic relaxation [236–238]. β is a stretching parameter, related to the specific type of polymer motion [239]. According to the polymer theory, and considering a system of polydisperse polymers as AC [240], the extent of β decreases when the entangled polymer length increases [239]. Therefore, the positive correlation between β and attenuation could be explained as follows: the higher the attenuation – thus, the higher the PGs content –, the lower is the length of the PGs sites entangled due to the molecules of $Ca4+$ electrostatically attracted to the sulfated GAGs, the higher β coefficient results to be.

Previous studies employing $Ca4+$ highlighted correlations between the attenuation of the CA and instantaneous [241,242] and viscous parameters [243] describing AC mechanical response. Nevertheless, and to the best knowledge of the authors, this is the first study investigating correlations between the features of AC by taking into account information related to both morphology – i.e., thickness – and composition – i.e., attenuation dependent on PGs content – of the AC layers. This approach could provide useful insights able to improve the knowledge about the link between functionality and structure/composition of AC. In this regard, the relationships herein found reached significancy – in terms of ρ^2 – higher than the correlation coefficients reported by the above-mentioned studies [241–243].

Last, some limitations must be highlighted. First, the framework provided by this study was unable to differentiate the effect of a FCD variation from the one induced by a change of osmolarity within AC. It is well known that osmolarity can induce alterations in the mechanical response of AC – by changing viscous and energy dissipation phenomena – due to a variation in both the permeability and the fluid volume fraction [228]. Nevertheless, and by focusing on the knee joint, it should be noted that the osmolarity of the solutions herein employed is close to the synovial and serum osmolarity range reported in literature, i.e., between 350 and 450 mOsm/kg [244–246]. Second, and toward the application of $Ca4+$ addressing clinical and biomechanical purposes, the present study highlighted a non-negligible alteration of the AC mechanical behaviour, i.e., of the tissue elastic response. Concerning the clinical point-of-view, this evidence suggests to avoid any excessive load until the complete removal of the CA from the synovial site [247]. In this regard, previous studies highlighted a complete removal of $Ca4+$ from AC, confirming the reversibility of the changes induced by the CA, at least in terms of AC composition [214,248]. Regarding the biomechanical point-of-view, the outcomes that will be retrieved from samples of soft tissues exposed to $Ca4+$ – e.g., AC of the OC unit, in the perspective of applying full-field approaches – i.e., DVC – to study the comprehensive response of such a unit – should be considered carefully. The softening of the tissue produced by the CA could produce a bias on the results, providing a variation in the field of displacement that will be computed. Third, the relatively small sample size investigated do not allow to assess the presence of preliminary correlations between structure/composition-related and mechanical parameters of AC with enough statistical power. Despite this limitation, the preliminary insights achieved suggest the presence of such correlations. Moreover, as previously highlighted by Study II (see Chapter 6), also the

findings retrieved herein suggest to investigate correlations between structure/composition-related and mechanical parameters by weighting the contributions of the AC individual layers, aiming to better understand the deep links between the AC features.

7.5 Conclusion and Future Perspectives

The primary aim of the study was to elucidate eventual effect induced by a cationic CA, i.e., Ca4+, on the AC viscoelastic response. A treated and control group – i.e., AC of OC cores exposed to Ca4+ and to a control solution, respectively – were investigated. The mechanical behaviour of AC was evaluated before and after exposing the tissue to such solutions, in particular by applying a nominal-deformation based indentation protocol. The OC cores exposed to Ca4+ were acquired by HRpQCT system, with the two-fold purpose of i) retrieving information about the AC features, i.e., PGs, and ii) achieving useful insights about the structure/composition-function relationships peculiar of AC. A significant effect of the CA on the AC elastic behaviour was highlighted, evidence that could be ascribed to a variation of tissue the FCD due to the partial charge shielding of PGs produced by the positively charged molecules of Ca4+. The analysis of HRpQCT images provided information about the thickness and the depth-dependent arrangement of AC. Preliminary but significant correlations were highlighted between the mechanical parameters describing the viscoelastic response of AC and the attenuation produced by Ca4+ within the tissue, which was strictly related to PGs content and distribution. These findings support the reliability of a contrast-enhanced HRpQCT approach in assessing the features of AC. Nevertheless, the non-negligible effect of Ca4+ highlighted suggests precaution in the employment of such a CA towards clinical and biomechanical purposes. Therefore, future studies will investigate an eventual reversibility of the effects induced by the Ca4+ on AC – i.e., enhancement of contrast and softening of the tissue –, in order to support the transfer of such a CA towards the clinical practice and the full-field biomechanical assessment of the OC unit.

8 Study IV – Suitability of Digital Volume Correlation Approach to Study the Comprehensive Behaviour of the Osteochondral Unit – A Validation Study

8.1 Introduction

The OC unit represents an essential part of load-bearing joints, being responsible of deploying the multiaxial forces developed during locomotion [249]. The damping function provided by the OC unit is ensured by its multi-level organization, defined by the local arrangement of AC, CC, SB, and TB [2]. AC leads the shock-absorption response of the OC unit thanks to its optimized architecture and composition [3]. CC and SB define a junction between AC and TB, ensuring the deployment of stress across different tissues [4]. Last, TB is composed by a porous, irregular network of minerals and collagen, which provides to the tissue the ability to withstand the external loads [34]. As a result of such heterogeneity, different magnitude of pressure, and strain occurred within the OC unit during musculoskeletal tasks [250,251]. As highlighted by the mechano-regulatory theories, the dynamic interaction between homeostasis and remodelling of the OC tissues is essential in maintaining joint functional capabilities [5–7]. The subtle balance in the crosstalk between OC tissues can be altered by several traumatic and degenerative pathologies, especially considering joints usually under mechanical stress, as the human knee [1]. OA is the main degenerative disease impairing human joints, representing a major healthcare issue due to its ever-growing incidence and to the serious mobility limitations [10], with important implications on both individual patient and overall society [11]. OA modifies the homeostasis of the joint, deregulating the crosstalk between cartilaginous and mineralized tissues and, consequently, impairing simultaneously i) structure, composition, and mechanical response of OC unit, and ii) cells signalling [13]. Although OA etiology is well known from a clinical point of view, the pathogenesis of OA at the tissue level is still an on-going debate. In this regard, the remodelling processes of AC and, in particular, of mineralized tissues seem to play a key role in the OA onset and progression [26]. As a consequence of the alteration induced by OA in the structure and mechanical response of the OC tissues changes in the strain distribution occur, leading to an impairment of their transfer within the OC unit [252,253]. Therefore, the development of reliable approaches providing a sound measurement of the strain induced inside biological tissues structure by external loads is critical to assess early disease-related changes within the OC unit, e.g., the initial changes in the strain distribution across the AC-bone tissue junction.

Extensometers and strain gauges are the reference methods to measure the strain within structures – including biological tissues as TB [254] –, providing an average strain value for the whole specimens, and the deformation into a few discrete points, respectively [252]. Therefore, such methods provide information through homogenisation approaches, with a degree of detail not adequate to evaluate the heterogeneity of biological tissues [255].

More suitable approaches for the assessment of strain gradient and local strain within heterogeneous structures are full-field techniques [252]. Among them, Digital Image Correlation (DIC) is a full-field technique computing the distribution of displacements and, consequently, of strains on the outer surface of

a structure [256]. Although DIC is relatively ease of use, further ensuring high level of accuracy [257], it is unable to provide a comprehensive assessment of the 3D strain distribution within biological tissues and biomaterials. DVC is a full-field technique that requires 3D images of a structure in the undeformed and deformed state [258], and exploits the images texture or grey levels gradients to compute the inner displacement and strain fields [259,260]. Despite DVC can be applied to datasets acquired by various imaging techniques – e.g., Computed Tomography [261], Synchrotron μCT [262], μCT [263], MRI [264] –, the majority of the findings are closely linked to X-ray imaging [258].

X-ray based DVC provided exhaustive measurements of the inner deformation within mineralized tissues [261,265–267] and, more recently, at the junction between AC and bone [215,262,268], but its application to the OC unit still represents an extremely challenging scenario. The different magnitude of displacement and strain developed within the OC tissues during loading, and the dimensional scale at which the features of the OC tissues are detectable – e.g., from a few to hundreds of micrometres for AC [269], and bone tissue, respectively – make it difficult to find a compromise between the employed setup, the spatial resolution, the overall sample dimension and, more importantly, the tissues to investigate. Regarding the latter point, employing X-ray based DVC to study the OC unit presents a major limitation, i.e., the low radiopacity of the AC and of its features [130]. To partially overcome this drawback, two main approaches are currently used. The first approach employs Phase-Contrast imaging, which proved to be suitable in detecting the microstructural features of soft tissues, e.g., by measuring the localised orientation and deformation of fibres within the annulus fibrosus of intervertebral disc [270,271], and by assessing the strain distribution at the cartilage-bone interface of knee OC unit [268]. Nevertheless, the application of Phase-Contrast in laboratory systems presents the main drawback of exposing the tissues to long period of irradiation – especially considering the demand of a double acquisition due to the in situ mechanics assessment required by DVC –, leading to possible degradation [259]. The second approach entails staining of soft tissues via radiopaque contrast agent (CA) in order to increase and to resolve their main features, e.g., local arrangement of chondrocyte lacunae [215,272]. However, exposing soft tissues to CA could present two main limitations, i) possible alteration of tissue morphology and mechanical response, and ii) the enhancement reached by the penetration of the CA could not induce the heterogenous pattern required by DVC algorithms, reducing – or even impairing – their potentiality. Taking into account the open issues related to the above reported approaches, performing X-ray based DVC of the OC unit is still a challenge beyond the possibilities allowed by the current experimental and imaging solutions.

Apart from that, efforts must be made also in terms of properly evaluating the DVC performance, e.g., precision and accuracy. By considering that the DVC performance is strictly related to the specific application – therefore including imaging type, resolution, set-up, and tissues to investigate –, DVC suitability to a particular scope should be investigated in the first instance and before operating efforts to combine in situ mechanics and imaging, especially towards the evaluation of heterogeneous structures as the OC unit. The suitability of DVC to a particular application is investigated generally by employing simplified conditions – e.g., zero-strain [259,268,273,274] – that represent unrealistic scenarios compared to the stimuli commonly induced during the functioning of biological tissues.

With the view of a thoughtful evaluation of the OC unit, the present study proposed a methodological framework to assess the accuracy of the outcomes computed by DVC, considering a loading scenario, material heterogeneity, and specimens geometry eligible for studying the response of such a specific unit. Specific specimens – named phantoms – with some features of the OC unit were created and tested in compression within a μCT system, by applying a load that would induce a contact pressure within the range developed inside knee during locomotion. Extensometers were used as a reference method to measure the

axial displacement and the global strain induced on the phantoms by the compressive test. A loading device was developed to replicate the compressive test within the µCT system. DVC performance was firstly investigated by performing a zero-strain study, which allowed to optimise a pre-processing pipeline. This pipeline was then used to investigate the DVC accuracy on loaded specimens, i.e., by comparing the axial displacements and strains computed by DVC with the ones provided by extensometers. Last, with the purpose of a full employment of the potential provided by DVC, a further analysis entailed the computation of the phantoms Poisson's ratio.

The sections of the study that involved in situ µCT testing, pre-processing of the relative images, and DVC were performed within the abroad period at the Insigneo Institute of the University of Sheffield (United Kingdom), under the lead of Prof. Enrico Dall'Ara of the Division of Clinical Medicine, School of Medicine and Population Health, Faculty of Health.

8.2 Materials and Methods

By considering the multiple steps that defined the pipeline of the current study, in the following the relative workflow was reported.

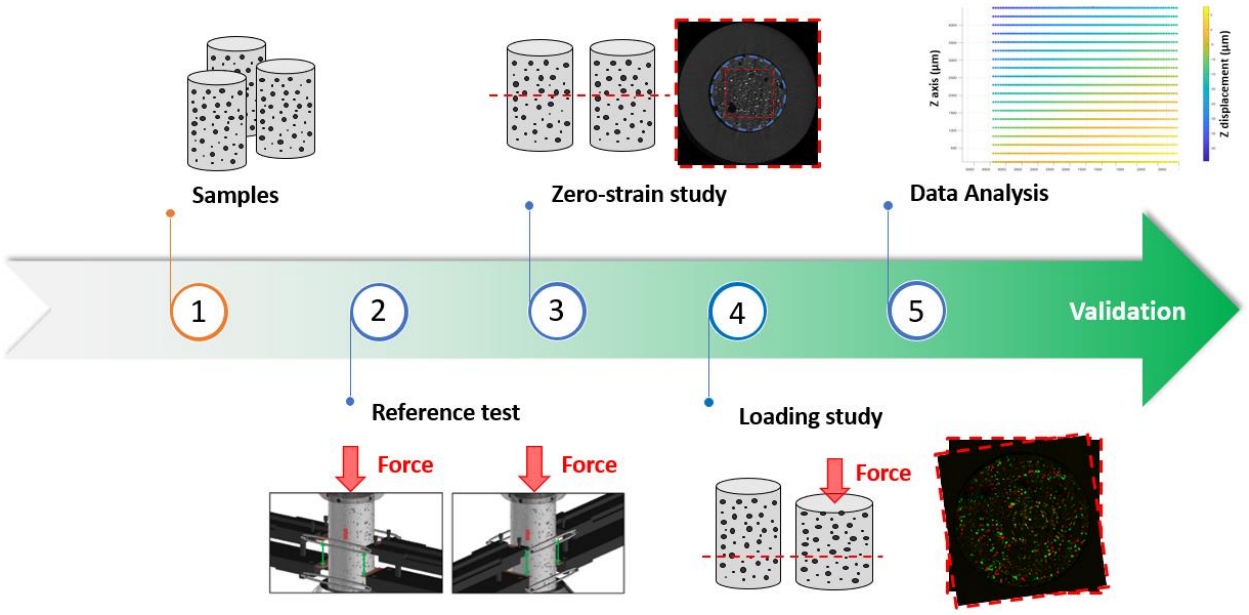

Fig. 8.1. The workflow of the study about the suitability of X-ray based DVC towards the OC unit study.

8.2.1 Specimens

Considering the view of applying X-ray based DVC to the OC unit, phantoms were created with some features of the OC unit, i.e., of the TB, moreover allowing to replicate in situ µCT the testing protocol performed in the experimental phase. Therefore, the following choices were made in manufacturing phantoms. First, geometry of phantoms was defined considering i) the possibility of testing them by a reference method, i.e., compressive test employing extensometers, and ii) the specifications of the available

μCT system – i.e., inner space allowed by the system (also with the perspective of hosting the device for in situ testing), resolution, and Field of View (FoV). Second, the composition of the phantoms was defined in order to detect clearly their features by μCT imaging and to provide mechanical properties, i.e., Elastic Modulus (E), close to TB. It should be noted that materials with mechanical properties close to AC, e.g., hydrogels [275], are not suitable to be investigated by contact extensometers and, moreover, to be repeatedly acquired by μCT imaging, which could degrade material due to prolonged X-ray exposition.

In agreement with such evidence, phantoms were developed by combining cold mounting resin and bovine bone particles, both chosen to obtain phantoms made by a homogeneous, low-attenuating matrix incorporating scattering, high-attenuating particles. Regarding resin, two different types were firstly considered, i.e., resin R1 (Technovit 4006, Kulzer GmbH, Germany) and R2 (Viafix, Struers, Denmark). A preliminary assessment was made on two cylinders – 10 mm in diameter, 5 mm thick, one for each resin type – aiming to evaluate the resin with the lower coefficient of attenuation. 3D images of the cylinders were acquired in the same scanning session by μCT (SkyScan 1072, Bruker, Belgium), by employing the following scanning protocol: X-ray tube voltage = 50 kV, current = 179 μA, 1-mm Al filter, pixel size = 15.6 μm. According to the analysis of such images (results not reported here), resin R2 provided the lower coefficient of attenuation. Concerning bovine bone particles, a preliminary assessment was performed – by applying the scanning protocol above reported – to evaluate the radiopacity of freshly morselised – obtained by morcellation of TB cores excised from the femoral condyles of bovine femurs – and bovine bone ash – obtained by a previous study, in which cylinders of TB from femoral condyles were burned in a muffle furnace [276]. Bone ash showed a higher coefficient of attenuation and, consequently, was chosen as high-attenuating particles. Phantoms were then moulded by mixing 4 g – 2 g powder, 2 g liquid – of could mounting resin R2 to 1 g of bovine bone ash. Regarding the latter, particles with different size were used – i.e., 0.75 g with size (50 ÷ 100) μm, and 0.25g with size (20 ÷ 50) μm –, thus to obtain an even more random pattern of particles. During polymerization phantoms were subjected to continuous stirrer in order to achieve a uniform distribution of the ash particles.

Therefore, N = 5 phantoms were retrieved, with dimensions evaluated by digital caliper (Mitutoyo, Minato-ku, Tokyo, Japan; resolution = 0.01 mm) (**Tab. 8.1**). The diameter of the phantoms was measured at three different quote, i.e., at the edges and at the center of the area on which extensometers would have been applied. The height of the phantoms was measured three times.

	H (mm)		**D (mm)**		**A (mm^2)**
Phantom	avg	sd	avg	sd	
#1	14.90	0.01	5.12	0.01	20.62
#2	15.20	0.01	5.05	0.02	20.03
#3	14.22	0.01	5.07	0.01	20.22
#4	13.86	0.01	5.02	0.08	19.82
#5	14.25	0.01	5.05	0.02	20.00

Tab. 8.1. Geometrical features of the phantoms, i.e., height (H), diameter (D), and cross-sectional area (A).

8.2.2 Compressive tests

Phantoms were tested in compression by using a Instron testing machine (Mod.8502, Instron, Norwood, MA, USA). Each phantom was positioned in the testing machine by using two aluminium sample holders (inner diameter of 5.3 mm) on the top and bottom. Two extensometers (Mod. 2620-601, Instron Corp., Canton, MA, USA) were simultaneously placed in contact to the phantom external surface by means of four rubber bands, in order to measure the axial displacement and strain. The combined use of two extensometers allowed to counterbalance eventual bending stress combined to compressive one, therefore avoiding potential misalignment. The extensometer gauge length was set at 9.55 mm, which represented a trade-off between the assessable volume and eventual edge effects.

Once the extensometers were positioned vertically, i.e., equidistant from the phantom planar surfaces, the loading system was vertically lowered in order to fit the upper part of the phantom within the top sample holder. A nominal preload of ~ 10 N was applied to ensure contact with the phantom. No preconditioning of the phantoms was performed. Then, a load of 200 N was applied monotonically in 10 seconds, producing a contact pressure of approximately 10 MPa, which corresponds to the average value developed within the knee during locomotion [277–280]. A stress-relaxation test followed, by maintaining the position of the loading system for 2 hours, which would have corresponded to the time required for the entire in situ µCT evaluation. Phantoms were tested twice on different days, by positioning the extensometers i) on 0° and 180°, and ii) on 90° and 270° generatrix, in a random order (**Fig. 8.2**).

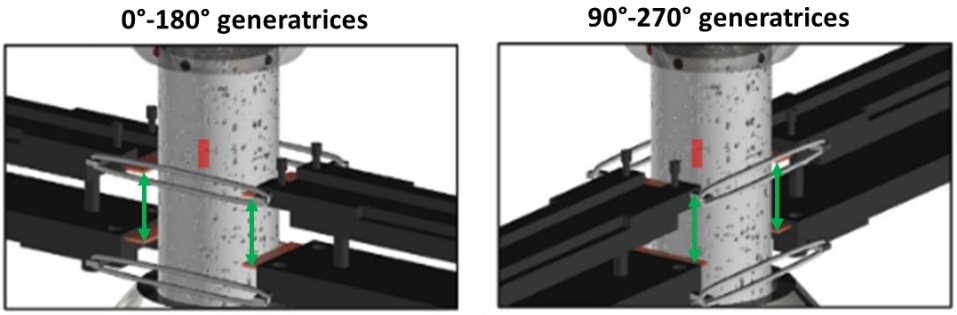

Fig. 8.2. Scheme of the axial strain measurement by using extensometers. The strain value computed for each phantom was the average value of the strain measured on the four generatrices at same stress value for the repetition combinations of the test, i.e., (Left) 0º-180º and (Right) 90º-270º. Green arrows indicate the extensometer gauge length, i.e., 9.55 µm, while the red lines indicate the reference point over the phantom surface.

8.2.3 In situ µCT testing device

With the purpose of replicating the testing protocol within µCT system, an in situ loading device was designed and manufactured. Size and materials were chosen based on the specifications of the µCT system, so that it would fit in the space available and it would reduce to a minimum the X-Ray absorption. The loading device was developed by assembling the following parts (**Fig. 8.3**): i) a Plexiglas cylinder – bottom part: inner and outer diameter of 5.2 mm and 9.4 mm, respectively; top part: inner and outer diameter of 10.5 mm and 30.7 mm, respectively; total height of 42 mm –, which hosted the phantom (bottom part), and the remaining part of the device; ii) a Plexiglas T-shape loader, transmitting the load to the phantom; iii) an

Aluminium end-cup, connected to i) by four conical screws – diameter 2.5 mm, 90° spaced around the diameter of the end-cup itself –, with a threated hole (8-mm in diameter) in the center; iv) a load cell (Model 8416, Range 5 kN, Output 10 V_{DC}, Sensitivity 1.0586 mV/V; Burster, Germany) placed between ii) and iii), and the relative amplifier (Model 9236-V300, Burster, Germany); v) a stainless steel flat head bolt with hexagon socket, inserted in iii), allowing the application of the load by an Allen key. The parts i) and iii) were developed by using a CNC milling machine (ProLIGHT Machining Center). A lateral groove – hosting the cable that connects the load cell to its amplifier – was made in the upper part of the Plexiglas cylinder. In this way it was possible to minimize the development and the transmission of shear forces between the load-chain and the phantom top surface, therefore producing a prevalent vertical translation of the load cell during loading. By taking into account the whole acquisition system, an overall sensitivity of ~ 1 N is considered.

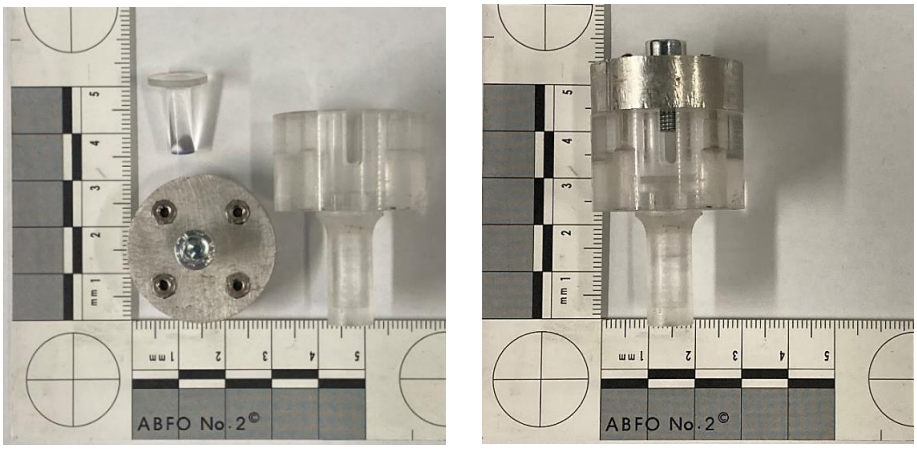

Fig. 8.3. Some of the parts composing the loading device, (Left) apart and (Right) combined.

8.2.4 Scanning protocol and Specimens Preparation

After positioning the phantom within the Plexiglas cylinder, first the T-shape loader, and then the load cell were placed over the phantom top surface. Therefore, the Aluminium end-cap was connected to the Plexiglas cylinder by the four screws, and the stainless steel bolt was then inserted in the Aluminium end-cap. All the steps were performed by monitoring the signal of the load cell, avoiding transmission of load to the phantom. The contact between the bottom surface of the T-shape loader and the phantom top surface was considered as occurred once a load value of ~ 2 N was reached. The in situ loading device containing the phantom was then positioned inside the µCT system (SkyScan 1172, Bruker, Belgium), and its vertical position was adjusted to focus the FoV center on the phantom height-center. The following scanning parameters were used: 10 Megapixel 12-bit digital cooled ORCA-HR CCD X-ray detector, 2000×1048 pixel; 50 kV X-ray tube voltage; 179 µA intensity; Exposure time equal to 1180 ms; Rotation step equal to 0.3°; Total rotation equal to 180°; Images average ×2; 0.5 mm Aluminium beam hardening filter. The zero-strain study was performed by acquiring images at both high and low resolution, i.e., voxel size of 4.9 µm and 9.8 µm, respectively. The FoV varied between 10 × 5 mm (width x height), and 20 × 10 mm for high and low resolution scans, respectively. Scans for the Loading study were performed by using the optimal

resolution among those above reported, obtained by evaluating the outcomes of the zero-strain study. Regardless of the resolution, each scan lasted for ~ 40 minutes.

8.2.5 Scanning in Zero-strain condition

The study of DVC accuracy and precision in zero-strain condition was performed by scanning twice a phantom (#1), with both high and low resolution. The acquisition protocol replicated the one reported in paragraph 8.2.4. The consecutive scans were performed without repositioning neither the loading device within the μCT system, nor the phantom within the loading device. High-resolution and low-resolution scans were performed on different days.

8.2.6 Scanning in Loading condition

All the phantoms were tested in situ μCT, aiming to validate the field of displacements provided by the DVC approach [273] to the results retrieved by the reference method. After performing the preload scan, the loading device was removed from the μCT, performing the test in a more controlled and secured way. The phantom was loaded until ~ 200 N in 10 seconds, leaving 40 minutes of relaxation. The load was applied through an Allen key connected to the hexagon socket of the flat head bolt. A timing of 40 minutes was enough to reach a constant slope of the load during relaxation (data not reported). During the 40 minutes of stress-relaxation the load was monitored once every 2 minutes in the first 10 minutes, then once every 5 minutes until 40 minutes. At the end of stress-relaxation the loading device was repositioned within the μCT system, as close as possible to the previous location. The time occurred between the end of the load-monitoring and the begin of the second scan was ~ 20 minutes. Afterwards, a second scan – lasting ~ 40 minutes – was performed, by applying the previous scanning protocol. The second scan was performed within the temporal range of (60 ÷ 100) minutes after the application of the load. At the end of the scan under load, the loading device was removed from the μCT, and the load was monitored for further 20 minutes.

8.2.7 Image Reconstruction

The images were reconstructed as stack of 16-bit TIFF images via NRecon program (Bruker). The specific alignment, slight beam hardening (20%) and ring artifact (10) were used as factors of correction. The obtained slices were then converted from 16 bit to 8 bit by Fiji-ImageJ software [281]. Slices including image artifacts at the bottom and at the top of the stack were removed. These steps were common for all the scans, i.e., applied to both zero-strain and loading study.

8.2.8 Zero-strain study: Pre-processing pipeline

The repeated scans – Scan1 and Scan2, at high resolution, voxel size 4.9 μm; Scan3 and Scan4, at low resolution, voxel size 9.8 μm – obtained for phantom #1 were aligned in pairs – i.e., Scan1 with Scan2, and Scan3 with Scan4 – along the vertical direction, obtaining datasets with the same number of slices, and with slices at both ends showing the same sections of the phantom. A pre-processing pipeline was developed, allowing to evaluate the impact of i) a subsampling of the images (only performed for the scans at high resolution, i.e., 4.9 μm), ii) a binarization of the images, iii) analysed sub-volume, and iv) the resolution on the DVC performance. Therefore, for the high resolution scans the following sub-images were identified and further analysed (**Fig. 8.4**).

- HR, Crop-1, Gray values. In Scan1 and Scan2, a parallelepiped – square cross section of 710 × 710 pixels (3.48 × 3.48 mm), height of 984 pixels (4.82 mm) – was cropped in the central portion of the phantom. Therefore, a volume-of-interest of 58.37 mm^3 was obtained, corresponding to 18.99 % of the phantom overall volume (307.24 mm^3).
- HR, Crop-1, Gray values, Subsampled. The images obtained in HR, Crop-1, Gray values were subsampled by a ×2 factor, thus performing an increase of the voxel size until 9.8 µm.
- HR, Crop-1, Binary. The images obtained in HR, Crop-1, Gray values were binarized, by applying a single level threshold chosen according to the volumetric histogram, i.e., the histogram of the gray values of all the slices within a single scan. The single level threshold was defined as equal to the value obtained by adding to the average gray value of the volumetric histogram the relative standard deviation multiplied by 3. The efficacy of this approach – over standard methods – in detecting the inner features of the phantom, i.e., bone ash particles, was assessed preliminary by visual inspection. In binarizing datasets, the same single level threshold – i.e., the higher of the two values obtained for the two datasets – was applied to Scan1 and Scan2.
- HR, Crop-2, Gray values, Subsampled. Scan1 and Scan2 were subsampled by a factor 2 (voxel size equal to 9.8 µm). Then, a cylinder – circular cross section of 500 pixels in diameter (4.90 mm), height of 984 pixels (4.82 mm) – was considered within the central portion of the phantom. To achieve this, a circular binary mask – image with value one inside, and zero elsewhere – was created from subsampled Scan1 and expanded to its full height. In such a way, the subsequent DVC analysis would focus only on the region within the cylindrical area. By applying such a mask, a volume-of-interest of 90.89 mm^3 was obtained, corresponding to 29.58% of the phantom overall volume.

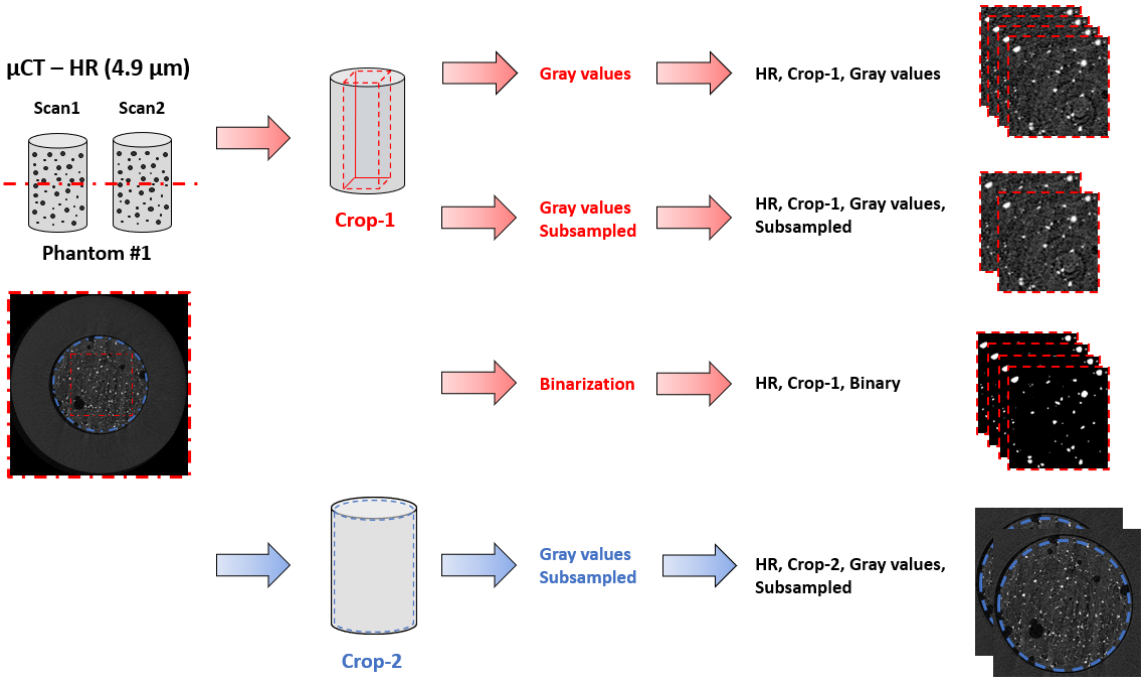

Fig. 8.4. Summarizing of the sub-images developed for the zero-strain study at high resolution.

Regarding scans at low resolution, the following scenarios were considered (**Fig. 8.5**).

- LR, Crop-1, Gray values. In Scan3 and Scan4, a parallelepiped – square cross section of 340×340 pixels (3.33×3.33 mm), height of 1008 pixels (9.88 mm) – was cropped in the central portion of the phantom. In such a way a volume-of-interest of 109.56 mm^3 was obtained, corresponding to 35.66% of the phantom overall volume.
- LR, Crop-1, Binary. The images obtained in LR, Crop-1, Gray values were binarized by a single level threshold chosen according to the procedure previously reported (see HR, Crop-1, Binarization).
- LR, Crop-2, Gray values. A cylinder – circular cross section of 500 pixels in diameter (4.90 mm), height of 1008 pixels (9.88 mm) – was considered within the central portion of the phantom in Scan3 and Scan4. To achieve this, it was applied the same procedure previously reported (see HR, Crop-2, Gray values, Subsampled). In this way, a volume-of-interest of 186.31 mm^3 was obtained, corresponding to 60.64% of the overall volume of the phantom (307.24 mm^3).

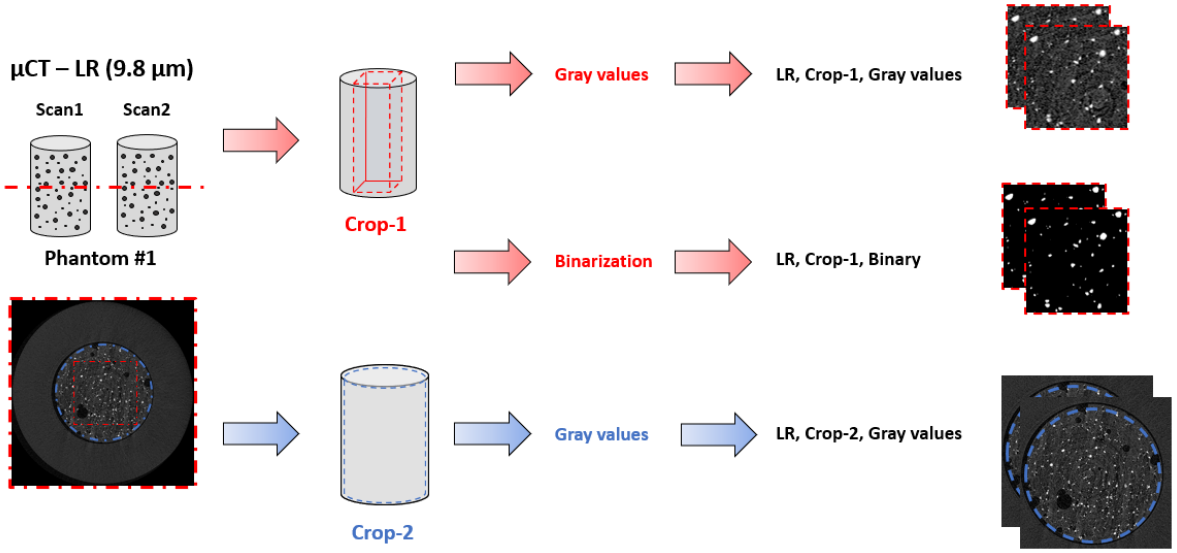

Fig. 8.5. Summarizing of the scenarios developed for the zero-strain study at low resolution.

All the pre-processing steps were performed by custom-made Matlab scripts (MATLAB 2022b, MathWorks, Natick, MA, USA), after validating their outcomes with a reference imaging software (Fiji-ImageJ).

8.2.9 Loading study: Pipeline

The scans in preloaded and loaded conditions of each phantom were firstly aligned, by using as reference the scan in the preloaded configuration. Two different registration approaches were employed. Since during the in situ test the bottom of the phantom was fixed, and the load was applied from the top surface, the first approach – named Local registration, and based on the local features of the scan – aimed at maximize the alignment of the bottom slice of the phantom between loaded and preloaded scans. To obtain such a result, a rigid rotation along the vertical direction was applied to maximize the overlap of the bottom slice of the loaded scan with the bottom slice of the preloaded scan. The second approach – named

Global registration, and based on global features – used a 3D rigid registration (Amira, FEI Visualization Sciences Group, France). More in detail, a Normalized Mutual Information was used as optimization criterion [282]. The transformation matrix obtained was applied to the original greyscale image, which was subsequently resampled using Lanczos interpolator [282]. The impact of the registration approach on the DVC outcomes was investigated. By following the registration, and regardless the approach, the pre-processing that maximized the accuracy of the DVC in the zero-strain study was applied.

8.2.10 Digital Volume Correlation

In this study, a deformable registration toolkit (Sheffield Image Registration Toolkit, ShIRT) [283–285] was used as DVC approach to compute the field of displacements within the phantoms. In brief, such an approach superimposed a homogeneous cubic grid – defined by the distance between the nodes of each cubic cell, namely Nodal Spacing, NS – to the images to be registered. The software computes the displacements that map each point of the undeformed image into the corresponding point of the deformed image, by using the grey levels gradients within the images. More in detail, the displacements are computed by solving the registration equations in the nodes of the homogeneous cubic grid, i.e., by interpolating such a function tri-linearly in order to estimate the full 3D field of displacements in each node of the cubic grid. According to the above reported information, the main parameter of the elastic registration algorithm is represented by NS, which represents the distance between two independent measurements of displacement and, therefore, the spatial resolution of the DVC assessment. Despite the dependence of the accuracy and precision of DVC on NS was already proved [273,286], the optimal NS should be investigated for any application. Within the zero-strain study, different NS values from 49 μm – 5 voxels and 10 voxels for the low and high resolution scans, respectively – to 490 μm – 50 voxels and 100 voxels for the low and high resolution scans, respectively. The value of NS that allowed to maximize DVC accuracy and precision in zero-strain condition was then applied to the Loading study.

8.2.11 Processing of DVC outcomes, and Evaluation of Axial Strain

The following procedure was applied to the DVC outcomes achieved by the zero-strain and the loading study. The field of displacements was processed by custom-made Matlab scripts (MATLAB 2022b, MathWorks, Natick, MA, USA) to compute the axial – vertical – strain within the phantoms. First, the same binary mask developed in the pre-processing pipeline was used to exclude from the analysis i) the background, and ii) the sub-volumes introduced by DVC around the effective volume of the phantom. More in detail, only cubic cells with at least one node within the binary mask were considered.

From the zero-strain study, information about the average Cartesian components of the displacement – avgX-disp (μm), avgY-disp (μm), and avgZ-disp (μm) – and their relative deviation within the phantom – sdX-disp (μm), sdY-disp (μm), sdZ-disp (μm) – were computed.

Second, the field of displacements within the phantom was processed through an approach named of the virtual extensometers. Considering that DVC provides the field of displacements at the nodes of the cubic grid, it was decided to investigate the field of displacements through the height of the scans by focusing on the vertical quote of such nodes. In such a way, a series of horizontal, equally spaced planes was obtained (**Fig. 8.6**).

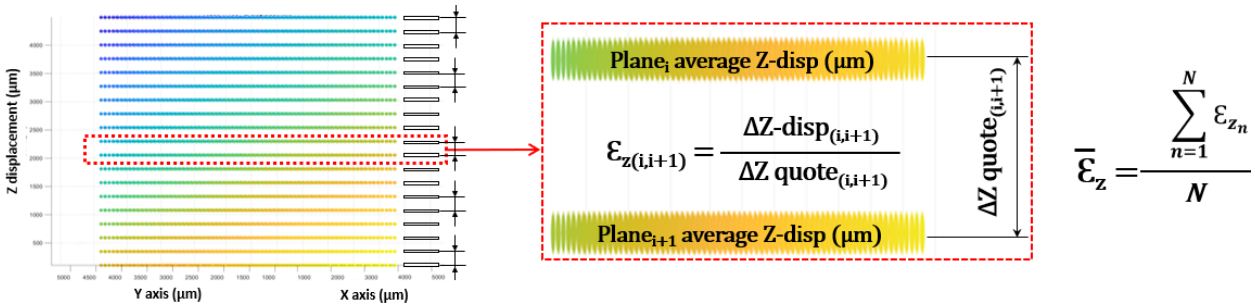

Fig. 8.6. Summarizing of the virtual extensometers approach. (Left) Clustering of the nodes of the cubic grid according to their vertical quote. This step allowed to obtain a series of equally spaced planes; the average X-, Y-, and Z-displacement was computed for each plane. (Center) Computation of the axial strain, $\varepsilon_{z(i,\,i+1)}$, among subsequent planes, obtained by dividing the average Z-displacement of each plane, ΔZ-disp, by the distance between planes, ΔZ quote. (Right) The global axial strain within the phantom, ε_z, was computed as average of the axial strain peculiar of the series of planes.

Third, the average field of displacement – with its relative standard deviation – was computed for each plane by averaging the displacements of the nodes with the same vertical quote, thus to evaluate variation of X-, Y-, and Z-displacement along the phantom height. In this regard, the global Z-displacement – Z-disp (µm) – was computed as the difference between the Z-displacement of the top and of the bottom planes. Fourth, the average axial strain of each plane, ε_{zi} (µε), was computed by dividing the average Z-displacement of the specific plane by the distance between subsequent planes. Regarding this latter distance, in this study its values was defined as a constant, specifically equal to the value of NS parameter. The computation of the strains within the phantom was limited to the axial component due to necessity of validating such an estimate against the measure provided by extensometers (reference method). Fifth, the global axial strain developed within the phantom – ε_z (µε) – was computed as average of the average axial strain developed within the planes.

8.2.12 Processing of DVC outcomes to compute Poisson's ratio

With the purpose of fully exploiting the potential provided by DVC, a further analysis of its outcomes was developed, by focusing on the scans retrieved by the Loading study. The purpose of this additional analysis was to compute the Poisson's ratio of the developed – and tested – phantoms. All the following processing steps were performed by custom-made Matlab scripts.

After replicating the first step reported in the previous paragraph – consisting in the removal of background and sub-volumes from scans, by the use of the binary mask developed according to paragraph 8.2.8 –, the analysis focused on identifying the edge nodes of the phantom. This choice was related to the possibility of evaluating nodes with a maximum displacement along the XY plane.

Consequently, the system of coordinates of the edge nodes cluster was changed, from a Cartesian to a Polar system. The cluster of edge nodes was then additionally divided, by replicating the same procedure reported in the previous paragraph; in particular, edge nodes were further divided according to their vertical quote, thus to cluster them in a series of horizontal, equally spaced planes.

Therefore, a scaling factor was applied to the entire cluster of edge nodes – i.e., by subtracting from their X- and Y-displacement the average displacement along such axes of all the edge nodes – aiming to

calculate properly the radial displacements – and the relative strain – required to compute the Poisson's ratio. Radial displacements were then calculated for each edge node, by considering the parameters that allowed to change the system of coordinates from Cartesian to Polar. By dividing the displacements so obtained for the distance between the edge nodes polar coordinates and the ones of the phantom center, it was then possible to compute the radial strain. By averaging such strain for all the edge nodes, the radial strain of the phantom, ε_r, was calculated.

Following this last step, a variation of the virtual extensometers approach explained in the previous paragraph was proposed. In particular, the average Z-displacement of the top and bottom planes was calculated, in this case by considering the entire set of nodes for each of the two planes. Therefore, the axial strain ε_z was computed by dividing the relative difference between the Z-displacement of the top and of the bottom planes by the distance between them, i.e., by subtracting their vertical quote. The radial strain of the phantom, ε_r, was calculated by averaging the values peculiar of all the edge nodes, regardless of their vertical quote. Last, radial Poisson's ratio were calculated by dividing ε_r for ε_z.

8.2.13 Data Analysis

Regarding the compressive testing, axial displacement and axial strain – Z-disp (μm), ε_z (με) – were computed by focusing on the data acquired in the temporal range corresponding to that of the μCT scan in loading condition, i.e., between 60 and 100 minutes of relaxation. For each repetition, Z-disp was computed by averaging the measures provided by the two extensometers; the nominal peak stress was calculated by dividing the maximum load – i.e., 200 N – by the phantom cross-section area; ε_z was computed as the ratio between Z-disp and the gauge length of the extensometers; elastic modulus, E (GPa) was calculated as the ratio between the nominal peak stress and ε_z, therefore assuming that tests were performed in the elastic regime. Parameters for each phantom were then computed by averaging the outcomes of the two testing repetitions, together with their percentage coefficient of variation (CoV%). Moreover, standard deviation and CoV% were also computed as measures of reliability across the specimens.

Concerning the zero-strain study, the precision of DVC in computing the field of displacements was defined as the standard deviation of the Cartesian components of such a field within the phantom, i.e., sdX-disp (μm), sdY-disp (μm), sdZ-disp (μm). This choice was made by considering that the standard deviation of the displacements within the phantom – i.e., by assuming that no rotation occurred between the two subsequent scans – was primarily related to the random error of the system, i.e., images noise. The accuracy of the axial strain was defined as the difference between the measured average axial strain – avgε_z (με) – within the phantom and the nominal imposed strain value (zero in this case), while the precision was defined as the standard deviation of the axial strain – sdε_z (με). Therefore, the optimal pre-processing pipeline among the ones investigated (see paragraph 8.2.8) was defined by focusing on i) the precision in the displacements computation – sdX-disp, sdY-disp, and sdZ-disp –, ii) the precision – sdε_z – and the accuracy – avgε_z – in the axial strain computation, and iii) the dependence of DVC performance on the NS parameter.

Concerning the loading study, Z-disp (μm) and ε_z (με) were computed for each registration approach performed – i.e., Local registration, based on a rotation along the vertical axis, and Global registration, based on a 3D-rigid registration –, and then compared to the results obtained by the reference method in order to estimate the accuracy of DVC in such a scenario.

8.3 Results

8.3.1 Reference method – Extensometers

Z-disp, ε_z, and E values of the phantoms were reported in **Tab. 8.2**. Dispersion – CoV% – among phantoms resulted to be 8.8%, 8.3%, and 9.7% for Z-disp, ε_z, and E, respectively. The highest intra-variabilities – CoV% among the two repetitions for the worst phantom, i.e., #4 – were 11.4% and 10.5% for Z-disp and ε_z, respectively.

Phantom	Z-disp (μm)			ε_z (με)			E (GPa)	
	avg	sd	CoV%	avg	sd	CoV%	avg	sd
#1	52.9	2.6	4.9	5574	182	3.3	1.74	0.06
#2	62.4	0.7	1.1	6532	72	1.1	1.45	0.02
#3	58.5	1.2	2.0	6238	53	0.8	1.59	0.01
#4	57.4	6.6	11.4	6037	636	10.5	1.68	0.18
#5	49.7	0.6	1.3	5312	87	1.6	1.88	0.03

Tab. 8.2. Outcomes – i.e., axial displacement, Z-disp, axial strain, ε_z, and elastic modulus, E – computed from the analysis of the extensometers data acquired during compressive testing of the phantoms.

8.3.2 Zero-strain study

Considering the various scenarios investigated aiming to develop an optimal pre-processing pipeline, results were divided into sections, to better highlight the impact of i) a subsampling of the images (only performed for the scans at high resolution, i.e., 4.9 μm), ii) a binarization of the images, and iii) the extent of volume evaluated within the phantom – i.e., by comparing the same scenarios but with a different resolution, 4.9 vs 9.8 μm – on the DVC performance.

Effect of Subsampling

The impact of subsampling on DVC performance was evaluated only for high resolution scans, i.e., 4.9 μm. Details about the relative results were reported in **Tab. 8.3**. The percentage difference between the outcomes of the different scenarios were expressed in comparison to the results achieved by "HR, Crop-1, Gray values" case. Less precision was highlighted in terms of in-plane displacements – i.e., sdX-disp, sdY –, and axial strain – i.e., sdε_z – when subsampled images were used. Conversely, higher precision for the axial displacement (sdZ-disp) and higher accuracy for the axial strain were found for the analyses based on subsampled images. Subsampling provided a speed up of the DVC computational time, i.e., 1h/NS vs 5min/NS.

	HR, Crop-1, Gray values Voxel size: 4.9 µm	HR, Crop-1, Gray values, Subsampled Voxel size: 9.8 µm	Percentage difference
sdX-disp (µm)	0.321	0.355	+10%
sdY-disp (µm)	0.343	0.389	+13%
sdZ-disp (µm)	0.384	0.350	-9%
avgε_z (µε)	273	247	-10%
sdε_z (µε)	30	38	+24%

Tab. 8.3. Variation in precision and accuracy of DVC for the zero-strain test between the scenarios employing the original resolution or subsampled images.

Regardless the approach, DVC precision in terms of displacement increased with increasing NS, reaching a local minimum around 244 µm. **Fig. 8.7** showed the trend for sdZ-disp, but the same was highlighted also by sdX-disp and sdY-disp (data not reported).

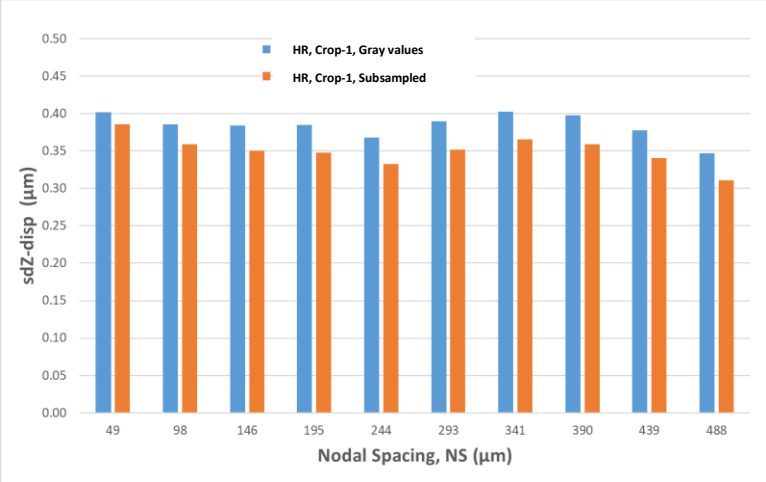

Fig. 8.7. Variation of DVC precision as a function of Nodal Spacing, NS, in terms of standard deviation of the axial displacement (sdZ-disp).

Concerning DVC precision in terms of strain (sdε_z), a stronger reduction was found in function of NS. Conversely, DVC accuracy for axial strain (avgε_z) was independent from NS (**Fig. 8.8**).

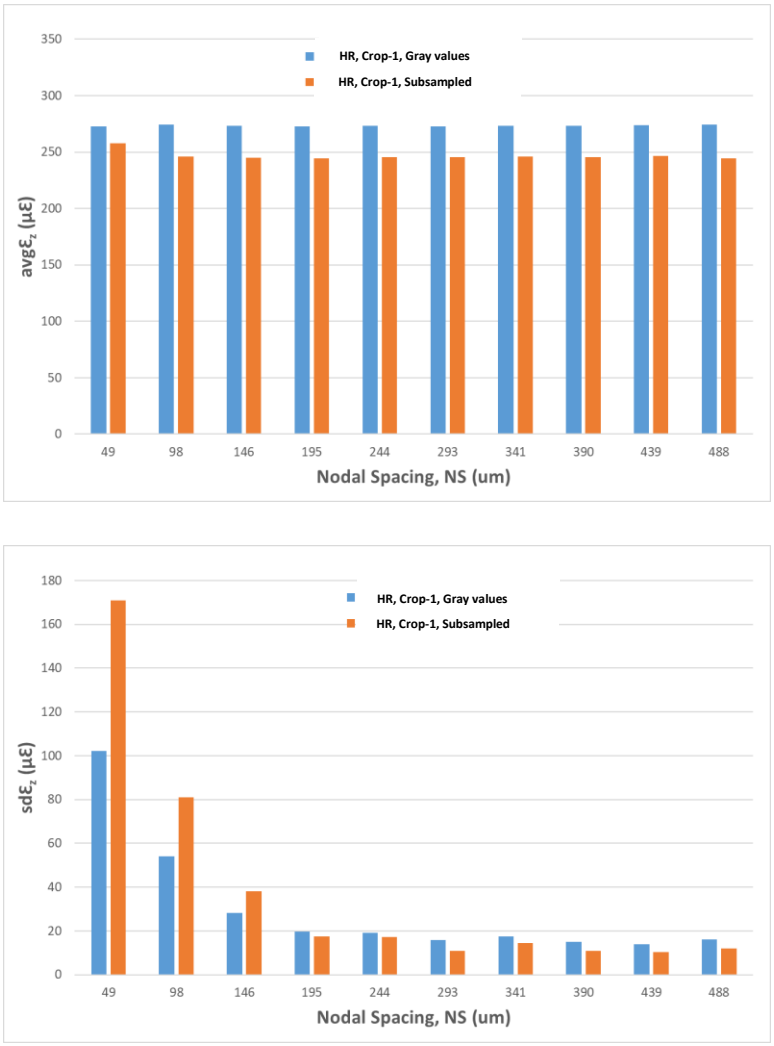

Fig. 8.8. Variation of DVC accuracy and precision as a function of Nodal Spacing, NS, in terms of (Top) average axial strain, avgε_z, and (Bottom) standard deviation of the axial strain, sdε_z.

Effect of Binarization

The impact of binarization on DVC performance was evaluated for high and low resolution. Details about the results were reported in **Tab. 8.4**. Concerning the images at high resolution (4.9 µm, **Tab. 8.4**, left side), binarizing images led to a lower precision of the computed displacements and strains (percentage difference was expressed in comparison to the results of HR, Crop-1, Gray values). Higher decrease in precision was found for the low resolution case (9.8 µm, **Tab. 8.4**, right side). Conversely, the accuracy in evaluating the axial strain was similar between the two cases. Therefore – and despite a speed up of the computational time was achieved, i.e., from 1h/Ns to 30min/NS, and from 10min/NS to 5min/NS, for high and low resolution, respectively –, binarization definitely reduced the DVC performance for this application.

	HR, Crop-1, Gray values Voxel size: 4.9 µm	HR, Crop-1, Binary Voxel size: 4.9 µm	Percentage difference	LR, Crop-1, Gray values Voxel size: 9.8 µm	LR, Crop-1, Binary Voxel size: 9.8 µm	Percentage difference
sdX-disp (µm)	0.321	0.379	+17%	0.164	0.393	+82%
sdY-disp (µm)	0.343	0.396	+15%	0.150	0.370	+86%
sdZ-disp (µm)	0.384	0.441	+14%	0.235	0.450	+63%
avgε_z (µε)	273	277	+1%	69	71	-2%
sdε_z (µε)	30	107	+112%	64	223	+110%

Tab. 8.4. Percentage difference in DVC precision and accuracy due to binarization of the original images, performed at (left) high resolution, and (right) low resolution.

The precision of displacements computed by DVC increased by increasing the NS, reaching a stable trend around 244 µm, regardless the resolution (**Fig. 8.9** and **Fig. 8.10**, respectively). Concerning strain, as reported for the subsampling scenario, no variation of the accuracy and an increase of the precision were highlighted by avgε_z and sdε_z, respectively (data not reported).

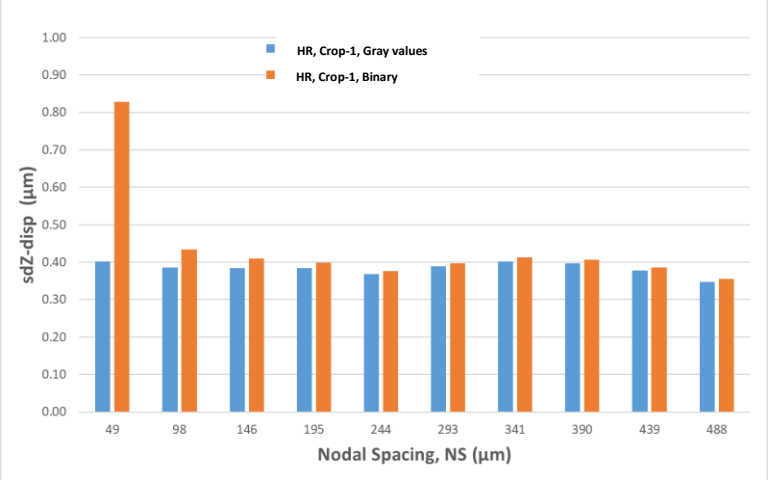

Fig. 8.9. Variation of the DVC precision – in terms of axial displacement, i.e., sdZ-disp – as a function of Nodal Spacing, in case of high resolution.

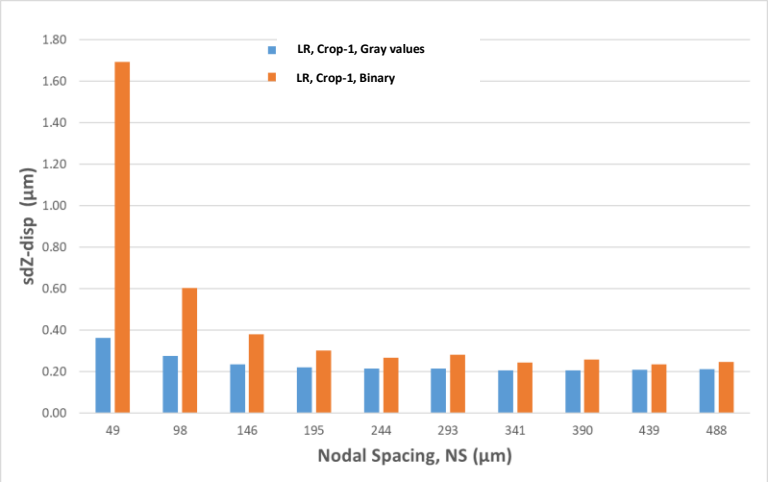

Fig. 8.10. Variation of the DVC precision – in terms of axial displacement, i.e., sdZ-disp – as a function of Nodal Spacing, in case of low resolution.

Effect of Volume

The impact of the assessed volume on the DVC precision and accuracy was evaluated for high and low resolution (**Tab. 8.5**). It must be highlighted that – in case of high resolution – such aspect was investigated by focusing on subsampled images, i.e., i) HR, Crop-1, Gray values, Subsampled, and ii) HR, Crop-2, Gray values, Subsampled.

	HR, Crop-1, Gray values, Subsampled Voxel size: 9.8 µm	**HR, Crop-2, Gray values, Subsampled Voxel size: 9.8 µm**	**Percentage difference**	**LR, Crop-1, Gray values Voxel size: 9.8 µm**	**LR, Crop-2, Gray values Voxel size: 9.8 µm**	**Percentage difference**
sdX-disp (µm)	0.355	0.431	+19%	0.164	0.173	+5%
sdY-disp (µm)	0.389	0.464	+19%	0.150	0.157	+4%
sdZ-disp (µm)	0.350	0.351	+1%	0.235	0.231	-1%
avgε_z (µε)	247	248	+1%	69	70	+1%
sdε_z (µε)	38	27	-33%	64	41	-45%

Tab. 8.5. Percentage difference of DVC precision and accuracy due to the extent of the volume evaluated, performed at (left) high (subsampled), and (right) low resolution.

Details about variation of the DVC performance induced by the investigated volume were reported in **Tab. 8.5**. Concerning the (subsampled) high resolution (**Tab. 8.5**, left side), an increase of the assessable volume slightly decreased the precision of DVC in computing displacements, moreover increasing the DVC precision in calculating strain; nevertheless, no impact was highlighted in terms of DVC accuracy in computing strain. Moving on the low resolution, basically no variation in the precision of computing displacements, and in the accuracy of calculating strain was highlighted (**Tab. 8.5**, right side). A reduced impact on the accuracy was obtained also in terms of the computation time requested – from 5min/Ns to 10min/NS, and from 10min/NS to 30min/NS, for high (subsampled) and low resolution, respectively. Concerning the impact of NS on DVC performance, an increase of precision was highlighted in terms of displacements (**Fig. 8.11**) up to 244 µm, regardless the resolution and the extent of the evaluated volume. Regarding the computed strain, once again no variation of the accuracy and an increase of the precision were showed by the average and the standard deviation of the axial strain, respectively (data not reported).

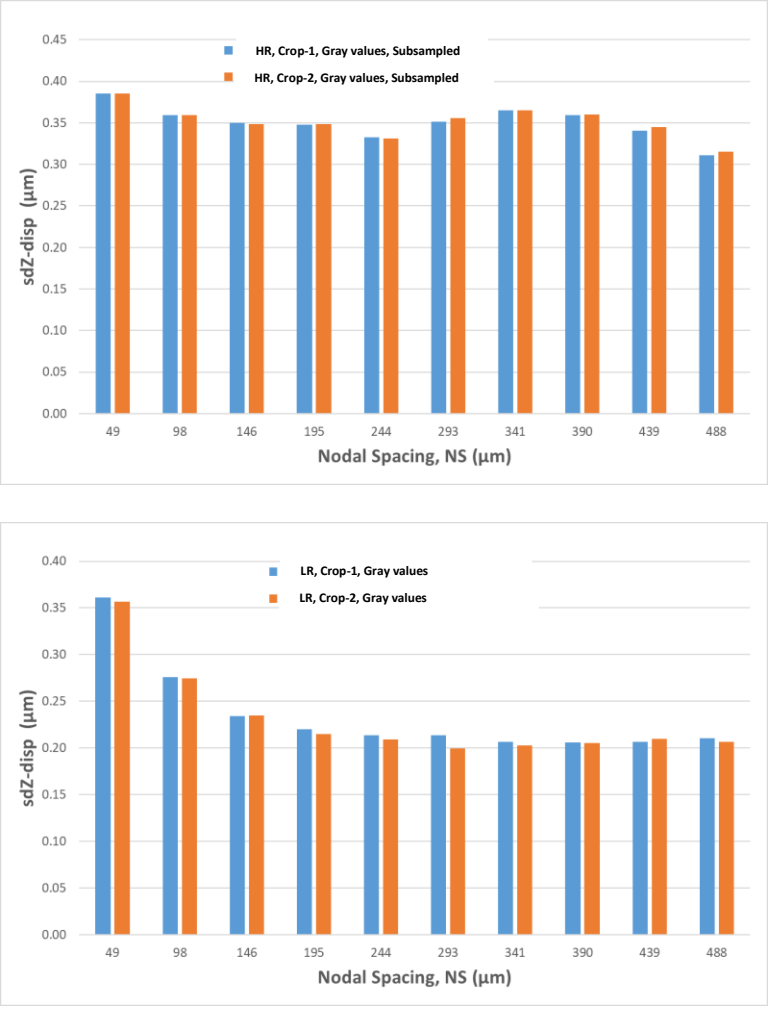

Fig. 8.11. Variation of DVC precision – in terms of axial displacement, i.e., sdZ-disp – as a function of Nodal Spacing, in case of (Top) high (subsampled), and (Bottom) low resolution.

Combined Effect of Resolution and Volume

The combined impact of resolution and volume was evaluated by considering two main scenarios: i) Crop-1, to evaluate the effect of both resolution and volume on the accuracy of DVC, and ii) Crop-2, to evaluated only the impact of the volume was assessed.

The evaluation of a larger volume – with a lower resolution in case of i) – allowed to increase DVC precision and accuracy in estimating the displacements and the axial strain, respectively (**Tab. 8.6**). Nevertheless, less precision in measuring strain was detected. In terms of the computation time requested, its increase was not considered as significant – i.e., from 1h/NS to 10 min/Ns, and from 10min/NS to 30 min/NS, for Crop-1 and Crop-2, respectively – taking into account the increase of accuracy reached.

	HR, Crop-1, Gray values Voxel size : 4.9 µm	**LR, Crop-1, Gray values Voxel size : 9.8 µm**	**Percentage difference**	**HR, Crop-2, Gray values, Subsampled Voxel size : 9.8 µm**	**LR, Crop-2, Gray values Voxel size : 9.8 µm**	**Percentage difference**
sdX-disp (µm)	0.321	0.164	-65%	0.431	0.173	-85%
sdY-disp (µm)	0.343	0. 150	-78%	0.464	0.157	-99%
sdZ-disp (µm)	0.384	0. 235	-48%	0.351	0.231	-41%
avgε_z (µε)	273	69	-120%	248	70	-112%
sdε_z (µε)	30	64	+73%	27	41	+39%

Tab. 8.6. Percentage differences of DVC precision and accuracy due to the combined effect of resolution and volume evaluated, performed for (left) Crop-1, and (right) Crop-2 cases.

Concerning the impact of NS on DVC performance, an increase of precision was highlighted in terms of displacements (**Fig. 8.12**) up to 244 µm, regardless the scenario. Regarding DVC computation of strain, NS produced the same impact even in case of a combined effect of resolution and volume, i.e., by inducing no variation of the accuracy and an increase of the precision in terms of the average and the standard deviation of the axial strain, respectively (data not reported).

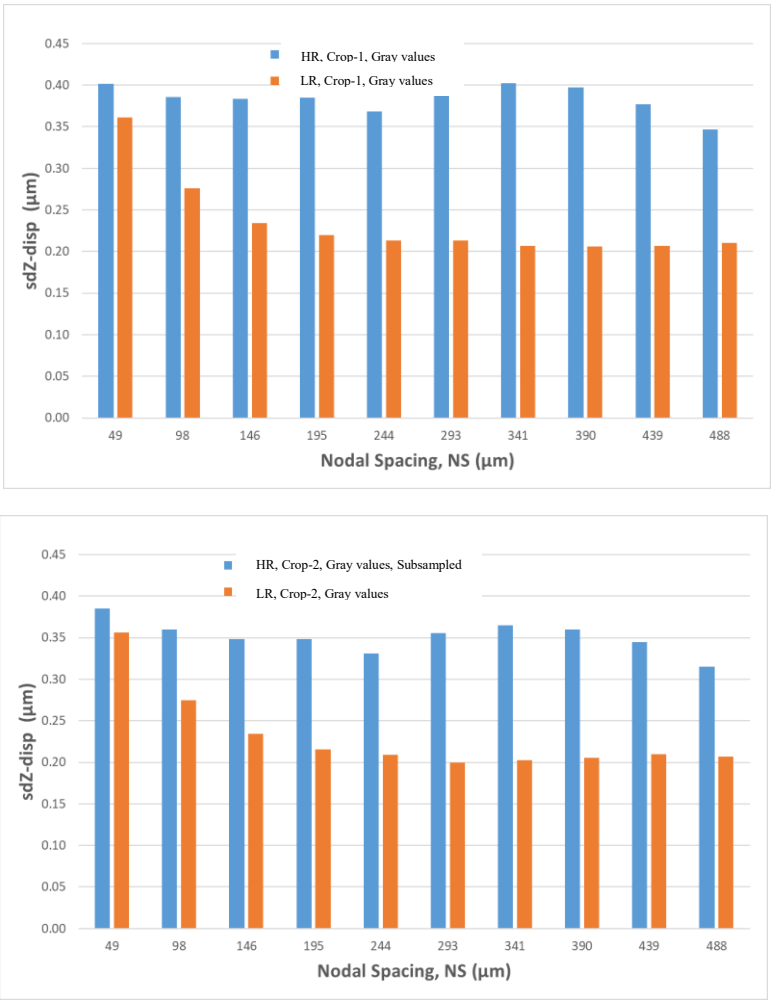

Fig. 8.12. Variation of DVC precision – in terms of axial displacement, i.e., sdZ-disp – as a function of Nodal Spacing, in case of (Top) Crop-, and (Bottom) Crop-2.

According to the evidence reported above, the optimal pre-processing pipeline was chosen for further analyses in the loaded condition included the following steps: i) maximization of the volume to investigate; ii) evaluation of gray level images, without binarization; iii) acquisition of low-resolution images; iv) NS parameter equal to 244 µm.

8.3.3 Loading study

By applying the pre-processing pipeline optimized by the zero-strain study – i.e., NS equal to 244 µm, and the approach reported in paragraph 8.2.11 – the displacement field within the loaded phantoms was evaluated (**Fig. 8.13** and **Fig. 8.14**). The displacement in the XY plane showed bands not perfectly oriented along horizontal directions (**Fig. 8.13**, left and right panel, for X- and Y-displacements, respectively), while quite regular bands were highlighted by the axial displacements (**Fig. 8.14**).

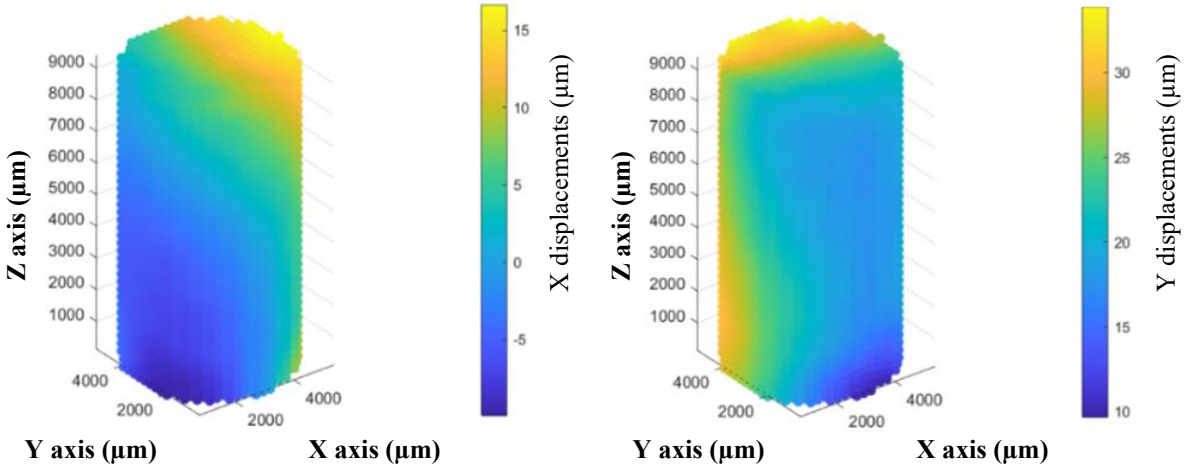

Fig. 8.13. Displacement maps – (Left) X- and (Right) Y-displacement – provided by DVC (phantom #2).

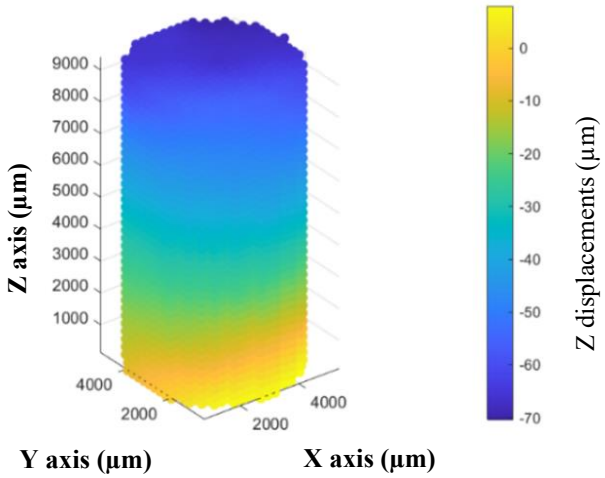

Fig. 8.14. Displacement map – i.e., Z-displacement – provided by DVC (phantom #2).

Regarding the impact of the registration approach on the axial displacement and strain, no substantial differences were highlighted (**Tab. 8.7**).

	Local registration			Global registration		
Phantom	**Z-disp (µm)**	**Ɛz (µƐ)**		**Z-disp (µm)**	**Ɛz (µƐ)**	
		avg	sd		avg	sd
#1	51.4	5857	302	51.2	5848	313
#2	59.3	6360	830	59.3	6358	830
#3	56.4	6129	155	56.4	6128	153
#4	60.6	6579	484	60.6	6578	482
#5	53.6	5804	428	53.6	5805	433

Tab. 8.7. Comparison of the axial displacement and strain achieved by applying DVC on images registered by a Local – i.e., rotation along the axial axis – and a Global registration approach – i.e., based on a 3D-rigid registration.

Considering the computational time required by each of the two registrations, Local registration approach was used to compare the outputs of DVC and of the standard mechanical testing with extensometers.

8.3.4 Validation of DVC strain over reference method

The axial displacement and strain measured by the reference method, i.e., extensometers, and computed by combining DVC technique and virtual extensometers approach were reported in **Tab. 8.8** and **Tab. 8.9**, respectively.

	Z-disp (µm)			
Phantom	**Extensometer**		**DVC**	**Percentage difference**
	avg	sd		
#1	52.9	2.6	51.4	2.9
#2	62.4	0.7	59.3	5.0
#3	58.5	1.2	56.4	3.6
#4	57.4	6.6	60.6	-5.3
#5	49.7	0.6	53.6	-7.5
Avg	56.2		56.2	-0.25
SD	4.9		3.8	5.7

Tab. 8.8. Axial displacement, Z-disp, measured by extensometers and computed by DVC. Percentage difference between the approaches was also reported.

ε_z (με)					
Phantom	**Extensometer**		**DVC**		**Percentage difference**
	avg	sd	avg	sd	
#1	5574	182	5857	302	-5.0
#2	6532	72	6360	830	2.7
#3	6238	53	6129	155	1.8
#4	6037	636	6579	484	-8.6
#5	5312	87	5804	428	-8.8
Avg	5939		6146		-3.6
SD	494		329		5.5

Tab. 8.9. Axial strain, ε_z (με), measured by extensometers, and computed from DVC axial displacement. Percentage difference between the approaches was also reported.

Percentage difference between the two approaches were in the range (-7.5 ÷ 5.0) % and (-8.8 ÷ 2.7) % for Z-disp and ε_z , respectively.

8.3.5 Estimate of phantoms Poisson's ratio through DVC

By processing the field of displacements computed by DVC, it was possible to estimate the radial strain at the edge of the phantom. Radial strain through the phantom (**Fig. 8.15**) were quite regular distributed. Furthermore, the sign of the radial strain values – i.e., positive – suggested the direction toward the outside of the phantom. The values of the Poisson's ratio fell within the range (0.37 ÷ 0.46).

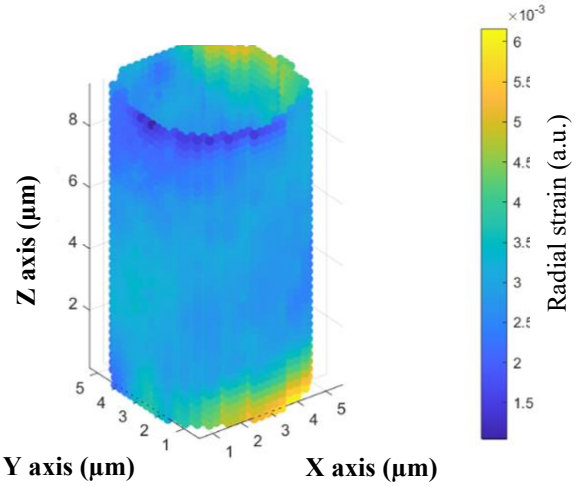

Fig. 8.15. Radial strains map achieved by processing the DVC field of displacements (phantom #5).

8.4 Discussion

The main goal of this study was to validate the DVC outcomes by considering a loading scenario, material heterogeneity, and specimens geometry eligible for studying the response of the OC unit tissues.

Specific specimens were developed with features detectable by μCT, and tested in compression. By employing extensometers during the test i) a reference measurement of the axial displacement and strain was obtained, ii) moreover allowing to compute the phantoms mechanical properties. A compressive response close to TB tissue was highlighted by the phantoms. A zero-strain study allowed to develop an optimal pre-processing pipeline of the images in terms of precision and accuracy. A pipeline based on gray levels images, acquired in low resolution, and investigated by setting NS equal to 244 μm allowed to maximize DVC performance. Therefore, a loading study was performed, in which phantoms were tested within μCT by replicating the reference testing protocol. 3D images were investigated by applying the optimal pre-processing pipeline previously developed. The comparison between the reference approach and the DVC results highlighted high similarity between the two approaches, endorsing the reliability of the DVC outcomes.

In this study extensometers were applied as a reference method to measure axial displacements and strain developed during a compressive test. Such an approach represents, to date, the reference technique in measuring the response of TB during monotonic test, especially by applying the four-extensometers approach [254]. The achieved evidence highlighted that the phantom mechanical response resulted quite similar to the one of TB, i.e., elastic property (E) between 1.45 GPa and 1.88 GPa [254,287,288]. Moreover, by applying the proposed testing protocol, axial strains below 1% were measured, corresponding to the deformation induced within the TB during locomotion [35,275,289]. High similarity among phantoms was highlighted, moreover achieving a quite low variability between the testing repetitions which suggests the replicability of the manufacturing process, and the reliability of the obtained data, respectively.

DVC precision and accuracy were firstly assessed through a zero-strain study performed on one phantom, with the purpose of developing a pre-processing pipeline able to maximize DVC performance. The results highlighted an impact of preliminary image-processing steps on the DVC performance. In particular, a common step in image-processing as binarization – generally applied to enhance the detection of the features-of-interest, and to reduce background artifacts and computational time – produced a worsening of DVC performance, with precision down to ~ 0.2 μm and accuracy down to ~ 200 με. Such a worsening could be ascribed to the high gradients around the particles after binarization. Concerning the impact of the extent of volume investigated on DVC performance, as expected no particular effect was highlighted. No substantial variation of DVC performance was also highlighted by subsampling the images. Resolution of the images induced a worsening of the DVC performance like the binarization steps. Regarding the impact of NS, results highlighted an increase of precision in estimating the displacements – sdX-disp, sdY-disp, and sdZ-disp – and in increase of precision in computing the strain – sdε_z – by increasing the size of the sub-volume investigated, i.e., up to 244 μm which, in this study, represented 25× and 50× the high and low resolution of the images, respectively. Interestingly, no impact of NS on DVC accuracy – avgε_z – was highlighted. Dependence of DVC performance on the sub-volume unit was previously highlighted by different imaging approaches and type of specimens [255,273], in particular by focusing on the computed strains. In this study, the same phenomenon was observed for displacement and for the standard deviation of the strain, but not for the average axial strain. The latter evidence might be related to the approach used to compute such a strain, i.e., as average of the contributes of the horizontal

planes in which were clustered the nodes provided by DVC. Taking into account the above-mentioned findings, the actual contribution of the resolution on the computation of displacement and strain should be assessed in depth before employing DVC to investigate local displacement and strain. The optimal pre-processing pipeline herein developed (no binarization, lower resolution images, larger analysed volume, NS equal to 244 μm) allowed to measure displacement and strain of approximately ~ 0.1 μm and ~ 70 με, respectively. These values are in the range of those reported by previous studies involving μCT approaches for bone applications [267].

The developed pre-processing pipeline was applied to compare DVC outputs over a reference method, i.e., extensometers. Considering the operating principle of such a technique, it was decided to apply a similar approach to compute axial displacement and axial strain from the field of displacements provided by DVC. Therefore, it was possible to investigate the DVC outputs within the phantoms for similar extent i.e., ~ 9.8 mm and ~ 9.6 mm of height for DVC and extensometers, respectively. Similar results were obtained by using extensometers or DVC, with absolute percentage difference in displacement and strain below 9%. These findings validate the accuracy of DVC in computing the axial displacement and strains developed within complex structure undergoing loading scenarios similar to those of human knee OC unit. However, it should be pointed out that the DVC approach can provide useful insights about local details within the structure of biological tissues and biomaterials, e.g., internal strain field, under complex loading scenarios.

To the best of the authors knowledge, this is the first study proposing a validation of DVC in realistic loading conditions, i.e., by evaluating deformed specimens. In fact, the accuracy of DVC is generally investigated by focusing on simplified condition, i.e., zero-strain condition [255,268,273,274] or in virtually imposed simplified conditions [290,291]. Consequently, it is not possible to compare the results herein obtained with the findings retrieved by previous studies. Considering that one of the major benefits provided by DVC entails the validation of the outcomes achieved by computational models based on laboratory and clinical images [265,292], investigating the accuracy of DVC in scenarios more realistic for biological applications – e.g., in case of heterogeneous deformations – represents an approach required to better assess DVC errors. In this regards, one of the main challenges is represented by the development of phantoms allowing the application of a reference method, with composition and structure that provide i) detectable features within μCT imaging and ii) mechanical properties close to those of the tissue-of-interest.

DVC outcomes were further analysed to exploit the potential of such a technique in achieving information required to compute a complex parameter as the Poisson's ratio. More in detail, such a parameter was computed by retrieving the radial displacement and the relative strain of the phantoms edge nodes. Results highlighted a Poisson's ratio within the range (0.37 ÷ 0.46). Considering the composite nature of the developed phantoms, the values of the Poisson's ratio herein computed cannot be compared to the ones of specimens obtained by the lone epoxy resin, which could not be investigated by a X-ray based DVC due to the absence of detectable features. Few studies focused on the behaviour of resins – but of a different type compared to the one used by this study – in compression, reporting a range of Poisson's ratio similar to the one herein computed [293,294]. In this regard, Poisson's ratio was estimated previously by a pulse echo method – based on the measurement of the ultrasonic velocity ,– and by numerical simulations. Other approaches employed in the estimation of the Poisson's ratio – regardless the material or the tissue – are strain gauges [295], Digital Image Correlation [296–300] and DVC [260,301]. Despite strain gauges represent a conventional method, their outcomes might be affected by bias, i.e., additional weight and stiffness [302], moreover providing insights related to a few discrete points [252,260]. DIC technique

succeeded in measuring Poisson's ratio of biomaterials and tissues by considering full-field phenomena, but without providing information about the inner structure of the specimen. In this regard, it is well known that the latter aspects could definitely affect the extent of the investigated mechanical parameters, e.g., Poisson's ratio, due to defects and discontinuity eventually related to issues of the manufacturing process, or to the impact of pathologies, in case of biomaterials and tissues, respectively. Regarding the use of DVC to compute Poisson's ratio, its application is usually combined with the virtual fields method (VFM) [301], in which the additional use of Finite Element models provides complementary information. Exploiting DVC outcomes to compute Poisson's ratio – even by employing a simple approach as the one herein proposed – could definitely provide useful insights about the structure of biological tissues and biomaterials, especially with the view of tailoring properly tissue engineering approaches to the complex mechanical response of the tissues composing the OC unit.

Finally, some limitations must be reported. First, with the purpose of validating DVC outcomes towards its application to OC unit, it was decided to investigate specimens with features similar to those of TB. Despite validating DVC outcomes in the restricting condition herein investigated represented a challenge, the choice to consider and to develop such kind of phantoms was strictly related to the employed imaging technique, i.e., X-ray. In this regard, the validation of DVC accuracy in condition close to those of AC, or of AC-bone tissue interface would have requested the development of phantoms made by soft biomaterials, i.e., hydrogels. Nevertheless, it was already proved that excessive exposure to X-rays during scanning appears to affect strain within soft tissues and biomaterials, in particular in case of AC [303,304]. Accordingly, the use of X-ray imaging in applying DVC to AC must be thoughtful properly, especially considering possible degradation phenomena related to prolonged exposition to ionizing radiations. In this regard, future works may start from the use of soft resin or silicone – within which scattering radiopaque particles – in order to develop phantoms with features close to AC. Second, differences between the reference and the in situ μCT testing could have occurred. The different stiffness of the setup employed – i.e., made by aluminium, and by an assembly of plexiglas and aluminium components, for the compressive test and the in situ loading device, respectively – could have affected differently the results provided by the two approaches. In this regard, the choice of the materials for the in situ loading device was strictly related to the specific imaging technique. Any discrepancies about this point could have been reduced by considering the material employed in the manufacturing of phantoms, i.e., a relative soft biomaterials as could epoxy resin compared to the setups materials. Third, differences in the alignment of the phantoms during the two tests – reference and in situ – could have occurred. Besides the purpose of validating DVC outcomes over the reference method, it was decided to focus the analysis on the axial displacement and strain also considering eventual differences on the X- and Y- displacement due to an alignment discrepancy. Fourth, the approach applied to compute strain from DVC outcomes – i.e., virtual extensometer – allowed to investigate only the axial deformation. Despite the assessment of the full-field of strains within the phantoms could have provided important information, it would not be possible to validate their extent with the insights retrieved by the reference method applied by this study – i.e., extensometers, which allowed to measure only the axial displacement and strain. Two alternative approaches could have been applied to measure the field of strains within the phantoms, i.e., rosette strain gages with three measuring grids arranged at different angles, and a bi-axial extensometer. Regarding the first, despite its employment would have provided a measure of the two principal strains, its application would have suffered of some limitations, i.e., i) not providing a measure of the displacement, ii) restricting the investigation to a reduced area of the phantoms – by retrieving information as a single point measurement it would not have been possible to detect eventual defects in the structure of the specimen – and, consequently, iii) avoiding to

compensate eventual bias induced by an imperfect parallelism of the phantom top and bottom surfaces. Concerning bi-axial extensometer, despite its use would have provided information about axial and longitudinal strains, its configuration and geometry would have allowed the employment of a single extensometer, avoiding to detect and to compensate – also in this case – bias induced by misalignment of the specimens.

8.5 Conclusion

The study aimed to propose a methodological and experimental framework to validate the outcomes of DVC, first considering a simplified, zero-strain condition and, second, a loading scenario eligible to study the OC unit tissues. The zero-strain study provided an optimal pre-processing pipeline of the μCT images, allowing to achieve an accuracy of ~ 0.1 μm and ~ 70 με for axial displacement and strain, respectively. Regarding the loading study, DVC provided measurements of axial displacement and strain close to the reference method, with errors below 9%. Last, the Poisson's ratio of the phantoms investigated by this study was estimated by exploiting the full potential of DVC. The findings retrieved by this study underlying the importance of evaluating the eligibility of DVC towards its application to biological tissues, in particular suggesting to perform such evaluations by considering specimens and loading scenarios similar to those peculiar of the tissues of interest. The development of approaches enabling to assess and to enhance the reliability of the information provided by DVC is of paramount importance, in particular considering i) the employment of such a technique towards the assessment of the subtle relationship between functionality and structure of complex structures as the OC unit, and ii) the improvement of tissue engineering approaches that respond to pathologies impairing such a unit, therefore allowing the development of scaffolds that reproduce the structure of OC tissues and, moreover, the way with which the field of displacements and strains spreads within it during realistic loading scenarios.

8.6 Future perspectives and explorative approaches towards the study of OC unit

With the view of a thoughtful application of DVC to the OC unit, future studies will investigate approaches allowing to image the entire set of OC tissues, in order to evaluate also AC. By focusing on X-ray imaging – primarily due to the high resolution provided –, two main approaches are to date applied to image AC, i.e., by enhancing the features of the tissue through CAs [215,305], or by applying specific imaging techniques, such Phase-contrast [268,306] or Synchrotron [262]. Despite the use of radiopaque CAs succeeded in resolving AC main features [215], their application addressing biomechanical purposes could produce results affected by a bias (see the findings of Chapter 7), e.g., possible degradation phenomena induced by acid and toxic contrast agents [305] –, and by the timing of treatment requested to reach an equilibrium of the diffusion phenomena, that could last from a few hours up to days [232]. An additional limitation on the use of CA – even considering the recent advancements for which solutions preserving AC integrity the most are achievable [307] – is related to the heterogeneity of their distribution within AC, which could affect the reliability of DVC performance. Regarding Phase-Contrast and Synchrotron imaging, their application allowed to retrieve meaningful findings – e.g., by enhancing the contrast between AC and mineralized tissues, thus to quantify the field of strain at AC-bone interface, or allowing to visualize hierarchical changes in the tissue structure [262] – but AC results to be exposed to long periods of irradiation, and to high dose of X-ray, respectively, which could affect tissue integrity. According to these evidences, and with the perspective of applying DVC to assess the field of displacements

and strains within the OC unit, the use of contrast agents and specific imaging solutions must be thoroughly evaluated.

By considering the above-reported findings, explorative activities were performed to preliminary apply DVC to the OC unit, in particular by focusing on a zero-strain condition. It must be noted that the CA proposed by Chapter 7 was not employed in these activities considering i) the changes that induced to AC mechanics and ii) that a reversibility study has not yet performed. The attempts reported in the following were performed within the abroad period at the Insigneo Institute and at the School of Medicine and Population Health, Faculty of Health of the University of Sheffield (United Kingdom).

8.6.1 Exploratory approach based on µCT imaging and markers

The first attempt regarded the use of the set-up employed by the validation study, i.e., by using the manufactured loading device (paragraph 8.2.3) and µCT device (SkyScan 1072, Bruker, Belgium). With the purpose of enhancing the detection of AC by X-ray imaging, the use of markers over the AC surface was considered, i.e., by using the bovine bone ash previously employed (see paragraph 8.2.1 for details).

An OC core (5-mm in diameter, 15-mm in height) excised from the articular surface of a bovine knee was employed. The OC core was defrosted in PBS – obtained by diluting a tablet of Oxoid PBS within 100 ml of distilled water – for 2 hours at room temperature (20 °C). In the meanwhile, the bovine bone ash previously used was mixed with silicone-based grease – i.e., 50/50 ratio, achieved by starting from 0.07 grams of both components – in order to provide the particles attachment over the AC surface. Therefore, a thin layer of the grease-and-particles mixture was spread on the AC top and lateral surfaces. The OC core was then placed within the plexiglass cylinder of the loading device (**Fig. 8.16**). PBS was poured within the plexiglass cylinder to avoid dehydration of the sample during scans. The T-shape loader was positioned on the top surface of the OC core, and the aluminium end-cup was secured to the plexiglass cylinder (**Fig. 8.16**).

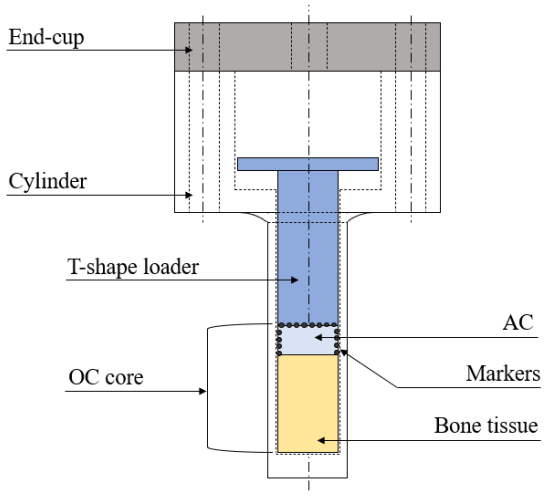

Fig. 8.16. Scheme of the setup employed to preliminary investigate the OC unit through µCT and markers.

The loading device containing the OC core was positioned inside µCT, and its vertical position was adjusted in order to include in the FoV the whole AC thickness and few millimetres of bone tissue. In this

regard, the FoV was set at 10 × 5 mm (width × height). The scanning protocol was the same as the one reported by paragraph 8.2.4, employing a voxel size of 4.9 µm. Two repeated scans – each lasted for ~ 40 minutes – were performed, without repositioning neither the loading device within the µCT system, nor the OC core within the loading device. The images were reconstructed according to the steps reported by paragraph 8.2.7. The analysis focused on gray-level images, subsampled by a ×2 factor, i.e., obtaining a virtual voxel size of 9.8 µm.

A circular binary mask – image with value one inside, and zero elsewhere – was created and expanded to images full height, aiming to reduce the DVC computational time. Therefore, ShIRT algorithm was applied to the two 3D images – without performing any preliminary registration – in order to compute the field of displacements. Processing of DVC output was computed according to paragraph 8.2.11. Therefore, the trend of the Cartesian components of the displacements – X-disp (µm), Y-disp (µm), and Z-disp (µm) – and their relative deviation – sdX-disp (µm), sdY-disp (µm), sdZ-disp (µm) – through the height of the scanned volume was investigated to detect changes based on the tissue or material – i.e., bone, AC, grease-ash mixture – and transition between them. In addition, sdX-disp (µm), sdY-disp (µm), sdZ-disp (µm) were computed for each value of NS between 49 µm – 10 voxels of the resolution scans – and 490 µm – 100 voxels –, in order to better investigate DVC precision.

The images highlighted a quite regular distribution of the silicon-based grease and bone ash over the AC surfaces (**Fig. 8.17**); nevertheless, the mixture over the lateral side of AC was very thin.

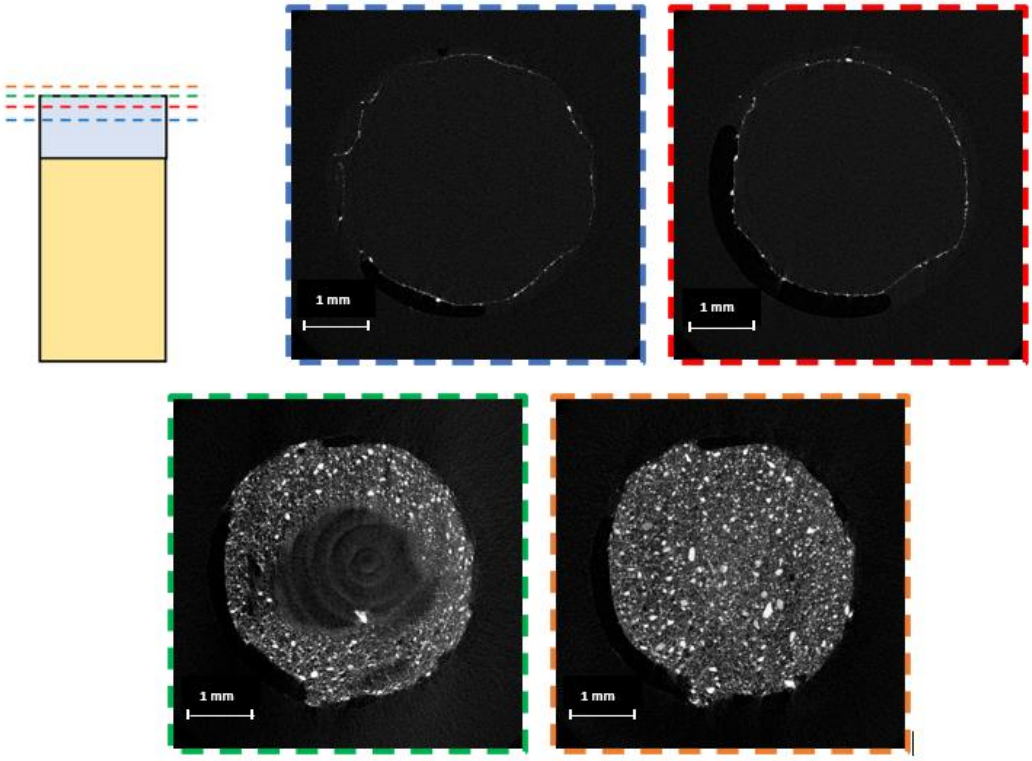

Fig. 8.17. Reconstructed µCT images highlighting the distribution – along the vertical direction of the sample – of the silicon-based grease and bone ash mixture over the OC core AC surfaces.

ShIRT algorithm allowed to compute the Cartesian components of displacements all over the OC core (**Fig. 8.18**, **8.19**, and **8.20**). Nevertheless, and regardless the displacement component, the markers layer on the AC lateral surface appears not to be detected, even considering the smaller voxel size employed – i.e., NS of 49 µm.

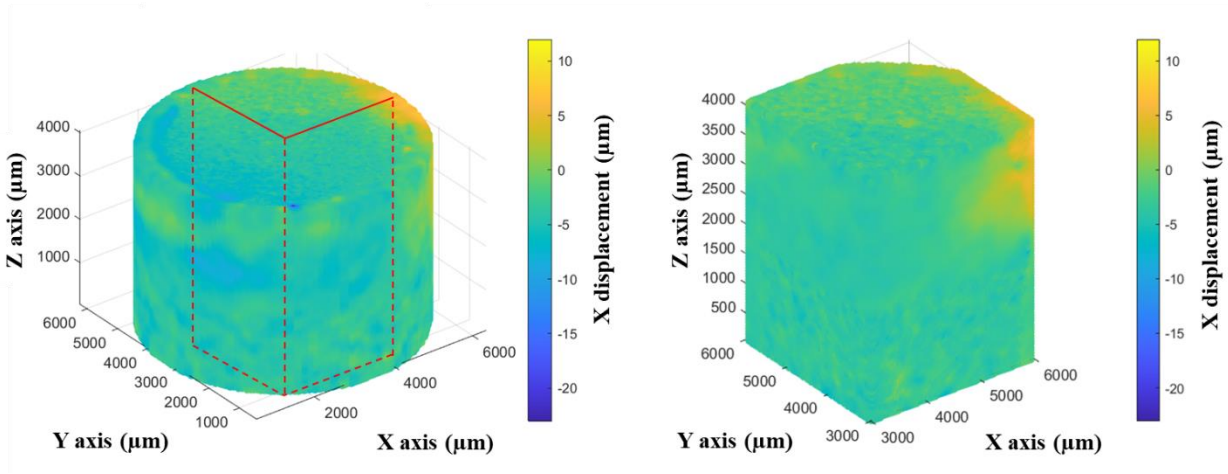

Fig. 8.18. X-displacement computed by ShIRT – with a NS of 49 µm – within the OC core. (Left) Markers seem not visible on the AC lateral surface, but on the top surface of the tissue. (Right) A recognizable pattern is highlighted in correspondence of the bone tissue and on the AC top surface – due to the presence of markers – but, as expected, no distinctive pattern is visible within AC volume.

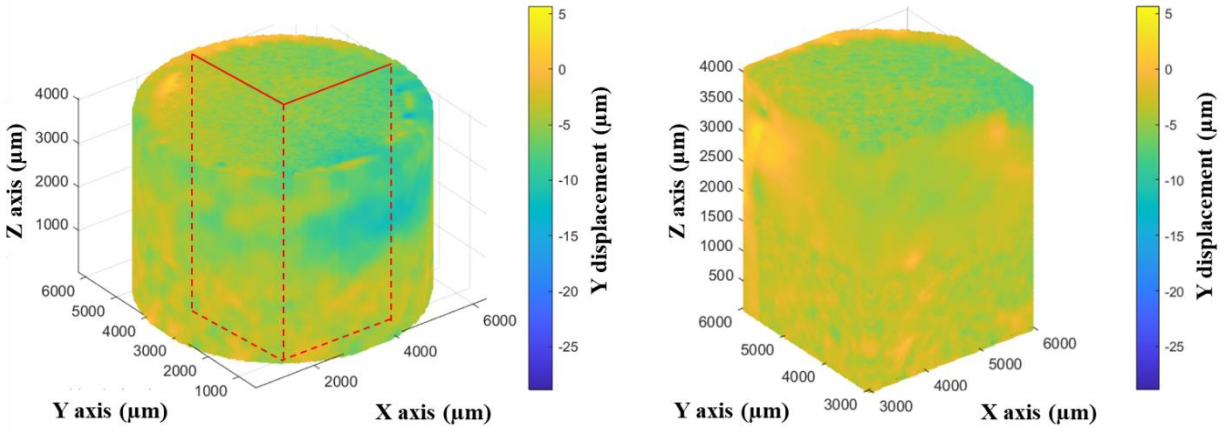

Fig. 8.19. Y-displacement computed by ShIRT – with a NS of 49 µm – within the OC core. (Left) Markers seem not visible on the AC lateral surface, but on the top surface of the tissue. (Right) A recognizable pattern is highlighted in correspondence of the bone tissue and on the AC top surface – due to the presence of markers – but, as expected, no distinctive pattern is visible within AC volume.

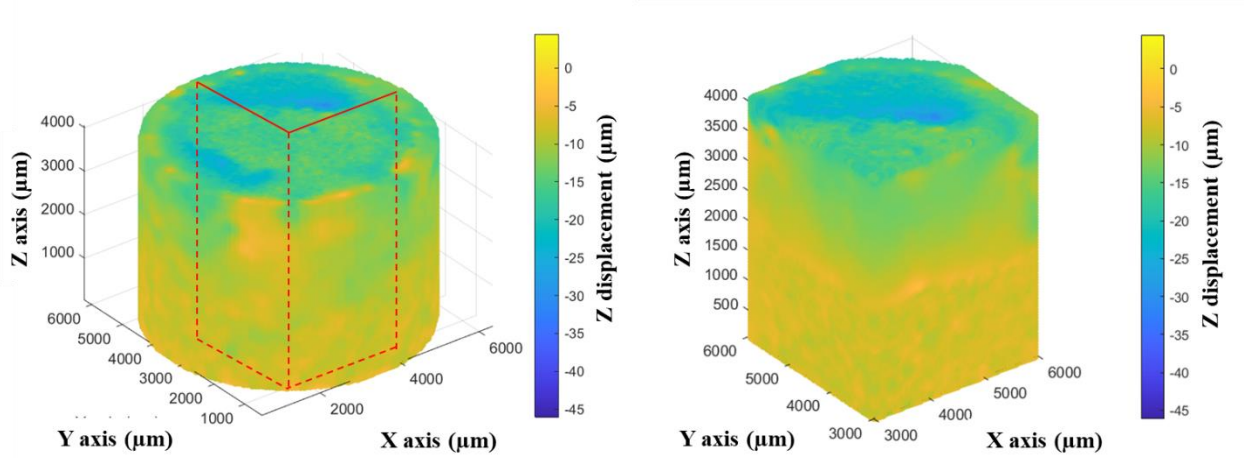

Fig. 8.20. Z-displacement computed by ShIRT – with a NS of 49 µm – within the OC core. (Left) Markers seem not visible on the AC lateral surface, but on the top surface of the tissue. (Right) A recognizable pattern is highlighted in correspondence of the bone tissue and on the AC top surface – due to the presence of markers – but, as expected, no distinctive pattern is visible within AC volume.

Concerning the trend of the displacement Cartesian components within the scanned volume, X-disp and Y-disp resulted almost independent of the depth (**Fig. 8.21**). Conversely, a progressive increase of Z-disp was highlighted moving from the bone tissue to AC/markers, and from the latter to pure markers (**Fig. 8.21**). In terms of standard deviation of the displacement Cartesian components, an increase of their extent was highlighted up to the transition between AC/ markers and pure markers, after which in-plane – i.e., X- and Y-disp – and axial – Z-disp – components diverging paths followed (**Fig. 8.22**). The trends of displacements and of their standard deviation resulted independent of the NS (data not reported).

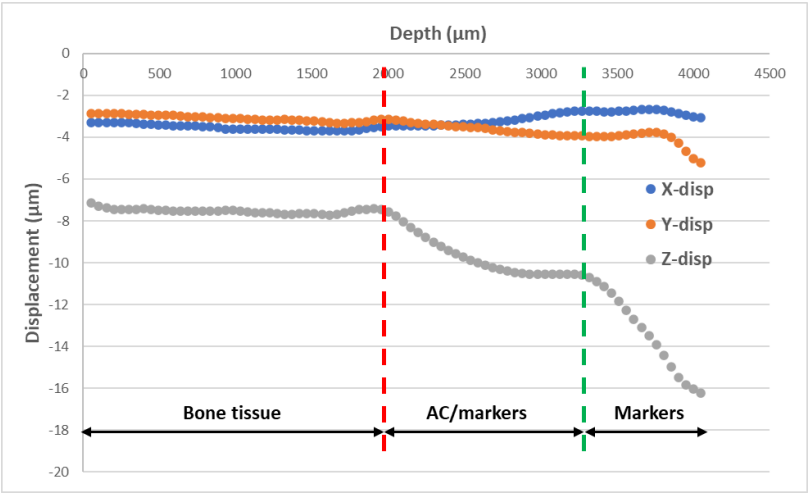

Fig. 8.21. Trend of the Cartesian components of the displacements – for a NS of 49 µm – within the OC core scanned volume. The red dotted line points the transition between bone and AC/markers.

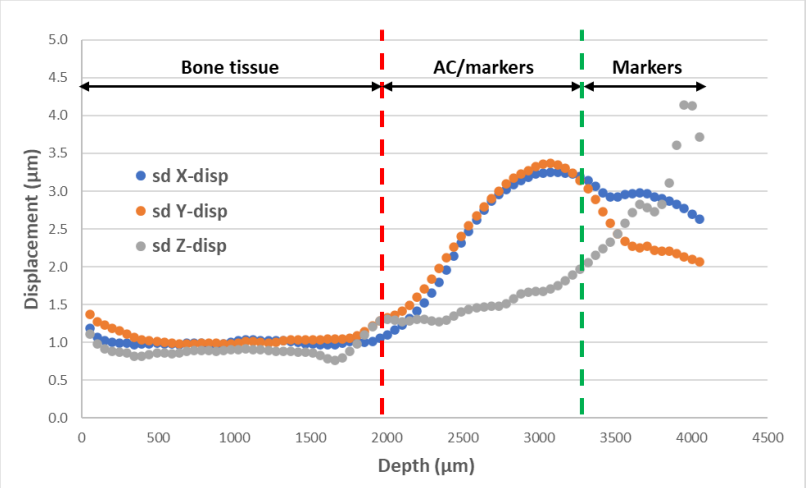

Fig. 8.22. Trend of the standard deviation of the Cartesian components of the displacements – for a NS of NS to 49 µm – within the OC core scanned volume. The red dotted line points the transition between bone and AC/markers.

DVC precision for the in-plane displacements increased with increasing NS, reaching a minimum in correspondence of 488 µm (**Fig. 8.23**). Conversely, the highest precision in computing the axial displacement was obtained in correspondence of a local minimum, i.e., NS equal to 293 µm (**Fig. 8.23**).

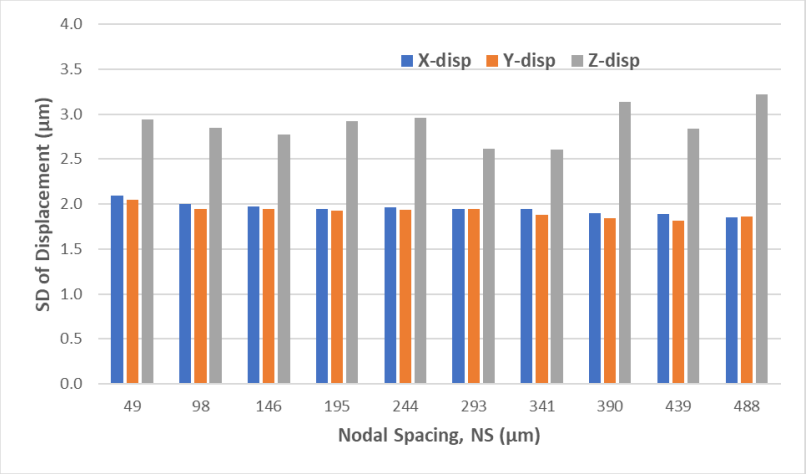

Fig. 8.23. Variation of DVC precision as a function of Nodal Spacing, NS, in terms of standard deviation of the Cartesian displacement (sdX-disp, sdY-disp, and sdZ-disp).

According to the preliminary results achieved, a decrease of DVC precision was highlighted in correspondence of the AC covered by markers. More in detail, DVC precision was reduced up to a ×3 factor, regardless of the displacement component. Such a worsening might be ascribed firstly to motion-artifacts of the bone ash particles, possibly related to a progressive softening of the silicon-based grease as

a consequence of the X-ray exposure. Moreover, the markers layer on the AC lateral surface might be not thick enough to allow a local convergence of ShIRT algorithm – as highlighted by **Fig. 8.18**, **8.19** and **8.20** –, enhancing the inaccuracy of the displacement computation in such regions. A modification of the loading device – i.e., by increasing the inner diameter in correspondence of which the AC of the OC core is located – could allow to spread a thicker layer of markers. Alternative solutions in terms of constraining markers on the AC outer surfaces might be also explored, e.g., by using glue or, conversely, a radiopaque staining.

An additional drawback of the proposed approach lies in the absence of information achievable about the field of displacements within AC. To partially overcome this issue, DVC outputs retrieved by employing markers on the AC outer surfaces might be coupled with Finite Element Models, e.g., by using the computed displacments as boundary conditions guiding the response of the full AC thickness to external loads.

8.6.2 Exploratory approach based on Phase-Contrast imaging

The second attempt of applying DVC to the OC unit employed Phase-Contrast imaging. This approach was considered due to the evidence retrieved by previous studies focusing on the interface between AC and bone tissue [262,268]. More in detail, such approaches exploited the natural tissue texture created by hypertrophic chondrocytes in the calcified cartilage as pattern to enhance cartilage detection and, therefore, to provide a more reliable information about the displacements and strains field within it.

Within this trial, the approach started by using the setup previously employed (see paragraph 8.6.1). In this case, after the 2 hours of defrosting at room temperature (20 °C) a bovine knee OC core (5-mm in diameter, 15-mm in height) was placed straight within the plexiglass cylinder of the loading device, without employing markers. Once the remaining steps were completed – i.e., positioning of the T-shape loader over the AC top surface, pouring of PBS, and securing the end-cup – the loading device was placed within the Phase-Contrast device (Xradia 620 Versa, Zeiss) taking care to center its position respect to both the source (**Fig. 8.24 left**) and the detector (**Fig. 8.24 right**).

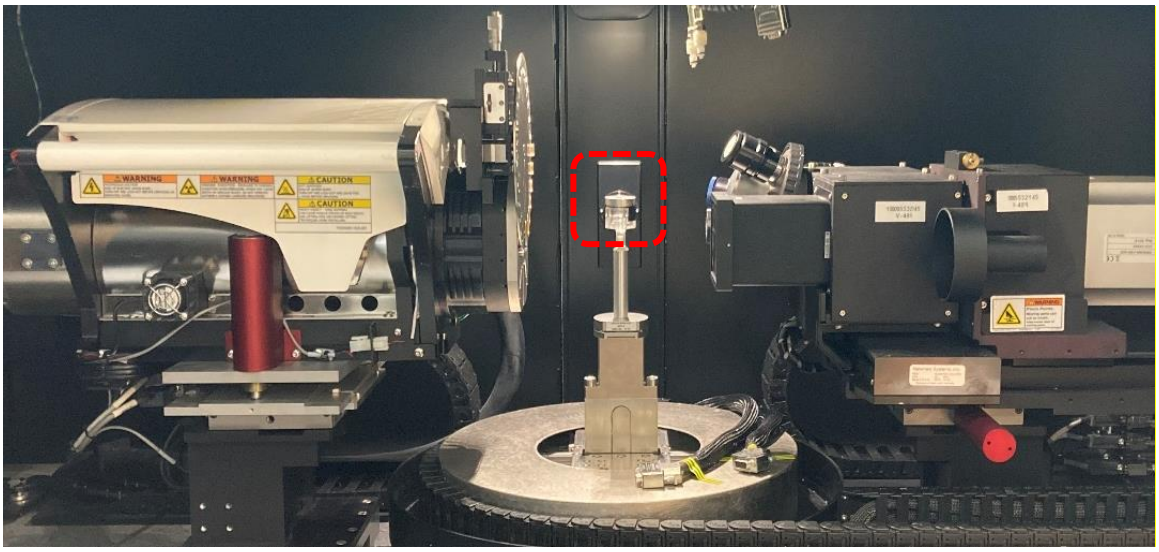

Fig. 8.24. The loading device containing the OC core (red square) within the Phase-Contrast device.

Therefore, the source-to-object and object-to-detector distances – SOD and ODD, respectively – were minimized in absorption to reduce the subsequent distances in propagation. More in detail, the minimum SOD and ODD achievable in absorption resulted 23 mm and 55 mm, respectively. By using such a setting and, moreover, the following scanning protocol – i.e., 2 µm resolution, 2 mm × 2 mm FoV, 40 keV – 3 W energy, 3001 projections [268] and, consequently, an optimal exposure time of 20 sec – a single scan in absorption would have lasted approximately ~ 24 hours. Therefore, the scanning time for propagation distances of 2×, 3×, and 4× resulted about ~ (61 ÷ 74) hours, ~ (124 ÷ 174) hours, and ~ (180 ÷ 214) hours, respectively. Such a timing was considered excessive, especially in the perspective of performing a zero-strain study, which requires two consecutive scans.

With the purpose of reducing the scanning time, the loading device was replaced in favour of a 0.2 ml eppendorf. Thank to this solution, SOD and ODD in absorption were reduced down to 13 mm and 31 mm, respectively. By setting the acquisition protocol above reported – in this case with 2400 projections, and 5 sec exposure time – a single scan in absorption would have lasted approximately ~ 7 hours, with a consequent scanning time at a propagation distance of 2× approximately of ~ 14 hours. Nevertheless – and considering that the latter setup would have not allowed to perform a loading study on the OC unit – no further activities were performed.

This explorative approach employing Phase-Contrast imaging towards the study of the OC unit by DVC allowed to retrieve the following evidence. Phase-Contrast requires minimal SOD and ODD in order to reduce the scanning time. In this perspective, the loading device developed within this dissertation not represent a suitable option due to its excessive size. Despite reducing the overall dimension of the device might be an option – but the diameter of miniature load cells is hardly below 10 mm, as the one employed in this dissertation (see paragraph 8.2.3) –, this would require to reduce also the size of the OC sample. With the perspective of studying the comprehensive mechanical response of the OC unit, evaluating and testing samples with a diameter lower than 5-mm could produce findings strongly dependent on the local microstructure of the OC tissues – in particular considering the bone tissues – and eventually not related to a tissue-level biomechanics.

The scanning time of Phase-Contrast imaging is also a crucial point in the evaluation of biological tissues, especially considering that performing a DVC study – both considering zero-strain and loading conditions – would require at least two different images. Therefore, and especially considering the perspective of studying pathological tissues to deepen the knowledge about the impact of diseases on the OC unit biomechanics – a progressive degradation of the tissues might occur through the scanning time.

Overall, these evidence highlight the need for careful planning research employing Phase-Contrast images as input to DVC aiming to evaluate the comprehensive mechanical response of the OC unit. Limiting X-ray exposure by employing staining or contrast agents could represent an option to reduce the scanning time and, therefore, to better preserve tissue integrity.

9 Summary and Conclusions

In this thesis, a multidisciplinary framework based on experimental techniques was developed with the purpose of providing sound information about the features of the articular cartilage (AC). Preliminary correlations between AC mechanical properties and quantitative parameters related to both structure and composition of the tissue were investigated. To achieve these targets, approaches based on mechanical testing, i.e., indentation, and experimental signalling and imaging – i.e., single-sided Nuclear Magnetic Resonance and contrast-enhanced X-ray micro-Computed Tomography, respectively – were implemented and employed. Moving toward a comprehensive assessment of the osteochondral (OC) unit, the potential of a contrast agent affine to AC structure was investigated. Last, the eligibility of a full-field X-ray-based approach to study the mechanical behaviour of the OC unit was assessed. The main conclusions of this thesis can be summarized as follows:

1. In evaluating the mechanical response of AC through experimental techniques, first it is mandatory to elucidate eventual effect of the main parameters defining the testing protocol. By focusing on indentation approach and aiming to map the mechanical response of AC on articular surfaces, the spatial resolution must be properly defined to avoid bias on the results induced by mutual influence between nearby indentations. Furthermore, applying a testing protocol based on nominal deformation and by employing a 6-mm spherical indenter allows to reduce data dispersion and to avoid bias in the estimate of AC elastic behaviour. This finding can be crucial aiming to provide reliable data that could be compared with both those retrieved by other studies focusing on AC mechanical response, and with the ones of composite scaffolds suitable to treat diseases of AC and, more widely, of the OC unit.

2. Regarding the study of the deep relationship between the mechanical behaviour of AC and its structure, the assessment of the last one should be performed through approaches allowing a depth-dependent evaluation, e.g., single-sided Nuclear Magnetic Resonance, thus highlighting the heterogeneity of the tissue structure. A further step should consist in combining properly the parameters retrieved by depth-dependent approaches, with the purpose of providing quantitative and comprehensive metrics describing the features of AC.

3. In considering the use of contrast agents specific to AC – e.g., cationic, iodine-based contrast agent electrostatically attracted to proteoglycans – towards diagnostic and biomechanical purposes, eventual effect induced by exposing the tissue to such contrast agents must be investigated, thus to avoid first clinical complications and, second, bias on the achieved findings.

4. Before considering the application of full-field techniques, i.e., Digital Volume Correlation, to investigate the mechanical behaviour of biological structures – as the OC unit –, it is essential to evaluate their suitability. In this regard, such evaluations must be performed by considering samples and testing protocols recreating scenarios close to the in vivo conditions peculiar of the tissues of interest.

This thesis provided experimental methods and analysis protocols allowing to retrieve reliable information about the features of AC, specifically by considering approaches not available or poorly explored by the relative literature. As main benefit, the insights highlighted by this thesis can deepen the knowledge about how the structure and composition of AC are related to the mechanical behaviour of the tissue. As a secondary gain, the experimental framework developed herein could be potentially extended to study the entire OC unit, with the purpose of elucidating its comprehensive response and, foremost, how degenerative pathologies impair the features of OC unit and the relationship between them. Third, the findings related to the mechanical response and the structure of AC retrieved by this thesis could drive tissue engineering efforts toward the development of scaffolds better mimicking the response of the tissue. Last, a multidisciplinary approach combining mechanical, structural, and compositional assessments as the one proposed by this thesis could improve the diagnosis of early osteoarthritis – eventually enhancing the current grading systems of such a pathology –, moreover representing a suitable framework to investigate the efficacy and the reliability of treatments responding to pathologies that impair the OC unit.

10 References

1. McMahon, L.; O'Brien, F.; Prendergast, P. Biomechanics and Mechanobiology in Osteochondral Tissues. *Regenerative Medicine* **2008**, *3*, 743–759, doi:10.2217/17460751.3.5.743.

2. Boi, M.; Marchiori, G.; Berni, M.; Gambardella, A.; Salamanna, F.; Visani, A.; Bianchi, M.; Fini, M.; Filardo, G. Nanoindentation: An Advanced Procedure to Investigate Osteochondral Engineered Tissues. *Journal of the Mechanical Behavior of Biomedical Materials* **2019**, *96*, 79–87, doi:10.1016/j.jmbbm.2019.04.042.

3. Trickey, W.R.; Vail, T.P.; Guilak, F. The Role of the Cytoskeleton in the Viscoelastic Properties of Human Articular Chondrocytes. *J Orthop Res* **2004**, *22*, 131–139, doi:10.1016/S0736-0266(03)00150-5.

4. Sophia Fox, A.J.; Bedi, A.; Rodeo, S.A. The Basic Science of Articular Cartilage: Structure, Composition, and Function. *Sports Health* **2009**, *1*, 461–468, doi:10.1177/1941738109350438.

5. Carter, D.R.; Blenman, P.R.; Beaupré, G.S. Correlations between Mechanical Stress History and Tissue Differentiation in Initial Fracture Healing. *J Orthop Res* **1988**, *6*, 736–748, doi:10.1002/jor.1100060517.

6. Teichtahl, A.J.; Wluka, A.E.; Wijethilake, P.; Wang, Y.; Ghasem-Zadeh, A.; Cicuttini, F.M. Wolff's Law in Action: A Mechanism for Early Knee Osteoarthritis. *Arthritis Res Ther* **2015**, *17*, 207, doi:10.1186/s13075-015-0738-7.

7. Leong, D.J.; Hardin, J.A.; Cobelli, N.J.; Sun, H.B. Mechanotransduction and Cartilage Integrity. *Ann N Y Acad Sci* **2011**, *1240*, 32–37, doi:10.1111/j.1749-6632.2011.06301.x.

8. Oliveira Silva, M.; Gregory, J.L.; Ansari, N.; Stok, K.S. Molecular Signaling Interactions and Transport at the Osteochondral Interface: A Review. *Front Cell Dev Biol* **2020**, *8*, 750, doi:10.3389/fcell.2020.00750.

9. Long, H.; Liu, Q.; Yin, H.; Wang, K.; Diao, N.; Zhang, Y.; Lin, J.; Guo, A. Prevalence Trends of Site-Specific Osteoarthritis From 1990 to 2019: Findings From the Global Burden of Disease Study 2019. *Arthritis & Rheumatology* **2022**, *74*, 1172–1183, doi:10.1002/art.42089.

10. Sharma, A.R.; Jagga, S.; Lee, S.-S.; Nam, J.-S. Interplay between Cartilage and Subchondral Bone Contributing to Pathogenesis of Osteoarthritis. *Int J Mol Sci* **2013**, *14*, 19805–19830, doi:10.3390/ijms141019805.

11. Kloppenburg, M.; Berenbaum, F. Osteoarthritis Year in Review 2019: Epidemiology and Therapy. *Osteoarthritis Cartilage* **2020**, *28*, 242–248, doi:10.1016/j.joca.2020.01.002.

12. Mandl, L.A. Osteoarthritis Year in Review 2018: Clinical. *Osteoarthritis Cartilage* **2019**, *27*, 359–364, doi:10.1016/j.joca.2018.11.001.

13. Peters, A.E.; Akhtar, R.; Comerford, E.J.; Bates, K.T. The Effect of Ageing and Osteoarthritis on the Mechanical Properties of Cartilage and Bone in the Human Knee Joint. *Sci Rep* **2018**, *8*, 5931, doi:10.1038/s41598-018-24258-6.

14. Belluzzi, E.; Todros, S.; Pozzuoli, A.; Ruggieri, P.; Carniel, E.L.; Berardo, A. Human Cartilage Biomechanics: Experimental and Theoretical Approaches towards the Identification of Mechanical Properties in Healthy and Osteoarthritic Conditions. *Processes* **2023**, *11*, 1014, doi:10.3390/pr11041014.

15. Korhonen, R.K.; Laasanen, M.S.; Töyräs, J.; Rieppo, J.; Hirvonen, J.; Helminen, H.J.; Jurvelin, J.S. Comparison of the Equilibrium Response of Articular Cartilage in Unconfined Compression, Confined Compression and Indentation. *J Biomech* **2002**, *35*, 903–909, doi:10.1016/s0021-9290(02)00052-0.

16. Vaienti, E.; Scita, G.; Ceccarelli, F.; Pogliacomi, F. Understanding the Human Knee and Its Relationship to Total Knee Replacement. *Acta Biomed* **2017**, *88*, 6–16, doi:10.23750/abm.v88i2-S.6507.

17. Welsch, M.A.; Williams, P.A.; Pollock, M.L.; Graves, J.E.; Foster, D.N.; Fulton, M.N. Quantification of Full-Range-of-Motion Unilateral and Bilateral Knee Flexion and Extension Torque Ratios. *Arch Phys Med Rehabil* **1998**, *79*, 971–978, doi:10.1016/s0003-9993(98)90097-1.

18. Tecklenburg, K.; Dejour, D.; Hoser, C.; Fink, C. Bony and Cartilaginous Anatomy of the Patellofemoral Joint. *Knee Surg Sports Traumatol Arthrosc* **2006**, *14*, 235–240, doi:10.1007/s00167-005-0683-0.

19. Sherman, S.L.; Plackis, A.C.; Nuelle, C.W. Patellofemoral Anatomy and Biomechanics. *Clin Sports Med* **2014**, *33*, 389–401, doi:10.1016/j.csm.2014.03.008.

20. Mow, V.C.; Ratcliffe, A.; Poole, A.R. Cartilage and Diarthrodial Joints as Paradigms for Hierarchical Materials and Structures. *Biomaterials* **1992**, *13*, 67–97, doi:10.1016/0142-9612(92)90001-5.

21. Asahara, H.; Inui, M.; Lotz, M.K. Tendons and Ligaments: Connecting Developmental Biology to Musculoskeletal Disease Pathogenesis. *J Bone Miner Res* **2017**, *32*, 1773–1782, doi:10.1002/jbmr.3199.

22. Otake, N.; Chen, H.; Yao, X.; Shoumura, S. Morphologic Study of the Lateral and Medial Collateral Ligaments of the Human Knee. *Okajimas Folia Anat Jpn* **2007**, *83*, 115–122, doi:10.2535/ofaj.83.115.

23. Makris, E.A.; Hadidi, P.; Athanasiou, K.A. The Knee Meniscus: Structure-Function, Pathophysiology, Current Repair Techniques, and Prospects for Regeneration. *Biomaterials* **2011**, *32*, 7411–7431, doi:10.1016/j.biomaterials.2011.06.037.

24. Luczkiewicz, P.; Daszkiewicz, K.; Witkowski, W.; Chróścielewski, J.; Ferenc, T.; Baczkowski, B. The Influence of a Change in the Meniscus Cross-Sectional Shape on the Medio-Lateral Translation of the Knee Joint and Meniscal Extrusion. *PLoS One* **2018**, *13*, e0193020, doi:10.1371/journal.pone.0193020.

25. Morejon, A.; Mantero, A.M.A.; Best, T.M.; Jackson, A.R.; Travascio, F. Mechanisms of Energy Dissipation and Relationship with Tissue Composition in Human Meniscus. *Osteoarthritis Cartilage* **2022**, *30*, 605–612, doi:10.1016/j.joca.2022.01.001.

26. Lepage, S.I.M.; Robson, N.; Gilmore, H.; Davis, O.; Hooper, A.; St John, S.; Kamesan, V.; Gelis, P.; Carvajal, D.; Hurtig, M.; et al. Beyond Cartilage Repair: The Role of the Osteochondral Unit in Joint Health and Disease. *Tissue Eng Part B Rev* **2019**, *25*, 114–125, doi:10.1089/ten.TEB.2018.0122.

27. Zhou, H.; Yuan, L.; Xu, Z.; Yi, X.; Wu, X.; Mu, C.; Ge, L.; Li, D. Mimicking the Composition and Structure of the Osteochondral Tissue to Fabricate a Heterogeneous Three-Layer Scaffold for the Repair of Osteochondral Defects. *ACS Appl Bio Mater* **2022**, *5*, 734–746, doi:10.1021/acsabm.1c01152.

28. Wang, W.; Ye, R.; Xie, W.; Zhang, Y.; An, S.; Li, Y.; Zhou, Y. Roles of the Calcified Cartilage Layer and Its Tissue Engineering Reconstruction in Osteoarthritis Treatment. *Front Bioeng Biotechnol* **2022**, *10*, 911281, doi:10.3389/fbioe.2022.911281.

29. Arkill, K.P.; Winlove, C.P. Solute Transport in the Deep and Calcified Zones of Articular Cartilage. *Osteoarthritis Cartilage* **2008**, *16*, 708–714, doi:10.1016/j.joca.2007.10.001.

30. Radin, E.L.; Rose, R.M. Role of Subchondral Bone in the Initiation and Progression of Cartilage Damage. *Clin Orthop Relat Res* **1986**, 34–40.

31. Burr, D.B.; Gallant, M.A. Bone Remodelling in Osteoarthritis. *Nat Rev Rheumatol* **2012**, *8*, 665–673, doi:10.1038/nrrheum.2012.130.

32. Stewart, H.L.; Kawcak, C.E. The Importance of Subchondral Bone in the Pathophysiology of Osteoarthritis. *Front Vet Sci* **2018**, *5*, 178, doi:10.3389/fvets.2018.00178.

33. Wang, F.; Metzner, F.; Osterhoff, G.; Zheng, L.; Schleifenbaum, S. The Role of Bone Marrow on the Mechanical Properties of Trabecular Bone: A Systematic Review. *BioMed Eng OnLine* **2022**, *21*, 80, doi:10.1186/s12938-022-01051-1.

34. Oftadeh, R.; Perez-Viloria, M.; Villa-Camacho, J.C.; Vaziri, A.; Nazarian, A. Biomechanics and Mechanobiology of Trabecular Bone: A Review. *J Biomech Eng* **2015**, *137*, 0108021–01080215, doi:10.1115/1.4029176.

35. Sanchez-Adams, J.; Leddy, H.A.; McNulty, A.L.; O'Conor, C.J.; Guilak, F. The Mechanobiology of Articular Cartilage: Bearing the Burden of Osteoarthritis. *Curr Rheumatol Rep* **2014**, *16*, 451, doi:10.1007/s11926-014-0451-6.

36. Solanki, K.; Shanmugasundaram, S.; Shetty, N.; Kim, S.-J. Articular Cartilage Repair & Joint Preservation: A Review of the Current Status of Biological Approach. *J Clin Orthop Trauma* **2021**, *22*, 101602, doi:10.1016/j.jcot.2021.101602.

37. Bhosale, A.M.; Richardson, J.B. Articular Cartilage: Structure, Injuries and Review of Management. *Br Med Bull* **2008**, *87*, 77–95, doi:10.1093/bmb/ldn025.

38. Ateshian, G.A. The Role of Interstitial Fluid Pressurization in Articular Cartilage Lubrication. *J Biomech* **2009**, *42*, 1163–1176, doi:10.1016/j.jbiomech.2009.04.040.

39. Akkiraju, H.; Nohe, A. Role of Chondrocytes in Cartilage Formation, Progression of Osteoarthritis and Cartilage Regeneration. *J Dev Biol* **2015**, *3*, 177–192, doi:10.3390/jdb3040177.

40. Archer, C.W.; Francis-West, P. The Chondrocyte. *Int J Biochem Cell Biol* **2003**, *35*, 401–404, doi:10.1016/s1357-2725(02)00301-1.

41. Stockwell, R.A. Chondrocytes. *J Clin Pathol Suppl (R Coll Pathol)* **1978**, *12*, 7–13.

42. Schumacher, B.L.; Block, J.A.; Schmid, T.M.; Aydelotte, M.B.; Kuettner, K.E. A Novel Proteoglycan Synthesized and Secreted by Chondrocytes of the Superficial Zone of Articular Cartilage. *Arch Biochem Biophys* **1994**, *311*, 144–152, doi:10.1006/abbi.1994.1219.

43. Klein, T.J.; Chaudhry, M.; Bae, W.C.; Sah, R.L. Depth-Dependent Biomechanical and Biochemical Properties of Fetal, Newborn, and Tissue-Engineered Articular Cartilage. *J Biomech* **2007**, *40*, 182–190, doi:10.1016/j.jbiomech.2005.11.002.

44. Roughley, P.J. The Structure and Function of Cartilage Proteoglycans. *Eur Cell Mater* **2006**, *12*, 92–101, doi:10.22203/ecm.v012a11.

45. Gao, Y.; Liu, S.; Huang, J.; Guo, W.; Chen, J.; Zhang, L.; Zhao, B.; Peng, J.; Wang, A.; Wang, Y.; et al. The ECM-Cell Interaction of Cartilage Extracellular Matrix on Chondrocytes. *Biomed Res Int* **2014**, *2014*, 648459, doi:10.1155/2014/648459.

46. Shoulders, M.D.; Raines, R.T. Collagen Structure and Stability. *Annu Rev Biochem* **2009**, *78*, 929–958, doi:10.1146/annurev.biochem.77.032207.120833.

47. Wu, Z.; Korntner, S.H.; Mullen, A.M.; Zeugolis, D.I. Collagen Type II: From Biosynthesis to Advanced Biomaterials for Cartilage Engineering. *Biomater Biosyst* **2021**, *4*, 100030, doi:10.1016/j.bbiosy.2021.100030.

48. Alcaide-Ruggiero, L.; Molina-Hernández, V.; Granados, M.M.; Domínguez, J.M. Main and Minor Types of Collagens in the Articular Cartilage: The Role of Collagens in Repair Tissue Evaluation in Chondral Defects. *Int J Mol Sci* **2021**, *22*, 13329, doi:10.3390/ijms222413329.

49. Hosseininia, S.; Weis, M.A.; Rai, J.; Kim, L.; Funk, S.; Dahlberg, L.E.; Eyre, D.R. Evidence for Enhanced Collagen Type III Deposition Focally in the Territorial Matrix of Osteoarthritic Hip Articular Cartilage. *Osteoarthritis Cartilage* **2016**, *24*, 1029–1035, doi:10.1016/j.joca.2016.01.001.

50. Mow, V.C.; Kuei, S.C.; Lai, W.M.; Armstrong, C.G. Biphasic Creep and Stress Relaxation of Articular Cartilage in Compression? Theory and Experiments. *J Biomech Eng* **1980**, *102*, 73–84, doi:10.1115/1.3138202.

51. LeRoux, M.A.; Arokoski, J.; Vail, T.P.; Guilak, F.; Hyttinen, M.M.; Kiviranta, I.; Setton, L.A. Simultaneous Changes in the Mechanical Properties, Quantitative Collagen Organization, and Proteoglycan Concentration of Articular Cartilage Following Canine Meniscectomy. *J Orthop Res* **2000**, *18*, 383–392, doi:10.1002/jor.1100180309.

52. Bruckner, P.; van der Rest, M. Structure and Function of Cartilage Collagens. *Microsc Res Tech* **1994**, *28*, 378–384, doi:10.1002/jemt.1070280504.

53. Korhonen, R.K.; Laasanen, M.S.; Töyräs, J.; Lappalainen, R.; Helminen, H.J.; Jurvelin, J.S. Fibril Reinforced Poroelastic Model Predicts Specifically Mechanical Behavior of Normal, Proteoglycan Depleted and Collagen Degraded Articular Cartilage. *J Biomech* **2003**, *36*, 1373–1379, doi:10.1016/s0021-9290(03)00069-1.

54. Korhonen, R.K.; Julkunen, P.; Wilson, W.; Herzog, W. Importance of Collagen Orientation and Depth-Dependent Fixed Charge Densities of Cartilage on Mechanical Behavior of Chondrocytes. *J Biomech Eng* **2008**, *130*, 021003, doi:10.1115/1.2898725.

55. Yeh, M.-L.; Luo, Z.-P. The Structure of Proteoglycan Aggregate Determined by Atomic Force Microscopy. *Scanning* **2004**, *26*, 273–276, doi:10.1002/sca.4950260604.

56. Yin, J.-H.; Xia, Y.; Ramakrishnan, N. Depth-Dependent Anisotropy of Proteoglycan in Articular Cartilage by Fourier Transform Infrared Imaging. *Vib Spectrosc* **2011**, *57*, 338–341, doi:10.1016/j.vibspec.2011.08.005.

57. Xia, Y.; Zheng, S.; Bidthanapally, A. Depth-Dependent Profiles of Glycosaminoglycans in Articular Cartilage by microMRI and Histochemistry. *J Magn Reson Imaging* **2008**, *28*, 151–157, doi:10.1002/jmri.21392.

58. Zimmerman, B.K.; Nims, R.J.; Chen, A.; Hung, C.T.; Ateshian, G.A. Direct Osmotic Pressure Measurements in Articular Cartilage Demonstrate Nonideal and Concentration-Dependent Phenomena. *J Biomech Eng* **2021**, *143*, 041007, doi:10.1115/1.4049158.

59. Mow, V.C.; Holmes, M.H.; Lai, W.M. Fluid Transport and Mechanical Properties of Articular Cartilage: A Review. *J Biomech* **1984**, *17*, 377–394, doi:10.1016/0021-9290(84)90031-9.

60. Torzilli, P.A.; Mow, V.C. On the Fundamental Fluid Transport Mechanisms through Normal and Pathological Articular Cartilage during Function--I. The Formulation. *J Biomech* **1976**, *9*, 541–552, doi:10.1016/0021-9290(76)90071-3.

61. Soltz, M.A.; Ateshian, G.A. Interstitial Fluid Pressurization during Confined Compression Cyclical Loading of Articular Cartilage. *Ann Biomed Eng* **2000**, *28*, 150–159, doi:10.1114/1.239.

62. Maroudas, A.I. Balance between Swelling Pressure and Collagen Tension in Normal and Degenerate Cartilage. *Nature* **1976**, *260*, 808–809, doi:10.1038/260808a0.

63. Mäkelä, J.T.A.; Han, S.-K.; Herzog, W.; Korhonen, R.K. Very Early Osteoarthritis Changes Sensitively Fluid Flow Properties of Articular Cartilage. *Journal of Biomechanics* **2015**, *48*, 3369–3376, doi:10.1016/j.jbiomech.2015.06.010.

64. Klein, T.J.; Malda, J.; Sah, R.L.; Hutmacher, D.W. Tissue Engineering of Articular Cartilage with Biomimetic Zones. *Tissue Eng Part B Rev* **2009**, *15*, 143–157, doi:10.1089/ten.TEB.2008.0563.

65. Müller, C.; Khabut, A.; Dudhia, J.; Reinholt, F.P.; Aspberg, A.; Heinegård, D.; Önnerfjord, P. Quantitative Proteomics at Different Depths in Human Articular Cartilage Reveals Unique Patterns of Protein Distribution. *Matrix Biol* **2014**, *40*, 34–45, doi:10.1016/j.matbio.2014.08.013.

66. Youn, I.; Choi, J.B.; Cao, L.; Setton, L.A.; Guilak, F. Zonal Variations in the Three-Dimensional Morphology of the Chondron Measured in Situ Using Confocal Microscopy. *Osteoarthritis Cartilage* **2006**, *14*, 889–897, doi:10.1016/j.joca.2006.02.017.

67. Hoemann, C.D.; Lafantaisie-Favreau, C.-H.; Lascau-Coman, V.; Chen, G.; Guzmán-Morales, J. The Cartilage-Bone Interface. *J Knee Surg* **2012**, *25*, 85–97, doi:10.1055/s-0032-1319782.

68. Eggli, P.S.; Herrmann, W.; Hunziker, E.B.; Schenk, R.K. Matrix Compartments in the Growth Plate of the Proximal Tibia of Rats. *Anat Rec* **1985**, *211*, 246–257, doi:10.1002/ar.1092110304.

69. Guilak, F.; Mow, V.C. The Mechanical Environment of the Chondrocyte: A Biphasic Finite Element Model of Cell-Matrix Interactions in Articular Cartilage. *J Biomech* **2000**, *33*, 1663–1673.

70. Vincent, T.L.; McClurg, O.; Troeberg, L. The Extracellular Matrix of Articular Cartilage Controls the Bioavailability of Pericellular Matrix-Bound Growth Factors to Drive Tissue Homeostasis and Repair. *Int J Mol Sci* **2022**, *23*, 6003, doi:10.3390/ijms23116003.

71. Mow, V.C.; Guo, X.E. Mechano-Electrochemical Properties of Articular Cartilage: Their Inhomogeneities and Anisotropies. *Annu Rev Biomed Eng* **2002**, *4*, 175–209, doi:10.1146/annurev.bioeng.4.110701.120309.

72. Krishnan, Y.; Grodzinsky, A.J. Cartilage Diseases. *Matrix Biol* **2018**, *71–72*, 51–69, doi:10.1016/j.matbio.2018.05.005.

73. Li, Y.; Wei, X.; Zhou, J.; Wei, L. The Age-Related Changes in Cartilage and Osteoarthritis. *Biomed Res Int* **2013**, *2013*, 916530, doi:10.1155/2013/916530.

74. Moyad, T.F. Cartilage Injuries in the Adult Knee: Evaluation and Management. *Cartilage* **2011**, *2*, 226–236, doi:10.1177/1947603510383973.

75. Marchiori, G.; Berni, M.; Boi, M.; Filardo, G. Cartilage Mechanical Tests: Evolution of Current Standards for Cartilage Repair and Tissue Engineering. A Literature Review. *Clin Biomech (Bristol, Avon)* **2019**, *68*, 58–72, doi:10.1016/j.clinbiomech.2019.05.019.

76. Thomas, A.C.; Hubbard-Turner, T.; Wikstrom, E.A.; Palmieri-Smith, R.M. Epidemiology of Posttraumatic Osteoarthritis. *J Athl Train* **2017**, *52*, 491–496, doi:10.4085/1062-6050-51.5.08.

77. Altman, R.; Asch, E.; Bloch, D.; Bole, G.; Borenstein, D.; Brandt, K.; Christy, W.; Cooke, T.D.; Greenwald, R.; Hochberg, M. Development of Criteria for the Classification and Reporting of Osteoarthritis. Classification of Osteoarthritis of the Knee. Diagnostic and Therapeutic Criteria Committee of the American Rheumatism Association. *Arthritis Rheum* **1986**, *29*, 1039–1049, doi:10.1002/art.1780290816.

78. Martel-Pelletier, J.; Barr, A.J.; Cicuttini, F.M.; Conaghan, P.G.; Cooper, C.; Goldring, M.B.; Goldring, S.R.; Jones, G.; Teichtahl, A.J.; Pelletier, J.-P. Osteoarthritis. *Nat Rev Dis Primers* **2016**, *2*, 16072, doi:10.1038/nrdp.2016.72.

79. Hunter, D.J.; March, L.; Chew, M. Osteoarthritis in 2020 and beyond: A Lancet Commission. *Lancet* **2020**, *396*, 1711–1712, doi:10.1016/S0140-6736(20)32230-3.

80. Jin, Z.; Wang, D.; Zhang, H.; Liang, J.; Feng, X.; Zhao, J.; Sun, L. Incidence Trend of Five Common Musculoskeletal Disorders from 1990 to 2017 at the Global, Regional and National Level: Results from the Global Burden of Disease Study 2017. *Ann Rheum Dis* **2020**, *79*, 1014–1022, doi:10.1136/annrheumdis-2020-217050.

81. Wu, D.; Wong, P.; Guo, C.; Tam, L.-S.; Gu, J. Pattern and Trend of Five Major Musculoskeletal Disorders in China from 1990 to 2017: Findings from the Global Burden of Disease Study 2017. *BMC Med* **2021**, *19*, 34, doi:10.1186/s12916-021-01905-w.

82. Lieberthal, J.; Sambamurthy, N.; Scanzello, C.R. Inflammation in Joint Injury and Post-Traumatic Osteoarthritis. *Osteoarthritis Cartilage* **2015**, *23*, 1825–1834, doi:10.1016/j.joca.2015.08.015.

83. Pritzker, K.P.H.; Gay, S.; Jimenez, S.A.; Ostergaard, K.; Pelletier, J.-P.; Revell, P.A.; Salter, D.; van den Berg, W.B. Osteoarthritis Cartilage Histopathology: Grading and Staging. *Osteoarthritis Cartilage* **2006**, *14*, 13–29, doi:10.1016/j.joca.2005.07.014.

84. Waldstein, W.; Perino, G.; Gilbert, S.L.; Maher, S.A.; Windhager, R.; Boettner, F. OARSI Osteoarthritis Cartilage Histopathology Assessment System: A Biomechanical Evaluation in the Human Knee. *J Orthop Res* **2016**, *34*, 135–140, doi:10.1002/jor.23010.

85. Goldring, M.B. Articular Cartilage Degradation in Osteoarthritis. *HSS J* **2012**, *8*, 7–9, doi:10.1007/s11420-011-9250-z.

86. Singh, P.; Marcu, K.B.; Goldring, M.B.; Otero, M. Phenotypic Instability of Chondrocytes in Osteoarthritis: On a Path to Hypertrophy. *Ann N Y Acad Sci* **2019**, *1442*, 17–34, doi:10.1111/nyas.13930.

87. Bobinac, D.; Spanjol, J.; Zoricic, S.; Maric, I. Changes in Articular Cartilage and Subchondral Bone Histomorphometry in Osteoarthritic Knee Joints in Humans. *Bone* **2003**, *32*, 284–290, doi:10.1016/s8756-3282(02)00982-1.

88. James, C.B.; Uhl, T.L. A Review of Articular Cartilage Pathology and the Use of Glucosamine Sulfate. *J Athl Train* **2001**, *36*, 413–419.

89. Muir, H. The Chondrocyte, Architect of Cartilage. Biomechanics, Structure, Function and Molecular Biology of Cartilage Matrix Macromolecules. *Bioessays* **1995**, *17*, 1039–1048, doi:10.1002/bies.950171208.

90. Eschweiler, J.; Horn, N.; Rath, B.; Betsch, M.; Baroncini, A.; Tingart, M.; Migliorini, F. The Biomechanics of Cartilage-An Overview. *Life (Basel)* **2021**, *11*, 302, doi:10.3390/life11040302.

91. Lu, X.L.; Mow, V.C. Biomechanics of Articular Cartilage and Determination of Material Properties. *Med Sci Sports Exerc* **2008**, *40*, 193–199, doi:10.1249/mss.0b013e31815cb1fc.

92. Hayes, W.C.; Bodine, A.J. Flow-Independent Viscoelastic Properties of Articular Cartilage Matrix. *J Biomech* **1978**, *11*, 407–419, doi:10.1016/0021-9290(78)90075-1.

93. Klets, O.; Mononen, M.E.; Tanska, P.; Nieminen, M.T.; Korhonen, R.K.; Saarakkala, S. Comparison of Different Material Models of Articular Cartilage in 3D Computational Modeling of the Knee: Data from the Osteoarthritis Initiative (OAI). *J Biomech* **2016**, *49*, 3891–3900, doi:10.1016/j.jbiomech.2016.10.025.

94. Evans, N.D.; Gentleman, E. The Role of Material Structure and Mechanical Properties in Cell-Matrix Interactions. *J Mater Chem B* **2014**, *2*, 2345–2356, doi:10.1039/c3tb21604g.

95. Hayes, W.C.; Keer, L.M.; Herrmann, G.; Mockros, L.F. A Mathematical Analysis for Indentation Tests of Articular Cartilage. *J Biomech* **1972**, *5*, 541–551, doi:10.1016/0021-9290(72)90010-3.

96. Armstrong, C.G.; Lai, W.M.; Mow, V.C. An Analysis of the Unconfined Compression of Articular Cartilage. *J Biomech Eng* **1984**, *106*, 165–173, doi:10.1115/1.3138475.

97. Hayes, W.C.; Mockros, L.F. Viscoelastic Properties of Human Articular Cartilage. *J Appl Physiol* **1971**, *31*, 562–568, doi:10.1152/jappl.1971.31.4.562.

98. Fung, Y.-C. *Biomechanics*; Springer New York: New York, NY, 1993; ISBN 978-1-4419-3104-7.

99. June, R.K.; Fyhrie, D.P. A Comparison of Cartilage Stress-Relaxation Models in Unconfined Compression: QLV and Stretched Exponential in Combination with Fluid Flow. *Comput Methods Biomech Biomed Engin* **2013**, *16*, 565–576, doi:10.1080/10255842.2011.629612.

100. Holmes, M.H.; Lai, W.M.; Mow, V.C. Singular Perturbation Analysis of the Nonlinear, Flow-Dependent Compressive Stress Relaxation Behavior of Articular Cartilage. *J Biomech Eng* **1985**, *107*, 206–218, doi:10.1115/1.3138545.

101. Suh, J.-K.; Bai, S. Finite Element Formulation of Biphasic Poroviscoelastic Model for Articular Cartilage. *Journal of Biomechanical Engineering* **1998**, *120*, 195–201, doi:10.1115/1.2798302.

102. Lai, W.M.; Hou, J.S.; Mow, V.C. A Triphasic Theory for the Swelling and Deformation Behaviors of Articular Cartilage. *J Biomech Eng* **1991**, *113*, 245–258, doi:10.1115/1.2894880.

103. Huyghe, J.M.; Janssen, J.D. Quadriphasic Mechanics of Swelling Incompressible Porous Media. *International Journal of Engineering Science* **1997**, *35*, 793–802, doi:10.1016/S0020-7225(96)00119-X.

104. Soulhat, J.; Buschmann, M.D.; Shirazi-Adl, A. A Fibril-Network-Reinforced Biphasic Model of Cartilage in Unconfined Compression. *J Biomech Eng* **1999**, *121*, 340–347, doi:10.1115/1.2798330.

105. Baaijens, F.P.T.; Trickey, W.R.; Laursen, T.A.; Guilak, F. Large Deformation Finite Element Analysis of Micropipette Aspiration to Determine the Mechanical Properties of the Chondrocyte. *Ann Biomed Eng* **2005**, *33*, 494–501, doi:10.1007/s10439-005-2506-3.

106. Arduino, A.; Pettenuzzo, S.; Berardo, A.; Salomoni, V.A.; Majorana, C.; Carniel, E.L. A Continuum-Tensegrity Computational Model for Chondrocyte Biomechanics in AFM Indentation and Micropipette Aspiration. *Ann Biomed Eng* **2022**, *50*, 1911–1922, doi:10.1007/s10439-022-03011-1.

107. Patel, J.M.; Wise, B.C.; Bonnevie, E.D.; Mauck, R.L. A Systematic Review and Guide to Mechanical Testing for Articular Cartilage Tissue Engineering. *Tissue Eng Part C Methods* **2019**, *25*, 593–608, doi:10.1089/ten.TEC.2019.0116.

108. Gao, L.; Liu, G.; Tan, Y.; Li, R.; Zhang, C.; Gao, H.; Zhao, B. Creep-Recovery Behaviors of Articular Cartilage under Uniaxial and Biaxial Tensile Loadings. *Front Bioeng Biotechnol* **2022**, *10*, 1085062, doi:10.3389/fbioe.2022.1085062.

109. Ahsanizadeh, S.; Li, L. Strain-Rate-Dependent Non-Linear Tensile Properties of the Superficial Zone of Articular Cartilage. *Connect Tissue Res* **2015**, *56*, 469–476, doi:10.3109/03008207.2015.1066779.

110. Li, L.P.; Buschmann, M.D.; Shirazi-Adl, A. Strain-Rate Dependent Stiffness of Articular Cartilage in Unconfined Compression. *J Biomech Eng* **2003**, *125*, 161–168, doi:10.1115/1.1560142.

111. Brand, R.A. Joint Contact Stress: A Reasonable Surrogate for Biological Processes? *Iowa Orthop J* **2005**, *25*, 82–94.

112. Carter, T.E.; Taylor, K.A.; Spritzer, C.E.; Utturkar, G.M.; Taylor, D.C.; Moorman, C.T.; Garrett, W.E.; Guilak, F.; McNulty, A.L.; DeFrate, L.E. In Vivo Cartilage Strain Increases Following Medial Meniscal Tear and Correlates with Synovial Fluid Matrix Metalloproteinase Activity. *J Biomech* **2015**, *48*, 1461–1468, doi:10.1016/j.jbiomech.2015.02.030.

113. Liu, F.; Kozanek, M.; Hosseini, A.; Van de Velde, S.K.; Gill, T.J.; Rubash, H.E.; Li, G. In Vivo Tibiofemoral Cartilage Deformation during the Stance Phase of Gait. *J Biomech* **2010**, *43*, 658–665, doi:10.1016/j.jbiomech.2009.10.028.

114. Hosseini, A.; Van de Velde, S.K.; Kozanek, M.; Gill, T.J.; Grodzinsky, A.J.; Rubash, H.E.; Li, G. In-Vivo Time-Dependent Articular Cartilage Contact Behavior of the Tibiofemoral Joint. *Osteoarthritis Cartilage* **2010**, *18*, 909–916, doi:10.1016/j.joca.2010.04.011.

115. Huang, C.Y.; Mow, V.C.; Ateshian, G.A. The Role of Flow-Independent Viscoelasticity in the Biphasic Tensile and Compressive Responses of Articular Cartilage. *J Biomech Eng* **2001**, *123*, 410–417, doi:10.1115/1.1392316.

116. Chan, D.D.; Cai, L.; Butz, K.D.; Trippel, S.B.; Nauman, E.A.; Neu, C.P. In Vivo Articular Cartilage Deformation: Noninvasive Quantification of Intratissue Strain during Joint Contact in the Human Knee. *Sci Rep* **2016**, *6*, 19220, doi:10.1038/srep19220.

117. Bursać, P.M.; Obitz, T.W.; Eisenberg, S.R.; Stamenović, D. Confined and Unconfined Stress Relaxation of Cartilage: Appropriateness of a Transversely Isotropic Analysis. *J Biomech* **1999**, *32*, 1125–1130, doi:10.1016/s0021-9290(99)00105-0.

118. Gannon, A.R.; Nagel, T.; Kelly, D.J. The Role of the Superficial Region in Determining the Dynamic Properties of Articular Cartilage. *Osteoarthritis Cartilage* **2012**, *20*, 1417–1425, doi:10.1016/j.joca.2012.08.005.

119. Sim, S.; Chevrier, A.; Garon, M.; Quenneville, E.; Lavigne, P.; Yaroshinsky, A.; Hoemann, C.D.; Buschmann, M.D. Electromechanical Probe and Automated Indentation Maps Are Sensitive Techniques in Assessing Early Degenerated Human Articular Cartilage. *J Orthop Res* **2017**, *35*, 858–867, doi:10.1002/jor.23330.

120. Hamsayeh Abbasi Niasar, E.; Li, L.P. Characterizing Site-Specific Mechanical Properties of Knee Cartilage with Indentation-Relaxation Maps and Machine Learning. *J Mech Behav Biomed Mater* **2023**, *142*, 105826, doi:10.1016/j.jmbbm.2023.105826.

121. Bae, W.C.; Schumacher, B.L.; Sah, R.L. Indentation Probing of Human Articular Cartilage: Effect on Chondrocyte Viability. *Osteoarthritis Cartilage* **2007**, *15*, 9–18, doi:10.1016/j.joca.2006.06.007.

122. Simha, N.K.; Jin, H.; Hall, M.L.; Chiravarambath, S.; Lewis, J.L. Effect of Indenter Size on Elastic Modulus of Cartilage Measured by Indentation. *J Biomech Eng* **2007**, *129*, 767–775, doi:10.1115/1.2768110.

123. Wahlquist, J.A.; DelRio, F.W.; Randolph, M.A.; Aziz, A.H.; Heveran, C.M.; Bryant, S.J.; Neu, C.P.; Ferguson, V.L. Indentation Mapping Revealed Poroelastic, but Not Viscoelastic, Properties Spanning Native Zonal Articular Cartilage. *Acta Biomater* **2017**, *64*, 41–49, doi:10.1016/j.actbio.2017.10.003.

124. Mak, A.F. Unconfined Compression of Hydrated Viscoelastic Tissues: A Biphasic Poroviscoelastic Analysis. *Biorheology* **1986**, *23*, 371–383, doi:10.3233/bir-1986-23406.

125. Akizuki, S.; Mow, V.C.; Müller, F.; Pita, J.C.; Howell, D.S.; Manicourt, D.H. Tensile Properties of Human Knee Joint Cartilage: I. Influence of Ionic Conditions, Weight Bearing, and Fibrillation on the Tensile Modulus. *J Orthop Res* **1986**, *4*, 379–392, doi:10.1002/jor.1100040401.

126. Fields, A.J.; Rodriguez, D.; Gary, K.N.; Liebenberg, E.C.; Lotz, J.C. Influence of Biochemical Composition on Endplate Cartilage Tensile Properties in the Human Lumbar Spine. *J Orthop Res* **2014**, *32*, 245–252, doi:10.1002/jor.22516.

127. Cohen, N.P.; Foster, R.J.; Mow, V.C. Composition and Dynamics of Articular Cartilage: Structure, Function, and Maintaining Healthy State. *J Orthop Sports Phys Ther* **1998**, *28*, 203–215, doi:10.2519/jospt.1998.28.4.203.

128. Darling, E.M.; Wilusz, R.E.; Bolognesi, M.P.; Zauscher, S.; Guilak, F. Spatial Mapping of the Biomechanical Properties of the Pericellular Matrix of Articular Cartilage Measured in Situ via Atomic Force Microscopy. *Biophys J* **2010**, *98*, 2848–2856, doi:10.1016/j.bpj.2010.03.037.

129. Braet, F.; Seynaeve, C.; De Zanger, R.; Wisse, E. Imaging Surface and Submembranous Structures with the Atomic Force Microscope: A Study on Living Cancer Cells, Fibroblasts and Macrophages. *J Microsc* **1998**, *190*, 328–338, doi:10.1046/j.1365-2818.1998.00333.x.

130. Novakofski, K.D.; Pownder, S.L.; Koff, M.F.; Williams, R.M.; Potter, H.G.; Fortier, L.A. High-Resolution Methods for Diagnosing Cartilage Damage In Vivo. *Cartilage* **2016**, *7*, 39–51, doi:10.1177/1947603515602307.

131. Brenneman Wilson, E.C.; Quenneville, C.E.; Maly, M.R. Integrating MR Imaging with Full-Surface Indentation Mapping of Femoral Cartilage in an Ex Vivo Porcine Stifle. *J Mech Behav Biomed Mater* **2023**, *139*, 105651, doi:10.1016/j.jmbbm.2023.105651.

132. Lakin, B.A.; Grasso, D.J.; Shah, S.S.; Stewart, R.C.; Bansal, P.N.; Freedman, J.D.; Grinstaff, M.W.; Snyder, B.D. Cationic Agent Contrast-Enhanced Computed Tomography Imaging of Cartilage Correlates with the Compressive Modulus and Coefficient of Friction. *Osteoarthritis Cartilage* **2013**, *21*, 60–68, doi:10.1016/j.joca.2012.09.007.

133. Burghardt, A.J.; Link, T.M.; Majumdar, S. High-Resolution Computed Tomography for Clinical Imaging of Bone Microarchitecture. *Clin Orthop Relat Res* **2011**, *469*, 2179–2193, doi:10.1007/s11999-010-1766-x.

134. Rüegsegger, P.; Koller, B.; Müller, R. A Microtomographic System for the Nondestructive Evaluation of Bone Architecture. *Calcif Tissue Int* **1996**, *58*, 24–29, doi:10.1007/BF02509542.

135. Fritz, B.; Fritz, J.; Fucentese, S.F.; Pfirrmann, C.W.A.; Sutter, R. Three-Dimensional Analysis for Quantification of Knee Joint Space Width with Weight-Bearing CT: Comparison with Non-Weight-Bearing CT and Weight-Bearing Radiography. *Osteoarthritis Cartilage* **2022**, *30*, 671–680, doi:10.1016/j.joca.2021.11.019.

136. Zumstein, V.; Kraljević, M.; Conzen, A.; Hoechel, S.; Müller-Gerbl, M. Thickness Distribution of the Glenohumeral Joint Cartilage: A Quantitative Study Using Computed Tomography. *Surg Radiol Anat* **2014**, *36*, 327–331, doi:10.1007/s00276-013-1221-2.

137. Lusic, H.; Grinstaff, M.W. X-Ray-Computed Tomography Contrast Agents. *Chem Rev* **2013**, *113*, 1641–1666, doi:10.1021/cr200358s.

138. Turunen, M.J.; Töyräs, J.; Lammi, M.J.; Jurvelin, J.S.; Korhonen, R.K. Hyperosmolaric Contrast Agents in Cartilage Tomography May Expose Cartilage to Overload-Induced Cell Death. *J Biomech* **2012**, *45*, 497–503, doi:10.1016/j.jbiomech.2011.11.049.

139. Tremoleda, J.L.; Khalil, M.; Gompels, L.L.; Wylezinska-Arridge, M.; Vincent, T.; Gsell, W. Imaging Technologies for Preclinical Models of Bone and Joint Disorders. *EJNMMI Res* **2011**, *1*, 11, doi:10.1186/2191-219X-1-11.

140. Gold, G.E.; Chen, C.A.; Koo, S.; Hargreaves, B.A.; Bangerter, N.K. Recent Advances in MRI of Articular Cartilage. *AJR Am J Roentgenol* **2009**, *193*, 628–638, doi:10.2214/AJR.09.3042.

141. Fragonas, E.; Mlynárik, V.; Jellús, V.; Micali, F.; Piras, A.; Toffanin, R.; Rizzo, R.; Vittur, F. Correlation between Biochemical Composition and Magnetic Resonance Appearance of Articular Cartilage. *Osteoarthritis Cartilage* **1998**, *6*, 24–32, doi:10.1053/joca.1997.0089.

142. Sewerin, P.; Schleich, C.; Vordenbäumen, S.; Ostendorf, B. Update on Imaging in Rheumatic Diseases: Cartilage. *Clin Exp Rheumatol* **2018**, *36 Suppl 114*, 139–144.

143. Paunipagar, B.K.; Rasalkar, D. Imaging of Articular Cartilage. *Indian J Radiol Imaging* **2014**, *24*, 237–248, doi:10.4103/0971-3026.137028.

144. van Tiel, J.; Reijman, M.; Bos, P.K.; Hermans, J.; van Buul, G.M.; Bron, E.E.; Klein, S.; Verhaar, J.A.N.; Krestin, G.P.; Bierma-Zeinstra, S.M.A.; et al. Delayed Gadolinium-Enhanced MRI of Cartilage (dGEMRIC) Shows No Change in Cartilage Structural Composition after Viscosupplementation in Patients with Early-Stage Knee Osteoarthritis. *PLoS One* **2013**, *8*, e79785, doi:10.1371/journal.pone.0079785.

145. Wheaton, A.J.; Casey, F.L.; Gougoutas, A.J.; Dodge, G.R.; Borthakur, A.; Lonner, J.H.; Schumacher, H.R.; Reddy, R. Correlation of T1rho with Fixed Charge Density in Cartilage. *J Magn Reson Imaging* **2004**, *20*, 519–525, doi:10.1002/jmri.20148.

146. Crețu, A.; Mattea, C.; Stapf, S. Low-Field and Variable-Field NMR Relaxation Studies of H2O and D2O Molecular Dynamics in Articular Cartilage. *PLoS One* **2021**, *16*, e0256177, doi:10.1371/journal.pone.0256177.

147. Rössler, E.; Mattea, C.; Stapf, S. Feasibility of High-Resolution One-Dimensional Relaxation Imaging at Low Magnetic Field Using a Single-Sided NMR Scanner Applied to Articular Cartilage. *J Magn Reson* **2015**, *251*, 43–51, doi:10.1016/j.jmr.2014.10.014.

148. Barbieri, M.; Fantazzini, P.; Testa, C.; Bortolotti, V.; Baruffaldi, F.; Kogan, F.; Brizi, L. Characterization of Structural Bone Properties through Portable Single-Sided NMR Devices: State of the Art and Future Perspectives. *Int J Mol Sci* **2021**, *22*, 7318, doi:10.3390/ijms22147318.

149. Rössler, E.; Mattea, C.; Stapf, S. NMR Dispersion Investigations of Enzymatically Degraded Bovine Articular Cartilage. *Magn Reson Med* **2015**, *73*, 2005–2014, doi:10.1002/mrm.25292.

150. Petrov, O.V.; Rössler, E.; Mattea, C.; Nieminen, M.T.; Lehenkari, P.; Karhula, S.; Saarakkala, S.; Stapf, S. Low-Field NMR Relaxation Times Distributions and Their Magnetic Field Dependence as a Possible Biomarker in Cartilage. In *EMBEC & NBC 2017*; Eskola, H., Väisänen, O., Viik, J., Hyttinen, J., Eds.; IFMBE Proceedings; Springer Singapore: Singapore, 2018; Vol. 65, pp. 952–955 ISBN 978-981-10-5121-0.

151. Liu, Y.; Shah, K.M.; Luo, J. Strategies for Articular Cartilage Repair and Regeneration. *Front Bioeng Biotechnol* **2021**, *9*, 770655, doi:10.3389/fbioe.2021.770655.

152. Saarakkala, S.; Julkunen, P.; Kiviranta, P.; Mäkitalo, J.; Jurvelin, J.S.; Korhonen, R.K. Depth-Wise Progression of Osteoarthritis in Human Articular Cartilage: Investigation of Composition, Structure and Biomechanics. *Osteoarthritis Cartilage* **2010**, *18*, 73–81, doi:10.1016/j.joca.2009.08.003.

153. Barbieri, M.; Fantazzini, P.; Bortolotti, V.; Baruffaldi, F.; Festa, A.; Manners, D.N.; Testa, C.; Brizi, L. Single-Sided NMR to Estimate Morphological Parameters of the Trabecular Bone Structure. *Magn Reson Med* **2021**, *85*, 3353–3369, doi:10.1002/mrm.28648.

154. Blümich, B.; Perlo, J.; Casanova, F. Mobile Single-Sided NMR. *Progress in Nuclear Magnetic Resonance Spectroscopy* **2008**, *52*, 197–269, doi:10.1016/j.pnmrs.2007.10.002.

155. Petrov, O.V.; Stapf, S. Multicomponent Analysis of T1 Relaxation in Bovine Articular Cartilage at Low Magnetic Fields. *Magn Reson Med* **2019**, *81*, 2858–2868, doi:10.1002/mrm.27624.

156. Mittal, S.; Pradhan, G.; Singh, S.; Batra, R. T1 and T2 Mapping of Articular Cartilage and Menisci in Early Osteoarthritis of the Knee Using 3-Tesla Magnetic Resonance Imaging. *Pol J Radiol* **2019**, *84*, e549–e564, doi:10.5114/pjr.2019.91375.

157. Barbieri, M.; Brizi, L.; Bortolotti, V.; Fantazzini, P.; Nogueira d'Eurydice, M.; Obruchkov, S.; Liu, H.; Galvosas, P. Single-Sided NMR for the Diagnosis of Osteoporosis: Diffusion Weighted Pulse Sequences for the Estimation of Trabecular Bone Volume Fraction in the Presence of Muscle Tissue. *Microporous and Mesoporous Materials* **2018**, *269*, 166–170, doi:10.1016/j.micromeso.2017.05.023.

158. Rößler, E.; Mattea, C.; Stapf, S.; Karhula, S.; Saarakkala, S.; Nieminen, M.T. Load-Dependent NMR Low-Field Profiling and Relaxation Dispersion Study of Osteoarthritic Articular Cartilage. *Microporous and Mesoporous Materials* **2018**, *269*, 160–165, doi:10.1016/j.micromeso.2017.02.069.

159. Seitz, A.M.; Osthaus, F.; Schwer, J.; Warnecke, D.; Faschingbauer, M.; Sgroi, M.; Ignatius, A.; Dürselen, L. Osteoarthritis-Related Degeneration Alters the Biomechanical Properties of Human Menisci Before the Articular Cartilage. *Front Bioeng Biotechnol* **2021**, *9*, 659989, doi:10.3389/fbioe.2021.659989.

160. Kumar, R.; Pierce, D.M.; Isaksen, V.; Davies, C. de L.; Drogset, J.O.; Lilledahl, M.B. Comparison of Compressive Stress-Relaxation Behavior in Osteoarthritic (ICRS Graded) Human Articular Cartilage. *Int J Mol Sci* **2018**, *19*, 413, doi:10.3390/ijms19020413.

161. Mohammadi, A.; Te Moller, N.C.R.; Ebrahimi, M.; Plomp, S.; Brommer, H.; van Weeren, P.R.; Mäkelä, J.T.A.; Töyräs, J.; Korhonen, R.K. Site- and Zone-Dependent Changes in Proteoglycan Content and Biomechanical Properties of Bluntly and Sharply Grooved Equine Articular Cartilage. *Ann Biomed Eng* **2022**, *50*, 1787–1797, doi:10.1007/s10439-022-02991-4.

162. Ebrahimi, M.; Ojanen, S.; Mohammadi, A.; Finnilä, M.A.; Joukainen, A.; Kröger, H.; Saarakkala, S.; Korhonen, R.K.; Tanska, P. Elastic, Viscoelastic and Fibril-Reinforced Poroelastic Material Properties of Healthy and Osteoarthritic Human Tibial Cartilage. *Ann Biomed Eng* **2019**, *47*, 953–966, doi:10.1007/s10439-019-02213-4.

163. Nickmanesh, R.; Stewart, R.C.; Snyder, B.D.; Grinstaff, M.W.; Masri, B.A.; Wilson, D.R. Contrast-Enhanced Computed Tomography (CECT) Attenuation Is Associated with Stiffness of Intact Knee Cartilage. *J Orthop Res* **2018**, *36*, 2641–2647, doi:10.1002/jor.24022.

164. Jin, H.; Lewis, J.L. Determination of Poisson's Ratio of Articular Cartilage by Indentation Using Different-Sized Indenters. *J Biomech Eng* **2004**, *126*, 138–145, doi:10.1115/1.1688772.

165. Liu, C.; Liu, C.; Ren, X.; Si, L.; Shen, H.; Wang, Q.; Yao, W. Quantitative Evaluation of Subchondral Bone Microarchitecture in Knee Osteoarthritis Using 3T MRI. *BMC Musculoskelet Disord* **2017**, *18*, 496, doi:10.1186/s12891-017-1865-x.

166. Nilsson, J.; Thorstensson, A. Adaptability in Frequency and Amplitude of Leg Movements during Human Locomotion at Different Speeds. *Acta Physiol Scand* **1987**, *129*, 107–114, doi:10.1111/j.1748-1716.1987.tb08045.x.

167. Wiesmath, A.; Filip, C.; Demco, D.E.; Blümich, B. NMR of Multipolar Spin States Excitated in Strongly Inhomogeneous Magnetic Fields. *J Magn Reson* **2002**, *154*, 60–72, doi:10.1006/jmre.2001.2458.

168. Li, G.; Lopez, O.; Rubash, H. Variability of a Three-Dimensional Finite Element Model Constructed Using Magnetic Resonance Images of a Knee for Joint Contact Stress Analysis. *J Biomech Eng* **2001**, *123*, 341–346, doi:10.1115/1.1385841.

169. Brown, C.P.; Nguyen, T.C.; Moody, H.R.; Crawford, R.W.; Oloyede, A. Assessment of Common Hyperelastic Constitutive Equations for Describing Normal and Osteoarthritic Articular Cartilage. *Proc Inst Mech Eng H* **2009**, *223*, 643–652, doi:10.1243/09544119JEIM546.

170. Maeda, T.; Kuriyama, S.; Yoshida, S.; Nishitani, K.; Nakamura, S.; Matsuda, S. Decreased Elastic Modulus of Knee Articular Cartilage Based on New Macroscopic Methods Accurately Represents Early Histological Findings of Degeneration. *Cartilage* **2023**, 19476035231194770, doi:10.1177/19476035231194770.

171. Berni, M.; Erani, P.; Lopomo, N.F.; Baleani, M. Optimization of In Situ Indentation Protocol to Map the Mechanical Properties of Articular Cartilage. *Materials (Basel)* **2022**, *15*, 6425, doi:10.3390/ma15186425.

172. Thambyah, A.; Nather, A.; Goh, J. Mechanical Properties of Articular Cartilage Covered by the Meniscus. *Osteoarthritis Cartilage* **2006**, *14*, 580–588, doi:10.1016/j.joca.2006.01.015.

173. Bae, W.C.; Temple, M.M.; Amiel, D.; Coutts, R.D.; Niederauer, G.G.; Sah, R.L. Indentation Testing of Human Cartilage: Sensitivity to Articular Surface Degeneration. *Arthritis Rheum* **2003**, *48*, 3382–3394, doi:10.1002/art.11347.

174. Kiviranta, P.; Lammentausta, E.; Töyräs, J.; Kiviranta, I.; Jurvelin, J.S. Indentation Diagnostics of Cartilage Degeneration. *Osteoarthritis Cartilage* **2008**, *16*, 796–804, doi:10.1016/j.joca.2007.10.016.

175. Temple, D.K.; Cederlund, A.A.; Lawless, B.M.; Aspden, R.M.; Espino, D.M. Viscoelastic Properties of Human and Bovine Articular Cartilage: A Comparison of Frequency-Dependent Trends. *BMC Musculoskelet Disord* **2016**, *17*, 419, doi:10.1186/s12891-016-1279-1.

176. Li, H.; Li, J.; Yu, S.; Wu, C.; Zhang, W. The Mechanical Properties of Tibiofemoral and Patellofemoral Articular Cartilage in Compression Depend on Anatomical Regions. *Sci Rep* **2021**, *11*, 6128, doi:10.1038/s41598-021-85716-2.

177. Moshtagh, P.R.; Pouran, B.; Korthagen, N.M.; Zadpoor, A.A.; Weinans, H. Guidelines for an Optimized Indentation Protocol for Measurement of Cartilage Stiffness: The Effects of Spatial Variation and Indentation Parameters. *J Biomech* **2016**, *49*, 3602–3607, doi:10.1016/j.jbiomech.2016.09.020.

178. Yin, J.; Xia, Y.; Lu, M. Concentration Profiles of Collagen and Proteoglycan in Articular Cartilage by Fourier Transform Infrared Imaging and Principal Component Regression. *Spectrochim Acta A Mol Biomol Spectrosc* **2012**, *88*, 90–96, doi:10.1016/j.saa.2011.12.002.

179. Vincent, T.L.; Wann, A.K.T. Mechanoadaptation: Articular Cartilage through Thick and Thin. *J Physiol* **2019**, *597*, 1271–1281, doi:10.1113/JP275451.

180. Jung, E.; Choi, H.J.; Lim, M.; Kang, H.; Park, H.; Han, H.; Min, B.-H.; Kim, S.; Park, I.; Lim, H. Quantitative Analysis of Water Distribution in Human Articular Cartilage Using Terahertz Time-Domain Spectroscopy. *Biomed Opt Express* **2012**, *3*, 1110–1115, doi:10.1364/BOE.3.001110.

181. Lüsse, S.; Claassen, H.; Gehrke, T.; Hassenpflug, J.; Schünke, M.; Heller, M.; Glüer, C.C. Evaluation of Water Content by Spatially Resolved Transverse Relaxation Times of Human Articular Cartilage. *Magn Reson Imaging* **2000**, *18*, 423–430, doi:10.1016/s0730-725x(99)00144-7.

182. Leskinen, H.P.P.; Hänninen, N.E.; Nissi, M.J. T2orientation Anisotropy Mapping of Articular Cartilage Using qMRI. *Phys Med Biol* **2023**, *68*, doi:10.1088/1361-6560/acc169.

183. Hannila, I.; Räinä, S.S.; Tervonen, O.; Ojala, R.; Nieminen, M.T. Topographical Variation of T2 Relaxation Time in the Young Adult Knee Cartilage at 1.5 T. *Osteoarthritis Cartilage* **2009**, *17*, 1570–1575, doi:10.1016/j.joca.2009.05.011.

184. Hayes, C.W.; Parellada, J.A. The Magic Angle Effect in Musculoskeletal MR Imaging. *Top Magn Reson Imaging* **1996**, *8*, 51–56.

185. Bieri, O.; Ganter, C.; Scheffler, K. Quantitative in Vivo Diffusion Imaging of Cartilage Using Double Echo Steady-State Free Precession. *Magn Reson Med* **2012**, *68*, 720–729, doi:10.1002/mrm.23275.

186. Gottardi, R.; Hansen, U.; Raiteri, R.; Loparic, M.; Düggelin, M.; Mathys, D.; Friederich, N.F.; Bruckner, P.; Stolz, M. Supramolecular Organization of Collagen Fibrils in Healthy and Osteoarthritic Human Knee and Hip Joint Cartilage. *PLoS One* **2016**, *11*, e0163552, doi:10.1371/journal.pone.0163552.

187. Rautiainen, J.; Nissi, M.J.; Salo, E.-N.; Tiitu, V.; Finnilä, M.A.J.; Aho, O.-M.; Saarakkala, S.; Lehenkari, P.; Ellermann, J.; Nieminen, M.T. Multiparametric MRI Assessment of Human Articular Cartilage Degeneration: Correlation with Quantitative Histology and Mechanical Properties. *Magn Reson Med* **2015**, *74*, 249–259, doi:10.1002/mrm.25401.

188. Namiranian, B.; Jerban, S.; Ma, Y.; Dorthe, E.W.; Masoud-Afsahi, A.; Wong, J.; Wei, Z.; Chen, Y.; D'Lima, D.; Chang, E.Y.; et al. Assessment of Mechanical Properties of Articular Cartilage with Quantitative Three-Dimensional Ultrashort Echo Time (UTE) Cones Magnetic Resonance Imaging. *J Biomech* **2020**, *113*, 110085, doi:10.1016/j.jbiomech.2020.110085.

189. Lammentausta, E.; Kiviranta, P.; Töyräs, J.; Hyttinen, M.M.; Kiviranta, I.; Nieminen, M.T.; Jurvelin, J.S. Quantitative MRI of Parallel Changes of Articular Cartilage and Underlying Trabecular Bone in Degeneration. *Osteoarthritis Cartilage* **2007**, *15*, 1149–1157, doi:10.1016/j.joca.2007.03.019.

190. Nissi, M.J.; Rieppo, J.; Töyräs, J.; Laasanen, M.S.; Kiviranta, I.; Nieminen, M.T.; Jurvelin, J.S. Estimation of Mechanical Properties of Articular Cartilage with MRI - dGEMRIC, T2 and T1 Imaging in Different Species with Variable Stages of Maturation. *Osteoarthritis Cartilage* **2007**, *15*, 1141–1148, doi:10.1016/j.joca.2007.03.018.

191. Hananouchi, T.; Satake, S.; Sakao, K.; Katsuda, H.; Shimada, N.; Dorthe, E.W.; D'Lima, D.D. Determining the Relationship between Mechanical Properties and Quantitative Magnetic Resonance Imaging of Joint Soft Tissues Using Patient-Specific Templates. *Bioengineering* **2023**, *10*, 1050, doi:10.3390/bioengineering10091050.

192. Wheaton, A.J.; Dodge, G.R.; Elliott, D.M.; Nicoll, S.B.; Reddy, R. Quantification of Cartilage Biomechanical and Biochemical Properties via T1rho Magnetic Resonance Imaging. *Magn Reson Med* **2005**, *54*, 1087–1093, doi:10.1002/mrm.20678.

193. Hatcher, C.C.; Collins, A.T.; Kim, S.Y.; Michel, L.C.; Mostertz, W.C.; Ziemian, S.N.; Spritzer, C.E.; Guilak, F.; DeFrate, L.E.; McNulty, A.L. Relationship between T1rho Magnetic Resonance Imaging, Synovial Fluid Biomarkers, and the Biochemical and Biomechanical Properties of Cartilage. *J Biomech* **2017**, *55*, 18–26, doi:10.1016/j.jbiomech.2017.02.001.

194. Nieminen, M.T.; Töyräs, J.; Laasanen, M.S.; Silvennoinen, J.; Helminen, H.J.; Jurvelin, J.S. Prediction of Biomechanical Properties of Articular Cartilage with Quantitative Magnetic Resonance Imaging. *J Biomech* **2004**, *37*, 321–328, doi:10.1016/s0021-9290(03)00291-4.

195. Julkunen, P.; Korhonen, R.K.; Nissi, M.J.; Jurvelin, J.S. Mechanical Characterization of Articular Cartilage by Combining Magnetic Resonance Imaging and Finite-Element Analysis: A Potential Functional Imaging Technique. *Phys Med Biol* **2008**, *53*, 2425–2438, doi:10.1088/0031-9155/53/9/014.

196. Reiter, D.A.; Peacock, A.; Spencer, R.G. Effects of Frozen Storage and Sample Temperature on Water Compartmentation and Multiexponential Transverse Relaxation in Cartilage. *Magn Reson Imaging* **2011**, *29*, 561–567, doi:10.1016/j.mri.2010.10.011.

197. Szarko, M.; Muldrew, K.; Bertram, J.E. Freeze-Thaw Treatment Effects on the Dynamic Mechanical Properties of Articular Cartilage. *BMC Musculoskelet Disord* **2010**, *11*, 231, doi:10.1186/1471-2474-11-231.

198. Qu, C.; Hirviniemi, M.; Tiitu, V.; Jurvelin, J.S.; Töyräs, J.; Lammi, M.J. Effects of Freeze-Thaw Cycle with and without Proteolysis Inhibitors and Cryopreservant on the Biochemical and Biomechanical Properties of Articular Cartilage. *Cartilage* **2014**, *5*, 97–106, doi:10.1177/1947603513515998.

199. Kennedy, E.A.; Tordonado, D.S.; Duma, S.M. Effects of Freezing on the Mechanical Properties of Articular Cartilage. *Biomed Sci Instrum* **2007**, *43*, 342–347.

200. Peters, A.E.; Comerford, E.J.; Macaulay, S.; Bates, K.T.; Akhtar, R. Micromechanical Properties of Canine Femoral Articular Cartilage Following Multiple Freeze-Thaw Cycles. *J Mech Behav Biomed Mater* **2017**, *71*, 114–121, doi:10.1016/j.jmbbm.2017.03.006.

201. Espino, D.M.; Shepherd, D.E.T.; Hukins, D.W.L. Viscoelastic Properties of Bovine Knee Joint Articular Cartilage: Dependency on Thickness and Loading Frequency. *BMC Musculoskelet Disord* **2014**, *15*, 205, doi:10.1186/1471-2474-15-205.

202. Shepherd, D.E.; Seedhom, B.B. Thickness of Human Articular Cartilage in Joints of the Lower Limb. *Ann Rheum Dis* **1999**, *58*, 27–34, doi:10.1136/ard.58.1.27.

203. Shah, R.F.; Martinez, A.M.; Pedoia, V.; Majumdar, S.; Vail, T.P.; Bini, S.A. Variation in the Thickness of Knee Cartilage. The Use of a Novel Machine Learning Algorithm for Cartilage Segmentation of Magnetic Resonance Images. *J Arthroplasty* **2019**, *34*, 2210–2215, doi:10.1016/j.arth.2019.07.022.

204. Oseni, A.O.; Butler, P.E.; Seifalian, A.M. Optimization of Chondrocyte Isolation and Characterization for Large-Scale Cartilage Tissue Engineering. *J Surg Res* **2013**, *181*, 41–48, doi:10.1016/j.jss.2012.05.087.

205. Mow, V.C.; Wang, C.C.; Hung, C.T. The Extracellular Matrix, Interstitial Fluid and Ions as a Mechanical Signal Transducer in Articular Cartilage. *Osteoarthritis Cartilage* **1999**, *7*, 41–58, doi:10.1053/joca.1998.0161.

206. Li, L.P.; Herzog, W. The Role of Viscoelasticity of Collagen Fibers in Articular Cartilage: Theory and Numerical Formulation. *Biorheology* **2004**, *41*, 181–194.

207. Hayes, W.C.; Bodine, A.J. Flow-Independent Viscoelastic Properties of Articular Cartilage Matrix. *J Biomech* **1978**, *11*, 407–419, doi:10.1016/0021-9290(78)90075-1.

208. Muir, H. Proteoglycans as Organizers of the Intercellular Matrix. *Biochemical Society Transactions* **1983**, *11*, 613–622, doi:10.1042/bst0110613.

209. Fujii, Y.; Liu, L.; Yagasaki, L.; Inotsume, M.; Chiba, T.; Asahara, H. Cartilage Homeostasis and Osteoarthritis. *Int J Mol Sci* **2022**, *23*, 6316, doi:10.3390/ijms23116316.

210. GBD 2019 Diseases and Injuries Collaborators Global Burden of 369 Diseases and Injuries in 204 Countries and Territories, 1990-2019: A Systematic Analysis for the Global Burden of Disease Study 2019. *Lancet* **2020**, *396*, 1204–1222, doi:10.1016/S0140-6736(20)30925-9.

211. Aula, A.S.; Jurvelin, J.S.; Töyräs, J. Simultaneous Computed Tomography of Articular Cartilage and Subchondral Bone. *Osteoarthritis and Cartilage* **2009**, *17*, 1583–1588, doi:10.1016/j.joca.2009.06.010.

212. Kroker, A.; Zhu, Y.; Manske, S.L.; Barber, R.; Mohtadi, N.; Boyd, S.K. Quantitative in Vivo Assessment of Bone Microarchitecture in the Human Knee Using HR-pQCT. *Bone* **2017**, *97*, 43–48, doi:10.1016/j.bone.2016.12.015.

213. Keen, C.E.; Whittier, D.E.; Firminger, C.R.; Edwards, W.B.; Boyd, S.K. Validation of Bone Density and Microarchitecture Measurements of the Load-Bearing Femur in the Human Knee Obtained Using In Vivo HR-pQCT Protocol. *J Clin Densitom* **2021**, *24*, 651–657, doi:10.1016/j.jocd.2021.01.004.

214. Stewart, R.C.; Patwa, A.N.; Lusic, H.; Freedman, J.D.; Wathier, M.; Snyder, B.D.; Guermazi, A.; Grinstaff, M.W. Synthesis and Preclinical Characterization of a Cationic Iodinated Imaging Contrast Agent (CA4+) and Its Use for Quantitative Computed Tomography of Ex Vivo Human Hip Cartilage. *J Med Chem* **2017**, *60*, 5543–5555, doi:10.1021/acs.jmedchem.7b00234.

215. Clark, J.N.; Tavana, S.; Clark, B.; Briggs, T.; Jeffers, J.R.T.; Hansen, U. High Resolution Three-Dimensional Strain Measurements in Human Articular Cartilage. *J Mech Behav Biomed Mater* **2021**, *124*, 104806, doi:10.1016/j.jmbbm.2021.104806.

216. Fantoni, S.; Gabucci, I.; Cardarelli, P.; Paternò, G.; Taibi, A.; Cristofori, V.; Trapella, C.; Bazzani, A.; Assenza, M.; Zanna Bonacorsi, A.; et al. A Cationic Contrast Agent in X-Ray Imaging of Articular Cartilage: Pre-Clinical Evaluation of Diffusion and Attenuation Properties. *Diagnostics (Basel)* **2022**, *12*, 2111, doi:10.3390/diagnostics12092111.

217. Hayes, W.C.; Keer, L.M.; Herrmann, G.; Mockros, L.F. A Mathematical Analysis for Indentation Tests of Articular Cartilage. *J Biomech* **1972**, *5*, 541–551, doi:10.1016/0021-9290(72)90010-3.

218. Bernal, J.L.; Cummins, S.; Gasparrini, A. Interrupted Time Series Regression for the Evaluation of Public Health Interventions: A Tutorial. *Int J Epidemiol* **2017**, *46*, 348–355, doi:10.1093/ije/dyw098.

219. Turner, S.L.; Karahalios, A.; Forbes, A.B.; Taljaard, M.; Grimshaw, J.M.; McKenzie, J.E. Comparison of Six Statistical Methods for Interrupted Time Series Studies: Empirical Evaluation of 190 Published Series. *BMC Med Res Methodol* **2021**, *21*, 134, doi:10.1186/s12874-021-01306-w.

220. Horkay, F. Interactions of Cartilage Extracellular Matrix Macromolecules. *J Polym Sci B Polym Phys* **2012**, *50*, 1699–1705, doi:10.1002/polb.23191.

221. Canal Guterl, C.; Hung, C.T.; Ateshian, G.A. Electrostatic and Non-Electrostatic Contributions of Proteoglycans to the Compressive Equilibrium Modulus of Bovine Articular Cartilage. *J Biomech* **2010**, *43*, 1343–1350, doi:10.1016/j.jbiomech.2010.01.021.

222. Han, E.; Chen, S.S.; Klisch, S.M.; Sah, R.L. Contribution of Proteoglycan Osmotic Swelling Pressure to the Compressive Properties of Articular Cartilage. *Biophys J* **2011**, *101*, 916–924, doi:10.1016/j.bpj.2011.07.006.

223. Chahine, N.O.; Chen, F.H.; Hung, C.T.; Ateshian, G.A. Direct Measurement of Osmotic Pressure of Glycosaminoglycan Solutions by Membrane Osmometry at Room Temperature. *Biophys J* **2005**, *89*, 1543–1550, doi:10.1529/biophysj.104.057315.

224. Lu, X.L.; Sun, D.D.N.; Guo, X.E.; Chen, F.H.; Lai, W.M.; Mow, V.C. Indentation Determined Mechanoelectrochemical Properties and Fixed Charge Density of Articular Cartilage. *Ann Biomed Eng* **2004**, *32*, 370–379, doi:10.1023/b:abme.0000017534.06921.24.

225. Guilak, F.; Erickson, G.R.; Ting-Beall, H.P. The Effects of Osmotic Stress on the Viscoelastic and Physical Properties of Articular Chondrocytes. *Biophys J* **2002**, *82*, 720–727, doi:10.1016/S0006-3495(02)75434-9.

226. Alcaide-Ruggiero, L.; Cugat, R.; Domínguez, J.M. Proteoglycans in Articular Cartilage and Their Contribution to Chondral Injury and Repair Mechanisms. *Int J Mol Sci* **2023**, *24*, 10824, doi:10.3390/ijms241310824.

227. June, R.K.; Mejia, K.L.; Barone, J.R.; Fyhrie, D.P. Cartilage Stress-Relaxation Is Affected by Both the Charge Concentration and Valence of Solution Cations. *Osteoarthritis Cartilage* **2009**, *17*, 669–676, doi:10.1016/j.joca.2008.09.011.

228. Hwang, J.W.; Chawla, D.; Han, G.; Eriten, M.; Henak, C.R. Effects of Solvent Osmolarity and Viscosity on Cartilage Energy Dissipation under High-Frequency Loading. *J Mech Behav Biomed Mater* **2022**, *126*, 105014, doi:10.1016/j.jmbbm.2021.105014.

229. Meloni, G.R.; Farran, A.; Mohanraj, B.; Guehring, H.; Cocca, R.; Rabut, E.; Mauck, R.L.; Dodge, G.R. Recombinant Human FGF18 Preserves Depth-Dependent Mechanical Inhomogeneity in Articular Cartilage. *Eur Cell Mater* **2019**, *38*, 23–34, doi:10.22203/eCM.v038a03.

230. Bansal, P.N.; Joshi, N.S.; Entezari, V.; Malone, B.C.; Stewart, R.C.; Snyder, B.D.; Grinstaff, M.W. Cationic Contrast Agents Improve Quantification of Glycosaminoglycan (GAG) Content by Contrast Enhanced CT Imaging of Cartilage. *Journal Orthopaedic Research* **2011**, *29*, 704–709, doi:10.1002/jor.21312.

231. Stewart, R.C.; Bansal, P.N.; Entezari, V.; Lusic, H.; Nazarian, R.M.; Snyder, B.D.; Grinstaff, M.W. Contrast-Enhanced CT with a High-Affinity Cationic Contrast Agent for Imaging Ex Vivo Bovine, Intact Ex Vivo Rabbit, and in Vivo Rabbit Cartilage. *Radiology* **2013**, *266*, 141–150, doi:10.1148/radiol.12112246.

232. Saukko, A.E.A.; Turunen, M.J.; Honkanen, M.K.M.; Lovric, G.; Tiitu, V.; Honkanen, J.T.J.; Grinstaff, M.W.; Jurvelin, J.S.; Töyräs, J. Simultaneous Quantitation of Cationic and Non-Ionic Contrast Agents in Articular Cartilage Using Synchrotron MicroCT Imaging. *Sci Rep* **2019**, *9*, 7118, doi:10.1038/s41598-019-43276-6.

233. Honkanen, M.K.M.; Saukko, A.E.A.; Turunen, M.J.; Xu, W.; Lovric, G.; Honkanen, J.T.J.; Grinstaff, M.W.; Lehto, V.-P.; Töyräs, J. Triple Contrast CT Method Enables Simultaneous Evaluation of Articular Cartilage Composition and Segmentation. *Ann Biomed Eng* **2020**, *48*, 556–567, doi:10.1007/s10439-019-02362-6.

234. Ateshian, G.A.; Chahine, N.O.; Basalo, I.M.; Hung, C.T. The Correspondence between Equilibrium Biphasic and Triphasic Material Properties in Mixture Models of Articular Cartilage. *J Biomech* **2004**, *37*, 391–400, doi:10.1016/s0021-9290(03)00252-5.

235. McCreery, K.P.; Luetkemeyer, C.M.; Calve, S.; Neu, C.P. Hyperelastic Characterization Reveals Proteoglycans Drive the Nanoscale Strain-Stiffening Response in Hyaline Cartilage. *J Biomech* **2023**, *146*, 111397, doi:10.1016/j.jbiomech.2022.111397.

236. Puxkandl, R.; Zizak, I.; Paris, O.; Keckes, J.; Tesch, W.; Bernstorff, S.; Purslow, P.; Fratzl, P. Viscoelastic Properties of Collagen: Synchrotron Radiation Investigations and Structural Model. *Philos Trans R Soc Lond B Biol Sci* **2002**, *357*, 191–197, doi:10.1098/rstb.2001.1033.

237. Mak, A.F. The Apparent Viscoelastic Behavior of Articular Cartilage--the Contributions from the Intrinsic Matrix Viscoelasticity and Interstitial Fluid Flows. *J Biomech Eng* **1986**, *108*, 123–130, doi:10.1115/1.3138591.

238. Huang, C.-Y.; Soltz, M.A.; Kopacz, M.; Mow, V.C.; Ateshian, G.A. Experimental Verification of the Roles of Intrinsic Matrix Viscoelasticity and Tension-Compression Nonlinearity in the Biphasic Response of Cartilage. *J Biomech Eng* **2003**, *125*, 84–93, doi:10.1115/1.1531656.

239. June, R.K.; Neu, C.P.; Barone, J.R.; Fyhrie, D.P. Polymer Mechanics as a Model for Short-Term and Flow-Independent Cartilage Viscoelasticity. *Mater Sci Eng C Mater Biol Appl* **2011**, *31*, 781–788, doi:10.1016/j.msec.2010.11.029.

240. Heinegård, D. Polydispersity of Cartilage Proteoglycans. Structural Variations with Size and Buoyant Density of the Molecules. *J Biol Chem* **1977**, *252*, 1980–1989.

241. Paakkari, P.; Inkinen, S.I.; Honkanen, M.K.M.; Prakash, M.; Shaikh, R.; Nieminen, M.T.; Grinstaff, M.W.; Mäkelä, J.T.A.; Töyräs, J.; Honkanen, J.T.J. Quantitative Dual Contrast Photon-Counting Computed Tomography for Assessment of Articular Cartilage Health. *Sci Rep* **2021**, *11*, 5556, doi:10.1038/s41598-021-84800-x.

242. Honkanen, M.K.M.; Saukko, A.E.A.; Turunen, M.J.; Shaikh, R.; Prakash, M.; Lovric, G.; Joukainen, A.; Kröger, H.; Grinstaff, M.W.; Töyräs, J. Synchrotron MicroCT Reveals the Potential of the Dual Contrast Technique for Quantitative Assessment of Human Articular Cartilage Composition. *J Orthop Res* **2020**, *38*, 563–573, doi:10.1002/jor.24479.

243. Nelson, B.B.; Mäkelä, J.T.A.; Lawson, T.B.; Patwa, A.N.; Snyder, B.D.; McIlwraith, C.W.; Grinstaff, M.W.; Goodrich, L.R.; Kawcak, C.E. Cationic Contrast-Enhanced Computed Tomography Distinguishes between Reparative, Degenerative, and Healthy Equine Articular Cartilage. *J Orthop Res* **2021**, *39*, 1647–1657, doi:10.1002/jor.24894.

244. Baumgarten, M.; Bloebaum, R.D.; Ross, S.D.; Campbell, P.; Sarmiento, A. Normal Human Synovial Fluid: Osmolality and Exercise-Induced Changes. *J Bone Joint Surg Am* **1985**, *67*, 1336–1339.

245. Urban, J.P.; Hall, A.C.; Gehl, K.A. Regulation of Matrix Synthesis Rates by the Ionic and Osmotic Environment of Articular Chondrocytes. *J Cell Physiol* **1993**, *154*, 262–270, doi:10.1002/jcp.1041540208.

246. Huang, Y.; Zhang, Y.; Ding, X.; Liu, S.; Sun, T. Osmolarity Influences Chondrocyte Repair after Injury in Human Articular Cartilage. *J Orthop Surg Res* **2015**, *10*, 19, doi:10.1186/s13018-015-0158-z.

247. Baylon, E.G.; Crowder, H.A.; Gold, G.E.; Levenston, M.E. Non-Ionic CT Contrast Solutions Rapidly Alter Bovine Cartilage and Meniscus Mechanics. *Osteoarthritis Cartilage* **2020**, *28*, 1286–1297, doi:10.1016/j.joca.2020.05.013.

248. Gao, X.; Patwa, A.N.; Deng, Z.; Utsunomiya, H.; Grinstaff, M.W.; Ruzbarsky, J.J.; Snyder, B.D.; Ravuri, S.; Philippon, M.J.; Huard, J. Influence of Fixation on CA4+ Contrast Enhanced microCT of Articular Cartilage and Subsequent Feasibility for Histological Evaluation. *Am J Transl Res* **2021**, *13*, 8921–8937.

249. Goldring, S.R.; Goldring, M.B. Changes in the Osteochondral Unit during Osteoarthritis: Structure, Function and Cartilage-Bone Crosstalk. *Nat Rev Rheumatol* **2016**, *12*, 632–644, doi:10.1038/nrrheum.2016.148.

250. Nowlan, N.C.; Murphy, P.; Prendergast, P.J. A Dynamic Pattern of Mechanical Stimulation Promotes Ossification in Avian Embryonic Long Bones. *Journal of Biomechanics* **2008**, *41*, 249–258, doi:10.1016/j.jbiomech.2007.09.031.

251. Wong, M.; Carter, D.R. Articular Cartilage Functional Histomorphology and Mechanobiology: A Research Perspective. *Bone* **2003**, *33*, 1–13, doi:10.1016/s8756-3282(03)00083-8.

252. Davis, S.; Karali, A.; Zekonyte, J.; Roldo, M.; Blunn, G. Development of a Method to Investigate Strain Distribution across the Cartilage-Bone Interface in Guinea Pig Model of Spontaneous Osteoarthritis Using Lab-Based Contrast Enhanced X-Ray-Computed Tomography and Digital Volume Correlation. *J Mech Behav Biomed Mater* **2023**, *144*, 105999, doi:10.1016/j.jmbbm.2023.105999.

253. Tamaddon, M.; Wang, L.; Liu, Z.; Liu, C. Osteochondral Tissue Repair in Osteoarthritic Joints: Clinical Challenges and Opportunities in Tissue Engineering. *Biodes Manuf* **2018**, *1*, 101–114, doi:10.1007/s42242-018-0015-0.

254. Acciaioli, A.; Falco, L.; Baleani, M. Measurement of Apparent Mechanical Properties of Trabecular Bone Tissue: Accuracy and Limitation of Digital Image Correlation Technique. *J Mech Behav Biomed Mater* **2020**, *103*, 103542, doi:10.1016/j.jmbbm.2019.103542.

255. Dall'Ara, E.; Tozzi, G. Digital Volume Correlation for the Characterization of Musculoskeletal Tissues: Current Challenges and Future Developments. *Front Bioeng Biotechnol* **2022**, *10*, 1010056, doi:10.3389/fbioe.2022.1010056.

256. Acciaioli, A.; Lionello, G.; Baleani, M. Experimentally Achievable Accuracy Using a Digital Image Correlation Technique in Measuring Small-Magnitude (<0.1%) Homogeneous Strain Fields. *Materials (Basel)* **2018**, *11*, 751, doi:10.3390/ma11050751.

257. Väänänen, S.P.; Amin Yavari, S.; Weinans, H.; Zadpoor, A.A.; Jurvelin, J.S.; Isaksson, H. Repeatability of Digital Image Correlation for Measurement of Surface Strains in Composite Long Bones. *J Biomech* **2013**, *46*, 1928–1932, doi:10.1016/j.jbiomech.2013.05.021.

258. Holmes, J.; Sommacal, S.; Das, R.; Stachurski, Z.; Compston, P. Digital Image and Volume Correlation for Deformation and Damage Characterisation of Fibre-Reinforced Composites: A Review. *Composite Structures* **2023**, *315*, 116994, doi:10.1016/j.compstruct.2023.116994.

259. Dall'Ara, E.; Tozzi, G. Digital Volume Correlation for the Characterization of Musculoskeletal Tissues: Current Challenges and Future Developments. *Front Bioeng Biotechnol* **2022**, *10*, 1010056, doi:10.3389/fbioe.2022.1010056.

260. Gillard, F.; Boardman, R.; Mavrogordato, M.; Hollis, D.; Sinclair, I.; Pierron, F.; Browne, M. The Application of Digital Volume Correlation (DVC) to Study the Microstructural Behaviour of Trabecular

Bone during Compression. *J Mech Behav Biomed Mater* **2014**, *29*, 480–499, doi:10.1016/j.jmbbm.2013.09.014.

261. Yan, L.; Cinar, A.; Ma, S.; Abel, R.; Hansen, U.; Marrow, T.J. A Method for Fracture Toughness Measurement in Trabecular Bone Using Computed Tomography, Image Correlation and Finite Element Methods. *J Mech Behav Biomed Mater* **2020**, *109*, 103838, doi:10.1016/j.jmbbm.2020.103838.

262. Madi, K.; Staines, K.A.; Bay, B.K.; Javaheri, B.; Geng, H.; Bodey, A.J.; Cartmell, S.; Pitsillides, A.A.; Lee, P.D. In Situ Characterization of Nanoscale Strains in Loaded Whole Joints via Synchrotron X-Ray Tomography. *Nat Biomed Eng* **2020**, *4*, 343–354, doi:10.1038/s41551-019-0477-1.

263. Wearne, L.S.; Rapagna, S.; Taylor, M.; Perilli, E. Micro-CT Scan Optimisation for Mechanical Loading of Tibia with Titanium Tibial Tray: A Digital Volume Correlation Zero Strain Error Analysis. *J Mech Behav Biomed Mater* **2022**, *134*, 105336, doi:10.1016/j.jmbbm.2022.105336.

264. Tavana, S.; N Clark, J.; Newell, N.; Calder, J.D.; Hansen, U. In Vivo Deformation and Strain Measurements in Human Bone Using Digital Volume Correlation (DVC) and 3T Clinical MRI. *Materials (Basel)* **2020**, *13*, 5354, doi:10.3390/ma13235354.

265. Palanca, M.; Oliviero, S.; Dall'Ara, E. MicroFE Models of Porcine Vertebrae with Induced Bone Focal Lesions: Validation of Predicted Displacements with Digital Volume Correlation. *J Mech Behav Biomed Mater* **2022**, *125*, 104872, doi:10.1016/j.jmbbm.2021.104872.

266. Hosseini, H.S.; Clouthier, A.L.; Zysset, P.K. Experimental Validation of Finite Element Analysis of Human Vertebral Collapse under Large Compressive Strains. *J Biomech Eng* **2014**, *136*, doi:10.1115/1.4026409.

267. Dall'Ara, E.; Peña-Fernández, M.; Palanca, M.; Giorgi, M.; Cristofolini, L.; Tozzi, G. Precision of Digital Volume Correlation Approaches for Strain Analysis in Bone Imaged with Micro-Computed Tomography at Different Dimensional Levels. *Front. Mater.* **2017**, *4*, 31, doi:10.3389/fmats.2017.00031.

268. Tozzi, G.; Peña Fernández, M.; Davis, S.; Karali, A.; Kao, A.P.; Blunn, G. Full-Field Strain Uncertainties and Residuals at the Cartilage-Bone Interface in Unstained Tissues Using Propagation-Based Phase-Contrast XCT and Digital Volume Correlation. *Materials (Basel)* **2020**, *13*, 2579, doi:10.3390/ma13112579.

269. Wehland, M.; Steinwerth, P.; Aleshcheva, G.; Sahana, J.; Hemmersbach, R.; Lützenberg, R.; Kopp, S.; Infanger, M.; Grimm, D. Tissue Engineering of Cartilage Using a Random Positioning Machine. *IJMS* **2020**, *21*, 9596, doi:10.3390/ijms21249596.

270. Disney, C.M.; Eckersley, A.; McConnell, J.C.; Geng, H.; Bodey, A.J.; Hoyland, J.A.; Lee, P.D.; Sherratt, M.J.; Bay, B.K. Synchrotron Tomography of Intervertebral Disc Deformation Quantified by Digital Volume Correlation Reveals Microstructural Influence on Strain Patterns. *Acta Biomater* **2019**, *92*, 290–304, doi:10.1016/j.actbio.2019.05.021.

271. Disney, C.M.; Mo, J.; Eckersley, A.; Bodey, A.J.; Hoyland, J.A.; Sherratt, M.J.; Pitsillides, A.A.; Lee, P.D.; Bay, B.K. Regional Variations in Discrete Collagen Fibre Mechanics within Intact Intervertebral Disc Resolved Using Synchrotron Computed Tomography and Digital Volume Correlation. *Acta Biomater* **2022**, *138*, 361–374, doi:10.1016/j.actbio.2021.10.012.

272. Clark, J.N.; Garbout, A.; Ferreira, S.A.; Javaheri, B.; Pitsillides, A.A.; Rankin, S.M.; Jeffers, J.R.T.; Hansen, U. Propagation Phase-Contrast Micro-Computed Tomography Allows Laboratory-Based Three-

Dimensional Imaging of Articular Cartilage down to the Cellular Level. *Osteoarthritis Cartilage* **2020**, *28*, 102–111, doi:10.1016/j.joca.2019.10.007.

273. Dall'Ara, E.; Barber, D.; Viceconti, M. About the Inevitable Compromise between Spatial Resolution and Accuracy of Strain Measurement for Bone Tissue: A 3D Zero-Strain Study. *J Biomech* **2014**, *47*, 2956–2963, doi:10.1016/j.jbiomech.2014.07.019.

274. Palanca, M.; Bodey, A.J.; Giorgi, M.; Viceconti, M.; Lacroix, D.; Cristofolini, L.; Dall'Ara, E. Local Displacement and Strain Uncertainties in Different Bone Types by Digital Volume Correlation of Synchrotron Microtomograms. *J Biomech* **2017**, *58*, 27–36, doi:10.1016/j.jbiomech.2017.04.007.

275. Steinmetz, N.J.; Aisenbrey, E.A.; Westbrook, K.K.; Qi, H.J.; Bryant, S.J. Mechanical Loading Regulates Human MSC Differentiation in a Multi-Layer Hydrogel for Osteochondral Tissue Engineering. *Acta Biomater* **2015**, *21*, 142–153, doi:10.1016/j.actbio.2015.04.015.

276. Schileo, E.; Dall'ara, E.; Taddei, F.; Malandrino, A.; Schotkamp, T.; Baleani, M.; Viceconti, M. An Accurate Estimation of Bone Density Improves the Accuracy of Subject-Specific Finite Element Models. *J Biomech* **2008**, *41*, 2483–2491, doi:10.1016/j.jbiomech.2008.05.017.

277. van Rossom, S.; Smith, C.R.; Thelen, D.G.; Vanwanseele, B.; Van Assche, D.; Jonkers, I. Knee Joint Loading in Healthy Adults During Functional Exercises: Implications for Rehabilitation Guidelines. *J Orthop Sports Phys Ther* **2018**, *48*, 162–173, doi:10.2519/jospt.2018.7459.

278. Meireles, S.; Wesseling, M.; Smith, C.R.; Thelen, D.G.; Verschueren, S.; Jonkers, I. Medial Knee Loading Is Altered in Subjects with Early Osteoarthritis during Gait but Not during Step-up-and-over Task. *PLoS One* **2017**, *12*, e0187583, doi:10.1371/journal.pone.0187583.

279. Gilbert, S.; Chen, T.; Hutchinson, I.D.; Choi, D.; Voigt, C.; Warren, R.F.; Maher, S.A. Dynamic Contact Mechanics on the Tibial Plateau of the Human Knee during Activities of Daily Living. *J Biomech* **2014**, *47*, 2006–2012, doi:10.1016/j.jbiomech.2013.11.003.

280. Thambyah, A.; Goh, J.C.H.; De, S.D. Contact Stresses in the Knee Joint in Deep Flexion. *Med Eng Phys* **2005**, *27*, 329–335, doi:10.1016/j.medengphy.2004.09.002.

281. Schindelin, J.; Arganda-Carreras, I.; Frise, E.; Kaynig, V.; Longair, M.; Pietzsch, T.; Preibisch, S.; Rueden, C.; Saalfeld, S.; Schmid, B.; et al. Fiji: An Open-Source Platform for Biological-Image Analysis. *Nat Methods* **2012**, *9*, 676–682, doi:10.1038/nmeth.2019.

282. Oliviero, S.; Giorgi, M.; Dall'Ara, E. Validation of Finite Element Models of the Mouse Tibia Using Digital Volume Correlation. *J Mech Behav Biomed Mater* **2018**, *86*, 172–184, doi:10.1016/j.jmbbm.2018.06.022.

283. Barber, D.C.; Hose, D.R. Automatic Segmentation of Medical Images Using Image Registration: Diagnostic and Simulation Applications. *J Med Eng Technol* **2005**, *29*, 53–63, doi:10.1080/03091900412331289889.

284. Barber, D.C.; Oubel, E.; Frangi, A.F.; Hose, D.R. Efficient Computational Fluid Dynamics Mesh Generation by Image Registration. *Med Image Anal* **2007**, *11*, 648–662, doi:10.1016/j.media.2007.06.011.

285. Khodabakhshi, G.; Walker, D.; Scutt, A.; Way, L.; Cowie, R.M.; Hose, D.R. Measuring Three-Dimensional Strain Distribution in Tendon. *J Microsc* **2013**, *249*, 195–205, doi:10.1111/jmi.12009.

286. Palanca, M.; Tozzi, G.; Cristofolini, L.; Viceconti, M.; Dall'Ara, E. Three-Dimensional Local Measurements of Bone Strain and Displacement: Comparison of Three Digital Volume Correlation Approaches. *J Biomech Eng* **2015**, *137*, doi:10.1115/1.4030174.

287. Choi, K.; Kuhn, J.L.; Ciarelli, M.J.; Goldstein, S.A. The Elastic Moduli of Human Subchondral, Trabecular, and Cortical Bone Tissue and the Size-Dependency of Cortical Bone Modulus. *J Biomech* **1990**, *23*, 1103–1113, doi:10.1016/0021-9290(90)90003-l.

288. Ciarelli, T.E.; Fyhrie, D.P.; Schaffler, M.B.; Goldstein, S.A. Variations in Three-Dimensional Cancellous Bone Architecture of the Proximal Femur in Female Hip Fractures and in Controls. *J Bone Miner Res* **2000**, *15*, 32–40, doi:10.1359/jbmr.2000.15.1.32.

289. Turunen, M.J.; Le Cann, S.; Tudisco, E.; Lovric, G.; Patera, A.; Hall, S.A.; Isaksson, H. Sub-Trabecular Strain Evolution in Human Trabecular Bone. *Sci Rep* **2020**, *10*, 13788, doi:10.1038/s41598-020-69850-x.

290. Comini, F.; Palanca, M.; Cristofolini, L.; Dall'Ara, E. Uncertainties of Synchrotron microCT-Based Digital Volume Correlation Bone Strain Measurements under Simulated Deformation. *Journal of Biomechanics* **2019**, *86*, 232–237, doi:10.1016/j.jbiomech.2019.01.041.

291. Ryan, M.K.; Oliviero, S.; Costa, M.C.; Wilkinson, J.M.; Dall'Ara, E. Heterogeneous Strain Distribution in the Subchondral Bone of Human Osteoarthritic Femoral Heads, Measured with Digital Volume Correlation. *Materials* **2020**, *13*, 4619, doi:10.3390/ma13204619.

292. Costa, M.C.; Tozzi, G.; Cristofolini, L.; Danesi, V.; Viceconti, M.; Dall'Ara, E. Micro Finite Element Models of the Vertebral Body: Validation of Local Displacement Predictions. *PLoS ONE* **2017**, *12*, e0180151, doi:10.1371/journal.pone.0180151.

293. Fu, Y.; Michopoulos, J.G.; Song, J.-H. On Investigating the Thermomechanical Properties of Cross-Linked Epoxy Via Molecular Dynamics Analysis. *Nanoscale and Microscale Thermophysical Engineering* **2017**, *21*, 8–25, doi:10.1080/15567265.2016.1263696.

294. Oral, I.; Guzel, H.; Ahmetli, G. Determining the Mechanical Properties of Epoxy Resin (DGEBA) Composites by Ultrasonic Velocity Measurement. *J of Applied Polymer Sci* **2013**, *127*, 1667–1675, doi:10.1002/app.37534.

295. McClung, A.J.W.; Tandon, G.P.; Goecke, K.E.; Baur, J.W. Non-Contact Technique for Characterizing Full-Field Surface Deformation of Shape Memory Polymers at Elevated and Room Temperatures. *Polymer Testing* **2011**, *30*, 140–149, doi:10.1016/j.polymertesting.2010.11.010.

296. Hoshino, Y.; Tamai, K.; Zhang, Y.; Yoneyama, S. Direct Measurement and Master Curve Construction of Viscoelastic Poisson's Ratio with Digital Image Correlation. *Strain* **2018**, *54*, e12294, doi:10.1111/str.12294.

297. Wang, C.C.-B.; Deng, J.-M.; Ateshian, G.A.; Hung, C.T. An Automated Approach for Direct Measurement of Two-Dimensional Strain Distributions within Articular Cartilage under Unconfined Compression. *J Biomech Eng* **2002**, *124*, 557–567, doi:10.1115/1.1503795.

298. Wang, C.C.-B.; Chahine, N.O.; Hung, C.T.; Ateshian, G.A. Optical Determination of Anisotropic Material Properties of Bovine Articular Cartilage in Compression. *J Biomech* **2003**, *36*, 339–353, doi:10.1016/s0021-9290(02)00417-7.

299. Elliott, D.M.; Narmoneva, D.A.; Setton, L.A. Direct Measurement of the Poisson's Ratio of Human Patella Cartilage in Tension. *J Biomech Eng* **2002**, *124*, 223–228, doi:10.1115/1.1449905.

300. Pritchard, R.H.; Lava, P.; Debruyne, D.; Terentjev, E.M. Precise Determination of the Poisson Ratio in Soft Materials with 2D Digital Image Correlation. *Soft Matter* **2013**, *9*, 6037, doi:10.1039/c3sm50901j.

301. Marter, A.D.; Dickinson, A.S.; Pierron, F.; Browne, M. A Practical Procedure for Measuring the Stiffness of Foam like Materials. *Exp Tech* **2018**, *42*, 439–452, doi:10.1007/s40799-018-0247-0.

302. Xu, Y.-X.; Juang, J.-Y. Measurement of Nonlinear Poisson's Ratio of Thermoplastic Polyurethanes under Cyclic Softening Using 2D Digital Image Correlation. *Polymers* **2021**, *13*, 1498, doi:10.3390/polym13091498.

303. Cash, H.; Dean, D. The Effects of Low-Dose Radiation on Articular Cartilage: A Review. *J Biol Eng* **2019**, *13*, 1, doi:10.1186/s13036-018-0125-4.

304. Cicek, E. Effect of X-Ray Irradiation on Articular Cartilage Mechanical Properties. *Acta Phys. Pol. A* **2016**, *129*, 200–202, doi:10.12693/APhysPolA.129.200.

305. Fowkes, M.M.; Das Neves Borges, P.; Cacho-Nerin, F.; Brennan, P.E.; Vincent, T.L.; Lim, N.H. Imaging Articular Cartilage in Osteoarthritis Using Targeted Peptide Radiocontrast Agents. *PLoS One* **2022**, *17*, e0268223, doi:10.1371/journal.pone.0268223.

306. Horng, A.; Stroebel, J.; Geith, T.; Milz, S.; Pacureanu, A.; Yang, Y.; Cloetens, P.; Lovric, G.; Mittone, A.; Bravin, A.; et al. Multiscale X-Ray Phase Contrast Imaging of Human Cartilage for Investigating Osteoarthritis Formation. *J Biomed Sci* **2021**, *28*, 42, doi:10.1186/s12929-021-00739-1.

307. de Bournonville, S.; Vangrunderbeeck, S.; Ly, H.G.T.; Geeroms, C.; De Borggraeve, W.M.; Parac-Vogt, T.N.; Kerckhofs, G. Exploring Polyoxometalates as Non-Destructive Staining Agents for Contrast-Enhanced Microfocus Computed Tomography of Biological Tissues. *Acta Biomater* **2020**, *105*, 253–262, doi:10.1016/j.actbio.2020.01.038.

Appendix A

Besides the studies reported in the previous chapters, additional research activities were performed during the PhD period. Most of such activities entailed the investigation of the mechanical behaviour of biological tissues involved in withstanding and deploying loads, with the final aim of better understanding the relationship between their response and their structure/composition. Moreover, a few activities entailed i) tissue engineering approaches to replace pathological tissues, ii) mathematical modelling of the mechanical response of biological tissues, and iii) a computational approach to quantify joint kinematics in physiological loading scenario. Accordingly, in the following the list of original scientific publications derived from these additional activities were reported, differentiated by topic.

- **Biological tissues**

  Marchiori G, Berni M, Cassiolas G, Vivarelli L, Lopomo NF, Fini M, Dallari D, Govoni M. Extra-Corporeal Membrane Oxygenation Cadaver Donors: What about Tissues Used as Allografts? Membranes (Basel). 2021 Jul 19;11(7):545. doi: 10.3390/membranes11070545. PMID: 34357195; PMCID: PMC8307999.

  Marchiori G, Lopomo NF, Bologna E, Spadaro D, Camarda L, Berni M, Visani A, Zito M, Zaffagnini S, Zingales M. How preconditioning and pretensioning of grafts used in ACLigaments surgical reconstruction are influenced by their mechanical time-dependent characteristics: Can we optimize their initial loading state? Clin Biomech (Bristol, Avon). 2021 Mar;83:105294. doi: 10.1016/j.clinbiomech.2021.105294. Epub 2021 Feb 27. PMID: 33667940.

  Veronesi F, Berni M (co-first), Marchiori G, Cassiolas G, Muttini A, Barboni B, Martini L, Fini M, Lopomo NF, Marcacci M, Kon E. Evaluation of cartilage biomechanics and knee joint microenvironment after different cell-based treatments in a sheep model of early osteoarthritis. Int Orthop. 2021 Feb;45(2):427-435. doi: 10.1007/s00264-020-04701-y. Epub 2020 Jul 14. PMID: 32661637.

  Berni M, Marchiori G, Cassiolas G, Grassi A, Zaffagnini S, Fini M, Lopomo NF, Maglio M. Anisotropy and inhomogeneity of permeability and fibrous network response in the pars intermedia of the human lateral meniscus. Acta Biomater. 2021 Nov;135:393-402. doi: 10.1016/j.actbio.2021.08.020. Epub 2021 Aug 16. PMID: 34411754.

  Berni M, Veronesi F, Fini M, Giavaresi G, Marchiori G. Relations between Structure/Composition and Mechanics in Osteoarthritic Regenerated Articular Tissue: A Machine Learning Approach. Int J Mol Sci 2023, 24(17), 13374. https://doi.org/10.3390/ijms241713374. PMID: 37686179.

Baleani M, Fraterrigo G, Erani P, Rota G, Berni M, Taddei F, Schileo E. Applying a homogeneous pressure distribution to the upper vertebral endplate: Validation of a new loading system, pilot application to human vertebral bodies, and finite element predictions of DIC measured displacements and strains. J Mech Behav Biomed Mater 2023, 140, 105706. https://doi.org/10.1016/j.jmbbm.2023.105706. PMID: 36841124.

- **Biomaterials**

Petretta M, Gambardella A, Boi M, Berni M, Cavallo C, Marchiori G, Maltarello MC, Bellucci D, Fini M, Baldini N, Grigolo B, Cannillo V. Composite Scaffolds for Bone Tissue Regeneration Based on PCL and Mg-Containing Bioactive Glasses. Biology (Basel). 2021 May 4;10(5):398. doi: 10.3390/biology10050398. PMID: 34064398; PMCID: PMC8147831.

- **Mathematical modelling**

Elmukashfi E, Marchiori G, Berni M, Cassiolas G, Lopomo NF, Rappel H, Girolami M, Barrera O. Model selection and sensitivity analysis in the biomechanics of soft tissues: a case study on the human knee meniscus. Adv Appl Mech. 2022; 425-511. doi: 10.48550/arXiv.2112.13434.

- **Computational approach**

Conconi M, De Carli F, Berni M, Sancisi N, Parenti-Castelli V, Monetti G. In-Vivo Quantification of Knee Deep-Flexion in Physiological Loading Condition trough Dynamic MRI. Appl Sci 2023, 13, 629. https://doi.org/10.3390/app13010629.

MODULO DI EMBARGO DELLA TESI
(da compilare solo se si richiede un periodo di segretazione della tesi)

Il/La sottoscritto/a **Matteo Berni** Nato/a il **28/03/1989**
a (indicare anche l'eventuale paese estero) **Ostiglia**
provincia di (ovvero sigla del paese estero) **Mantova, Italia**
Dottorato di Ricerca in **Technology for Health**

DICHIARA

- che il contenuto della tesi **non può essere immediatamente consultabile per il seguente motivo**

Gli approcci metodologici, i relativi risultati, e le conclusioni ad essi correlati sono al momento in fase di discussione con i ricercatori che hanno collaborato al loro sviluppo, al fine di valutare la possibilità di redigere relative pubblicazioni scientifiche su riviste peer-review.

La motivazione deve essere dettagliata e controfirmata obbligatoriamente dal Primo Supervisore di tesi
(Brevetto, segreto industriale, motivi di priorità nella ricerca, motivi editoriali, altro)

- che il testo completo della tesi potrà essere reso consultabile dopo:

□ 6 mesi dalla data di conseguimento titolo
X 12 mesi dalla data di conseguimento titolo

- che sarà comunque consultabile immediatamente l'abstract della tesi, che viene caricato in Esse3, profilo studente.

Brescia, 21/12/2023

Firma del Dichiarante

Matteo Berni

Controfirma del Primo Supervisore di tesi
per la motivazione di embargo e il periodo.

Nicola Lopomo